**Title**
Consequences of Confinement in Zeolite Acid Catalysis



**Author**
Gounder, Rajamani Pachayappan

**Publication Date**
2011

Peer reviewed|Thesis/dissertation

# Consequences of Confinement in Zeolite Acid Catalysis

By

Rajamani Pachayappan Gounder

A dissertation submitted in partial satisfaction of the

requirements for the degree of

Doctor of Philosophy

in

Chemical Engineering

in the

Graduate Division

of the

University of California, Berkeley

Committee in charge:

Professor Enrique Iglesia, Chair
Professor Alexander Katz
Professor Martin Head-Gordon

Fall 2011

Consequences of Confinement in Zeolite Acid Catalysis



by

Rajamani Pachayappan Gounder

Abstract

Consequences of Confinement in Zeolite Acid Catalysis

by

Rajamani Pachayappan Gounder

Doctor of Philosophy in Chemical Engineering

University of California, Berkeley

Professor Enrique Iglesia, Chair

The catalytic consequences of confinement within zeolite voids were examined for several elimination (alkane cracking and dehydrogenation, alkene cracking, alkanol dehydration) and addition (alkene hydrogenation, alkylation and oligomerization) reactions catalyzed by Brønsted solid acids. These reactions are mediated by cationic transition states that are confined within voids of molecular dimensions (0.4-1.3 nm) and proceed at rates that reflect the Gibbs free energies of late ion-pairs at transition states relative to those for the relevant reactants. Ion-pair stabilities depend on electrostatic interactions between organic cations and catalyst conjugate anions and on dispersion interactions between these cations and framework oxygen atoms. The former interactions are essentially unaffected by confinement, which influences weakly Brønsted acid strength, while the latter depend strongly on the sizes and shapes of voids and the species confined within them. The catalytic effects of confinement in stabilizing ion-pairs are prevalent when transition states are measured relative to gaseous reactants, but are attenuated and in some cases become irrelevant when measured with respect to confined reactants that are similar in composition and size.

Zeolite voids solvate confined species by van der Waals forces and mediate compromises in their enthalpic and entropic stabilities. Confinement is generally preferred within locations that benefit enthalpic stability over entropic freedom at low temperatures, in which free energies depend more strongly on enthalpic than entropic factors. For example, the carbonylation of dimethyl ether (400-500 K) occurs with high specificity within eight-membered (8-MR) zeolite voids, but at undetectable rates within larger voids. This specificity reflects the more effective van der Waals stabilization of carbonylation transition states within the former voids. In contrast, entropic consequences of confinement become preeminent in high temperature reactions. Alkane activation turnovers (700-800 K) are much faster on 8-MR than 12-MR protons of mordenite zeolites because the relevant ion-pairs are confined only partially within shallow 8-MR side pockets and to lesser extents than within 12-MR channels.

The site requirements and confinement effects found initially for elimination reactions were also pertinent for addition reactions mediated by ion-pair transition states of similar size

and structure. Ratios of rate constants for elimination and addition steps involved in the same mechanistic sequence (e.g., alkane dehydrogenation and alkene hydrogenation) reflected solely the thermodynamic equilibrium constant for the stoichiometric gas-phase reaction. These relations are consistent with the De Donder non-equilibrium thermodynamic treatments of chemical reaction rates, in spite of the different reactant pressures used to measure rates in forward and reverse directions. The De Donder relations remained relevant at these different reaction conditions because the same elementary step limited rates and surfaces remained predominantly unoccupied in both directions.

Rate constants for elementary steps catalyzed by zeolitic Brønsted acids reflect the combined effects of acid strength and solvation. Their individual catalytic consequences can be extricated using Born-Haber thermochemical cycles, which dissect activation energies and entropies into terms that depend on specific catalyst and reactant properties. This approach was used to show that thermal, chemical and cation-exchange treatments, which essentially change the sizes of faujasite supercage voids by addition or removal of extraframework aluminum species, influence solvation properties strongly but acid strength only weakly. These findings have clarified controversial interpretations that have persisted for decades regarding the origins of chemical reactivity and acid strength on faujasite zeolites.

Born-Haber thermochemical relations, together with Marcus theory treatments of charge transfer reaction coordinates, provide a general framework to examine the effects of reactant and catalyst structure on ion-pair transition state enthalpy and entropy. The resulting structure-function relations lead to predictive insights that advance our understanding of confinement effects in zeolite acid catalysis beyond the largely phenomenological descriptions of shape selectivity and size exclusion. These findings also open new opportunities for the design and selection of microporous materials with active sites placed within desired void structures for reasons of catalytic rate or selectivity. The ability of zeolite voids to mimic biological catalysts in their selective stabilization of certain transition states by dispersion forces imparts catalytic diversity, all the more remarkable in light of the similar acid strengths among known aluminosilicates. This offers significant promise to expand the ranges of materials used and of reactions they catalyze.

# TABLE OF CONTENTS

# LIST OF FIGURES

## CHAPTER TWO



## CHAPTER THREE

**CHAPTER FOUR**

## CHAPTER FIVE



## CHAPTER SIX

**CHAPTER EIGHT**

# LIST OF SCHEMES

## CHAPTER FIVE



## CHAPTER SIX

## CHAPTER SEVEN



## CHAPTER EIGHT

# LIST OF TABLES

## CHAPTER TWO



## CHAPTER THREE

## CHAPTER SIX



## CHAPTER SEVEN



## CHAPTER EIGHT

# ACKNOWLEDGEMENTS

First and foremost, I thank my advisor, Professor Enrique Iglesia, for his scientific and professional guidance. It has been an invaluable experience to learn from someone with such an intense and insightful approach to conducting and communicating scientific research. His mentorship has shaped me into the scholar, teacher, and writer that I am today.

Next, I acknowledge Prof. Johannes Lercher, Prof. Raul Lobo, Prof. Matthew Neurock and Dr. Stacey Zones for many stimulating and thoughtful discussions. I thank the Neurock group for teaching me about theoretical chemistry. On behalf of all LSAC group members that visited Charlottesville, I thank Matt for his concern about our personal safety when making lodging arrangements. I also thank Stacey for his guidance and appreciate the contrast it provided to Prof. Iglesia's in nearly every aspect other than scientific scholarship and rigor.

I would like to thank all LSAC members for their help and support during my time at Berkeley. I am especially grateful for having the opportunity to work closely with Aditya Bhan, a former postdoctoral researcher in the group with an infectious dedication to science. I also acknowledge Rob Carr, Andrew Jones, Josef Macht and Dante Simonetti as part of the informal acid catalysis subgroup for their helpful discussions and experimental contributions. I thank these individuals together with Dave Flaherty, Sebastian Kunz and Brett Loveless for their camaraderie, especially toward the latter stages of my graduate career.

Acknowledgements for specific technical and intellectual contributions to this research are given in each chapter; here, I thank Markus Neumann and Ivan Tiet, two undergraduate students with whom I worked, for their technical assistance. I also acknowledge with thanks the financial support from the Chevron Energy Technology Company.

Finally, I thank my friends and family for their support, Hunter for being my faithful four-legged running partner, and Nicole for handling difficult situations with grace and for reminding me of what really matters in life.

# CHAPTER ONE

# Introduction to Zeolite Acid Catalysis

## 1.1 Introduction

Acids are used widely in petrochemical refining and chemical production because they catalyze a broad range of organic chemical reactions including isomerization, cracking, and alkylation [1]. Corrosive and environmentally-harmful liquid acids, in some cases, have been replaced by solid acids (e.g., $SiO_2$-$Al_2O_3$, zeolites) because they also cause desired changes in catalytic rate or selectivity and improve processing and separation energy efficiencies [2,3]. Acidic zeolites are crystalline, microporous forms of silica containing Brønsted acidic protons that balance the anionic charges resulting from the replacement of framework Si atoms by heteroatoms of lower valence (Al, B, Fe, Ga). Historically, their catalytic allure has reflected the geometric and topological diversity of their microporous voids, which are of molecular dimensions (0.4-1.3 nm) and can select reactants, products or transition states on the basis of size and shape [4,5].

The choice and design of zeolitic solid acids to meet specific catalytic targets have relied largely on phenomenological considerations of size exclusion for several reasons. First, the interpretation of chemical reactivity on heterogeneous catalysts is invariably more complex than on homogeneous systems because catalytic turnovers, which often occur on surfaces with non-uniform active sites, are coupled with transport and thermodynamic phenomena within external fluid phases, within porous solids and at their interfaces [6]. Second, efforts to examine the independent consequences of acid strength and confinement in zeolite catalysis have often been obstructed by their inextricable contributions to the rate and equilibrium constants of elementary steps and by the presence of a diverse range of confining environments within a given microporous solid. Third, the solvation effects involved in acid-base interactions and the heterogeneity of acid sites in solid media obfuscate experimental protocols to characterize the strengths of such sites, precluding an accurate measure of acid strength analogous to the acidity functions (e.g., Hammett) defined for liquid acids [7,8].

The strength of a Brønsted acid (HA) is rigorously reflected in its deprotonation energy (DPE), defined as the energy required to separate a proton ($H^+$) and the anionic conjugate base ($A^-$) to non-interacting distances, because it is independent of probe and solvation effects. Brønsted acid-catalyzed elementary steps involve charge separation into ion-pairs at transition states [9,10]; in turn, activation free energies for these steps predominantly reflect the electrostatic penalty of separating charge at the relevant transition states. In general, ion-pairs at transition states become more stable energetically as acid sites become stronger (lower DPE values) and as organic fragments are able to accommodate more charge (higher proton affinity values). The exact sensitivities of the corresponding activation barriers to both acid site deprotonation energy and reactant proton affinity, however, depend on the amount and distribution of positive charge in organic fragments at transition states [11,12].

Brønsted acid sites within aluminosilicates are weaker and less diverse in composition and strength than in mesoporous or liquid acids [13-15]; yet, turnover rates on zeolitic acids are

often higher than on stronger acids and depend sensitively on the nanostructure of the confining voids. These effects reflect the solvation of transition states by van der Waals forces when confined within voids of molecular dimensions. Dispersion forces between framework oxygen atoms and species confined within microporous voids, which lead to compromises between enthalpies and entropies of the latter, mediate chemical reactions in a manner reminiscent of the solvation effects within enzyme pockets and with analogous consequences for catalytic specificity.

This research aims to examine how confined species are stabilized by electrostatic and dispersion forces in order to understand the fundamental consequences of confinement in zeolite acid catalysis. In doing so, it aims to extend the prevailing discourse based on size exclusion to include predictive criteria for the remarkable catalytic diversity and, in some cases, the enzyme-like specificity of zeolite voids. Reaction pathways mediated by intramolecular and intermolecular hydride transfer steps, classified generally as elimination and addition reactions, are examined here because of their ubiquitous role in the catalysis of organic substrates. Within specific contexts, these events are labeled as cracking or alkylation when alkyl groups are respectively moved within or between molecules, and dehydrogenation or hydrogen transfer when H-atoms are respectively transferred intramolecularly or intermolecularly. In spite of the specific nomenclature used to identify and distinguish these pathways from other historical elimination reactions in acid catalysis (e.g., alkanol dehydration), they become mechanistically related at the molecular level of bond-making and bond-breaking, as transition states for these elementary steps require the formation and stabilization of ion-pairs [9,10]. Thus, mechanistic details and site requirements for one of these reactions can be used to gain significant insight into a more diverse range of acid-catalyzed chemical reactions.

Catalytic turnover rates, within the context of transition state theory, depend on local void structure to the extent that confinement influences the Gibbs free energies of transition states relative to the relevant reactants. Turnover rates in Brønsted acid catalysis must be normalized rigorously by the number of protons, preferably measured directly by chemical titration and if possible using *in situ* methods, because structural surrogates for these active sites (framework Al atoms in aluminosilicates) are typically measured *ex situ* and are present in non-stoichiometric amounts. This normalization must occur prior to any attempts to mechanistically interpret the origins of catalytic reactivity or any effects of confinement on ion-pair stability, which additionally require protocols to unambiguously locate acid sites within different microporous structures. These principles are underscored throughout the analysis and discussion in this dissertation.

Measured turnover rates of monomolecular alkane activation reflect free energies of transition states stabilized within zeolite voids with respect to gaseous reactants. They increase systematically (>100-fold) with chain size for cracking of $C_3$-$C_6$ n-alkanes on H-MFI (773 K). Yet, this increase does not reflect increasing intrazeolitic concentrations caused by the more exothermic adsorption enthalpies of larger alkanes, the prevalent and incorrect notion in previous studies. A ubiquitous compensation between adsorption enthalpies and entropies leads to similar adsorption equilibrium constants for $C_3$-$C_6$ n-alkanes (<2-fold) at temperatures relevant for monomolecular activation. As discussed in Chapter 2, cracking turnover rate differences instead reflect predominantly differences in intrinsic activation entropies with n-alkane size.

The influence of local zeolite environments around Brønsted acid sites on the stability of adsorbed reactants and cationic transition states in monomolecular alkane activation is probed in Chapter 3. Born-Haber thermochemical cycles that apply generally to reactions catalyzed by Brønsted acids are used to determine the dependence of alkane activation barriers on catalyst and reactant properties, such as deprotonation energies and gas-phase proton affinities. Turnover rates for cracking and dehydrogenation of propane and n-butane differ markedly on acid sites within zeolites of different structure (H-MFI, H-FER, H-MOR) and within the two different void environments in H-MOR (8-MR side pockets, 12-MR main channels). Alkane activation transition states are only partially confined within 8-MR MOR pockets, leading to entropic gains that compensate losses in enthalpic stability to give lower free energies than for transition states in 12-MR channels. As a result, alkane cracking and dehydrogenation turnovers occur preferentially within small 8-MR pockets. Kinetic preferences for 8-MR pockets and partial confinement are stronger for dehydrogenation, with later and looser transition states, than for cracking of both propane and n-butane. Alkane cracking-to-dehydrogenation and terminal-to-central C-C bond cleavage selectivities vary systematically with the distribution of acid sites between 8-MR and 12-MR MOR environments. These findings and conclusions provide strategies to design microporous solids with acid sites positioned within specific void structures and with predictable consequences for catalytic rates and selectivities.

The effects of reactant and void structure on monomolecular alkane activation barriers and turnover rates, defined by Born-Haber thermochemical cycles, are generalized to branched alkanes in Chapter 4. Monomolecular isobutane cracking and dehydrogenation reactions also occur preferentially within 8-MR MOR pockets than in 12-MR channels, yet kinetic preferences for 8-MR locations are stronger for isobutane cracking than for dehydrogenation, in sharp contrast with the reverse trends found for n-alkanes. Ion-pair transition states for isobutane cracking are higher in energy than for dehydrogenation because protonation of C-C bonds form less stable cations than protonation of tertiary C-H bonds. Higher energy ion-pairs are also looser and occur later along reaction coordinates, consistent with the crossing potential treatments by Bell and Marcus for charge transfer reactions. The entropic benefits of partial confinement preferentially stabilize later and looser ion-pairs that mediate charge transfer reactions, irrespective of reactant identity.

Gibbs free energy differences between reactants and transition states, however, determine turnover rates within the context of transition state theory. The free energies of confined species, which are influenced by van der Waals interactions with microporous voids, depend more sensitively on enthalpic effects at low temperatures and on entropic effects at high temperatures. As discussed in Chapter 5, transition states that mediate low temperature reactions such as dimethyl ether carbonylation (400-500 K) prefer a tighter fit and enthalpic stability, while those involved in high temperature reactions such as monomolecular alkane activation (700-800 K) prefer a looser fit and entropic stability. Comparative studies of alkanes ($C_3$-$C_6$ n-alkanes, isobutane) and zeolites (H-FAU, H-FER, H-MFI, H-MOR) of different size and structure, together with Born-Haber thermochemical cycles and Marcus theory, are used to rigorously connect reactant and catalyst properties to turnover rates and selectivities in solid acid catalysis. Relative gas-phase proton affinities of alkane C-C and C-H bonds determine whether cracking or dehydrogenation transition states are higher in enthalpy and in entropy. Later and looser transition states are selectively stabilized when partially confined within shallow 8-MR MOR

pockets; as a result, reactant proton affinities cause changes in reaction selectivity with void structure. Additionally, the rotational entropy gained upon C-C bond protonation increases systematically with n-alkane size and causes intrinsic cracking turnover rates to increase concomitantly. These findings identify how voids of molecular dimensions selectively stabilize ion-pair transition states via van der Waals interactions and extend interpretations of confinement effects in zeolite catalysis beyond descriptive criteria governed largely by phenomenological consequences of size exclusion.

The mechanistic details and site requirements for monomolecular alkane dehydrogenation on acidic zeolites are extended to bimolecular alkene-$H_2$ hydrogenation reactions in Chapter 6. Ion-pair transition states also mediate propene hydrogenation at high temperatures (>700 K) on zeolitic Brønsted acid sites (H-FER, H-MFI, H-MOR) without detectable contributions from adventitious metal or cationic species. Rate constants, activation energies, and activation entropies for propene hydrogenation and monomolecular propane dehydrogenation are uniquely related to each other by thermodynamic constraints of the stoichiometric gas-phase reaction. As a result, acid sites or catalytic materials that exhibit high turnover rates (e.g., 8-MR MOR pockets) in one reaction direction (alkane dehydrogenation), do so to the same extent in the reverse direction (alkene hydrogenation). This kinetic behavior is consistent with the De Donder treatments of non-equilibrium thermodynamics, indicating that the two reactions proceed via the same sequence of elementary steps in spite of the different conditions used to measure respective rates. The De Donder treatments do not rigorously apply in such cases unless the same elementary step limits rates and the surface remains predominantly unoccupied at the different reaction conditions used to measure rates in forward and reverse directions. These findings suggest that direct reactions of $H_2$ with alkoxide species are ubiquitously involved in the scavenging of reactive or unreactive surface species during oligomerization, alkylation, and cracking reactions and account for $H_2$ effects on product selectivity and catalyst stability.

Zeolitic Brønsted acid sites (H-FER, H-MFI, H-MOR) also catalyze the direct alkylation of ethene with methane at high temperatures (>700 K), as discussed in Chapter 7. The adherence of rate constants for alkene-alkane alkylation and monomolecular alkane cracking to the De Donder relations indicate these two paths are connected mechanistically, as in the case of alkane dehydrogenation and alkene hydrogenation. Isotopic tracers show that methane-ethene alkylation occurs in parallel with ethene dimerization routes, which proceed at rates that can be predicted from the De Donder relations, gas-phase thermodynamic data and rate constants measured for its reverse reaction (monomolecular butene cracking). The selectivity between alkylation and dimerization paths depends on local void structure because their respective ion-pair transition states are different in size and structure and, in turn, are stabilized to different extents within a given channel environment.

Finally, in Chapter 8, kinetic and spectroscopic evidence is presented indicating that thermal and chemical treatments of FAU zeolites, which change the distribution of aluminum atoms between framework ($Al_f$) and extraframework ($Al_{ex}$) phases, weakly influence the solvation properties of their supercage voids but not the strength of their Brønsted acid sites. Chemical titration of $H^+$ sites with $Na^+$, with $CH_3$ groups (from dimethyl ether) and with 2,6-di-*tert*-butyl pyridine (during methanol dehydration catalysis) give similar values for the number of

protons on each sample, but much smaller values than the number of $Al_f$ atoms determined from $^{27}Al$ NMR spectra and X-ray diffraction. These findings indicate that the ubiquitous use of $Al_f$ atoms as structural proxies for $H^+$ sites has led to the inaccurate attribution of the catalytic effects of $Na^+$ titration and thermal treatments to minority 'super-acid' sites. In fact, isobutane cracking and dehydrogenation turnover rates (763 K), normalized rigorously by the number of residual protons, are independent of $Na^+$ content on all FAU samples, reflecting the stoichiometric replacement of uniform $H^+$ sites by $Na^+$. Methanol dehydration rate constants indicate that reactivity differences among FAU samples do not reflect acid strength effects but instead solvation properties. The van der Waals stabilization of confined species becomes stronger with decreasing supercage void size, as a result of $Al_{ex}$ moieties that occlude void space. These conclusions challenge previous interpretations of the controversial effects of $Na^+$ titration and thermal treatment and illustrate the distractions brought forth by the use of structural proxies for Brønsted acid sites in crystalline aluminosilicates.

## 1.2 References


(1) Corma, A. *Chem. Rev.* **1995**, *95*, 559.
(2) Venuto, P. B. *Microporous Mater.* **1994**, *2*, 297.
(3) Corma, A. *Curr. Opin. Solid State Mat. Sci.* **1997**, *2*, 63.
(4) Csicsery, S. M. *Zeolites* **1984**, *4*, 202.
(5) Degnan, T. F. *J. Catal.* **2003**, *216*, 32.
(6) Boudart, M.; Djéga-Mariadassou, G. *Kinetics of Heterogeneous Catalytic Reactions*; Princeton University Press: Princeton, **1984**.
(7) Farneth, W. E.; Gorte, R. J. *Chem. Rev.* **1995**, *95*, 615.
(8) Gorte, R. J. *Catal. Lett.* **1999**, *62*, 1.
(9) van Santen, R. A.; Kramer, G. J. *Chem. Rev.* **1995**, *95*, 637.
(10) Rigby, A. M.; Kramer, G. J.; van Santen, R. A. *J. Catal.* **1997**, *170*, 1.
(11) Macht, J.; Carr, R. T.; Iglesia, E. *J. Am. Chem. Soc.* **2009**, *131*, 6554.
(12) Carr, R. T.; Neurock, M.; Iglesia, E. *J. Catal.* **2011**, *278*, 78.
(13) Brändle, M.; Sauer, J. *J. Am. Chem. Soc.* **1998**, *120*, 1556.
(14) Eichler, U.; Brändle, M.; Sauer, J. *J. Phys. Chem. B* **1997**, *101*, 10035.
(15) Sauer, J.; Sierka, M. *J. Comput. Chem.* **2000**, *21*, 1470.

# CHAPTER TWO

## Entropy Considerations in Monomolecular Cracking of Alkanes on Acidic Zeolites


### Abstract

Compensation between adsorption entropies and enthalpies results in less than a two-fold variation in adsorption equilibrium constants for $C_3$-$C_6$ alkanes at temperatures relevant for monomolecular cracking; the size-independent activation energy for C-C bond activation in $C_3$-$C_6$ alkanes indicates that the marked increase in monomolecular cracking turnover rates observed with alkane chain size reflects a concurrent increase in activation entropies. Thermodynamic treatments for non-ideal systems rigorously describe confinement effects within zeolite channels and show that pre-exponential factors depend on solvation effects of the zeolite-host environment through variations in the thermodynamic activity of the zeolitic proton. Observed differences in rates and selectivities of monomolecular alkane activation with zeolite structure, after normalization to intrazeolitic concentrations, reflect differences in intrinsic rate constants.


### 2.1 Results and Discussion

Monomolecular cracking of alkanes via the Haag-Dessau mechanism prevalent at high temperature and low conversions (<1%) is purported to occur via cationic transition states with three-center/two-electron bonds that include both carbon atoms in the C-C bond being cleaved and a proton acting as a Brønsted acid (Scheme 2.1) [1-4]. In cracking of n-alkanes, Haag et al. [5], Narbeshuber et al. [6], Kotrel et al. [2], Babitz et al. [7], and Ramachandran et al. [8] attributed differences in turnover rates (per $H^+$) among acidic zeolites with different structures and among alkanes of varying size to differences in the prevalent concentration of physisorbed alkanes within zeolite channels. These authors concluded that no residual effects of Brønsted acid strength or of zeolite topology were required to account for variations in cracking rates with alkane size or zeolite structure.

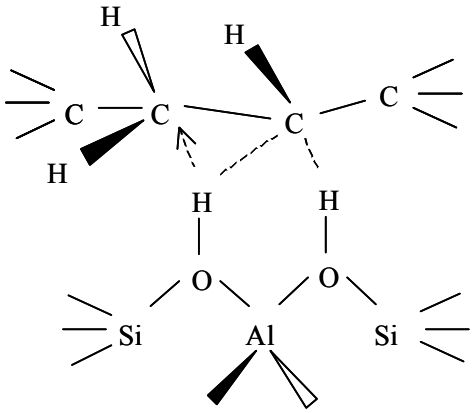


**Scheme 2.1.** Monomolecular cracking of alkanes on $H^+$ sites in zeolites proposed based on computational studies; reproduced from [3].

We comment here about how a ubiquitous compensation between alkane adsorption enthalpies ($\Delta H_{ads}$) and entropies ($\Delta S_{ads}$) leads to differences in adsorption constants that cannot possibly account for the strong effects of alkane size and zeolite structure on monomolecular cracking turnover rates at typical reaction conditions (773 K, 0.1-10 kPa alkane). We propose instead that intrinsic cracking rate constants vary with zeolite topology and carbon number. In the specific case when C-C bond activation barriers do not change with carbon number, the strong increase in cracking rates (per $H^+$) with carbon number reflects correspondingly higher activation entropies. Our analysis focuses on monomolecular cracking of $C_3$-$C_6$ alkanes; these pathways differ in concept and detail from bimolecular pathways prevalent for larger alkanes, which involve cyclopropyl carbenium-ion-like transition states and β-scission pathways mediated by hydride transfer [9-11].

Zeolites can 'solvate' molecules by confining them within channels of molecular dimensions. These channels provide a thermodynamically non-ideal environment and lead to concentrating effects mediated by equilibrium between intrachannel and external fluid phases. Transition state treatments for chemical reactions in thermodynamically non-ideal media rigorously describe the effects of solvation and intrachannel concentrations on rates of reactions catalyzed by zeolites [12]. In monomolecular cracking, alkanes adsorb onto channels ($P_z$) from the contacting fluid phase ($P_g$) in quasi-equilibrated steps and acquire the requisite conformation for reaction with Brønsted acid sites to form a precursor state ($P_{zr}$) in subsequent quasi-equilibrated steps. Alkanes in this precursor state then react with Brønsted sites via transition states that form cracking products (Scheme 2.2).

1. $P_g \rightleftharpoons P_z$
2. $P_z \rightleftharpoons P_{zr}$
3. $P_{zr} + H^+Z \rightleftharpoons ‡ \rightarrow$ Products

**Scheme 2.2.** Plausible reaction sequence for monomolecular paraffin cracking in zeolite channels.

These transition state treatments lead to cracking rates given by:

$$r = \frac{k_B T}{h} \exp\left(\frac{-\Delta G^{\circ\dagger}}{R_g T}\right) \times \frac{\gamma_{H^+Z} C_{H^+Z} \gamma_{P_{zr}} C_{P_{zr}}}{\gamma^\dagger} \tag{2.1}$$

The assumption of equilibrium between $P_{zr}$ and $P_z$,

$$K_r = \frac{a_{P_{zr}}}{a_{P_z}} = \frac{\gamma_{P_{zr}} C_{P_{zr}}}{\gamma_{P_z} C_{P_z}} \tag{2.2}$$

allows Eq. (2.1) to be recast as

$$r = \frac{k_B T}{h} K_r \frac{\gamma_{H^+Z} \gamma_{P_z}}{\gamma^\dagger} C_{H^+Z} \exp\left(\frac{\Delta S^{\circ\dagger}}{R_g}\right) \times \exp\left(\frac{-\Delta H^{\circ\dagger}}{R_g T}\right) C_{P_z} \tag{2.3}$$

in which $\Delta S^{\circ\dagger}$ and $\Delta H^{\circ\dagger}$ are the entropy and enthalpy of activation, respectively. This expression contains pre-exponential (A) and activation energy terms ($\Delta H^{\circ\dagger}$)

$$r = A\exp\left(\frac{-\Delta H^{\circ\dagger}}{R_g T}\right)C_{P_z} \tag{2.4}$$

The parameter A contains the equilibrium constant ($K_r$) and the ratio of activity coefficients $\gamma_{H^+Z}\gamma_{P_z}/\gamma^{\dagger}$; both depend on the properties of the zeolite channels and of the acid sites within them. When the precursor and the transition state are solvated to the same extent by the intrachannel environment, as is likely to occur in monomolecular cracking because of the chemical resemblance between precursors and transition states, their respective activity coefficients fortuitously cancel. Then, only the activity coefficient for the Brønsted acid sites remains in the rate equation. This activity coefficient, together with $K_r$, reflects the role of the chemical properties of acid sites and of the channel structure on pre-exponential factors. We note that this fortuitous cancellation renders rates rigorously proportional to the concentration of adsorbed alkanes within zeolite channels:

$$r = \frac{k_B T}{h} K_r \gamma_{H^+Z} C_{H^+Z} \exp\left(\frac{\Delta S^{\circ\dagger}}{R_g}\right) \times \exp\left(\frac{-\Delta H^{\circ\dagger}}{R_g T}\right) C_{P_z} = kC_{P_z} \tag{2.5}$$

in agreement with experiments [1-6].

Narbeshuber et al. [6] noted that cracking rates for $C_3$-$C_6$ alkanes on H-MFI increased markedly with size, while apparent activation energies concurrently decreased (Figs. 2.2 and 2.3; Supporting Information). The reaction conditions used led to predominantly unoccupied $H^+$ sites in H-MFI, in which case $C_{pz}$ is proportional to alkane pressure (P):

$$r = k \cdot K \cdot P \tag{2.6}$$

In Eq. (2.6), k is the cracking rate constant for alkane-derived intermediates and K is the adsorption equilibrium constant for a given alkane. K values measured from adsorption isotherms predominantly reflect interactions of alkanes via van der Waals interactions with framework oxygen atoms, because of the weak nature of the specific induced-dipole interactions of alkanes with protons [13-15]. The temperature dependences of K and k are given by:

$$K = e^{(-\Delta G_{ads}/RT)} = e^{(-\Delta H_{ads}/RT)} e^{(\Delta S_{ads}/R)} \tag{2.7}$$

$$k = Ae^{(-E/RT)} \tag{2.8}$$

Combining Eqs. (2.6), (2.7) and (2.8), we obtain the apparent rate constants ($k_{app}$), activation energies ($E_{app}$), and pre-exponential factors ($A_{app}$) in terms of the thermodynamic properties of adsorbed reactants and transition states:

$$k_{app} = k \cdot K \tag{2.9}$$

$$E_{app} = E_{act} + \Delta H_{ads} \tag{2.10}$$

$$\ln\left(A_{app}\right) = \ln\left(A_{act}\right) + \left(\Delta S_{ads} / R\right) \tag{2.11}$$

Eder and Lercher [13-15] used calorimetry and infrared spectroscopy to show that non-specific van der Waals interactions of alkanes with framework oxygens led to more negative adsorption enthalpies with increasing chain size. Narbeshuber et al. [6] noted that the lower apparent activation energies (Eq. (2.10); Fig. 2.2 Supporting Information) measured for larger alkanes predominantly reflect their more exothermic adsorption, and consequently that intrinsic activation barriers for monomolecular cracking from adsorbed reactants are very similar for $C_3$-$C_6$ alkanes ($E_{int}$ = 194-198 kJ $mol^{-1}$; 7% standard deviation). The selectivity for cleaving the various C-C bonds in n-$C_5H_{12}$ was insensitive to temperature, indicating that activation energies were similar for all C-C bonds in each alkane. These findings are in marked contrast with the strong effects of alkane size and the high specificity for activation of C-C bonds β to tertiary carbons for the case of larger alkanes reacting via cyclopropyl carbocationic transition states [9-11]. The higher monomolecular cracking reactivity of larger alkanes (n-$C_6H_{14}$ is ~120 times more reactive than $C_3H_8$ at 773 K) has been ascribed to the relative adsorption constants for n-alkane reactants [6].

The stronger adsorption of larger alkanes within a channel (or of each alkane as channels become smaller) also leads to more constrained adsorbed species and to more negative adsorption entropies. These compensation effects between $\Delta H_{ads}$ and $\Delta S_{ads}$ for adsorption of alkanes on zeolites (Fig. S.3, Supporting Information), shown by Eder and Lercher [14,15], lead, in turn, to much weaker effects of molecular size on K values than expected from measured adsorption enthalpies. The data of Eder and Lercher [14,15] on H-MFI (with the reasonable approximation that $\Delta H_{ads}$ and $\Delta S_{ads}$ are insensitive to temperature; see Supporting Information) give the K values in Table 2.1 for alkanes of varying size. We note that differences in K, which are evident at 373 K, become much smaller at temperatures relevant for monomolecular cracking (~773 K). Configurational-bias Monte Carlo simulations also concluded that compensation between entropy and enthalpy terms leads to intrazeolitic concentrations that vary by a factor of ~2 for $C_3$-$C_6$ alkanes adsorbed on MFI at 775 K [16]. Larger differences in intrazeolitic concentrations may prevail for larger alkanes ($C_8$-$C_{20}$) because of their larger heats of adsorption and of the lower temperatures at which they crack via monomolecular pathways [17]. At high temperatures (945 K), however, very similar intrazeolitic concentrations of $C_2$-$C_{20}$ alkanes in MFI primarily resulting from adsorption enthalpy-entropy compensation were computed by Maesen et al. [16]. As a result, differences in K among alkanes cannot account for the large differences in cracking rates measured for propane and n-hexane (>100-fold in rate with K values differing by less than a factor of 2). Yet, adsorption enthalpies indeed account fully for the measured differences in apparent activation energies for the cracking of these two molecules (Eq.

(2.10)) [6]. Differences of 30 kJ/mol in the true activation barriers for the monomolecular cracking of adsorbed alkanes would be required to account for the measured 100-fold cracking rate differences between $C_3H_8$ and n-$C_6H_{14}$ in contradiction with the constant values measured (194-198 ± 14 kJ $mol^{-1}$ for $C_3$-$C_6$ alkanes) [6].

**Table 2.1.** $\Delta H_{ads}$ and $\Delta S_{ads}$ for $C_3$-$C_6$ alkanes on H-MFI taken from Eder et al. [14,15]. K calculated from Eq. (2.7) by assuming $\Delta H_{ads}$ and $\Delta S_{ads}$ to be independent of temperature.

| Carbon Number | $\Delta H_{ads}$ [kJ $mol^{-1}$] | $\Delta S_{ads}$ [J $mol^{-1}K^{-1}$] | K (373 K) | K ($/10^{-4}$) (773 K) |
|---|---|---|---|---|
| 3 | -45 | -102 | 10 | 55 |
| 4 | -58 | -119 | 78 | 51 |
| 5 | -69 | -135 | 494 | 46 |
| 6 | -83 | -152 | 4410 | 46 |

**Table 2.2.** Pre-exponential factor (A), entropy of activation ($\Delta S_{act}$) and the fraction of entropy ($\Delta S_{act}$ / $|\Delta S_{ads}|$) regained at the transition state for $C_3$-$C_6$ alkane cracking on H-MFI calculated using data from Narbeshuber et al. [6] and Eder et al. [14,15] and Eq. (2.6). Turnover frequencies reported at 773 K.

| Carbon Number | TOF ($/10^{-3}$) [$s^{-1}$ $bar^{-1}$] | A ($/10^{13}$) [$s^{-1}$] | $\Delta S_{act}$ [J $mol^{-1}K^{-1}$] | $\Delta S_{act}$ / $|\Delta S_{ads}|$ |
|---|---|---|---|---|
| 3 | 1.31 | 0.57 | -8.6 | -0.08 |
| 4 | 5.80 | 2.3 | 3.0 | 0.03 |
| 5 | 22.3 | 6.2 | 11 | 0.08 |
| 6 | 60.0 | 27 | 23 | 0.15 |

Hence, differences in cracking rates (Eq. (2.6)) and rate constants (Eq. (2.9)) among $C_3$-$C_6$ alkanes at ~773 K must reflect a significant increase in pre-exponential factors (Eq. (2.8)) and activation entropies (Eq. (2.11)) with alkane chain size. Table 2.2 shows pre-exponential factors and activation entropies calculated from measured rates (after correcting for the number of C-C bonds in each molecule) and activation energies [6]. Table 2.2 also shows the fraction of the adsorption entropy loss that is ultimately recovered as adsorbed alkanes reach the transition state for monomolecular cracking. The size-independent barrier for this transition [6] suggests that the extent of charge separation and the C-H-C bond configuration in transition states, relative to those in adsorbed alkanes, is essentially independent of chain size. The larger entropy loss upon adsorption of larger alkanes ultimately leads to a larger entropy gain as they form higher energy complexes along the reaction coordinate towards the transition states required for C-C bond activation, as shown by the linear trend of $\Delta S_{act}$ with carbon number in Figure 2.1.

Monomolecular cracking reactions lead to substantial entropy gains as six internal modes are incipiently converted into three translational and rotational degrees of freedom in the transition state [18]. A part of this entropy gain arises from rocking vibrations of the two fragments, which become hindered rotations as C-C bonds are elongated in the transition state, a process inferred from *ab initio* and density functional calculations [19,20]. This process decreases the directionality and restoring forces for the movement of one fragment relative to the other. We *surmise* that the entropy gains that favor reactions of larger alkanes arise from an

increase in the number of accessible configurations from the adsorbed state to the transition state and from the mass of the two fragments involved in these hindered rotations [18].

The effects of zeolite structure on monomolecular cracking rates have also been ascribed to intrazeolitic concentration effects based on adsorption enthalpies for propane [21] and n-hexane [22], suggesting that activation barriers are unaffected by structure. We note, however, that these effects on measured rates (per $H^+$) cannot be accurately described by mere differences in intrachannel reactant concentrations stabilized by the zeolite solvent. Xu et al. [21] measured propane cracking and dehydrogenation rates (per $H^+$; 823 K, <5% conversion) on H-MFI, H-MOR, and H-BEA. Table 2.3 shows these rate data together with $\Delta H_{ads}$ and $\Delta S_{ads}$ for propane adsorption (Fig 2.4, Supporting Information) from Eder and Lercher [14,15]. Equilibrium constants (assuming H-BEA and H-MOR to have similar adsorption thermodynamics), apparent activation energies, and intrinsic rate constants are also shown for these zeolites in Table 2.3. Rate constants for monomolecular cracking of propane are clearly influenced by the structure and solvating properties of zeolite channels. These effects of environment on rate parameters reflect the thermodynamic activity of zeolitic protons (Eqs. (2.3), (2.4), (2.5)) through pre-exponential factors, but also possibly because of effects on activation energies. The systematic changes in intrinsic activation barriers reported with changes in channel structure have not been measured with the precision required to discern whether structural effects on rates arise solely from activation entropies or from combined entropy and energy changes induced by channel geometry.

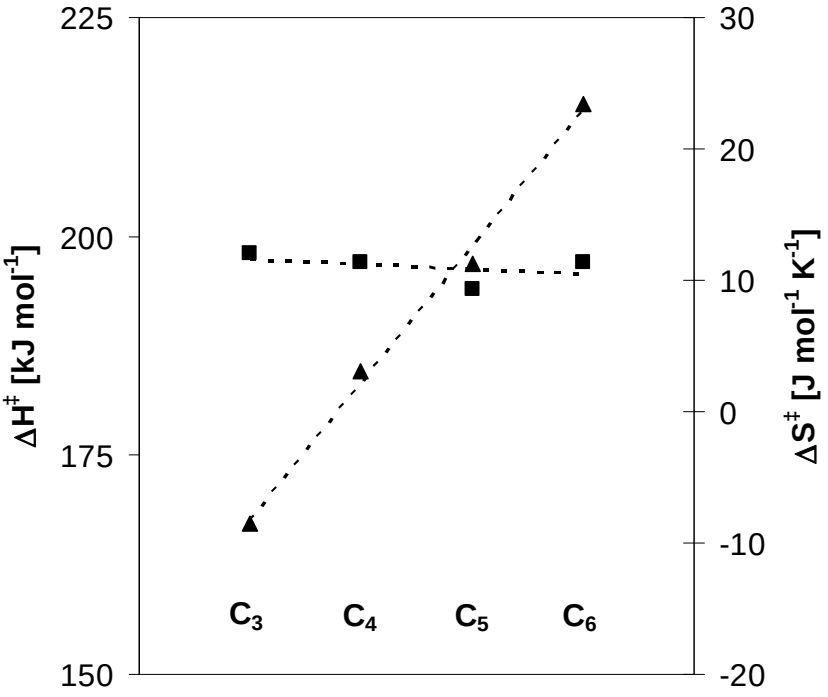


**Figure 2.1.** Activation enthalpy (■) and entropy (▲) for $C_3$-$C_6$ alkane cracking in H-MFI from data reported in Narbeshuber et al. [6].

**Table 2.3.** Intrinsic rate constant for propane cracking, $k_{int}$ on H-MFI (Si/Al=39), H-MOR (Si/Al=9.9), H-BEA (Si/Al=10.5) calculated using rates and activation energies from Xu et al. [21] and adsorption parameters from Eder et al. [14,15]. Turnover frequencies are reported as apparent turnover frequencies at 823 K.

| Zeolite | TOF ($/10^{-3}$) [$s^{-1}$ $bar^{-1}$] | $\Delta H_{ads}$ [kJ $mol^{-1}$] | $\Delta S_{ads}$ [J $mol^{-1}K^{-1}$] | K ($/10^{-3}$) (823 K) | $E_{app}$ [kJ $mol^{-1}$] | $k_{int}$ [mol (mol $H^{+}$)$^{-1}$ $s^{-1}$] |
|---|---|---|---|---|---|---|
| H-MFI | 23.6 | -45.3 | -101.9 | 3.55 | 147 | 6.6 |
| H-MOR | 22.2 | -41.3 | -84.6 | 15.9 | 145 | 1.4 |
| H-BEA | 6.9 | -41.3[a] | -84.6[a] | 15.9 | 157 | 0.4 |

[a] $\Delta H_{ads}$ and $\Delta S_{ads}$ for H-BEA considered to be similar to those for H-MOR

The predominant effects of activation entropy in monomolecular cracking rates of light alkanes have not been clearly recognized in previous studies. These effects account for the marked effects of chain size on cracking rates and to a large extent for the varying reactivity of various zeolite structures. Residual contributions from channel constraints on activation barriers cannot be discerned from available data and require more precise measurements of the effects of geometry on monomolecular cracking rates. The approach and concepts discussed here are applicable to other acid-catalyzed reactions for which the effects of molecular and channel structure on the entropy and energy of activation remain unresolved and controversial.

## 2.2 Acknowledgements

I acknowledge Aditya Bhan and Josef Macht for their helpful discussions and their significant intellectual contributions to this work. The authors acknowledge Chevron Energy Technology Company for financial support.

## 2.3 Supporting Information

### *2.3.1 Variation in Enthalpic and Entropic Adsorption Parameters with Temperature*

Entropy and enthalpy of adsorption constitute basic thermochemical data for determining the Gibbs free energy and hence adsorption equilibrium parameters. The temperature dependence of enthalpic and entropic terms is given by:

$$\Delta H_T^o = \Delta H_{T_0}^o + \int_{T_0}^{T} (\Delta C_P^o) dT \tag{2.12}$$

$$\Delta S_T^o = \Delta S_{T_0}^o + \int_{T_0}^{T} (\frac{\Delta C_P^o}{T}) dT \tag{2.13}$$

Benson has shown that $\Delta C_P^o$ for reactions tends to be very small and changes very little over intervals of 500 K [18]. In an effort to determine an upper bound for $\Delta C_P^o$ for alkane adsorption we considered $\Delta C_P^o$ for $C_3H_8 \rightarrow CH_4 + C_2H_4$, a reaction that involves carbon-carbon bond cleavage and surmise that adsorption of propane should involve a smaller value of $\Delta C_P^o$ since no

chemical bonds are broken or formed during adsorption. The $\Delta C_P^o$ for propane cracking is 5 J mol$^{-1}$ K$^{-1}$; furthermore, since $\Delta C_P^o$ is small and nearly invariant with temperature, the above equations can be integrated and recast in the form:

$$\Delta H_T^o = \Delta H_{T_0}^o + \Delta C_P^o (T - T_0) \tag{2.14}$$

$$\Delta S_T^o = \Delta S_{T_0}^o + 2.303 \Delta C_P^o \log\left(\frac{T}{T_0}\right) \tag{2.15}$$

Substituting T = 773 K, $T_0$ = 323 K, $\Delta C_P^o$ = 5 J mol$^{-1}$ K$^{-1}$, $\Delta H_{T_0}^o$ = -45 kJ mol$^{-1}$ and $\Delta S_{T_0}^o$ = -102 J mol$^{-1}$ K$^{-1}$, we calculate:

$$\Delta H(773K) = \text{ - 45 + 2.3 kJ mol}^{-1} \tag{2.16}$$

$$\Delta S(773K) = \text{ -102 + 4.4 J mol}^{-1}\text{K}^{-1} \tag{2.17}$$

With this conservative estimate for $\Delta C_P^o$, enthalpic and entropic terms change by less than 5% over a temperature range of 450 K. The K value for $C_3H_8$ adsorption changes by 15% if the above temperature dependence of $\Delta H_{ads}$ and $\Delta S_{ads}$ is included, however, we note that similar changes in K will also pertain to $C_4$-$C_6$ alkanes and the temperature-corrected K values will still vary by less than a factor of two across $C_3$-$C_6$ alkanes at temperatures relevant for monomolecular cracking.

### *2.3.2 Supplementary Figures*

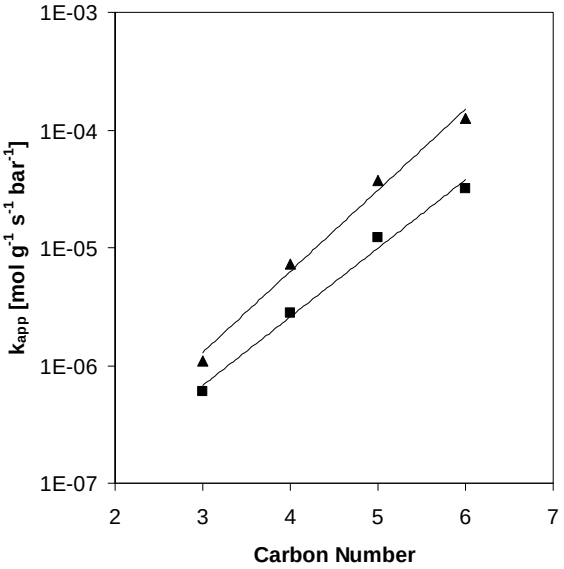


**Figure 2.2.** Apparent rate constants of cracking (▲) and dehydrogenation (■) of linear alkanes over H-MFI at 773 K vs. the carbon chain length. Adapted with permission from Narbeshuber et al. [6].

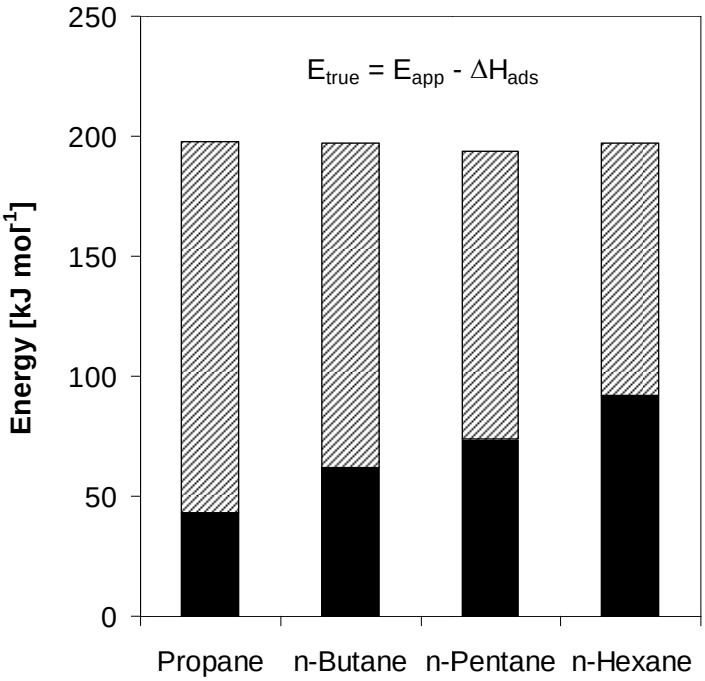


**Figure 2.3.** Absolute value of enthalpy of adsorption (■) and apparent energy of activation for cracking (▨) of n-alkanes over H-MFI. Adapted with permission from Narbeshuber et al. [6].

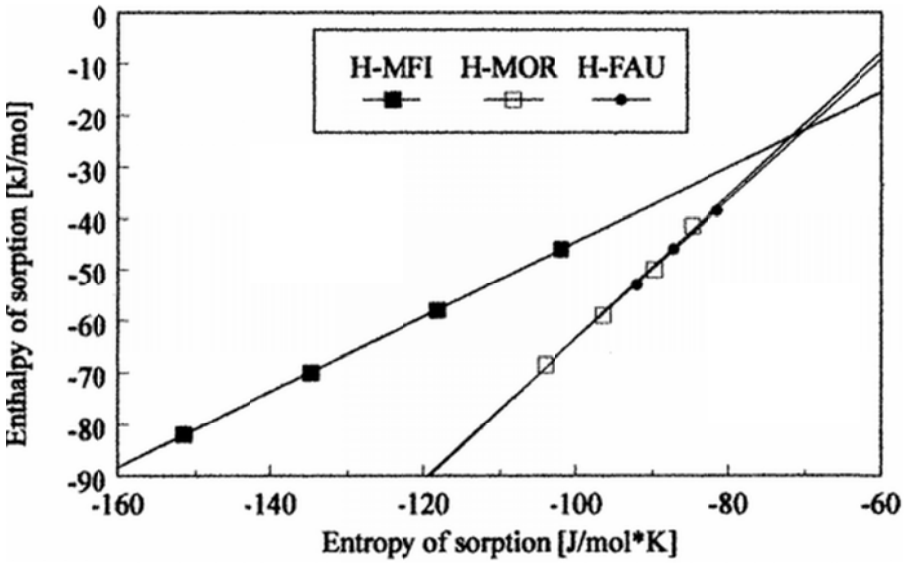


**Figure 2.4.** Interdependencies of enthalpies and entropies of sorption of n-alkanes on H-MFI, H-MOR, and H-FAU. Reproduced with permission from Eder et al. [14].

## 2.4 References


(1) Haag, W. O.; Dessau, R. M. *Proc. 8th Int. Congr. Catalysis, Berlin* **1984**, *2*, 305.
(2) Kotrel, S.; Rosynek, M. P.; Lunsford, J. H. *J. Phys. Chem. B* **1999**, *103*, 818.
(3) Lercher, J. A.; van Santen, R. A.; Vinek, H. *Catal. Lett.* **1994**, *27*, 91.
(4) Kotrel, S.; Knözinger, H.; Gates, B. C. *Microporous Mesoporous Mater.* **2000**, *35-6*, 11.
(5) Haag, W. O. *Stud. Surf. Sci. Catal.* **1994**, *84*, 1375.
(6) Narbeshuber, T. F.; Vinek, H.; Lercher, J. A. *J. Catal.* **1995**, *157*, 388.
(7) Babitz, S. M.; Williams, B. A.; Miller, J. T.; Snurr, R. Q.; Haag, W. O.; Kung, H. H. *Appl. Catal. A* **1999**, *179*, 71.
(8) Ramachandran, C. E.; Williams, B. A.; van Bokhoven, J. A.; Miller, J. T. *J. Catal.* **2005**, *233*, 100.
(9) Sie, S. T. *Ind. Eng. Chem. Res.* **1992**, *31*, 1881.
(10) Sie, S. T. *Ind. Eng. Chem. Res.* **1993**, *32*, 403.
(11) Sie, S. T. *Ind. Eng. Chem. Res.* **1993**, *32*, 397.
(12) Madon, R. J.; Iglesia, E. *J. Mol. Catal. A* **2000**, *163*, 189.
(13) Eder, F.; Lercher, J. A. *J. Phys. Chem. B* **1997**, *101*, 1273.
(14) Eder, F.; Stockenhuber, M.; Lercher, J. A. *J. Phys. Chem. B* **1997**, *101*, 5414.
(15) Eder, F.; Lercher, J. A. *Zeolites* **1997**, *18*, 75.
(16) Maesen, T. L. M.; Beerdsen, E.; Calero, S.; Dubbeldam, D.; Smit, B. *J. Catal.* **2006**, *237*, 278.
(17) Wei, J. *Chem. Eng. Sci.* **1996**, *51*, 2995.
(18) Benson, S. W. *Thermochemical Kinetics*; John Wiley & Sons, Inc.: New York, **1976**.
(19) Zheng, X. B.; Blowers, P. *J. Phys. Chem. A* **2005**, *109*, 10734.
(20) Zygmunt, S. A.; Curtiss, L. A.; Zapol, P.; Iton, L. E. *J. Phys. Chem. B* **2000**, *104*, 1944.
(21) Xu, B.; Sievers, C.; Hong, S. B.; Prins, R.; van Bokhoven, J. A. *J. Catal.* **2006**, *244*, 163.
(22) van Bokhoven, J. A.; Williams, B. A.; Ji, W.; Koningsberger, D. C.; Kung, H. H.; Miller, J. T. *J. Catal.* **2004**, *224*, 50.

# CHAPTER THREE

# Catalytic Consequences of Spatial Constraints and Acid Site Location for Monomolecular Alkane Activation on Zeolites


## Abstract

The location of Brønsted acid sites within zeolite channels strongly influences reactivity because of the extent to which spatial constraints determine the stability of reactants and of cationic transition states relevant to alkane activation catalysis. Turnover rates for monomolecular cracking and dehydrogenation of propane and n-butane differed among zeolites with varying channel structure (H-MFI, H-FER, H-MOR) and between OH groups within 8-membered ring (8-MR) side pockets and 12-MR main channels in H-MOR. Measured monomolecular alkane activation barriers depended on catalyst and reactant properties, such as deprotonation enthalpies and proton affinities, respectively, consistent with Born-Haber thermochemical cycles that define energy relations in acid catalysis. Monomolecular alkane cracking and dehydrogenation turnovers occurred with strong preference on acid sites contained within smaller 8-MR pockets in H-MOR, while rates on sites located within 12-MR channels were much lower and often undetectable. This strong specificity reflects transition states that are confined only partially within 8-MR pockets; as a result, entropic gains compensate enthalpic penalties caused by their incomplete containment to give a lower free energy for transition states within small 8-MR side pockets. These effects of entropy are stronger for dehydrogenation, with a later and looser transition state, than for cracking in the case of both propane and n-butane; therefore, selectivity can be tuned by the selective positioning or titration of OH groups within specific environments, the number of which was assessed in H-MOR by rigorous deconvolution of their infrared spectra. Specifically, cracking-to-dehydrogenation ratios for propane and n-butane were much smaller and terminal-to-central C-C bond cleavage ratios for n-butane were much larger on 8-MR than on 12-MR acid sites as a result of partial confinement, a concept previously considered phenomenologically as pore mouth catalysis. These marked effects of spatial constraints and of entropic factors on acid site reactivity and selectivity, also inferred for MFI from titration of OH groups by $Na^+$, have not been previously proposed or recognized and appear to be unprecedented in hydrocarbon catalysis. These findings and their conceptual interpretations open opportunities for the design of microporous solids by the rational positioning of acid sites within specific channel locations and with predictable consequences for catalytic rates and selectivities.


## 3.1 Introduction

The design and selection of acidic zeolites for specific reactions requires that we consider the consequences of the number, structure, and acid strength of active sites, and of intrachannel environments, within which sites stabilize adsorbed intermediates and transition states relevant to chemical transformations. At an early and defining moment in catalysis by zeolites, cracking rates of n-hexane on H-MFI zeolites were reported to depend only on the number of acid sites [1,2], irrespective of Al content and, by inference, of the distribution of Al among the twelve

crystallographic T-sites in MFI. Quantum chemical descriptions, however, indicated that the location of the Al atoms in MFI influenced Brønsted acid strength and reactivity [3]. Later studies rigorously accounted for long-range electrostatic interactions and found that deprotonation enthalpies (DPE) were instead similar for all Al sites in MFI (1229-1240 kJ $mol^{-1}$) [4,5]. Acid strength, reflected rigorously in these DPE values, strongly influences activation barriers for reactions involving cationic transition states that are stabilized by electrostatic interactions with framework oxygens, which also stabilize protons removed in deprotonation events [6,7]. In contrast, acid strength influences only weakly reactions requiring activated complexes with low charge, which are stabilized by covalent bonds with the zeolite framework [6,7].

We have recently reported the remarkable enzyme-like specificity of eight-membered ring (8-MR) channels in MOR zeolites for CO insertion into methyl groups, an elementary step that involves cationic transition states [8]. In contrast, the exchange of $CD_4$ with OH, which proceeds via essentially uncharged covalent transition states, showed similar rates on Brønsted acid sites present within 8-MR and 12-MR environments in MOR zeolites [9]. Strong effects of the local environment around Brønsted acid sites are not evident in previous studies of hydrocarbon catalysis, for which some studies have claimed no effects of Al content and, by inference, of their location [1,2]. Any catalytic consequences of site location, however, are essential to choose and synthesize inorganic microporous structures with specific reactivity and selectivity.

Here, we report evidence for strong effects of local structure on the catalytic cracking and dehydrogenation of alkanes on acidic zeolites. These reactions can occur via bimolecular pathways involving carbenium-ion chain cycles [10,11] or via monomolecular routes requiring penta-coordinated carbonium ions at the transition state. Monomolecular routes prevail at low alkane conversions and pressures [12,13] and form $H_2$, smaller alkanes, and the respective alkenes as primary products (propane [14]; n-butane [15,16]). Isotopic studies indicate that products of monomolecular pathways initiate bimolecular routes mediated by carbenium ions, which then propagate via hydride transfer [17,18]. Monomolecular alkane reactions are useful probes of the catalytic consequences of confinement in acid catalysis, because they form relatively unreactive primary products of cracking (e.g., $CH_4$ and $C_2H_4$ from $C_3H_8$) and dehydrogenation (e.g., $C_3H_6$ and $H_2$ from $C_3H_8$) events. Deviations from equimolar yields provide a rigorous experimental kinetic marker for bimolecular or secondary reactions.

We interpret measured rate parameters here using thermochemical cycles that rigorously define the contributions of enthalpy and entropy to chemical reactions catalyzed by Brønsted acids. This approach illustrates the essential role of spatial constraints in the stabilization of adsorbed reactants and of ion-pairs relevant for the late transition states prevalent in monomolecular alkane reactions. Energy-entropy tradeoffs at the transition state, mediated by local spatial constraints, are essential contributors to the enzyme-like specificity of certain locations within microporous solids for alkane activation on Brønsted acid sites.

## 3.2 Methods

### *3.2.1 Catalyst Synthesis*

MFI, FER and MOR zeolite samples (Table 3.1) in their $NH_4^+$ form were treated in flowing dry air (2.5 $cm^3$ $g^{-1}$ $s^{-1}$, zero grade, Praxair) by increasing the temperature to 773 K (0.0167 K $s^{-1}$) and holding for 4 h to convert $NH_4^+$ to $H^+$. H-zeolites were pelleted, crushed, and sieved to retain 180-250μm (60-80 mesh) aggregates. Zeolite samples (~14 g) were exchanged with $Na^+$ cations to varying extents using 0.5 L aqueous solutions with different $NaNO_3$ (99%, EMD Chemicals, 0.014-2.44 M) concentrations at 353 K for 12 h. The exchanged zeolite samples were rinsed with 2 L deionized water, isolated by filtration, and treated in flowing dry air as described above. Si, Al, Na and trace metal contents (Table 3.1) were determined by inductively coupled plasma optical emission spectroscopy (ICP-OES; Galbraith Laboratories). The amounts of Al in framework and extra-framework locations (Table 3.1) were measured by $^{27}$Al MAS NMR spectroscopy. Experimental methods and NMR spectra are shown in Section 3.6.1 of the supporting information.

**Table 3.1.** Elemental composition and site and structure characterization of zeolite samples.

| Zeolite | Source | Si/Al Ratio[a] | Na/Al Ratio[a] | $Al_{EF}$[b] (%) | $L_1$ IR Band Area[c] | $L_2$ IR Band Area[c] | $OH_{8\text{-}MR}$[d] (%) | $OH_{12\text{-}MR}$[d] (%) |
|---|---|---|---|---|---|---|---|---|
| H-FER | Zeolyst | 10.3 | 0.002 | 15 | 2.1 | 2.9 | - | - |
| H-MFI-1 | Chevron | 19 | - | 24 | 0.6 | 0.1 | - | - |
| H-MFI-2 | Zeolyst | 16.5 | 0.004 | 12 | 0.9 | 0.5 | - | - |
| $H_{85}Na_{15}$MFI-2 | Zeolyst | 16.1 | 0.15 | 12 | - | - | - | - |
| H-MFI-3 | Zeolyst | 25 | - | 11 | 0.3 | < 0.1 | - | - |
| H-MFI-4 | Zeolyst | 40 | - | 11 | 0.2 | < 0.1 | - | - |
| H-MOR-T | Tosoh | 8.9 | 0.001 | 19 | 5.0 | 8.6 | 78 | 22 |
| H-MOR-S | Sud-Chemie | 10.1 | 0.001 | 21 | 10.4 | 4.9 | 60 | 40 |
| H-MOR-Z | Zeolyst | 10.0 | 0.001 | 22 | 2.8 | 3.9 | 56 | 44 |
| $H_{83}Na_{17}$MOR-Z | Zeolyst | 10.0 | 0.17 | 22 | - | - | 36 | 64 |
| $H_{73}Na_{27}$MOR-Z | Zeolyst | 10.0 | 0.27 | 22 | - | - | 27 | 73 |
| $H_{59}Na_{41}$MOR-Z | Zeolyst | 10.0 | 0.41 | 22 | - | - | 20 | 80 |
| $H_{45}Na_{55}$MOR-Z | Zeolyst | 10.0 | 0.55 | 22 | - | - | 13 | 87 |

[a]Determined from elemental analysis (ICP-OES; Galbraith Laboratories).
[b]Extra-framework Al content ($Al_{EF}$) determined from $^{27}$Al MAS NMR spectra (details given in Section 3.6.1 of the supporting information).
[c]Areas of $L_1$ (2224 $cm^{-1}$) and $L_2$ (2196 $cm^{-1}$) infrared bands for CO adsorbed at 123 K on Lewis acid sites (details shown in Section 3.6.2 of the supporting information). Areas (x $10^3$) are normalized to Si-O-Si overtone band areas (2100-1750 $cm^{-1}$).
[d]Distribution of acid sites in MOR samples determined from infrared spectral band deconvolution [8].

### *3.2.2 Infrared Assessment of the Number and Location of Intracrystalline Hydroxyl Groups and Lewis Acid Centers*

Infrared spectra were collected using a Nicolet NEXUS 670 infrared spectrometer equipped with a Hg-Cd-Te (MCT) detector. Spectra were measured with 2 $cm^{-1}$ resolution in the 4000-400 $cm^{-1}$ range by averaging 64 scans. Self-supporting wafers (~20-40 mg) were sealed within a quartz vacuum infrared cell equipped with NaCl windows. Samples were treated in

flowing dry air (1.67 $cm^3$ $s^{-1}$, zero grade, Praxair) by heating to 723 K (0.033 K $s^{-1}$), holding for 2 h, and then evacuating for at least 2 h at 723 K using a diffusion pump (<0.01 Pa dynamic vacuum; Edwards E02) before cooling to 303 K in vacuum and collecting spectra.

Strong ($L_1$) and weak ($L_2$) Lewis acid centers were measured from infrared spectra of CO adsorbed at 123 K [19], and specifically from CO bands at 2224 and 2196 $cm^{-1}$, respectively [20]. A constant flow of liquid $N_2$ was used to cool zeolites to 123 K before dosing CO (UHP, Praxair) incrementally, without intervening evacuation; spectra were collected 120 s after each CO dose. Integrated $L_1$ and $L_2$ band areas (normalized to those for Si-O-Si overtones; 2100-1750 $cm^{-1}$) are proportional to the density of Lewis centers (per g) in the sample and are shown in Table 3.1. The characterization of Lewis acid centers by these infrared methods is treated in more detail in Section 3.6.2 of the supporting information.

### *3.2.3 Catalytic Rates of Monomolecular Alkane Activation*

Steady-state alkane cracking and dehydrogenation rates were measured in a tubular packed-bed quartz reactor (7.0 mm inner diameter) with plug-flow hydrodynamics under differential conditions (<2% conversion). Catalyst samples (0.02-0.2 g) were supported on a coarse quartz frit and the temperature was maintained with a resistively-heated three-zone furnace (Applied Test Systems Series 3210). Each zone was controlled independently by Watlow controllers (96 Series); catalyst temperatures were recorded using K-type thermocouples contained within a thermowell placed at the external surface of the quartz reactor.

Catalysts were treated in a mixture of 5% $O_2$ in He (16.7 $cm^3$ $g^{-1}$ $s^{-1}$, 99.999%, Praxair) at 803 K (0.0167 K $s^{-1}$) for 2 h before catalytic measurements. The samples were then treated in He (16.7 $cm^3$ $g^{-1}$ $s^{-1}$, 99.999%, Praxair) for 0.5 h, while propane (10% $C_3H_8$, 99.999%, diluted in 5% Ar, 85% He, Praxair) or n-butane (10% n-$C_4H_{10}$, 99.99%, diluted in 5% Ar, 85% He, Praxair) reactants were sent via heated transfer lines held at 423 K to a gas chromatograph (Agilent HP-6890GC) for calibration purposes. Reactants and products were separated using GS-AL\KCl capillary (0.530 mm ID x 50 m; Agilent) and HayeSep DB packed columns (100-120 mesh, 10 ft.; Sigma-Aldrich); their respective effluents were measured by flame ionization and thermal conductivity detection.

Reactant pressures were changed by dilution with He (99.999%, Praxair). Reactant flows were varied ($10^{-6}$-$10^{-4}$ mol alkane $g^{-1}$ $s^{-1}$) to probe primary and secondary pathways and any contributions from bimolecular or secondary reactions. The absence of bimolecular pathways and secondary reactions was confirmed by the equimolar ratios of cracking products ($1.0 \pm 0.1$) measured for $C_3H_8$ ($C_2H_4/CH_4$) and n-$C_4H_{10}$ ($C_3H_6/CH_4$, $C_2H_4/C_2H_6$) reactants, which did not depend on space velocity, and by the absence of hydrocarbons larger than the respective alkane reactants. Activation energies and pre-exponential factors were obtained from rate constants measured as a function of temperature (718-778 K). Rates and selectivities measured after ~100 ks on stream were similar (within 5%) to those at the start of each experiment on all catalyst samples. Transport corruptions of measured rates were ruled out using Mears criteria; the detailed analysis is shown in Section 3.6.3 of the supporting information.

## 3.3 Results and Discussion

### *3.3.1 Assessment of Kinetic Parameters for Monomolecular Propane Cracking and Dehydrogenation Using Transition State Theory and Thermochemical Cycles*

Table 3.2 shows rate constants (per $H^+$) for propane cracking and dehydrogenation and cracking-to-dehydrogenation rate ratios at 748 K on H-MFI, H-FER, and H-MOR, together with activation energies and entropies calculated from the temperature dependence of these rate constants. Monomolecular rate constants differ among these zeolites (by up to factors of 4) and even among H-MOR samples with similar Si/Al ratios but of different provenance (by up to factors of 2). Measured activation energies for dehydrogenation were consistently higher than for cracking (by 25-42 kJ $mol^{-1}$) on all samples, in contrast with activation energies for $C_3H_8$ dehydrogenation on H-MFI that vary widely among previous reports [21-26]. Measured activation entropies were also higher for dehydrogenation than for cracking, consistent with later transition states for dehydrogenation, in which the H-H bond is nearly formed at the transition state [27]. Rate parameters differ among these zeolites because their transition states differ in their energy and entropy relative to the gas-phase alkanes, as we discuss later in the context of the relevant thermochemical cycles; as a result, these rate parameters probe specific and subtle effects of local environment on the structure and energy of these transition states.

Accepted pathways for monomolecular reactions of alkanes (B) on intrazeolite Brønsted acids ($H^+Z^-$) are depicted schematically in Scheme 3.1a. Alkanes adsorb from the extracrystalline phase (B(g)) onto a Brønsted acid site within zeolite channels (B(z)) in quasi-equilibrated and essentially non-activated steps. Transition state formalisms require that monomolecular rearrangements of adsorbed alkanes on Brønsted acid sites depend rigorously on the thermodynamic activity of reactants [28]. These treatments, shown in greater detail in Section 3.6.4 of the supporting information, give a rate expression of the form:

$$r = \frac{k_B T}{h} \exp\left(\frac{-\Delta G^{\circ\dagger}}{R_g T}\right) \times \frac{\gamma_{H^+Z} C_{H^+Z} \gamma_{B_z} C_{B_z}}{\gamma_{\dagger}} . \quad (3.1)$$

**Table 3.2.** Monomolecular propane cracking and dehydrogenation rate constants ($k_{meas}$) and cracking-to-dehydrogenation (C/D) rate ratios at 748 K and measured activation energies ($E_{meas}$) and entropies ($\Delta S_{meas}$) on acidic zeolites.

| **Zeolite** | **$k_{meas}$ (/ $10^{-3}$ mol [(mol $H^+$)-s-bar]$^{-1}$)** | | **C/D Ratio** | **$E_{meas}$ (kJ $mol^{-1}$)** | | **$\Delta S_{meas}$ (J $mol^{-1}$ $K^{-1}$)** | |
|---|---|---|---|---|---|---|---|
| | Cracking | Dehyd. | | Cracking[a] | Dehyd.[b] | Cracking[c] | Dehyd.[d] |
| H-MFI | 2.0 | 2.1 | 0.9 | 158 | 200 | -99 | -54 |
| H-FER | 6.2 | 3.2 | 2.0 | 157 | 195 | -91 | -57 |
| H-MOR-T | 2.0 | 3.0 | 0.7 | 160 | 189 | -97 | -71 |
| H-MOR-S | 1.3 | 1.9 | 0.7 | 167 | 192 | -93 | -66 |
| H-MOR-Z | 1.4 | 2.2 | 0.7 | 160 | 198 | -99 | -56 |

[a]Errors are ± 5 kJ $mol^{-1}$.
[b]Errors are ± 7 kJ $mol^{-1}$.
[c]Errors are ± 8 J $mol^{-1}$ $K^{-1}$.
[d]Errors are ± 10 J $mol^{-1}$ $K^{-1}$.

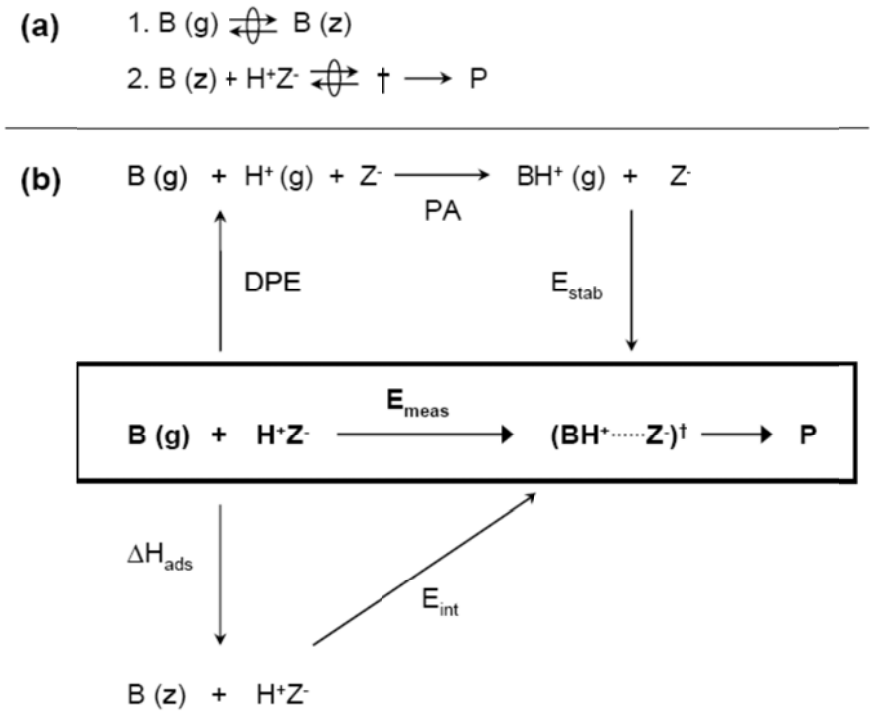


**Scheme 3.1.** (a) Reaction sequence for monomolecular alkane activation (B denotes a reactant base and P denotes products) on Brønsted acid sites located within zeolite channels ($H^+Z^-$). (b) Corresponding thermochemical cycle for monomolecular reactions of alkanes in zeolite channels. Measured activation energies for ($E_{meas}$) are related to zeolite deprotonation enthalpies (DPE), gas-phase proton affinities (PA) and ion-pair stabilization energies within zeolite channels ($E_{stab}$). The dependence of intrinsic activation energies ($E_{int}$) on adsorption enthalpies ($\Delta H_{ads}$) and $E_{meas}$ (Eq. (3.6)) is also shown.

Monomolecular alkane activation pathways require high temperatures, which favor low intrazeolite concentrations ($C_{Bz}$) and $H^+$ sites that remain essentially unoccupied during catalysis (evidence in Section 3.6.3 of the supporting information). Calorimetric, gravimetric and infrared studies on various acidic zeolites have shown that $C_3$-$C_6$ n-alkanes adsorb specifically onto Brønsted acid sites with adsorption enthalpies that remain constant up to saturation coverages at all $H^+$ sites [29-31]. Thus, Langmuir adsorption models accurately describe the siting of alkanes onto Brønsted acid sites of uniform binding properties. The concentrations (per active site) ($C_i$) of adsorbed alkanes ($B_z$) and transition states (†) are related to their real ($P_B$) or hypothetical ($P_†$) gas-phase pressures by:

$$C_i = \frac{K_i P_i}{1 + K_B P_B + K_† P_†}, \tag{3.2}$$

in which the $K_i$ terms are their adsorption constants. Thermodynamic treatments of Langmuir surfaces give activity coefficients ($\gamma_i$) for each species of the form (derived in detail in Section 3.6.4 of the supporting information):

$$\gamma_i = a_i^o \left(1 + K_B P_B + K_\dagger P_\dagger\right), \tag{3.3}$$

where $a_i^o$ is the thermodynamic activity at the reference state; activity coefficients (Eq. (3.3)) include a configurational entropy term that reflects the number of configurations of N molecules adsorbed onto M adsorption sites [32]. Reaction rates are strictly proportional to intrazeolite alkane concentrations ($C_{Bz}$) when activity coefficients for alkane reactants ($\gamma_{Bz}$) and transition states ($\gamma_\dagger$) cancel in Eq. (3.1); this occurs in this case, irrespective of their structure and solvation, because both species reside on the same site and therefore have identical activity coefficients. Moreover, $C_{H^+Z}$ and $\gamma_{H^+Z}$ approach unity because $H^+$ sites are predominantly unoccupied during monomolecular reactions, for which the rates given by Eq. (3.1) become:

$$r = \frac{k_B T}{h} \exp\left(\frac{\Delta S^{o\dagger}}{R_g}\right) \times \exp\left(\frac{-\Delta H^{o\dagger}}{R_g T}\right) C_{B_z}. \tag{3.4}$$

Intrazeolite concentrations ($C_{Bz}$) become proportional to external pressures ($P_B$) and to the adsorption constants ($K_B$) in the low-coverage limit (Eq. (3.2)), where reaction rates (Eq. (3.4)) are given by:

$$r = k_{\text{int}} \cdot K_B \cdot P_B. \tag{3.5}$$

Measured activation energies and pre-exponential factors are then given by:

$$E_{meas} = E_{\text{int}} + \Delta H_{ads}, \tag{3.6}$$

$$\ln(A_{meas}) = \ln(A_{\text{int}}) + (\Delta S_{ads} / R), \tag{3.7}$$

$$\Delta S_{meas} = \Delta S_{\text{int}} + \Delta S_{ads}, \tag{3.8}$$

where $\Delta H_{ads}$ and $\Delta S_{ads}$ are the enthalpy and entropy of adsorption, respectively, and $E_{meas}$ and $A_{meas}$ ($\Delta S_{meas}$) are measured rate parameters referenced to gas phase alkanes. $E_{int}$ and $A_{int}$ ($\Delta S_{int}$) are intrinsic rate parameters for elementary reactions of adsorbed alkanes relating the properties of adsorbed reactants to the corresponding transition states [21,33-36]. We define the measured entropy of activation as:

$$\Delta S_{meas} = R \cdot [\ln(A_{meas}) - \ln(k_B T / h)], \tag{3.9}$$

where $A_{meas}$ is rigorously normalized by the number of acid sites and by the number of bonds available for each type of reaction. These measured activation entropies reflect a mathematical manipulation that simply redacts $A_{meas}$ in terms of thermodynamic properties of reactants and transition states.

Table 3.3 shows intrinsic activation energies and entropies for monomolecular propane cracking and dehydrogenation on H-MFI, H-FER, and H-MOR; these values were estimated

from measured rate constants (Table 3.2), using Eqs. (3.6)-(3.9) and previously reported adsorption enthalpies and entropies [29,30]. Intrinsic activation barriers for monomolecular $C_3H_8$ cracking were similar on H-MFI, H-FER and H-MOR (201-208 kJ $mol^{-1}$; Table 3.3), in agreement with previous data for $C_3H_8$ cracking on H-MFI (187-200 kJ $mol^{-1}$) [21-26]. Their magnitude and insensitivity to zeolite structure also agree with previous reports for $C_3H_8$ cracking on H-MFI, H-MOR, H-BEA and H-FAU [26] and for the cracking of larger $C_3$-$C_{20}$ n-alkanes on H-MFI [21,33,37]. Energies of monomolecular cracking transition states (reflected in $E_{meas}$) relative to those of adsorbed reactants are independent of chain size and of local channel environments, which appear to stabilize adsorbed reactants and transition states identically. As a result, intrinsic activation barriers ($E_{int}$) for cracking reactions on different zeolite structures are similar within the accuracy of the rate and adsorption data used to estimate them (Table 3.3), as long as adsorption and rate measurements probe the same intrachannel environment.

Intrinsic activation energies for monomolecular propane dehydrogenation were also similar on H-MFI, H-FER, and H-MOR (229-245 kJ $mol^{-1}$; Table 3.3) and larger than for cracking (by 25-42 kJ $mol^{-1}$). These data contrast previous reports of intrinsic dehydrogenation barriers that varied widely for $C_3H_8$ among various H-MFI studies (135-205 kJ $mol^{-1}$) [21-26] and which ranged from smaller barriers (by 60 kJ $mol^{-1}$) [21-23] than for cracking to similar values [24,25] or even slightly larger values [26] than cracking barriers. Density functional theory (DFT) studies on small T3 zeolite clusters [27] concluded that transition states are ~60 kJ $mol^{-1}$ higher in energy for dehydrogenation than cracking of propane. Figure 3.1 compares the temperature dependence of propane cracking-to-dehydrogenation rate ratios on H-MFI with DFT estimates [27] and previous data [21,24,26]. Only activation barriers were reported in DFT studies [27], so we have used the pre-exponential factors (shown as $\Delta S_{meas}$ in Table 3.2) measured in this study to estimate cracking-to-dehydrogenation rate ratios from DFT activation barriers. All previous data show weaker temperature effects on rate ratios than reported here and predicted by theory (Fig. 3.1). As we discuss below, higher barriers for dehydrogenation relative to cracking are also expected from the relative stabilities of protonated C-H and C-C bonds in $C_3H_8$ to form gas-phase structures resembling those in the respective transition states for these two reactions.

**Table 3.3.** Intrinsic activation energies ($E_{int}$) and entropies ($\Delta S_{int}$) for monomolecular propane cracking and dehydrogenation on acidic zeolites.

| Zeolite | $\Delta H_{ads}$ (/ kJ $mol^{-1}$) | $\Delta S_{ads}$ (/ J $mol^{-1}$ $K^{-1}$) | $E_{int}$ (/ kJ $mol^{-1}$) | | $\Delta S_{int}$ (/ J $mol^{-1}$ $K^{-1}$) | |
|---|---|---|---|---|---|---|
| | | | Cracking[a] | Dehyd.[b] | Cracking[c] | Dehyd.[d] |
| H-MFI | -45[e] | -102[e] | 204 | 245 | 3 | 47 |
| H-FER | -49[f] | -109[f] | 205 | 244 | 17 | 51 |
| H-MOR-T | -41[g] | -85[g] | 202 | 229 | -12 | 13 |
| H-MOR-S | -41[g] | -85[g] | 208 | 234 | -8 | 18 |
| H-MOR-Z | -41[g] | -85[g] | 201 | 239 | -14 | 28 |

[a]Errors are ± 7 kJ $mol^{-1}$.
[b]Errors are ± 9 kJ $mol^{-1}$.
[c]Errors are ± 10 J $mol^{-1}$ $K^{-1}$.
[d]Errors are ± 13 J $mol^{-1}$ $K^{-1}$.
[e]Adsorption data reported in [29].
[f]Adsorption data reported in [30].
[g]Adsorption data reported *only* for 12-MR channels of H-MOR in [29].

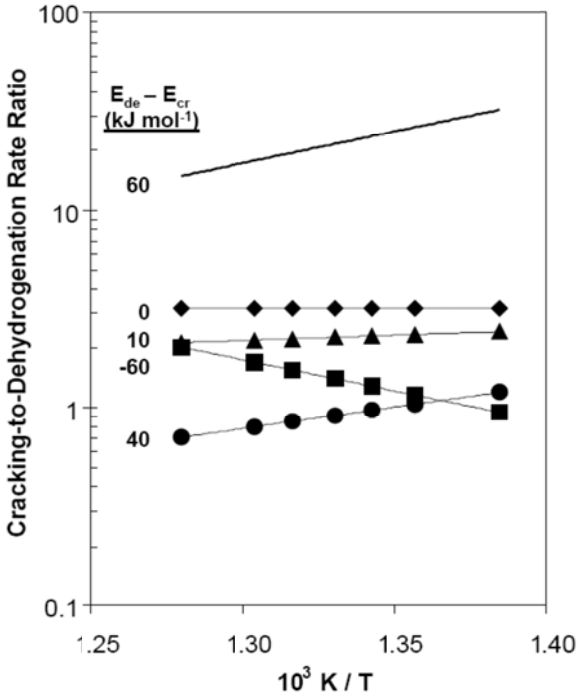


**Figure 3.1.** Temperature dependence of monomolecular propane cracking-to-dehydrogenation rate ratios on H-MFI. Differences in dehydrogenation ($E_{de}$) and cracking ($E_{cr}$) activation energies are reflected in the slope. Symbols denote experimentally measured rate ratios in this study (●) and rate ratios extrapolated from data reported in previous experimental studies (Ref. [21]: ■, Ref. [24]: ◆, Ref. [26]: ▲) and in a theoretical study (Ref. [27]: —).

We use Born-Haber thermochemical cycles (Scheme 3.1b) to interpret the stabilization of reactants and transition states in acid catalysis by zeolites [38,39] and the contributions of intrachannel environments and transition state structure and charge to activation barriers. Measured activation energies ($E_{meas}$) reflect the stability of carbonium ion-like transition states stabilized within channels relative to gaseous reactants (B(g)). These barriers depend on the deprotonation enthalpies (DPE) of Brønsted acid sites, on proton affinities (PA) of gaseous reactants, and on transition state stabilization energies ($E_{stab}$) (Scheme 3.1b). The relations between measured activation energies ($E_{meas}$), reactant adsorption enthalpies ($\Delta H_{ads}$), and intrinsic activation barriers ($E_{int}$) described by Eq. (3.6) are also depicted in Scheme 3.1b. In the context of this thermochemical cycle formalism, the following expressions relate measured and intrinsic activation barriers to properties of the acid, the molecules, and their ion-pair at the transition state:

$$E_{meas} = DPE + PA + E_{stab}\,, \tag{3.10}$$

$$E_{\text{int}} = DPE + PA + E_{stab} - \Delta H_{ads}\,. \tag{3.11}$$

Deprotonation requires electron transfer from H atoms to the zeolite lattice (Z), cleavage of H-Z bonds, and separation of the $H^+$ and $Z^-$ fragments to non-interacting distances. DPE values thus reflect contributions from homolytic H-Z bond dissociation energies (BDE), the ionization energy (IE) of H atoms, electron affinities (EA) of lattice oxygen atoms, and

electrostatic interactions that stabilize the ion-pair ($H^+$-$Z^-$) as separation proceeds. Any variation in DPE values among zeolite structures reflects predominantly the effects of the local environment on the electrostatic stabilization of the ion-pair, because BDE, IE and EA values are likely to depend weakly on spatial constraints. Hybrid quantum mechanical and interatomic potential methods indicate that DPE values for Brønsted acid sites at different T-sites in H-MFI (1229-1240 kJ $mol^{-1}$) [4] and for the most stable Al location among H-MFI, H-FER, H-MOR zeolites (1218-1235 kJ $mol^{-1}$) [5,40] are in fact similar. These similar deprotonation enthalpies reflect the predominant contributions from long-range interactions with the zeolite lattice to the electrostatic stabilization of protons, which overwhelm other contributions resulting from subtle variations in channel geometry.

Proton affinities reflect the energy required to protonate neutral gas-phase molecules (B) to form $BH^+$ complexes, which differ for cracking and dehydrogenation events because the C-C-H and C-H-H three-center/two-electron complexes formed by protonation of C-C and C-H bonds in alkanes differ in energy. Theoretical estimates [41,42] of gas-phase carbonium ion energies indicate that protonation of C-H bonds in $C_3H_8$ forms C-H-H three-center/two-electron species that are less stable by ~20-40 kJ $mol^{-1}$ than the C-C-H analogues formed via protonation of C-C bonds in $C_3H_8$.

Transition state energies reflect both electrostatic stabilization of ion-pairs that form as $BH^+$ and $Z^-$ interact and van der Waals stabilization of the organic cation in the transition state complex. Alkane adsorption enthalpies reflect predominantly van der Waals stabilization by framework oxygens and, to a lesser extent, any induced dipole interactions with $H^+$, where the latter do not depend on the size of alkane reactants or zeolite channels [29-31]. The positive charge (+0.9e) at the alkyl fragment in late monomolecular transition states is stabilized by long-range electrostatic interactions with the zeolite framework [6,7,43,44], rendering subtle effects of channel size inconsequential for $E_{stab}$, the term that accounts for electrostatic stabilization in thermochemical cycles; similar long-range electrostatic considerations account for the weak dependence of DPE values on Brønsted acid site location or zeolite environment [4,5,40]. In contrast, van der Waals stabilization of adsorbed alkanes depends strongly on channel size and structure [45]; by inference, such stabilization is essential also for monomolecular transition states that resemble in structure their adsorbed alkane precursors. As a result, we conclude that differences in transition state stability ($E_{stab}$) among zeolite locations or structures are almost entirely compensated by commensurate differences in reactant stability ($\Delta H_{ads}$), as evidenced by intrinsic activation barriers ($E_{int}$) that do not change with variations in the size or structure of zeolite channels (Table 3.3) or n-alkane reactants [21,33,37].

The intrinsic activation barriers for alkane cracking and dehydrogenation on a given zeolite (or a given location within a zeolite) differ from each other primarily in the respective affinities for protonation of an alkane at C-C or C-H bonds, because DPE and $\Delta H_{ads}$ are independent of the specific reaction path for a given alkane and acid site (Eq. (3.11)). The similar magnitude (+0.9e) and extent of charge delocalization in the organic fragment at cracking and dehydrogenation transition states [6,7,43,44] suggest that electrostatic stabilization (contained in $E_{stab}$) must also be insensitive to reaction path. The differences in intrinsic activation barriers for $C_3H_8$ dehydrogenation and cracking (estimated from rate data) for a given zeolite (25-42 kJ $mol^{-1}$; Table 3.3) must then reflect the calculated energy differences between three-center/two-

electron C-H-H bonds (dehydrogenation) and C-C-H bonds (cracking) in the gas-phase (~20-40 kJ $mol^{-1}$) [41,42], consistent with the thermochemical cycle in Scheme 3.1b and Eq. (3.11).

Thermochemical cycles that relate transition state energies to either gas-phase or adsorbed reactants (Scheme 3.1b) can also be used to describe the contributions of various catalyst and molecule properties to activation entropies. Measured activation entropies for cracking and dehydrogenation reflect differences in entropies between their respective transition states, because both are referenced to the same gas-phase reactant. Measured activation entropies for propane dehydrogenation are ~40 J $mol^{-1}$ $K^{-1}$ larger than for cracking on H-MFI, H-FER, and H-MOR (Table 3.2), consistent with later transition states for dehydrogenation, in which H-H bonds are nearly formed (0.079 nm vs. 0.074 nm in $H_2$(g)) [27]. The late transition states prevalent in monomolecular alkane reactions [27,43,44] lead to hindered rotations and rocking vibrations [46] that increase entropy upon formation of the transition state from adsorbed reactants. As a result, intrinsic rate constants for monomolecular n-hexane cracking are ~50 times larger than for propane cracking on H-MFI [36], even though both reactions show similar intrinsic activation barriers. We *surmise* that such late transition states for dehydrogenation allow greater rotational and vibrational freedom for $C_3H_7$ and $H_2$ fragments than for the corresponding $C_2H_5$ and $CH_4$ groups at the earlier transition states involved in cracking reactions.

Scheme 3.2 depicts a hypothetical reaction coordinate diagram for acid sites within two environments with different spatial constraints, as a result of differences in either the identity of the zeolites or the siting of the acid within a specific location in a given zeolite structure. The more constrained environment in Scheme 3.2a stabilizes both adsorbed molecules and transition states more effectively than the more open structure in Scheme 3.2b through concerted interactions that influence the adsorption enthalpies of the reactants and the stabilization energies of the transition states [45,47], assuming their *complete containment* within the smaller environment. Thus, intrinsic activation barriers for cracking (or dehydrogenation) are more weakly affected by local environment than measured activation energies, which reflect differences between transition states and gas-phase reactants. Measured turnover rates therefore depend on transition state energies and entropies, which depend, in turn, on the channel environment that stabilizes transition states but not reactants in the gas phase external to the zeolite.

H-MOR contains Al atoms that reside at four unique T-sites and corresponding Brønsted acid sites that reside within two distinct channel environments: 8-MR side pockets or 12-MR main channels. The distribution of Brønsted acid sites among 8-MR and 12-MR locations can be measured from the frequency and intensity of their antisymmetric vibrations in infrared spectra (3550-3650 $cm^{-1}$) [8]. Such methods are unable to establish the specific location of OH groups in H-MFI, however, because of the greater diversity of T-sites and because intrachannel environments are more uniform in local structure in MFI than in MOR [48]. All acid sites in H-MFI reside within 10-MR channels or their intersection, precluding the use of titrants of varying size to probe local environment. In light of these considerations, we choose to examine the catalytic consequences of Al siting in the bimodal distribution of channel environments of H-MOR. Al siting was previously shown to influence strongly the stability of charged transition states involved in CO insertion into methyl groups [8], but not symmetric and essentially neutral transition states involved in exchange reactions [9].

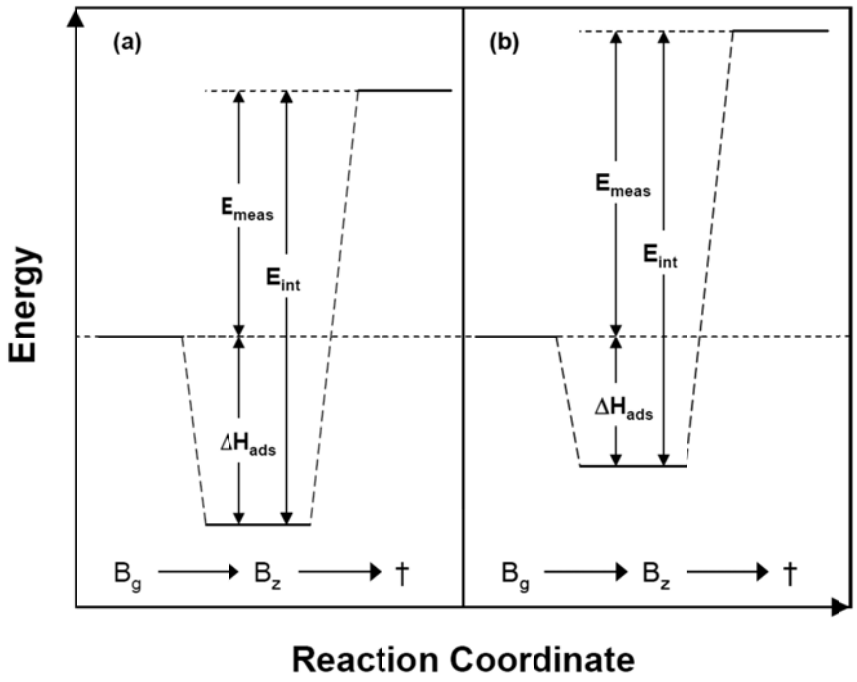


**Scheme 3.2.** Relations between measured activation energies ($E_{meas}$), adsorption enthalpies ($\Delta H_{ads}$) and intrinsic activation energies ($E_{int}$) are shown schematically for two different channel environments. Adsorbed reactants and transition states in location (a) are stabilized to a greater extent than in location (b).

### *3.3.2 Catalytic Consequences of 8-MR and 12-MR Environments Within MOR in Monomolecular Cracking and Dehydrogenation of Propane*

Monomolecular propane cracking and dehydrogenation turnover rates (per $H^+$) differ by factors of ~2 (Table 3.2) on H-MOR zeolites with similar Al content. This range of reactivity does not reflect differences in the number of extraframework Al species or Lewis acid centers among these samples, as shown by the NMR and IR data in Sections 3.6.1 and 3.6.2, respectively, of the supporting information. Table 3.4 shows propane cracking and dehydrogenation rate constants (per total $H^+$) and cracking-to-dehydrogenation rate ratios at 748 K on H-MOR samples partially exchanged with $Na^+$, together with measured activation energies and entropies. Cracking and dehydrogenation rate constants (per residual $H^+$) decreased and their rate ratio increased as $H^+$ species within H-MOR were selectively replaced by $Na^+$. Measured activation entropies for both cracking and dehydrogenation (Eq. (3.9); from rate constants normalized by residual $H^+$ sites) decreased monotonically with the extent of $Na^+$ exchange, but measured activation energies remained essentially constant.

The number of OH groups within 8-MR and 12-MR environments in H-MOR was measured from the intensity of antisymmetric OH stretches (~3550-3650 $cm^{-1}$) using reported methods [8]. Singular value decomposition was used to extract principal component spectra for OH bands in 8-MR and 12-MR locations centered at 3592 $cm^{-1}$ and 3611 $cm^{-1}$, respectively [8]. These values are similar to those reported earlier on H-MOR (8-MR: ~3590 $cm^{-1}$; 12-MR: ~3610 $cm^{-1}$) [49-51] and to those for residual OH groups after selective titration of 12-MR sites by

pyridine [8,49,50]. The contribution from each pure component band was determined by least-squares regression methods that allowed each pure component band center to shift up to 3 $cm^{-1}$ and assumed similar molar extinction coefficients for OH groups in the two locations. The deconvoluted infrared spectra for H-MOR-T and H-MOR-S are shown in Figure 3.2 and elsewhere for partially $Na^+$-exchanged H-MOR-Z samples [8]. The number of OH groups within 8-MR and 12-MR locations is listed in Table 3.1 for all MOR samples used in this study.

**Table 3.4.** Monomolecular propane cracking and dehydrogenation rate constants ($k_{meas}$) and cracking-to-dehydrogenation rate ratios measured at 748 K and measured activation energies ($E_{meas}$) and entropies ($\Delta S_{meas}$) on partially $Na^+$ exchanged MOR-Z samples.

| Zeolite | $k_{meas}$ (/ $10^{-3}$ mol [(mol $H^+$)-s-bar]$^{-1}$) | | C/D Ratio | $E_{meas}$ (kJ $mol^{-1}$) | | $\Delta S_{meas}$ (J $mol^{-1}$ $K^{-1}$) | |
|---|---|---|---|---|---|---|---|
| | Cracking | Dehyd. | | Cracking[a] | Dehyd.[b] | Cracking[c] | Dehyd.[d] |
| $H_{100}Na_0$MOR-Z | 1.4 | 2.2 | 0.7 | 160 | 198 | -99 | -56 |
| $H_{83}Na_{17}$MOR-Z | 1.2 | 1.2 | 1.0 | 160 | 201 | -101 | -58 |
| $H_{73}Na_{27}$MOR-Z | 1.1 | 0.8 | 1.4 | 157 | 201 | -105 | -60 |
| $H_{59}Na_{41}$MOR-Z | 0.9 | 0.6 | 1.5 | 155 | 196 | -110 | -69 |
| $H_{45}Na_{55}$MOR-Z | 0.6 | 0.3 | 1.7 | 153 | 198 | -115 | -72 |

[a]Errors are ± 5 kJ $mol^{-1}$.
[b]Errors are ± 7 kJ $mol^{-1}$.
[c]Errors are ± 8 J $mol^{-1}$ $K^{-1}$.
[d]Errors are ± 10 J $mol^{-1}$ $K^{-1}$.

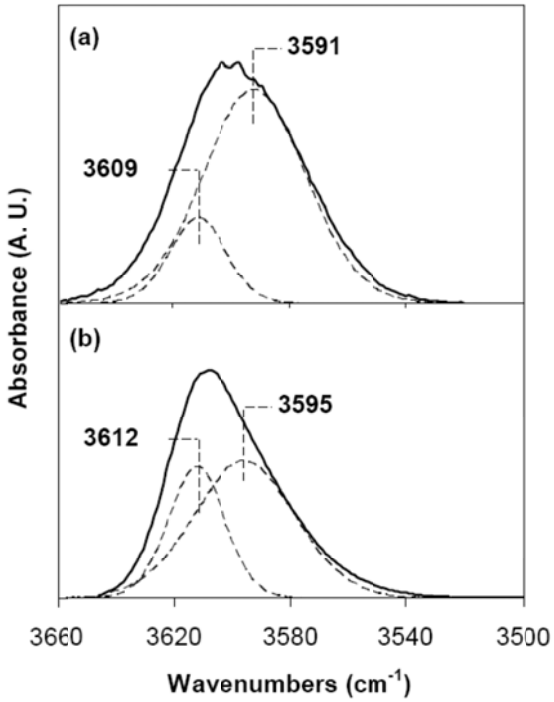


**Figure 3.2.** Infrared spectra (—) of (a) H-MOR-T (OH in 8-MR = 78 ± 5%) and (b) H-MOR-S (OH in 8-MR = 60 ± 5%). Deconvoluted bands (- -) for 8-MR and 12-MR OH groups are shown along with their respective band centers.

Infrared spectra showed that $Na^+$ cations selectively replace protons within constrained 8-MR side pockets in MOR [8,49,52] (Fig. 3.3), because more electropositive alkali cations appear to be stabilized more effectively than $H^+$ by the stronger dispersive forces prevalent within such smaller environments. Rate constants for $C_3H_8$ dehydrogenation (per residual $H^+$) decreased even more strongly with $Na^+$ exchange than for cracking (Table 3.4), reflecting a greater specificity of 8-MR pockets for dehydrogenation reactions compared with 12-MR channels. Measured activation entropies became more negative for both cracking and dehydrogenation as $Na^+$ replaced $H^+$ within 8-MR side pockets (Table 3.4), demonstrating that the more constrained environment provided by such pockets actually stabilizes looser transition states than the larger 12-MR main channels in MOR for both reactions.

We can extract from these data the specific contributions of OH groups within 8-MR and 12-MR locations in H-MOR by expressing measured rate constants for $C_3H_8$ cracking and dehydrogenation as linear combinations of rate constants in the two locations:

$$k = k_{8-MR} \cdot X_{8-MR} + k_{12-MR} \cdot X_{12-MR} . \tag{3.12}$$

Here, $X_{8\text{-}MR}$ and $X_{12\text{-}MR}$ represent the fraction of all OH groups located within 8-MR and 12-MR locations, respectively, and $k_{8\text{-}MR}$ and $k_{12\text{-}MR}$ the corresponding monomolecular rate constants in each environment. The latter were determined by regressing overall rate constants on seven MOR samples with different acid site densities and location; the details of the regression analysis are shown in Section 3.6.5 of the supporting information. Measured rate constants (shown at 748 K in Table 3.5) for $C_3H_8$ cracking were larger (by factors of ~3) in 8-MR than in 12-MR environments; $C_3H_8$ dehydrogenation rates on OH groups within 12-MR channels were undetectable within the accuracy of these measurements.

**Table 3.5.** Monomolecular propane cracking and dehydrogenation rate constants ($k_{meas}$) at 748 K within 8-MR and 12-MR locations of MOR and measured activation energies ($E_{meas}$) and entropies ($\Delta S_{meas}$). Uncertainties in regressed rate parameters are reported as twice the standard error.

| **Reaction (Location)** | **$k_{meas}$[a] (/ $10^{-3}$ mol [(mol $H^+$)-s-bar]$^{-1}$)** | **$E_{meas}$ (kJ mol$^{-1}$)** | **$\Delta S_{meas}$ (J mol$^{-1}$ K$^{-1}$)** |
|---|---|---|---|
| Cracking (8-MR) | 2.0 ± 0.5 | 164 ± 5 | -91 ± 9 |
| Cracking (12-MR) | 0.7 ± 0.4 | 151 ± 5 | -117 ± 14 |
| Dehydrogenation (8-MR) | 3.2 ± 0.7 | 197 ± 7 | -54 ± 11 |
| Dehydrogenation (12-MR) | n.d.* | n.d.* | n.d.* |

[a]Rate parameters determined by least-squares regression (supporting text shown in Section 3.3.2).
*n.d., not detected.

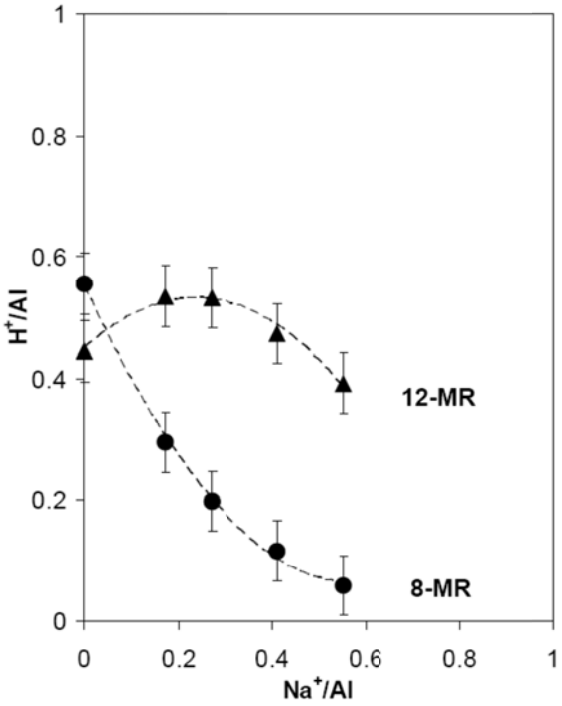


**Figure 3.3.** Number of residual protons (per Al) in 8-MR pockets (●) and 12-MR channels (▲) of MOR-Z samples with varying $Na^+$ content (per Al) determined by infrared spectral band deconvolution (supporting text in Section 3.3.2 and in Ref. [8]).

Brønsted acid sites within the more constrained 8-MR side pockets in H-MOR catalyze monomolecular cracking and dehydrogenation reactions of $C_3H_8$ preferentially (Table 3.5) over sites of similar acid strength [53] within the less constrained 12-MR channels. Propane dehydrogenation rates (per g) are strictly proportional to the number of residual $H^+$ within 8-MR environments (per g) and do not depend on the number of residual $H^+$ within 12-MR channels (per g) (Fig. 3.4), consistent with the exclusive reactivity of Brønsted acid sites of OH groups within 8-MR pockets at the conditions of these experiments (Table 3.5). Such remarkable specificity demonstrates the essential role of local environment on the enthalpic or entropic stabilization of dehydrogenation transition states. These data also illustrate how reactivity, as reflected here in turnover rates, varies significantly among the diverse T-site locations even within a given zeolite structure. These trends resemble those reported recently for CO insertion into adsorbed methyl groups derived from dimethyl ether, which formed acetyl groups (and ultimately methyl acetate after subsequent methoxylation with dimethyl ether) only on sites contained within 8-MR environments in H-MOR and H-FER [8].

The systematic increase in cracking-to-dehydrogenation rate ratios (0.7 to 1.7; Table 3.4) as $Na^+$ replaced $H^+$ within 8-MR environments reflects the stronger effects of local environment on dehydrogenation transition states compared with cracking transition states. Propane cracking rates (per g) were also proportional to the number of $H^+$ sites present within 8-MR environments (per g), but detectable cracking contributions from OH groups in 12-MR channels cause a non-zero intercept (Fig. 3.5). The rigorous subtraction of the 12-MR OH contributions (the second term in Eq. (3.12)) from measured rates led to a strictly linear dependence of residual rates on the number of OH groups within 8-MR pockets and to a zero intercept, as shown by the dashed line in Figure 3.5.

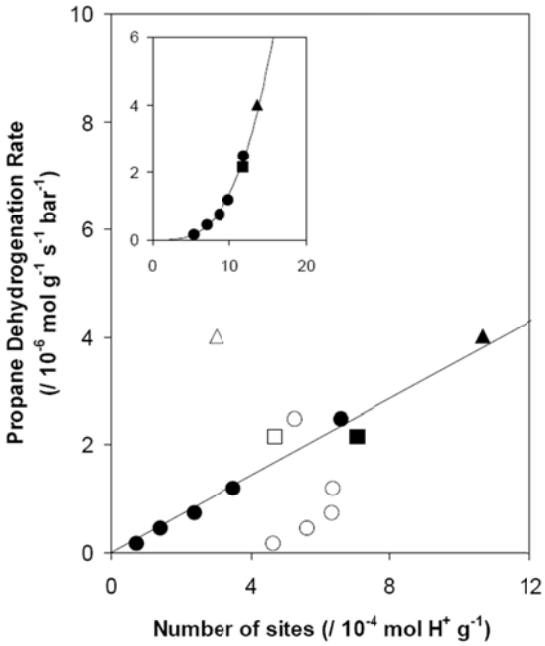


**Figure 3.4.** Propane dehydrogenation rates (per g) at 748 K in H-MOR and $Na^+$-exchanged MOR samples (MOR-Z: ●, MOR-S: ■, MOR-T: ▲) plotted against the density of Brønsted acid sites (per g) in the 8-MR pockets of MOR (closed symbols) and 12-MR channels of MOR (open symbols). Inset shows propane dehydrogenation rates (per g) plotted against the total density of Brønsted sites (per g).

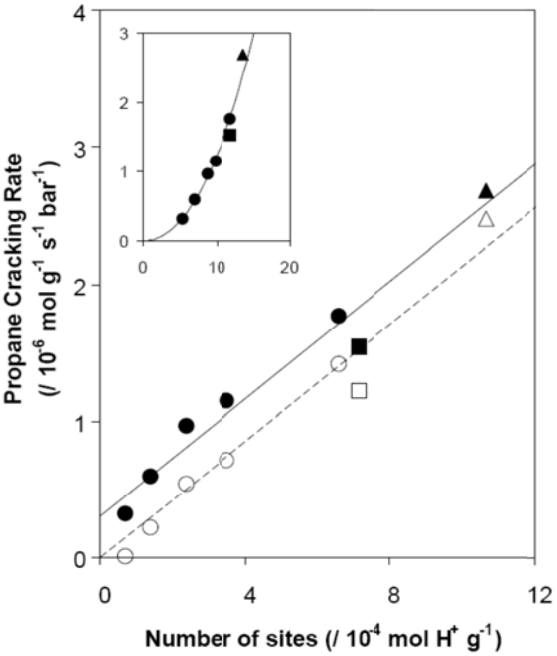


**Figure 3.5.** Measured propane cracking rates (per g) (closed symbols) and residual cracking rates after correction for the contribution from 12-MR sites (per g) (open symbols) at 748 K in H-MOR and $Na^+$-exchanged MOR samples (MOR-Z: ●, MOR-S: ■, MOR-T: ▲) plotted against the density of Brønsted acid sites (per g) in 8-MR pockets. Inset shows total propane cracking rates (per g) plotted against the total density of Brønsted sites (per g).

These data demonstrate that propane cracking and dehydrogenation occur preferentially within 8-MR pockets at 718-778 K on H-MOR. Yet, infrared bands of OH groups in 8-MR pockets of H-MOR were not perturbed by contact with $C_3H_8$ at near ambient temperatures (323 K) [29], suggesting that propane molecules have restricted access to or weaker interactions with 8-MR compared with 12-MR OH groups. $^{13}$C-NMR spectra [54] and theoretical simulations [55], however, have shown that $C_3H_8$ adsorbs preferentially within 8-MR H-FER channels of similar size at ambient temperatures. Such specificity for adsorption within 12-MR channels in H-MOR reflects stronger dispersive forces within constrained environments that can *fully* contain the adsorbate molecules [45] and the consequently more negative adsorption enthalpies that reflect more effective van der Waals contacts with framework oxygens [29-31]. Correlations that relate adsorption enthalpies to the effective channel diameters for different zeolites [45] predict that $C_3H_8$ would indeed adsorb more strongly (by ~12 kJ mol$^{-1}$) *if fully contained* within channels 0.41 nm in diameter, such as those in 8-MR MOR pockets, than within the larger channels (0.67 nm) formed by 12-MR structures in MOR. $C_3H_8$ molecules (~0.65 nm in length) extend, however, beyond the depth of the 8-MR pockets (~0.37 nm) and must protrude into connecting 12-MR channels (procedures used for estimating channel and molecular dimensions are described in Sections 3.6.6 and 3.6.7, respectively, of the supporting information). These dimensions preclude van der Waals interactions between the entire propane molecule and the framework oxygens in 8-MR pockets. As a result, $C_3H_8$ adsorbs preferentially within larger 12-MR channels, which interact with the entire molecule, albeit more weakly than 8-MR channels able to contain the entire molecule.

Regressed rate constants on acid sites within 8-MR and 12-MR locations are shown as a function of temperature in Figure 3.6; these data were used to estimate activation energies and entropies within these two distinct MOR environments (Table 3.5). Cracking turnover rates were larger on sites present within 8-MR pockets than on acid sites of similar strength within 12-MR channels, even though measured activation energies were actually higher on 8-MR OH groups (by 13 kJ mol$^{-1}$), apparently because of looser transition states with higher entropies (Table 3.5). The adsorption enthalpy of $C_3H_8$ on 12-MR MOR channels was measured to be -41 kJ mol$^{-1}$ using calorimetry [29], in agreement with the adsorption enthalpy predicted from its correlation to channel size [45]. Taken together with the measured activation energy on 12-MR channels (151 kJ mol$^{-1}$), this enthalpy gives an intrinsic cracking activation barrier of 192 $\pm$ 7 kJ mol$^{-1}$ for acid sites within 12-MR channels (Eq. (3.6)). These data agree well with values for $C_3H_8$ cracking on H-MFI, H-FER and H-MOR (201-208 kJ mol$^{-1}$; Table 3.3). $C_3H_8$ adsorption enthalpies on 8-MR pockets are not available, but we can extend arguments and data indicating that intrinsic activation barriers are independent of zeolite structure or location (because they lead to equivalent stabilization of adsorbed precursors and transition states) to estimate such adsorption enthalpies from measured activation energies on 8-MR OH groups. Adsorption enthalpies for $C_3H_8$ within 8-MR H-MOR pockets would then be -30 kJ mol$^{-1}$ in order for intrinsic cracking activation barriers to be the same as those determined on 12-MR H-MOR channels (~190 kJ mol$^{-1}$). These data and arguments lead us to conclude that $C_3H_8$ adsorption is much weaker on 8-MR pockets in MOR than predicted based on channel size considerations (-53 kJ mol$^{-1}$; Section 3.6.6 of the supporting information). Thus, we conclude that both adsorbed $C_3H_8$ molecules and their monomolecular transition states are only *partially* contained within shallow 8-MR pockets and protrude into neighboring 12-MR channels. These data and

conclusions are consistent with measured transition state entropies ($\Delta S_{meas}$), which are significantly higher on 8-MR than on 12-MR acid sites (Table 3.5).

We conclude that transition states are less stable, in terms of enthalpy, within 8-MR pockets, which can confine only in part cracking and dehydrogenation transition states, than within 12-MR channels, which provide more effective van der Waals stabilization for both the transition states and the adsorbed molecules. We note that partial containment destabilizes species by decreasing van der Waals contacts with parts of the molecules, but such contacts are not essential for electrostatic stabilization of the positive charge (+0.9e) at the three-atom/two-electron center in the transition state; in late transition states for monomolecular alkane reactions, the positive charge is localized at the carbon atom in the alkyl fragment left behind upon elimination of the neutral molecule ($H_2$ or $CH_4$) from the transition state. Turnover rates are higher for these partially confined species, in spite of the concomitant enthalpic destabilization caused by partial confinement, indicating that their free energies are in fact lower than for similar species fully contained within 12-MR channels. These findings illustrate the dominant role of entropy in the stabilization of adsorbed species and transition states within confined environments and further extend our previous studies that concluded the exponential increase in monomolecular cracking rates of $C_3$-$C_6$ n-alkanes on H-MFI to reflect predominantly larger transition state entropies [36].

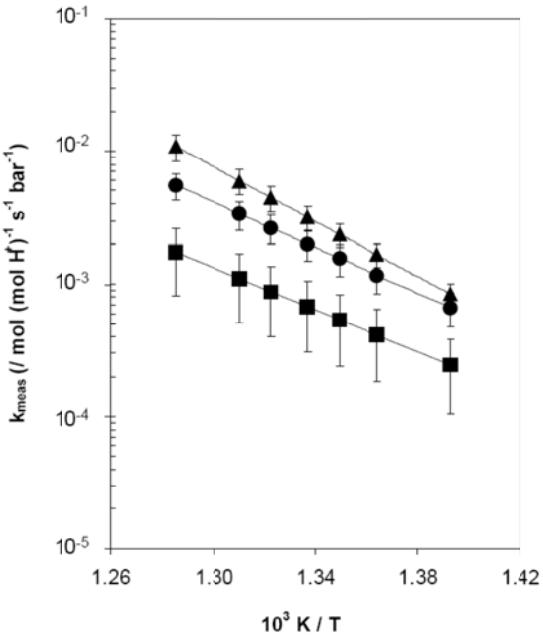


**Figure 3.6.** Measured rate constants ($k_{meas}$) for monomolecular propane cracking in 8-MR pockets (●) and 12-MR channels (■) and dehydrogenation in 8-MR pockets (▲) determined from least-squares regression analysis. Dehydrogenation rate constants were not detected in 12-MR channels. Error bars are shown as twice the standard error in regressed rate constants.

The entropy component of transition state free energies, and, by extension, the benefits of the trade-offs mediated by partial containment, becomes increasingly significant for later transition states involving dissociation and elimination of a fragment from the activated complex, and causes atypically large pre-exponential factors ($10^{15}$-$10^{17}$ $s^{-1}$) for gas-phase fission reactions [46]. As a result, the specificity of 8-MR channels is even stronger for dehydrogenation than for cracking transition states, because of the later nature of the former [27], as found experimentally (Table 3.5). We were unable to detect dehydrogenation contributions from 12-MR sites because of their low reactivity at the conditions of our measurements, precluding a similar analysis to that used above for 8-MR pockets to infer partial containment and enthalpy-entropy trade-offs in cracking transition state free energies. The similar nature of cracking and dehydrogenation transition states, however, leads us to conclude that similar effects of partial containment are responsible for the preferential stabilization of dehydrogenation transition states within 8-MR pockets in MOR.

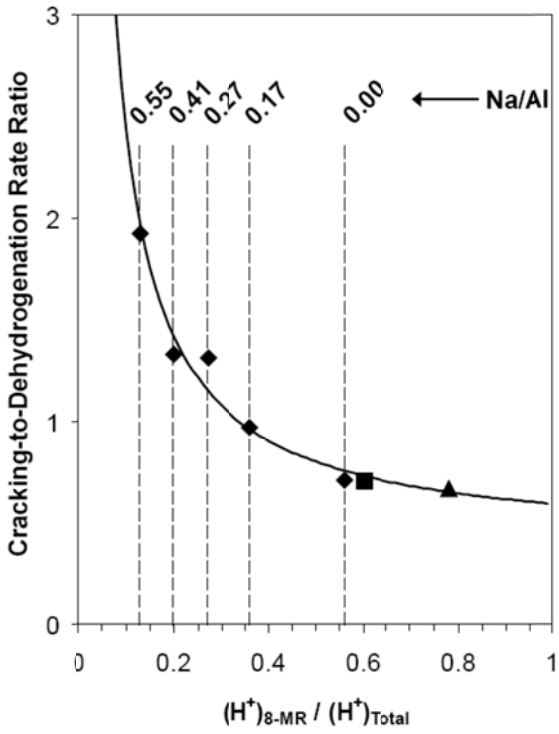


**Figure 3.7.** The dependence of propane cracking-to-dehydrogenation rate ratios at 748 K on the fraction of Brønsted acid sites in 8-MR pockets of MOR, predicted using regressed rate constants (Table 3.5) and Eq. (3.12), is given by the solid curve. Data at 748 K are shown (MOR-Z: ●, MOR-S: ■, MOR-T: ▲) along with Na/Al ratios for MOR-Z samples.

The less negative transition state entropies (relative to reactants in the gas phase) measured for OH groups within 8-MR pockets (Table 3.5) reflect the strong effects of local environment on cracking and dehydrogenation rate constants and on cracking-to-dehydrogenation rate ratios and the concomitant changes in these properties among H-MOR samples with different OH distributions (Tables 3.2 and 3.4). The dependence of propane cracking-to-dehydrogenation rate ratios (at 748 K) on the fraction of all OH groups present

within 8-MR H-MOR pockets is shown in Figure 3.7, together with values predicted from Eq. (3.12) and regressed rate constants (Table 3.5), which agree well with data on H-MOR samples of different provenance and for H-MOR samples in which $Na^+$ exchange was used to selectively titrate 8-MR OH groups.

We conclude that selectivity in alkane activation reactions can be tuned using the location of acid sites within a given zeolite structure. Temperature, which exploits differences in activation energies between dehydrogenation and cracking pathways, can also be used to control selectivity, but rely solely on intrinsic differences in relative stabilities of reactants protonated at various positions or bonds; these relative intrinsic barriers for cracking and dehydrogenation are therefore independent of zeolite structures or channel location (Table 3.3), as predicted by the thermochemical cycle in Scheme 3.1b. Our findings provide an alternate strategy for selectivity control, which exploits location-specific differences in entropy between dehydrogenation and cracking transition states. To our knowledge, the ability to exploit location and zeolite structure to tune the selectivity of cracking and dehydrogenation pathways and the interpretation of the resulting effects in terms of the dominant effects of transition state entropies have not been previously recognized in zeolite catalysis. These data and conclusions provide design strategies for the placement of Al sites within specific locations in order to promote specific reactions via rigorous considerations of the position of their respective transition states along the reaction coordinate.

To our knowledge, the enzyme-like specificity of spatial environments within 8-MR pockets in H-MOR or the marked effects of partial confinement have not been previously recognized or demonstrated for alkane activation reactions. These findings resemble, however, the reported specificity of 8-MR pockets for CO insertion into $CH_3$ groups during dimethyl ether carbonylation to methyl acetate at ~450 K [8]. The sole mechanistic connection between these reactions and the alkane activation reactions that we discuss here is the common involvement of cationic transition states. Such specificity was not observed for isotopic exchange reactions on zeolites, for which transition states are symmetrical and essentially uncharged [9]. We conclude that this remarkable specificity and the partial confinement effects responsible for it are general features of chemical reactions occurring via transition states with highly localized cationic centers within constrained environments. We provide next evidence for the role of partial confinement on the relative reactivity of various C-C bonds within alkanes in monomolecular cracking reactions and demonstrate the ability of H-MOR side pockets to selectively crack terminal C-C bonds in n-butane as a result of partial confinement configurations.

### *3.3.3 Partial Confinement Effects and Preferential Terminal Cracking Selectivity in n-Butane Activation on MOR*

Concepts of pore mouth catalysis [56], a form of partial confinement, have been used as a phenomenological description of processes in which molecules penetrate small zeolite channels only partially as they react. Propane reactions in MOR may well fit this empirical concept, because reactants cannot fully enter the 8-MR pockets within which they preferentially react, and remain in part within connecting 12-MR channels (detailed treatments for estimating channel and molecular dimensions shown in Sections 3.6.6 and 3.6.7, respectively, of the supporting information). The resulting transition states would preferentially activate terminal C-C and C-H

bonds, but such preferences lead to identical products for propane reactants. Any terminal C-C bond activation preference arising from partial confinement would be apparent for n-butane reactants, but specific activation of terminal C-H bonds may be impossible to detect because of fast hydride shifts on both 8-MR and 12-MR acid sites. Indeed, equilibrated n-butene isomers were detected at all conditions on all catalysts (data shown in Section 3.6.8 of the supporting information). We use here terminal-to-central C-C bond cleavage rate ratios to probe how molecules access active sites within 8-MR and 12-MR environments and to demonstrate the effects of partial confinement on n-butane dehydrogenation and cracking turnover rates.

Rate constants of terminal and central C-C bond cracking and dehydrogenation of n-$C_4H_{10}$ (per residual $H^+$) and their rate ratios are shown at 748 K in Table 3.6 for five MOR samples with varying $Na^+$ content; the corresponding measured activation energies and entropies are shown in Table 3.7. Figure 3.8 shows the temperature dependence of monomolecular rate constants (per residual $H^+$) for terminal and central C-C bond cleavage (Fig. 3.8a) and of their rate ratio (Fig. 3.8b) on MOR samples with 56% ($H_{100}Na_0$MOR-Z) and 13% ($H_{45}Na_{55}$MOR-Z) of $H^+$ sites within 8-MR pockets. As $Na^+$ selectively replaced $H^+$ within 8-MR locations, terminal and central C-C bond cracking and dehydrogenation rate constants (per total $H^+$) decreased, while cracking-to-dehydrogenation rate ratios concurrently increased (Table 3.6, Fig. 3.8). These trends resemble those for propane cracking and dehydrogenation, suggesting that the specificity of OH groups in 8-MR pockets for both reactions, and especially for dehydrogenation, is not restricted to the smaller $C_3H_8$ reactants. Measured activation energies for terminal and central C-C bond cracking are similar to each other on all samples (Table 3.7), consistent with the lack of temperature effects on n-$C_4H_{10}$ terminal cracking selectivities on H-MOR (718-778 K; Fig. 3.8b) and of n-$C_5H_{12}$ cracking selectivities on H-MFI (750-810 K) [22]. The absence of enthalpic preferences for the cleavage of one of the two types of C-C bonds in n-butane via late carbonium ions as transition states is consistent with the similar gas-phase protolytic cracking enthalpies for the various C-C bonds in n-decane estimated by theory [57]. The terminal-to-central C-C bond cracking selectivity decreased monotonically as $H^+$ sites within 8-MR pockets were selectively replaced by $Na^+$ (Table 3.6), suggesting that terminal bonds are activated preferentially on 8-MR OH sites, as expected from partial confinement of n-butane within these side pockets.

**Table 3.6.** Monomolecular n-butane cracking and dehydrogenation rate constants ($k_{meas}$) (per total $H^+$) and rate ratios at 748 K experimentally measured on MOR-Z samples and estimated within 8-MR and 12-MR locations of MOR.

| **Zeolite** | **$k_{meas}$ (/ $10^{-3}$ mol [(mol $H^+$)-s-bar]$^{-1}$)** | | | **Rate Ratios** | |
|---|---|---|---|---|---|
| | Term. C-C Cracking | Cent. C-C Cracking | Dehyd. | Term./Cent. C-C Cracking | Cracking/ Dehyd. |
| $H_{100}Na_0$MOR-Z | 13.0 | 3.2 | 13.8 | 4.0 | 1.1 |
| $H_{83}Na_{17}$MOR-Z | 10.2 | 2.9 | 12.8 | 3.5 | 1.0 |
| $H_{73}Na_{27}$MOR-Z | 6.9 | 2.7 | 4.9 | 2.6 | 2.0 |
| $H_{59}Na_{41}$MOR-Z | 6.4 | 2.4 | 4.4 | 2.6 | 2.0 |
| $H_{45}Na_{55}$MOR-Z | 4.0 | 1.6 | 2.1 | 2.6 | 2.6 |
| 8-MR[a] | 20.8 ± 5.4 | 4.1 ± 2.0 | 31.5 ± 6.0 | 5.0 | 0.9 |
| 12-MR[a] | n.d.* | 1.8 ± 1.2 | n.d.* | n.d.* | n.d.* |

[a]Rate parameters for 8-MR and 12-MR locations determined by least-squares regression. Uncertainties in regressed rate parameters are reported as twice the standard error.
*n.d., not detected

Monomolecular rate constants for $H^+$ sites within 8-MR and 12-MR locations were estimated from measured rate constants (per $H^+$) on the five MOR-Z catalysts (using Eq. (3.12) and treatments similar to those in Section 3.6.5 of the supporting information). These rate constants (733-763 K; shown at 748 K in Table 3.6) were used to determine activation energies and entropies on acid sites within these two environments (Table 3.7). As in the case of $C_3H_8$, n-$C_4H_{10}$ cracking and dehydrogenation rate constants were larger on 8-MR than on 12-MR acid sites. The rates of dehydrogenation and of terminal C-C cracking on 12-MR acid sites were too small to be estimated accurately from overall rate constants, because both reactions occurred much faster on 8-MR acid sites. Measured terminal-to-central cracking rate ratios increased from essentially zero on 12-MR acid sites to 5.0 on sites within 8-MR pockets (Table 3.6). These data indicate that the partial confinement of n-$C_4H_{10}$ reactants into 8-MR pockets leads to a configurational preference for cracking at terminal C-C bonds in n-butane.

**Table 3.7.** Measured activation energies ($E_{meas}$) and entropies ($\Delta S_{meas}$) for monomolecular n-butane cracking and dehydrogenation on MOR samples and estimated values within 8-MR and 12-MR locations of MOR.

| **Zeolite** | **$E_{meas}$ (/ kJ mol$^{-1}$)** | | | **$\Delta S_{meas}$ (/ J mol$^{-1}$ K$^{-1}$)** | | |
|---|---|---|---|---|---|---|
| | Term. C-C Cracking[a] | Cent. C-C Cracking[a] | Dehyd.[b] | Term. C-C Cracking[c] | Cent. C-C Cracking[c] | Dehyd.[d] |
| $H_{100}Na_0$MOR-Z | 156 | 153 | 203 | -86 | -96 | -36 |
| $H_{83}Na_{17}$MOR-Z | 160 | 152 | 227 | -83 | -98 | -4 |
| $H_{73}Na_{27}$MOR-Z | 139 | 145 | 213 | -114 | -108 | -31 |
| $H_{59}Na_{41}$MOR-Z | 148 | 146 | 231 | -102 | -108 | -8 |
| $H_{45}Na_{55}$MOR-Z | 145 | 139 | n.d.[*] | -110 | -120 | n.d.[*] |
| 8-MR[e] | 163 ± 15 | 159 ± 11 | 215 ± 11 | -72 ± 23 | -86 ± 19 | -13 ± 17 |
| 12-MR[e] | n.d.[*] | 134 ± 10 | n.d.[*] | n.d.[*] | -126 ± 22 | n.d.[*] |

[a]Errors for experimentally determined cracking $E_{meas}$ are ± 6 kJ mol$^{-1}$.
[b]Errors for experimentally determined dehydrogenation $E_{meas}$ are ± 10 kJ mol$^{-1}$.
[c]Errors for experimentally determined cracking $\Delta S_{meas}$ are ± 9 J mol$^{-1}$ K$^{-1}$.
[d]Errors for experimentally determined dehydrogenation $\Delta S_{meas}$ are ± 15 J mol$^{-1}$ K$^{-1}$.
[e]Rate parameters for 8-MR and 12-MR locations determined by least-squares regression. Uncertainties in regressed rate parameters are reported as twice the standard error.
[*]n.d., not detected.

Measured activation energies for central C-C bond cracking of n-$C_4H_{10}$ (Table 3.7) were higher on sites within 8-MR pockets (159 ± 11 kJ mol$^{-1}$), where this reaction actually occurs at higher rates, than in 12-MR channels (134 ± 10 kJ mol$^{-1}$), as also found for $C_3H_8$ cracking. Adsorption enthalpies of n-$C_4H_{10}$ in 12-MR channels of H-MOR (-50 kJ mol$^{-1}$) [29] lead to an estimated intrinsic activation barrier for central C-C bond cracking of 184 ± 12 kJ mol$^{-1}$ (using Eq. (3.6)); this barrier is similar to that reported here for $C_3H_8$ cracking on 12-MR channels of H-MOR (192 ± 7 kJ mol$^{-1}$) and in previous studies for cracking of $C_3$-$C_6$ n-alkanes on H-MFI (194-198 ± 14 kJ mol$^{-1}$) [21]. If we assume that intrinsic activation barriers for central C-C bond cracking within 8-MR pockets were also similar to these values in 12-MR channels, then we estimate n-butane adsorption energies of -25 kJ mol$^{-1}$ from Eq. (3.6), indicating that n-butane binding is weaker than expected from complete confinement within 8-MR pockets (-59 kJ mol$^{-1}$; Section 3.6.6 of the supporting information). These findings indicate that van der Waals interactions stabilize only part of the n-butane molecule (0.83 nm length) and of its terminal

cracking transition state within shallow 8-MR pockets (0.37 nm depth). Even for central C-C bond cleavage in n-butane, turnover rates were higher in 8-MR than 12-MR locations, in spite of weaker enthalpic stabilization of cracking transition states in 8-MR pockets, because of concomitantly larger activation entropies (Table 3.7). These compensating entropic effects appear to reflect the partial protrusion of adsorbed reactants and transition states into connecting 12-MR channels, which decrease the free energy of the transition state, the relevant thermodynamic property that describes its stability. These transition state free energies, referenced to gas phase reactants, determine measured turnover rates at the conditions of our study (Eq. (3.5)) and account for the effects of reactant and acid site environment on the rate and selectivity of alkane activation reactions.

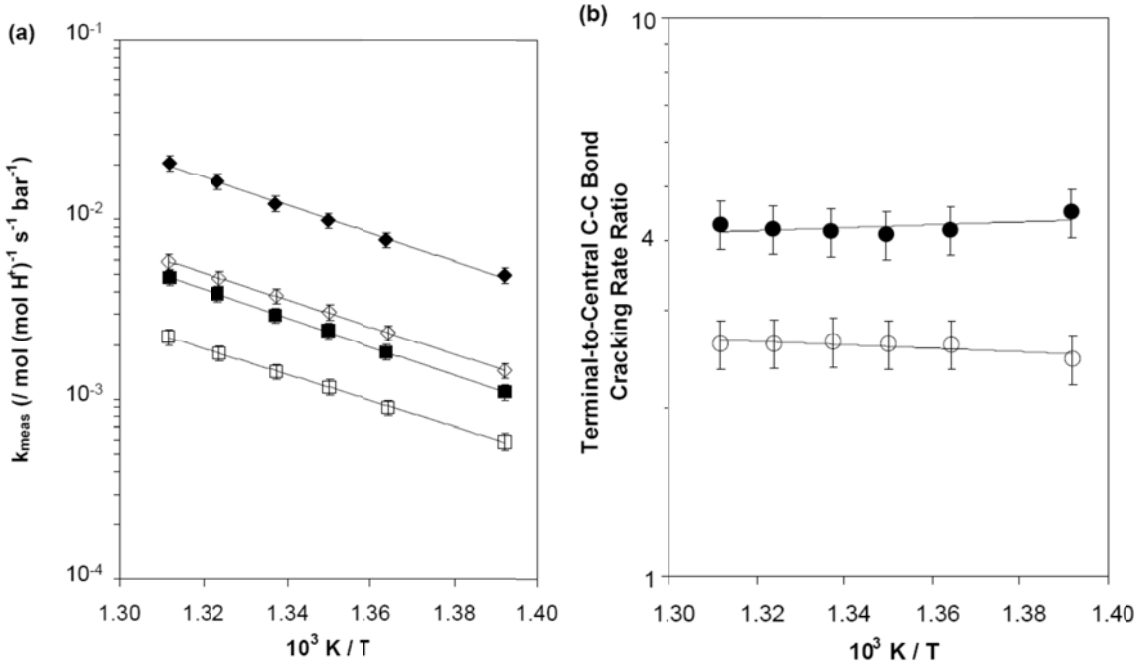


**Figure 3.8.** (a) Measured rate constants ($k_{meas}$) (per total $H^+$) for terminal C-C bond cracking in n-butane (◆,◇) and central C-C bond cracking in n-butane (■,□) on H-MOR-Z (closed symbols) and $H_{45}Na_{55}$MOR-Z (open symbols). (b) Dependence of terminal-to-central C-C bond cracking rate ratios of n-butane on temperature on H-MOR-Z (●) and $H_{45}Na_{55}$MOR-Z (○).

Next, we examine whether local spatial constraints also influence reactivity via these entropic effects on transition state stability as the zeolite structure changes. Specifically, we address the role of intrachannel environment on Brønsted acid site reactivity for H-MFI zeolites, for which the structural diversity of T-sites makes Al and OH distributions inaccessible to experiment using existing tools.

*3.3.4 Monomolecular Propane Activation on H-MFI Zeolites*

Rate constants for propane cracking and dehydrogenation (per $H^+$) and cracking-to-dehydrogenation rate ratios at 748 K, and measured cracking and dehydrogenation activation energies are shown in Table 3.8 on H-MFI samples of different provenance and acid site density. Measured activation barriers were 40-50 kJ $mol^{-1}$ higher for dehydrogenation than for cracking, as also found for H-MOR. Consequently, cracking-to-dehydrogenation rate ratios decreased with increasing temperature on all H-MFI samples. Cracking and dehydrogenation turnover rates (per $H^+$) varied among these H-MFI samples (by up to factors of 5), without any systematic trends with their Al content. These turnover rates (or their ratios) did not correlate with the concentration of extraframework Al atoms or Lewis acid centers, as shown by the NMR and IR data in Sections 3.6.1 and 3.6.2, respectively, of the supporting information.

**Table 3.8.** Monomolecular propane cracking and dehydrogenation rate constants ($k_{meas}$) and cracking-to-dehydrogenation (C/D) rate ratios measured at 748 K on different H-MFI samples and measured activation energies ($E_{meas}$).

| **Zeolite** | **$k_{meas}$ (/ $10^{-3}$ mol (mol $H^+$)$^{-1}$ $s^{-1}$ $bar^{-1}$)** | | **C/D Ratio** | **$E_{meas}$ (/ kJ $mol^{-1}$)** | |
|---|---|---|---|---|---|
| | Cracking | Dehyd. | | Cracking[a] | Dehyd.[b] |
| H-MFI-1 | 2.0 | 2.1 | 0.9 | 158 | 200 |
| H-MFI-2 | 6.3 | 3.9 | 1.6 | 155 | 204 |
| $H_{85}Na_{15}$MFI-2 | 3.9 | 1.5 | 2.7 | 150 | 193 |
| H-MFI-3 | 4.4 | 3.5 | 1.3 | 150 | 200 |
| H-MFI-4 | 1.5 | 0.8 | 1.9 | 150 | 194 |

[a]Errors are ± 5 kJ $mol^{-1}$.
[b]Errors are ± 7 kJ $mol^{-1}$.

These turnover rate differences (Table 3.8) suggest that Brønsted acid sites at the 12 T-sites in MFI are not identical in reactivity and that these samples differ in their distribution of Al among these locations. In contrast, earlier studies reported n-hexane cracking activities that did not depend on Al content [1,2,33] and inferred that the location of the sites were also inconsequential for reactivity. These data would also be consistent with location-specific reactivity but for a set of samples in which Al is similarly distributed among T-sites for all Al contents, a possibility mentioned in the original article [33], but largely ignored thereafter. In spite of similar acid strength, the reactivity of Brønsted acid sites in MFI depends on location, as shown here for H-MOR (Section 3.2) and appears to account for the turnover rate differences among our H-MFI samples (Table 3.8). We conclude that previous studies in which n-hexane cracking rates were independent of Al content [1,2,33] may have used H-MFI samples with a similar distribution of acid sites among locations of different reactivity. We cannot comment further about these discrepancies or about the extent to which bimolecular pathways prevailed during these previous studies, because precise experimental conditions were not given and the cracking data were reported as catalytic activities (arbitrary units) that were likely measured under integral reactor conditions.

The replacement of just 15% of $H^+$ sites in H-MFI-2 by $Na^+$ decreased $C_3H_8$ cracking and dehydrogenation turnover rates (per $H^+$) (by ~1.5 and ~2.5 factors, respectively) and increased their selectivity ratios (from 1.6 to 2.7) (Table 3.8), but measured activation energies for neither

cracking nor dehydrogenation were affected. These effects of $Na^+$ exchange on monomolecular $C_3H_8$ cracking and dehydrogenation turnover rates (per $H^+$) on H-MFI resemble those attributed here in the case of H-MOR to the preferential replacement of $H^+$ by $Na^+$ at locations where cracking and dehydrogenation catalysis is most effective (Table 3.4). These effects of alkali exchange are also similar to those reported for i-$C_4H_{10}$ [58] and n-$C_6H_{14}$ [59] cracking on H-USY, in which cracking rates were rendered undetectable upon titration of just 20-33% of the $H^+$ species associated with framework Al atoms. Our data show that $Na^+$ cations preferentially replace Brønsted acid sites with the highest reactivity for reactions involving cationic transition states. We conclude also that electropositive $Na^+$ cations preferentially reside within smaller channel environments, where entropy-enthalpy trade-offs resulting from partial confinement are most consequential. In MFI, however, the structural diversity of T-site locations precludes rigorous assessment of Al siting and prevents unequivocal and specific interpretations of the effects of local environment on cracking and dehydrogenation of alkanes.

The preferential reactivity of specific channel environments reported here for alkane activation on Brønsted acid sites and earlier for CO insertion into surface methyls[8] appear to represent general features of catalytic reactions involving cationic transition states. Spatial constraints imposed by zeolite channels, frequently proposed to select transition states based simply on their size and shape, play a more fundamental and consequential role in acid catalysis via solvation of cationic transition states and specifically via its mediation of enthalpy and entropy factors, predominantly in ways that favor entropic stabilization even at the expense of enthalpic penalties. We expect that similar effects will prevail for bimolecular alkane reaction pathways that propagate via hydride transfer and beta-scission and oligomerization cycles, channel environments permitting the formation of the bulkier transition states involved, because these pathways also require the formation of cationic transition states [6,7]. Our findings about the dominant role of entropy and of partial containment provide a conceptual path forward towards a more rigorous assessment of local environment effects on transition state stability and therefore on site reactivity and selectivity and towards more rational design and selection strategies for microporous catalysts with specific catalytic properties.

## 3.4. Conclusions

Turnover rate (per $H^+$) differences for monomolecular cracking and dehydrogenation of propane and n-butane with changes in zeolite structure (H-MFI, H-FER and H-MOR) and acid site location (H-MOR: 8-MR side pocket, 12-MR main channel) reflect the strong dependence of cationic transition state free energy on local channel environment. In agreement with Born-Haber thermochemical cycles that define energy relations in acid catalysis, intrinsic activation barriers for both monomolecular propane cracking (201-208 kJ $mol^{-1}$) and dehydrogenation (229-245 kJ $mol^{-1}$) were similar on H-MFI, H-FER, H-MOR samples and were consistently larger for dehydrogenation (by 25-42 kJ $mol^{-1}$). The insensitivity of these barriers to zeolite structure reflects similar zeolite deprotonation enthalpies and commensurate differences in the stabilization of transition states and reactants by different channel environments. Transition states for dehydrogenation are higher in energy than for cracking, reflecting respective affinities for protonation at C-C and C-H bonds in gas-phase alkanes, and are higher in entropy than for

cracking, consistent with the later and looser transition states for the former pathways as suggested by theory.

Monomolecular cracking and dehydrogenation reactions of propane and n-butane occurred predominantly on Brønsted acid sites located within 8-MR side pockets of H-MOR, a consequence of spatially constrained environments that allow only partial containment of reactants and transition states. Partial transition state confinement results in entropy gains that compensate for concomitant enthalpy losses and decrease transition state free energies. Such strong effects of channel environment and, by extension, acid site location on reactivity allowed for systematic and precise control of cracking-to-dehydrogenation selectivities and of terminal-to-central C-C bond cleavage selectivities by selective titration of OH groups in 8-MR pockets of MOR with $Na^+$.

These findings reflect the broad range of reactivities likely to prevail among acid sites located within different channels of the same zeolite structure, shown explicitly for MOR samples of varying provenance and acid site distribution and consistent with data obtained on different MFI samples. In what appears to be a consideration specific to and consequential for acid catalysis by zeolite, channel environments influence the formation of cationic transition states, more fundamentally than simple considerations of size and shape, through their solvation of transition states and mediation of compromises in enthalpy and entropy factors. These findings and their conceptual interpretations offer specific design and selection strategies for microporous solids of specific channel structure and acid site location with predictable consequences for acid catalysis.

## 3.5 Acknowledgements

The authors thank Dr. Stacey I. Zones (Chevron) for the MFI samples. We thank Dr. Zones along with Prof. Aditya Bhan (University of Minnesota at Twin Cities), Josef Macht (University of California at Berkeley) and Prof. Johannes A. Lercher (Technische Universität München) for helpful discussions. We also thank Dr. Sonjong Hwang (California Institute of Technology) and Dr. Chul Kim (California Institute of Technology) for collecting the $^{27}$Al NMR spectra reported here. Finally, we acknowledge with thanks the financial support from Chevron Energy Technology Company.

## 3.6. Supporting Information

### *3.6.1 $^{27}$Al MAS NMR Spectroscopy of Zeolite Samples*

Relative amounts of aluminum in framework and extra-framework locations were determined from integrated areas of peaks respectively centered at 55 ppm (tetrahedral) and 0 ppm (octahedral), referenced to a 1.0 M aqueous solution of $Al(NO_3)_3$, in their $^{27}$Al MAS NMR spectra (Fig. 3.9). NMR spectra were collected at the Caltech Solid State NMR Facility on a Bruker Avance 500 MHz spectrometer in a wide bore 11.7 Tesla magnet. $^{27}$Al MAS NMR spectra were measured at 130.35 MHz using a 4 mm CPMAS probe with the application of

strong proton decoupling and with a magic angle spinning rate of 13 kHz. NMR spectra were recorded at ambient temperature by averaging 512 scans with a 0.5 μs pulse and a 6 s delay. Zeolite samples were packed into a 4mm $ZrO_2$ rotor and were fully hydrated by placing them in a desiccator containing a 1.0 M KCl aqueous solution (~100% relative humidity) for at least 48 h prior to sealing the rotors with a kel-F cap and acquiring NMR spectra.

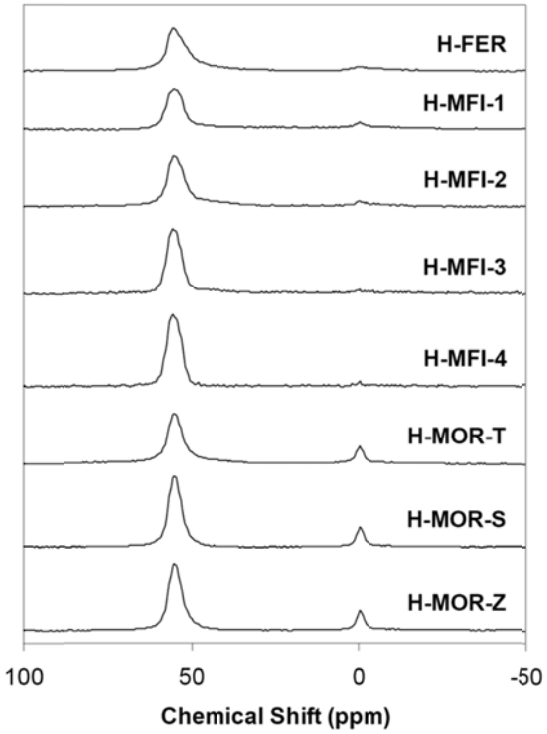


**Figure 3.9.** $^{27}$Al MAS NMR spectra of zeolite samples. Corresponding extra-framework aluminum content for each sample is given in Table 3.1.

### *3.6.2 Infrared Spectroscopic Studies of Zeolite Samples Upon Exposure to CO at 123 K*

Experimental methods for the acquisition of infrared spectra, adapted from previously reported methods [19], are given in Section 2.2. Infrared spectra taken after successive CO doses to H-MOR-S (Fig. 3.10) show that CO initially interacted only with strong ($L_1$; extra-framework $Al^{3+}$) and weak ($L_2$; penta-coordinated $Al^{3+}$) Lewis acid sites, producing infrared bands for C-O stretches centered at 2224 $cm^{-1}$ and 2196 $cm^{-1}$, respectively [20]. CO interacted with Brønsted acid sites through hydrogen bonding (2173 $cm^{-1}$) [20] and with zeolite channel walls via van der Waals interactions (2137 $cm^{-1}$) [20] only after $L_1$ and $L_2$ sites were saturated with CO (Fig. 3.10). The density of $L_1$ and $L_2$ sites (per g) among different zeolite samples are proportional to their integrated peak areas after normalization to those for Si-O-Si overtones (2100-1750 $cm^{-1}$). Infrared spectra upon saturation of Lewis centers by CO at 123 K for three H-MOR samples of varying provenance are shown in Figure 3.11. Turnover rates for $C_3H_8$ cracking and dehydrogenation (per g) did not vary systematically with either $L_1$ or $L_2$ integrated peak areas among different H-MOR (Fig. 3.12) or H-MFI (Fig. 3.13) samples.

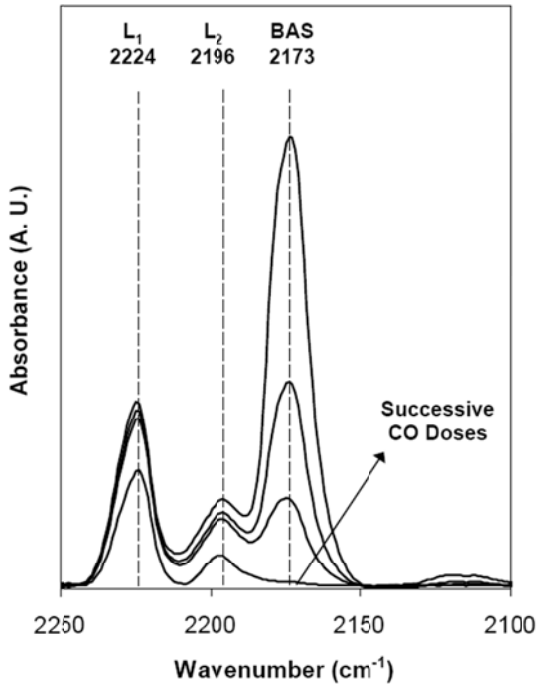


**Figure 3.10.** Infrared spectra of H-MOR-S upon incremental CO doses at 123 K.

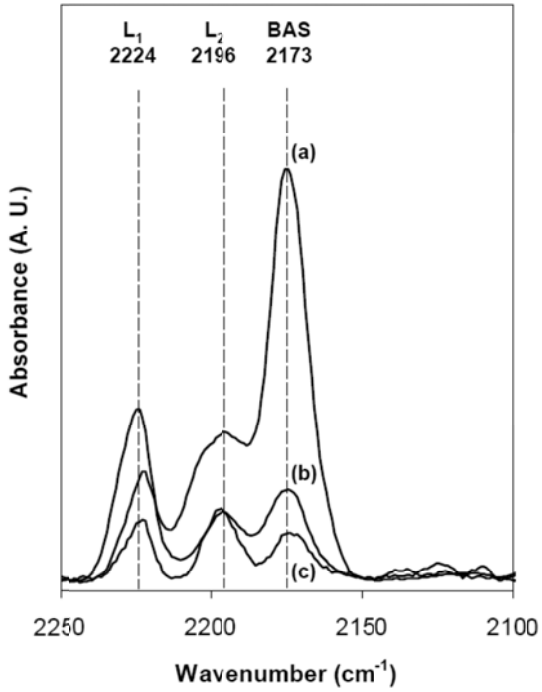


**Figure 3.11.** Infrared spectra of (a) H-MOR-T, (b) H-MOR-S and (c) H-MOR-Z upon saturation of $L_1$ and $L_2$ sites with CO at 123 K.

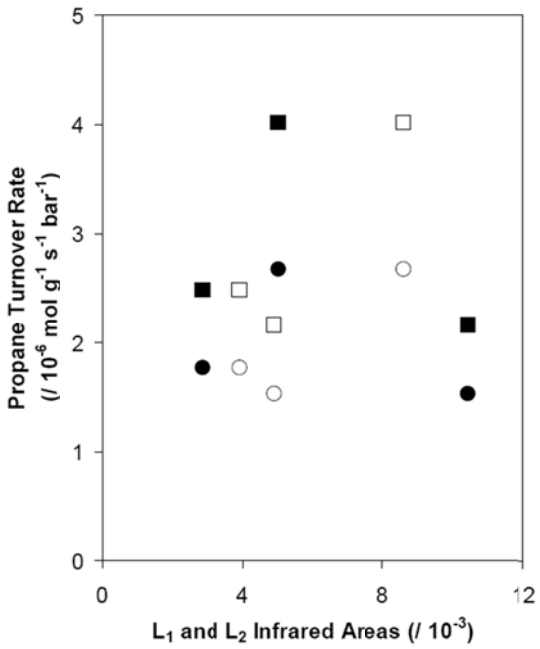


**Figure 3.12.** Propane cracking (●,○) and dehydrogenation (■,□) turnover rates (per g) measured at 748 K on H-MOR-T, H-MOR-S and H-MOR-Z samples plotted against infrared band areas (normalized to Si-O-Si overtone band areas; 2100-1750 $cm^{-1}$) for $L_1$ (closed symbols) and $L_2$ (open symbols) Lewis acid centers upon saturation by CO at 123 K.

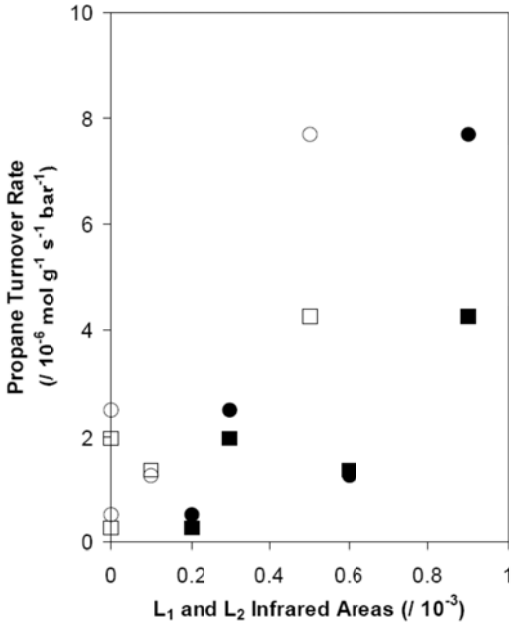


**Figure 3.13.** Propane cracking (●,○) and dehydrogenation (■,□) turnover rates (per g) measured at 748 K on H-MFI-1, H-MFI-2, H-MFI-3, and H-MFI-4 samples plotted against infrared band areas (normalized to Si-O-Si overtone band areas; 2100-1750 $cm^{-1}$) for $L_1$ (closed symbols) and $L_2$ (open symbols) Lewis acid centers upon saturation by CO at 123 K.

*3.6.3 Assessment of Transport Corruptions of Kinetic Measurements*

The Mears criterion was used to assess intraparticle mass transport limitations by assuming isothermal and spherical particles. This criterion asserts that intraparticle concentration gradients are negligible when the inequality:

$$\frac{R_v r_p}{C_s D_e} < 1 \tag{3.13}$$

is satisfied at the conditions of the experiments. Here, $R_v$ is the observed reaction rate per unit volume, $r_p$ is the crystallite radius, $C_s$ is the reactant concentration at the crystallite surface, and $D_e$ is the effective reactant diffusivity [60].

The largest measured rate constants were ~0.005 mol (mol $H^+$)$^{-1}$ $s^{-1}$ $bar^{-1}$ (Table 3.2) and typical experimental conditions for monomolecular alkane reactions (0.2 bar alkane, 780 K, H-MFI, Si/Al = 15) correspond to a per volume reaction rate ($R_v$) of ~0.2 mol $s^{-1}$ $m^{-3}$. The crystallite radius ($r_p$) was conservatively assumed to be 1000 nm; scanning electron microscopy (SEM) images (not included) indicated that crystallites were 100-250 nm in their longest dimension.

The reactant concentration at the external crystallite surface ($C_s$) was estimated to be 0.3 mol $m^{-3}$ at 0.02 bar($C_3H_8$) using the adsorption constant at 780 K on H-MFI ($K_{ads}$ ~ 0.005 $bar^{-1}$), which was calculated using Eq. (3.32) and reported adsorption parameters for $C_3H_8$ on H-MFI ($\Delta H_{ads}$ = -46 kJ $mol^{-1}$, $\Delta S_{ads}$ = -102 J $mol^{-1}$ $K^{-1}$) [29], the saturation loading of $C_3H_8$ on H-MFI ($q_{sat}$ ~ 1.5 mol $kg^{-1}$) [29], and the framework density of MFI ($\rho$ ~ 1.8 x $10^6$ g $m^{-3}$). We note that typical acid site densities ($C_{H+}$ ~ 1 x $10^{-3}$ mol($H^+$) $g^{-1}$; H-MFI, Si/Al = 15) and intrazeolite reactant concentrations ($C_{C3H8,z}$ ~ 0.3 mol $m^{-3}$) result in a fractional site coverage of ~0.0002, indicating that acid sites remain predominantly unoccupied at monomolecular reaction conditions (i.e., high temperatures, low alkane partial pressures).

The effective reactant diffusivity ($D_e$) was estimated to be 1 x $10^{-4}$ $cm^2$ $s^{-1}$, a conservative estimate because $D_e$ = 3 x $10^{-4}$ $cm^2$ $s^{-1}$ for n-$C_6H_{12}$ at 811 K in MFI [61]. These values result in a ratio of reaction to diffusion rates smaller than $10^{-4}$ in Eq. (3.13) and satisfy the Mears criterion for neglecting intracrystallite mass transport limitations and the resulting concentration gradients.

Corruptions arising from heat transfer limitations are expected to be insignificant because of the differential conditions used and the endothermic nature of monomolecular cracking and dehydrogenation reactions. Kinetic measurements were also independent of catalyst bed volume, indicating that homogeneous reactions do not contribute to measured reaction rates and selectivities.

*3.6.4 Transition State Treatments of Monomolecular Reaction Rate Laws and the Derivation of Activity Coefficients for Adsorbed Molecules Described by Langmuir Isotherms*

Monomolecular reactions of alkanes on Brønsted acid sites occur via the pathways shown in Scheme 3.3. Alkanes in the gas phase ($B_g$) adsorb onto Brønsted acid sites ($H^+$) located within

the zeolite channel ($B_z$) in a quasi-equilibrated step. Transition state treatments define reaction rates by the frequency ($\nu$) at which activated complexes (†), formed upon reactions of adsorbed alkanes with Brønsted acid sites ($H^+$), cross the activation barrier:

$$r = \nu C_{\dagger}, \tag{3.14}$$

$$1.\ B_g \rightleftarrows B_z$$
$$2.\ B_z + H^+Z \rightleftarrows \dagger \rightarrow P$$

**Scheme 3.3.** Reaction sequence for monomolecular reactions of alkanes (B denotes a reactant base and P denotes products) on Brønsted acid sites ($H^+$) located within zeolite channels.

In thermodynamically non-ideal systems, the conversion of reactants into the activated complex is given by an equilibrium constant ($K_{\dagger}$) that depends on the activities of the relevant species:

$$K_{\dagger} = \frac{a_{\dagger}}{a_{H^+Z} a_{B_z}} = \frac{\gamma_{\dagger} C_{\dagger}}{\gamma_{H^+Z} C_{H^+Z} \gamma_{B_z} C_{B_z}}. \tag{3.15}$$

Combining Eqs. (3.14) and (3.15) results in the following rate expression:

$$r = \frac{k_B T}{h} \exp\left(\frac{-\Delta G^{\circ\dagger}}{R_g T}\right) \times \frac{\gamma_{H^+Z} C_{H^+Z} \gamma_{B_z} C_{B_z}}{\gamma_{\dagger}}, \tag{3.16}$$

which can be recast in terms of enthalpies ($\Delta H^{\circ\dagger}$) and entropies ($\Delta S^{\circ\dagger}$) of activation

$$r = \frac{k_B T}{h} \frac{\gamma_{H^+Z} \gamma_{B_z}}{\gamma_{\dagger}} C_{H^+Z} \exp\left(\frac{\Delta S^{\circ\dagger}}{R_g}\right) \times \exp\left(\frac{-\Delta H^{\circ\dagger}}{R_g T}\right) C_{B_z}. \tag{3.17}$$

The concentrations (per active site; $H^+$) ($C_i$) of adsorbed species ($B_z$, †) are related to their real ($P_B$) or hypothetical ($P_{\dagger}$) gas-phase pressures by Langmuir isotherms:

$$C_i = \frac{K_i P_i}{1 + K_B P_B + K_{\dagger} P_{\dagger}}. \tag{3.18}$$

Alkanes adsorbed within zeolite channels ($B_z$) are in equilibrium with alkanes in the gas-phase ($B_g$) at a given pressure ($P_B$) when their chemical potentials are equal:

$$\mu_{B_z} = \mu_{B_g}. \tag{3.19}$$

Assuming that gaseous alkanes behave ideally, their chemical potentials are defined as

$$\mu_{B_g} = \mu_{B_g}{}^{o} + RT \ln\left(\frac{P_B}{P^o}\right), \tag{3.20}$$

where $\mu_{Bg}{}^{o}$ is the standard gas-phase chemical potential at the reference pressure ($P^o$) of 1 bar. Chemical potentials of adsorbed species can be analogously written as

$$\mu_{B_z} = \mu_{B_z}{}^{o} + RT \ln\left(\frac{a_{B_z}}{a_{B_z}{}^{o}}\right), \tag{3.21}$$

where $a_{Bz}$ is the activity of the adsorbed alkanes and $\mu_{Bz}{}^{o}$ is their standard chemical potential at the reference activity $a_{Bz}{}^{o}$.

The combination of Eqs. (3.19)-(3.21) results in the following relationship

$$\mu_{B_z}{}^{o} - \mu_{B_g}{}^{o} = RT \ln\left(\frac{P_B}{P^o}\frac{a_{B_z}{}^{o}}{a_{B_z}}\right), \tag{3.22}$$

that defines the dimensionless equilibrium constant ($K_{eq}$),

$$K_{eq} = \frac{P^o}{P_B}\frac{a_{B_z}}{a_{B_z}{}^{o}}, \tag{3.23}$$

which can be further related to $K_B$:

$$a_{B_z} = K_B P_B a_{B_z}{}^{o}, \tag{3.24}$$

where $K_{eq} = K_B * P^o$.

Activities are related to concentrations through activity coefficients ($\gamma$):

$$a_{B_z} = \gamma_{B_z} c_{B_z}, \tag{3.25}$$

and combining Eqs. (3.18), (3.24) and (3.25) results in the following expression for $\gamma$:

$$\gamma_{B_z} = a_{B_z}{}^{o}\left(1 + K_B P_B + K_{\dagger} P_{\dagger}\right). \tag{3.26}$$

A similar derivation follows for the activity coefficients of transition states, whose surface concentrations are in equilibrium with hypothetical gas-phase pressures and are related by a respective Langmuir adsorption constant.

Activity coefficients for alkanes and transition states in Eq. (3.17) ($\gamma_{Bz}$, $\gamma_{\dagger}$) are identical and cancel because alkanes and hypothetical transition states in the gas-phase competitively adsorb onto the same site ($H^+$). Furthermore, monomolecular alkane activation requires temperatures that favor low intrazeolite concentrations ($C_{Bz}$) in which $H^+$ sites are predominantly unoccupied and both $C_{H^+Z}$ and $\gamma_{H^+Z}$ approach unity. Reaction rates therefore become strictly proportional to intrazeolite alkane concentrations ($C_{Bz}$):

$$r = \frac{k_B T}{h} \exp\left(\frac{\Delta S^{\circ\dagger}}{R_g}\right) \times \exp\left(\frac{-\Delta H^{\circ\dagger}}{R_g T}\right) C_{B_z} . \tag{3.27}$$

These rates can be rewritten in terms of pre-exponential (A) and activation energy ($\Delta H^{\circ\dagger}$) components:

$$r = A \exp\left(\frac{-\Delta H^{\circ\dagger}}{R_g T}\right) C_{B_z} . \tag{3.28}$$

Intrazeolite concentrations ($C_{Bz}$) become proportional to external pressures ($P_B$) and to the adsorption constants ($K_B$) in the low-coverage limit (Eq. (3.18)) and reaction rates (Eq. (3.28)) then become:

$$r = k_{\text{int}} \cdot K_B \cdot P_B , \tag{3.29}$$

with measured rate constants ($k_{meas}$):

$$k_{meas} = k_{\text{int}} \cdot K_B , \tag{3.30}$$

and temperature dependences for $k_{int}$ and $K_B$:

$$k_{\text{int}} = A_{\text{int}} e^{(-E_{\text{int}} / RT)} , \tag{3.31}$$

$$K_B = e^{(-\Delta G_{ads} / RT)} = e^{(-\Delta H_{ads} / RT)} e^{(\Delta S_{ads} / R)} , \tag{3.32}$$

where $\Delta H_{ads}$ and $\Delta S_{ads}$ are the enthalpy and entropy of adsorption, respectively. Measured activation energies and pre-exponential factors are given by:

$$E_{meas} = E_{\text{int}} + \Delta H_{ads} , \tag{3.33}$$

$$\ln(A_{meas}) = \ln(A_{\text{int}}) + (\Delta S_{ads} / R) , \tag{3.34}$$

$$\Delta S_{meas} = \Delta S_{\text{int}} + \Delta S_{ads} , \tag{3.35}$$

where $E_{meas}$ and $A_{meas}$ ($\Delta S_{meas}$) are measured rate parameters referenced to gas phase alkanes, and $E_{int}$ and $A_{int}$ ($\Delta S_{int}$) are intrinsic rate parameters referenced to adsorbed alkanes. We define the measured entropy of activation as:

$$\Delta S_{meas} = R \cdot [\ln(A_{meas}) - \ln(k_B T / h)], \tag{3.36}$$

where $A_{meas}$ is rigorously normalized by the number of acid sites and the number of bonds available for each reaction. This measured activation entropy, although calculated, is simply a redaction of $A_{meas}$ and therefore a measured quantity.

### *3.6.5 Least-Squares Estimation of Rate Constants for Monomolecular Propane Activation in 8-MR and 12-MR Locations of MOR*

The individual contributions of OH groups within 8-MR and 12-MR in H-MOR to measured rate constants were estimated by weighing their respective rate constants by the fraction of OH sites within each environment (Eq. (3.11)). These rate constants were determined by a least-squares regression of rate data on seven MOR samples with different acid site distributions (Table 3.1). This system of equations can be expressed in matrix notation:

$$\begin{bmatrix} k_{meas,H_{100}Na_0MOR-Z} \\ k_{meas,H_{83}Na_{17}MOR-Z} \\ k_{meas,H_{73}Na_{27}MOR-Z} \\ k_{meas,H_{59}Na_{41}MOR-Z} \\ k_{meas,H_{45}Na_{55}MOR-Z} \\ k_{meas,H-MOR-T} \\ k_{meas,H-MOR-S} \end{bmatrix} = \begin{bmatrix} x_{H^+,8MR,H_{100}Na_0MOR-Z} & x_{H^+,12MR,H_{100}Na_0MOR-Z} \\ x_{H^+,8MR,H_{83}Na_{17}MOR-Z} & x_{H^+,12MR,H_{83}Na_{17}MOR-Z} \\ x_{H^+,8MR,H_{73}Na_{27}MOR-Z} & x_{H^+,12MR,H_{73}Na_{27}MOR-Z} \\ x_{H^+,8MR,H_{59}Na_{41}MOR-Z} & x_{H^+,12MR,H_{59}Na_{41}MOR-Z} \\ x_{H^+,8MR,H_{45}Na_{55}MOR-Z} & x_{H^+,12MR,H_{45}Na_{55}MOR-Z} \\ x_{H^+,8MR,H-MOR-T} & x_{H^+,12MR,H-MOR-T} \\ x_{H^+,8MR,H-MOR-S} & x_{H^+,12MR,H-MOR-S} \end{bmatrix} \begin{bmatrix} k_{meas,8MR} \\ k_{meas,12MR} \end{bmatrix}, \tag{3.37}$$

where $\underline{k_{meas}}$ is a column vector (7 x 1) containing measured rate constants, $\underline{\underline{x}}$ is a matrix (7 x 2) containing the fraction of Brønsted acid sites within 8-MR and 12-MR locations, and $\underline{k_{loc}}$ is a column vector (2 x 1) of measured first-order rate constants in 8-MR and 12-MR locations. Regressed rate constants are shown in Table 3.9 at different temperatures, with uncertainties reported as twice the standard deviation. Dehydrogenation rate constants in 12-MR locations are much smaller (by factors of $> 10$) than rate constants in 8-MR locations and are zero within the error of the regression; these rates were set to zero and the 8-MR dehydrogenation rate constants were regressed again to give final values (shown in Table 3.9).

**Table 3.9.** Regressed first-order rate constants for cracking and dehydrogenation of propane in the 8-MR pockets and 12-MR channels of MOR at different temperatures; uncertainties reported as twice the standard error. Corrected 8-MR dehydrogenation rate constants were calculated by forcing the 12-MR rate constants to be zero.

| **Temperature** (K) | **$k_{meas}$ (8-MR)** (/ $10^{-3}$ mol (mol $H^+$)$^{-1}$ $s^{-1}$ $bar^{-1}$) | | | **$k_{meas}$ (12-MR)** (/ $10^{-3}$ mol (mol $H^+$)$^{-1}$ $s^{-1}$ $bar^{-1}$) | |
|---|---|---|---|---|---|
| | Cracking | Dehyd. | Dehyd (corr.) | Cracking | Dehyd. |
| 718 | 0.7 ± 0.2 | 0.8 ± 0.3 | 0.8 ± 0.2 | 0.3 ± 0.1 | 0.05 ± 0.2 |
| 733 | 1.2 ± 0.3 | 1.5 ± 0.6 | 1.7 ± 0.3 | 0.4 ± 0.2 | 0.1 ± 0.4 |
| 741 | 1.6 ± 0.4 | 2.2 ± 0.8 | 2.4 ± 0.5 | 0.5 ± 0.3 | 0.2 ± 0.6 |
| 748 | 2.0 ± 0.5 | 2.9 ± 1.2 | 3.2 ± 0.7 | 0.7 ± 0.4 | 0.3 ± 0.8 |
| 756 | 2.6 ± 0.7 | 4.0 ± 1.7 | 4.4 ± 0.9 | 0.9 ± 0.5 | 0.4 ± 1.2 |
| 763 | 3.4 ± 0.8 | 5.4 ± 2.2 | 5.9 ± 1.3 | 1.1 ± 0.6 | 0.5 ± 1.6 |
| 778 | 5.5 ± 1.3 | 9.7 ± 4.2 | 10.8 ± 2.4 | 1.7 ± 0.9 | 1.0 ± 3.0 |

### *3.6.6 Estimation of Adsorption Enthalpy and Entropy of Propane and n-Butane Within 8-MR Pockets of H-MOR, Assuming Complete Confinement*

Calorimetric measurements of alkane adsorption on acidic zeolites showed that both isosteric heats of alkane adsorption and the incremental heat of adsorption per methyl or methylene group correlated strongly with the effective pore radius of the zeolite channel [45]. Here, we attempt to estimate differences in the adsorption enthalpy of $C_3H_8$ and n-$C_4H_{10}$ between the 12-MR channel and the 8-MR pocket of H-MOR, assuming that these molecules can be *fully contained* within 8-MR side pockets.

The effective pore diameter, defined to span the centers of the framework oxygen atoms, was calculated by averaging the minor and major axes of the elliptical channel after adding the oxygen atom diameter (0.27 nm). In MOR, the effective pore radii of the 12-MR channel (0.70 x 0.65 nm) and 8-MR pocket (0.26 x 0.57 nm) are 0.47 nm and 0.34 nm, respectively. We note that the effective pore radius for the 8-MR pocket in MOR (0.34 nm) is very similar to the radii for the 8-MR channel (0.34 nm) and 10-MR channel (0.37 nm) in FER, and make the reasonable assumption that the adsorption enthalpy for $CH_4$ in the 8-MR pocket of MOR is the same as in H-FER ($\Delta H_{ads}$ = -27.7 kJ $mol^{-1}$) [45]. The incremental adsorption enthalpy per $CH_2$ group in H-FER ($\Delta Q_{st}$ = 12.8 kJ $mol^{-1}$) predicts and adsorption enthalpy of -53.3 kJ $mol^{-1}$ for $C_3H_8$ in the 8-MR pocket of H-MOR, in agreement with the value reported for $C_3H_8$ in H-FER [45].

Therefore, adsorption parameters for $C_3H_8$ in 8-MR locations of H-MOR will be estimated as those reported for adsorption in H-FER ($\Delta H_{ads}$ = -49 kJ $mol^{-1}$, $\Delta S_{ads}$ = -103 J $mol^{-1}$ $K^{-1}$) [30]. Adsorption parameters for $C_3H_8$ in the 12-MR channel of H-MOR were directly measured by calorimetric, gravimetric and infrared spectroscopic methods ($\Delta H_{ads}$ = -41 kJ $mol^{-1}$, $\Delta S_{ads}$ = -85 J $mol^{-1}$ $K^{-1}$) [29]. Similarly, if n-$C_4H_{10}$ were to be completely contained within 8-MR side pockets of H-MOR, we predict adsorption enthalpies would resemble values measured in H-FER ($\Delta H_{ads}$ = -59 kJ $mol^{-1}$) [30]. The adsorption enthalpy of n-$C_4H_{10}$ in 12-MR H-MOR channels was directly measured to be -50 kJ $mol^{-1}$ [29].

*3.6.7 Estimation of Kinetic Diameters of Propane and n-Butane and 8-MR Pocket Depth in MOR*

The kinetic diameters of propane and n-butane [62] are shown in Scheme 3.4. Both molecules have a minimum kinetic diameter of 0.43 nm, which corresponds to their minimum cross-sectional diameters. Propane and n-butane have minimum equilibrium diameters of 0.65 nm and 0.83 nm, respectively, which correspond to their longest dimension. The MOR structure viewed along [001] is shown in Scheme 3.5 [63]. A rough estimate for the depth of the 8-MR side pocket was taken to be half the distance between the edges of adjacent 12-MR channels (0.37 nm) by scaling against the small diameter of the 12-MR ring (0.65 nm).

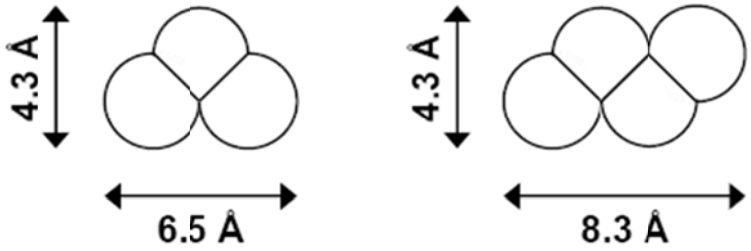


**Scheme 3.4.** Kinetic diameters of propane and n-butane.

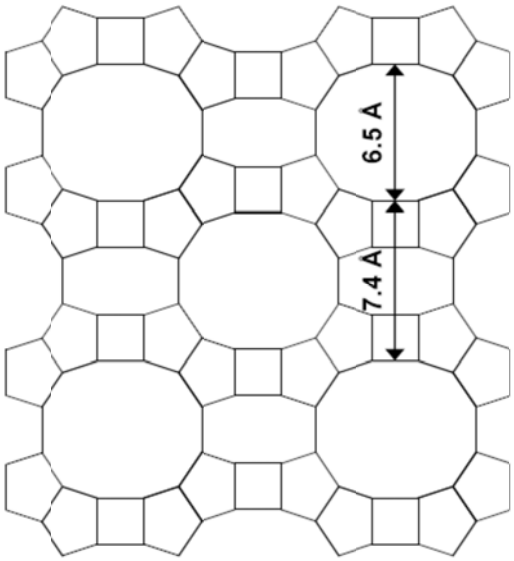


**Scheme 3.5.** MOR crystal structure viewed along [001].

*3.6.8 Distribution of Butene Isomers Observed During n-Butane Dehydrogenation on MOR Samples*

Butene isomer ratios measured in the reactor effluent upon n-butane dehydrogenation on $H_{100}Na_0$MOR-Z and $H_{45}Na_{55}$MOR-Z samples at 748 K are plotted against inverse space velocity in Figure 3.14. Product chromatograms were corrected for feed butene impurities when calculating dehydrogenation turnover rates, but were not corrected for these impurities when calculating isomer ratios because they equilibrate with the butene products of n-butane dehydrogenation reactions.

n-Butane dehydrogenation turnover rates (per total $H^+$) were lower (by a factor of ~7) on $H_{45}Na_{55}$MOR-Z than on $H_{100}Na_0$MOR-Z (Table 3.6) because the former sample contained a smaller fraction of Brønsted acid sites within 8-MR locations (0.13) than the latter (0.56), which were found to exclusively catalyze dehydrogenation turnovers (Section 3.3). Butene isomer distributions at 748 K, however, were similar on $H_{100}Na_0$MOR-Z and $H_{45}Na_{55}$MOR-Z (Fig. 3.14), in spite of large differences in dehydrogenation turnover rates (per total $H^+$) on the two samples. The position of initial C-H bond activation cannot be preserved in the alkene products because linear butene isomers equilibrate via rapid protonation-deprotonation with intervening hydride shifts. The ratio of isobutene to 1-butene isomers depends on the space velocity and is not equilibrated upon extrapolation to zero conversion, but it is non-zero only because of isobutene impurities present in the feed. This ratio approaches the equilibrated ratio (3.7 at 748 K) [64] at longer residence times (Fig. 3.14), indicating that skeletal rearrangements are not as rapid as double-bond isomerization events at typical reaction temperatures (700-800 K).

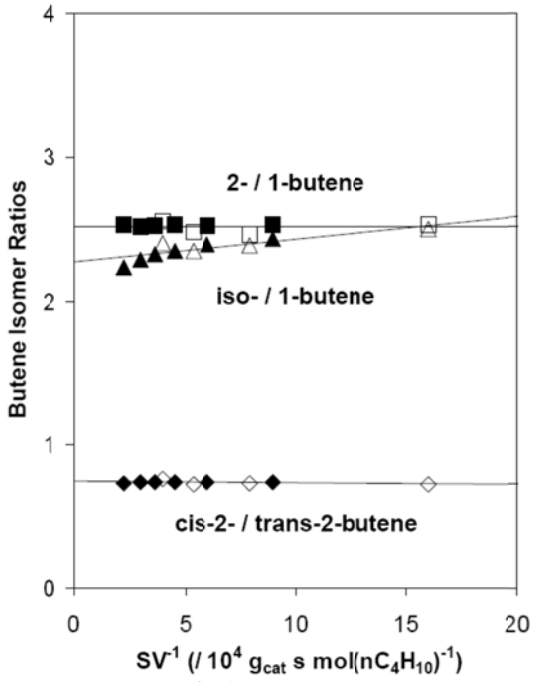


**Figure 3.14.** Ratios of cis-2-butene/trans-2-butene (◆,◇), 2-butene/1-butene (■,□) and iso-butene/1-butene (▲,△) isomers in the reactor effluent at 748 K on $H_{100}Na_0$MOR-Z (closed symbols) and $H_{45}Na_{55}$MOR-Z (open symbols) are plotted against inverse space velocity.

### 3.7. References


(1) Olson, D. H.; Haag, W. O.; Lago, R. M. *J. Catal.* **1980**, *61*, 390.
(2) Haag, W. O.; Lago, R. M.; Weisz, P. B. *Nature* **1984**, *309*, 589.
(3) Kazansky, V. B. *Acc. Chem. Res.* **1991**, *24*, 379.
(4) Eichler, U.; Brandle, M.; Sauer, J. *J. Phys. Chem. B* **1997**, *101*, 10035.
(5) Sauer, J.; Sierka, M. *J. Comput. Chem.* **2000**, *21*, 1470.
(6) van Santen, R. A.; Kramer, G. J. *Chem. Rev.* **1995**, *95*, 637.
(7) Rigby, A. M.; Kramer, G. J.; van Santen, R. A. *J. Catal.* **1997**, *170*, 1.
(8) Bhan, A.; Allian, A. D.; Sunley, G. J.; Law, D. J.; Iglesia, E. *J. Am. Chem. Soc.* **2007**, *129*, 4919.
(9) Bhan, A.; Iglesia, E. *Acc. Chem. Res.* **2008**, *41*, 559.
(10) Greensfelder, B. S.; Voge, H. H.; Good, G. M. *Ind. Eng. Chem.* **1949**, *41*, 2573.
(11) Thomas, C. L. *Ind. Eng. Chem.* **1949**, *41*, 2564.
(12) Haag, W. O.; Dessau, R. M. In *Proc. 8th Int. Congr. Catalysis, Berlin*; Verlag-Chemie: Weinheim, **1984**; Vol. 2, p 305.
(13) Kotrel, S.; Knözinger, H.; Gates, B. C. *Microporous Mesoporous Mater.* **2000**, *35-6*, 11.
(14) Kwak, B. S.; Sachtler, W. M. H.; Haag, W. O. *J. Catal.* **1994**, *149*, 465.
(15) Krannila, H.; Haag, W. O.; Gates, B. C. *J. Catal.* **1992**, *135*, 115.
(16) Lercher, J. A.; van Santen, R. A.; Vinek, H. *Catal. Lett.* **1994**, *27*, 91.
(17) Ivanova, II; Pomakhina, E. B.; Rebrov, A. I.; Derouane, E. G. *Top. Catal.* **1998**, *6*, 49.
(18) Ivanova, II; Rebrov, A. I.; Pomakhina, E. B.; Derouane, E. G. *J. Mol. Catal. A* **1999**, *141*, 107.
(19) Cheung, P.; Bhan, A.; Sunley, G. J.; Law, D. J.; Iglesia, E. *J. Catal.* **2007**, *245*, 110.
(20) Benco, L.; Bucko, T.; Hafner, J.; Toulhoat, H. *J. Phys. Chem. B* **2004**, *108*, 13656.
(21) Narbeshuber, T. F.; Vinek, H.; Lercher, J. A. *J. Catal.* **1995**, *157*, 388.
(22) Narbeshuber, T. F.; Brait, A.; Seshan, K.; Lercher, J. A. *J. Catal.* **1997**, *172*, 127.
(23) Wang, X.; Carabineiro, H.; Lemos, F.; Lemos, M.; Ribeiro, F. R. *J. Mol. Catal. A* **2004**, *216*, 131.
(24) Bandiera, J.; Dufaux, M.; Ben Taarit, Y. *Appl. Catal. A* **1997**, *148*, 283.
(25) Bandiera, J.; Ben Taarit, Y. *Appl. Catal.* **1990**, *62*, 309.
(26) Xu, B.; Sievers, C.; Hong, S. B.; Prins, R.; van Bokhoven, J. A. *J. Catal.* **2006**, *244*, 163.
(27) Zheng, X. B.; Blowers, P. *J. Phys. Chem. A* **2005**, *109*, 10734.
(28) Madon, R. J.; Iglesia, E. *J. Mol. Catal. A* **2000**, *163*, 189.
(29) Eder, F.; Stockenhuber, M.; Lercher, J. A. *J. Phys. Chem. B* **1997**, *101*, 5414.
(30) Eder, F.; Lercher, J. A. *J. Phys. Chem. B* **1997**, *101*, 1273.
(31) Eder, F.; Lercher, J. A. **1997**, *18*, 75.
(32) Denbigh, K. *The Principles of Chemical Equilibrium*; 4th ed.; Cambridge University Press: Cambridge, **1981**.
(33) Haag, W. O. *Stud. Surf. Sci. Catal.* **1994**, *84*, 1375.
(34) van Bokhoven, J. A.; Williams, B. A.; Ji, W.; Koningsberger, D. C.; Kung, H. H.; Miller, J. T. *J. Catal.* **2004**, *224*, 50.
(35) Babitz, S. M.; Williams, B. A.; Miller, J. T.; Snurr, R. Q.; Haag, W. O.; Kung, H. H. *Appl. Catal. A* **1999**, *179*, 71.
(36) Bhan, A.; Gounder, R.; Macht, J.; Iglesia, E. *J. Catal.* **2008**, *253*, 221.
(37) Wei, J. *Chem. Eng. Sci.* **1996**, *51*, 2995.

(38) Aronson, M. T.; Gorte, R. J.; Farneth, W. E. *J. Catal.* **1986**, *98*, 434.
(39) Macht, J.; Janik, M. J.; Neurock, M.; Iglesia, E. *J. Am. Chem. Soc.* **2008**, *130*, 10369.
(40) Nieminen, V.; Sierka, M.; Murzin, D. Y.; Sauer, J. *J. Catal.* **2005**, *231*, 393.
(41) Esteves, P. M.; Mota, C. J. A.; Ramírez-Solís, A.; Hernández-Lamoneda, R. *J. Am. Chem. Soc.* **1998**, *120*, 3213.
(42) Collins, S. J.; O' Malley, P. J. *Chem. Phys. Lett.* **1994**, *228*, 246.
(43) Zygmunt, S. A.; Curtiss, L. A.; Zapol, P.; Iton, L. E. *J. Phys. Chem. B* **2000**, *104*, 1944.
(44) Frash, M. V.; van Santen, R. A. *Top. Catal.* **1999**, *9*, 191.
(45) Savitz, S.; Siperstein, F.; Gorte, R. J.; Myers, A. L. *J. Phys. Chem. B* **1998**, *102*, 6865.
(46) Benson, S. W. *Thermochemical Kinetics*; John Wiley & Sons, Inc.: New York, **1976**.
(47) Hunger, B.; Heuchel, M.; Clark, L. A.; Snurr, R. Q. *J. Phys. Chem. B* **2002**, *106*, 3882.
(48) Busca, G. *Chem. Rev.* **2007**, *107*, 5366.
(49) Makarova, M. A.; Wilson, A. E.; van Liemt, B. J.; Mesters, C.; de Winter, A. W.; Williams, C. *J. Catal.* **1997**, *172*, 170.
(50) Datka, J.; Gil, B.; Kubacka, A. *Zeolites* **1997**, *18*, 245.
(51) Maache, M.; Janin, A.; Lavalley, J. C.; Benazzi, E. *Zeolites* **1995**, *15*, 507.
(52) Veefkind, V. A.; Smidt, M. L.; Lercher, J. A. *Appl. Catal. A* **2000**, *194*, 319.
(53) Brändle, M.; Sauer, J. *J. Am. Chem. Soc.* **1998**, *120*, 1556.
(54) van Well, W. J. M.; Cottin, X.; de Haan, J. W.; Smit, B.; Nivarthy, G.; Lercher, J. A.; van Hooff, J. H. C.; van Santen, R. A. *J. Phys. Chem. B* **1998**, *102*, 3945.
(55) van Well, W. J. M.; Cottin, X.; Smit, B.; van Hooff, J. H. C.; van Santen, R. A. *J. Phys. Chem. B* **1998**, *102*, 3952.
(56) Degnan, T. F. *J. Catal.* **2003**, *216*, 32.
(57) Hunter, K. C.; East, A. L. L. *J. Phys. Chem. A* **2002**, *106*, 1346.
(58) Beyerlein, R. A.; McVicker, G. B.; Yacullo, L. N.; Ziemiak, J. J. *Abstr. Pap.-Am. Chem. Soc.* **1986**, *191*, 7.
(59) Fritz, P. O.; Lunsford, J. H. *J. Catal.* **1989**, *118*, 85.
(60) Mears, D. E. *Ind. Eng. Chem. Process Design Develop.* **1971**, *10*, 541.
(61) Haag, W. O.; Lago, R. M.; Weisz, P. B. *Faraday Discuss.* **1981**, *72*, 317.
(62) Breck, D. W. *Zeolite Molecular Sieves*; John Wiley & Sons, Inc.: New York, **1974**.
(63) International Zeolite Association website: http://www.iza-online.org/
(64) Calculated using thermodynamic data from: D. R. Stull, E. F. Westrum, G. C. Sinke, *The Chemical Thermodynamics of Organic Compounds*, Wiley: New York, 1987.

# CHAPTER FOUR

# Effects of Partial Confinement on the Specificity of Monomolecular Alkane Reactions for Acid Sites in Side Pockets of Mordenite

## 4.1 Results and Discussion

The location of Brønsted acid sites within zeolites influences catalytic rates and selectivities when their diverse intrachannel environments stabilize transition states to different extents [1]. Mordenite zeolites in their proton-form (H-MOR) contain acid sites located within two environments: eight-membered ring (8-MR) side pockets and 12-MR main channels. The location of these acid sites can be determined by rigorous deconvolution of OH infrared bands and by titration with molecules of varying size [2,3], allowing catalytic turnover rates to be described in terms of the respective contributions from sites within these two locations.

We have shown previously that monomolecular cracking and dehydrogenation of propane and *n*-butane occur preferentially within constrained 8-MR pockets, where transition states and adsorbed reactants are only partially confined [2]. Such configurations lead to entropy gains that compensate for the weaker binding of partially confined structures to give lower free energies for transition states within 8-MR pockets [2]. For *n*-alkanes, monomolecular dehydrogenation reactions show greater specificity for 8-MR locations than cracking and also show higher activation barriers [2], predominantly because $(C\text{-}H\text{-}H)^+$ species involved in transition states for dehydrogenation reactions are less stable than the $(C\text{-}C\text{-}H)^+$ carbonium ions in cracking transition states (proponium [4]; *n*-butonium [5]). Activation entropies were also higher for *n*-alkane dehydrogenation than for cracking [2], consistent with crossing potential curve descriptions of charge transfer reaction coordinates [6-8], which indicate that transition states with higher energies are looser and occur later along the reaction coordinates. Thus, it seems plausible that reactions involving later and looser transition states, with more fully-formed ion-pairs, benefit preferentially from entropy gains caused by partial confinement within 8-MR side pockets. The electrostatic underpinnings of these entropy benefits resemble those for proton-transfer [7] and electron-transfer [8] reactions in solvated systems, for which the entropies for molecular and charge reorganization are essential in stabilizing the ion-pairs formed upon charge transfer.

Here, we probe and extend these concepts of 8-MR pocket specificity in ion-pair stabilization to monomolecular reactions of branched alkanes. We show that isobutane cracking has a stronger preference than dehydrogenation for 8-MR locations in MOR, in sharp contrast with the trends for *n*-alkane reactions. Transition state energies are higher for isobutane cracking than for dehydrogenation, consistent with the less stable cations formed upon protonation of C-C bonds instead of the tertiary C-H bond in isobutene [9]. We propose that, as for monomolecular *n*-alkane dehydrogenation, isobutane cracking shows a stronger preference than dehydrogenation for 8-MR acid sites because it involves later and looser transition states, which benefit more strongly from entropy gains arising from partial confinement.

The fraction of the Brønsted acid sites located within 8-MR pockets varies widely (10-80%) among H-MOR samples [10] prepared by partial exchange of $H^+$ with $Na^+$ and also among H-MOR samples of different provenance [2]. Rate constants for monomolecular isobutane cracking (per total $H^+$; 748 K; Fig. 4.1a) and dehydrogenation (Fig. 4.1b) increased monotonically as the fraction of the protons located within 8-MR pockets increased. As for *n*-alkanes, these data show that both reactions occur preferentially on sites located within 8-MR pockets. Isobutane cracking-to-dehydrogenation rate ratios *increased* with increasing 8-MR $H^+$ fraction, in contrast with those measured for propane and *n*-butane (Fig. 4.2); thus, cracking shows a stronger kinetic preference for 8-MR sites than dehydrogenation for isobutane reactants (700-780 K; Section 4.4.1, Supporting Information). The rate constants for isobutane dehydrogenation and cracking on 8-MR and 12-MR acid sites were extracted from their respective dependences on the number of sites at each location for each temperature (Section 4.4.2, Supporting Information) [2]. At 748 K, dehydrogenation rate constants were ~7 times larger on 8-MR than on 12-MR sites, while cracking rate constants were not detectable on 12-MR sites (Table 4.1).

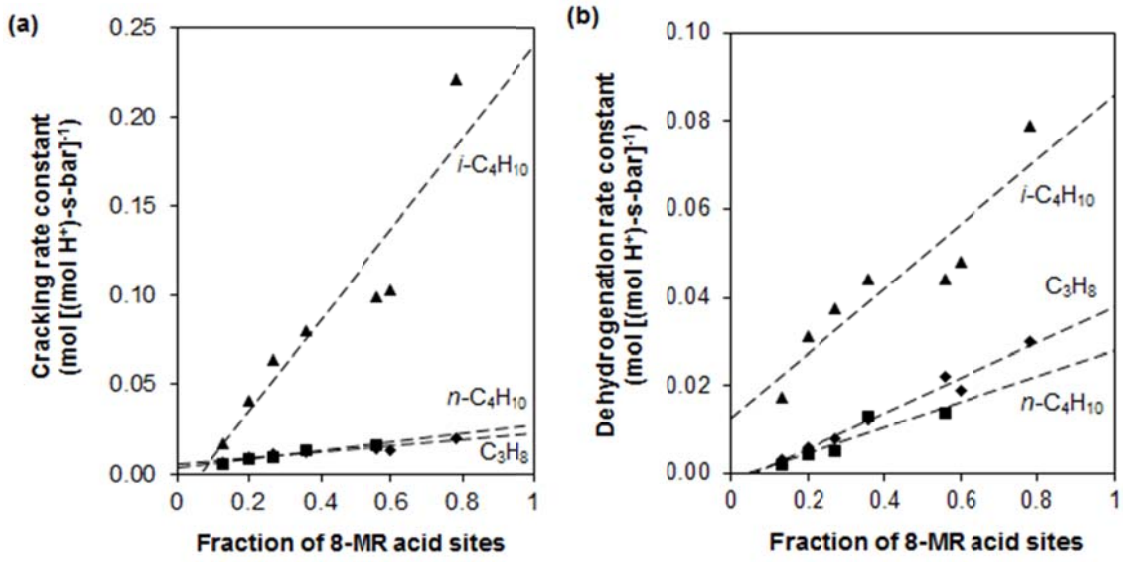


**Figure 4.1.** Dependence of rate constants (748 K) for monomolecular (a) cracking and (b) dehydrogenation of propane (x10; ◆), *n*-butane (■) and isobutane (▲) on the fraction of 8-MR acid sites in H-MOR catalysts.

Monomolecular alkane activation involves carbonium ion-like transition states [11,12] formed via interactions of adsorbed reactants ($A_z$) with Brønsted acid sites ($H^+$); adsorbed reactants are in quasi-equilibrium with those in the extracrystalline gas phase ($A_g$) (Scheme 4.1). Reaction rates (Eq. (4.1)) are first-order in alkane pressure ($P_A$):

$$r = k_{int} \cdot K_A \cdot P_A = k_{meas} \cdot P_A . \tag{4.1}$$

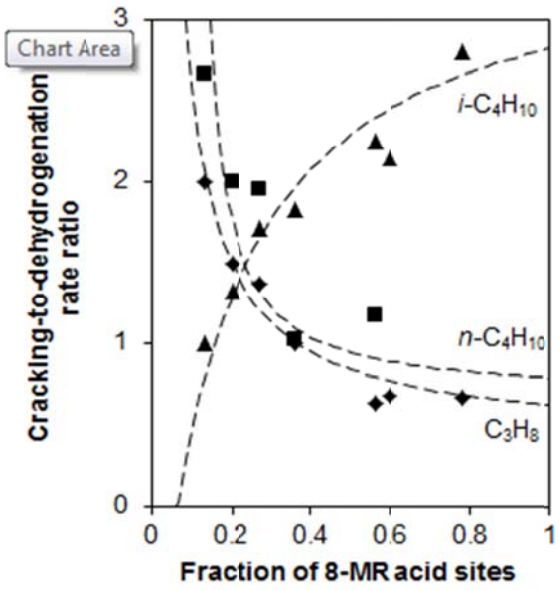


**Figure 4.2.** Cracking-to-dehydrogenation rate ratios (748 K) for propane (◆), *n*-butane (■) and isobutane (▲) on H-MOR catalysts with different fractions of Brønsted acid sites within 8-MR side pockets; rate ratios predicted using regressed rate constants are given by the dashed curves.

$k_{int}$ and $k_{meas}$ are intrinsic and measured rate constants, respectively, and $K_A$ is the adsorption equilibrium constant (Section 4.4.3, Supporting Information) [2,13-16]. The combined temperature dependences of $k_{int}$ and $K_A$ show that $k_{meas}$ depends only on free energy differences between gaseous reactants and transition states (Eq. (4.2)) and is determined solely by the consequences of confinement for transition state stability.

$$k_{meas} = \exp\left(-\left(\Delta G^{\circ}_{\dagger} - \Delta G^{\circ}_{Ag}\right)/RT\right). \tag{4.2}$$

Cracking (C) to dehydrogenation (D) rate ratios reflect, in turn, differences in the stability of the ion-pairs involved in their respective transition states (Eq. (4.3)).

$$k_{meas,C} / k_{meas,D} = \exp\left(-\left(\Delta G^{\circ}_{\dagger,C} - \Delta G^{\circ}_{\dagger,D}\right)/RT\right). \tag{4.3}$$

**Table 4.1.** Monomolecular isobutane cracking and dehydrogenation rate constants ($k_{meas}$) at 748 K on acid sites within 8-MR and 12-MR locations of MOR.

| Reaction | $k_{meas}$ (8-MR)[a] | $k_{meas}$ (12-MR)[a] |
|---|---|---|
| Cracking | 25.8 ± 3.2 | n.d.[b] |
| Dehydrogenation | 9.1 ± 1.0 | 1.3 ± 0.7 |

[a] [$10^{-2}$ mol (mol $H^+$)$^{-1}$ $s^{-1}$ $bar^{-1}$]; rate parameters determined by linear regression methods; uncertainties reported as one standard deviation (details in Section 4.4.2 of the Supporting Information).
[b] n.d., not detected.

This treatment highlights the pre-eminence of activation free energies, instead of the separate effects of activation entropies and enthalpies, in the dynamics of chemical reaction, a conclusion also evident from enthalpy-entropy compromises mediated by solvation within zeolite voids.

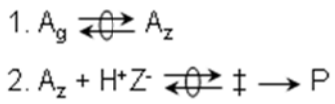


**Scheme 4.1.** Reaction sequence for monomolecular activation of alkanes (A) on Brønsted acid sites located within zeolite channels ($H^+Z^-$) to form products (P); adapted from [2].

Measured activation barriers are ~14-19 kJ mol$^{-1}$ larger for cracking than for dehydrogenation of isobutane on all MOR samples (Table 4.2), consistent with previous data on H-MFI and H-USY [17-21] and with theoretical estimates on 20 T-atom MFI clusters [22]. Isobutane cracking-to-dehydrogenation rate ratios, as a result, increased with temperature (Fig. 4.3), in sharp contrast with ratios that *decreased* with temperature for propane and *n*-butane, as a result of the larger barriers for *n*-alkane dehydrogenation than cracking [2]. We note that alkane cracking-to-dehydrogenation rate ratios that increased with temperature (Fig. 4.3) also increased with the fraction of protons within 8-MR pockets (Fig. 4.2). We conclude that reaction paths with higher activation barriers show greater specificity for 8-MR locations, apparently because later and looser transition states involved in these paths capture a greater benefit of the entropy gains resulting from partial confinement.

**Table 4.2.** Measured activation energies ($E_{meas}$) for monomolecular isobutane cracking (C) and dehydrogenation (D) on MOR samples.

| Zeolite | $E_{meas,C}$[a] (kJ mol$^{-1}$) | $E_{meas,D}$[b] (kJ mol$^{-1}$) |
|---|---|---|
| $H_{100}Na_0$MOR-T | 191 | 177 |
| $H_{100}Na_0$MOR-Z | 208 | 194 |
| $H_{45}Na_{55}$MOR-Z | 205 | 186 |

[a] ± 8 kJ mol$^{-1}$.
[b] ± 15 kJ mol$^{-1}$.

Monomolecular cracking and dehydrogenation paths for normal alkanes [23,24] and iso-alkanes [22,25,26] involve ion-pairs with alkyl fragments containing a nearly full positive charge (+0.9). These transition states are stabilized by electrostatic interactions with the negatively-charged framework and by van der Waals interactions that also stabilize adsorbed alkane reactants to the same extent. Born-Haber thermochemical cycles [2] (Section 4.4.4, Supporting Information) indicate that differences in cracking and dehydrogenation barriers predominantly reflect enthalpy differences for protonation of C-C bonds and C-H bonds in gas-phase alkanes (Fig. 4.4); this analysis also showed [2] that larger *n*-alkane dehydrogenation barriers reflect less stable cations formed upon protonation of C-H bonds instead of C-C bonds in *n*-alkanes [4,5]. Higher activation barriers for cracking than dehydrogenation of isobutane (by 14-19 kJ mol$^{-1}$; Table 4.2) reflect the less exothermic gas-phase protonation of C-C bonds (-682 kJ mol$^{-1}$) than of tertiary C-H bonds (-696 kJ mol$^{-1}$) [9]. The resulting gas-phase cations are ($CH_4$)-(*iso*-$C_3H_7^+$) and ($H_2$)-(*tert*-$C_4H_9^+$) van der Waals complexes formed by protonation of isobutane at its C-C and

tertiary C-H bonds, respectively [9]; these structures resemble the fully-formed ion-pairs at late transition states for both reactions suggested by density functional theory [22,25,26]. Thus, we conclude that differences in monomolecular cracking and dehydrogenation barriers for linear and branched alkanes reflect enthalpy differences for gas-phase protonation at their C-C and C-H bonds (Fig. 4.4), resulting in predictable effects of temperature (Fig. 4.3) and acid site location (Fig. 4.2) on selectivity.

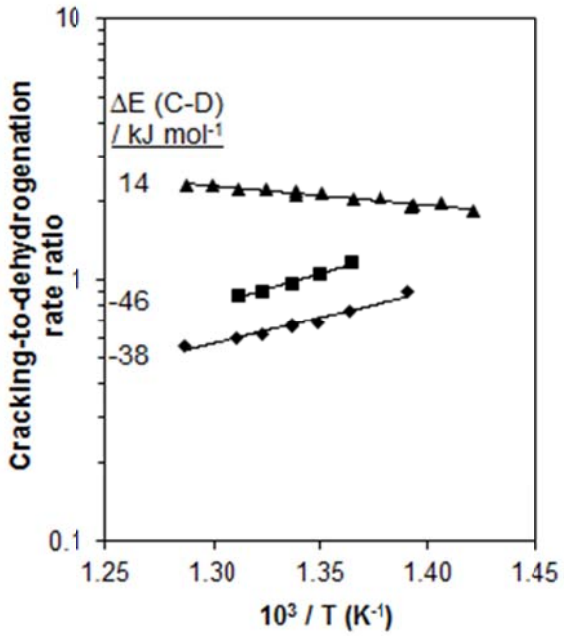


**Figure 4.3.** Dependence of monomolecular propane (◆), *n*-butane (■) and isobutane (▲) cracking-to-dehydrogenation rate ratios ($H_{100}Na_0$MOR-Z) on temperature; differences in cracking (C) and dehydrogenation (D) activation energies are reflected in the slope.

Rate constants as a function of temperature can be used to estimate activation energies for cracking and dehydrogenation at 8-MR and 12-MR locations. Activation energies for monomolecular *n*-alkane cracking were higher on 8-MR than on 12-MR sites, because of weaker binding and less intimate van der Waals contacts for both reactants and transition states, which can be confined only partially within 8-MR pockets [2]. Activation energies for isobutane cracking and dehydrogenation on 8-MR acid sites were $188 \pm 8$ kJ mol$^{-1}$ and $175 \pm 15$ kJ mol$^{-1}$, respectively. The rate constants on 12-MR sites were too small for accurate estimates of their activation energies. Thus, we infer that partial confinement of reactants and transition states within 8-MR pockets enables entropy-enthalpy compromises, as in the case of *n*-alkanes and consistent with geometric considerations [27].

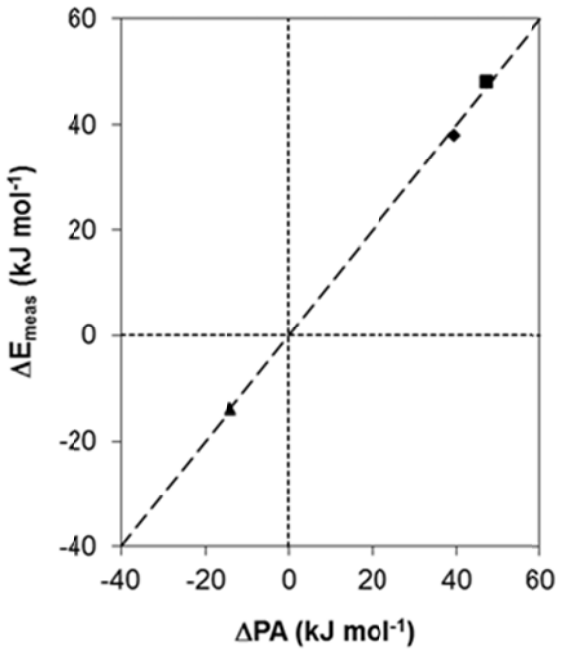


**Figure 4.4.** Difference in dehydrogenation and cracking activation barriers ($\Delta E_{meas}$) measured on $H_{100}Na_0$MOR-Z for propane (◆), *n*-butane (■) and isobutane (▲) plotted against the difference in gas-phase proton affinities of their C-H and C-C bonds (ΔPA) (Section 4.4.5, Supporting Information).

As for *n*-alkanes, we conclude that acid sites confined within 8-MR pockets are much more active for monomolecular isobutane reactions than sites of similar acid strength [28] within 12-MR channels (Table 4.3) because partially confined transition states have lower standard free energies as a result of entropy-enthalpy trade-offs. These compromises and their dependence on catalyst structure appear to be ubiquitous and consequential for reactivity in acid catalysis as the concerted alignment of van der Waals contacts becomes ultimately unfavorable as a result of concomitant losses in rotational and vibrational entropy in the transition state ion-pairs. Entropy gains mediated by partial confinement benefit most strongly the highest energy transition states among possible parallel pathways, because they are looser and occur later along the reaction coordinate. Thus, for monomolecular alkane activation, the higher energy pathway involves the less stable protonated-alkane ion-pair (Fig. 4.4) and has a greater specificity for 8-MR locations in H-MOR (Fig. 4.2).

**Table 4.3.** Ratio of 8-MR to 12-MR rate constants ($k_{meas}$) at 748 K for monomolecular cracking and dehydrogenation of propane, *n*-butane and isobutane.

| **Reaction** | **$k_{meas}$ (8-MR) / $k_{meas}$ (12-MR)** | | |
|---|---|---|---|
| | *Propane* | *n-Butane* | *Isobutane* |
| Cracking | 2.9 | >6.2[a,b] | >14.3[b] |
| Dehydrogenation | >10.7[b] | >15.8[b] | 6.8 |

[a] Total cracking rate ratio. Ratios are >10.4 and 2.3 for terminal and central C-C cracking, respectively.

[b] Rate constants on 12-MR sites were zero, within the error of regression. Lower limits on 8-MR-to-12-MR rate ratios were calculated from the maximum value of the 12-MR rate constant, estimated as the upper bound of the confidence interval containing one standard deviation.

These findings and concepts highlight the preeminent role of entropy and free energy in determining reactivity and selectivity in chemical reactions [2,29,30], the strong effects of location in the preferential stabilization of specific transition states [1,2], and the rigor of thermochemical analyses in dissecting the effects of catalyst and reactant properties on the stability of bound reactants and ion-pairs at the transition state.

## 4.2 Experimental Section

H-zeolites were prepared by treating $NH_4^+$-zeolites in flowing dry air (2.5 $cm^3$ $g^{-1}$ $s^{-1}$, zero grade, Praxair) at 773 K (at 0.0167 K $s^{-1}$) for 4 h and then pelleting, crushing, and sieving to retain 180-250 μm (60-80 mesh) aggregates. The methods used to prepare the $Na^+$-exchanged zeolites, determine their elemental composition and obtain $^{27}$Al-NMR and infrared spectra are reported elsewhere [2]. Catalytic cracking and dehydrogenation rates were measured under differential conditions (<2% conversion) in a plug-flow tubular quartz reactor [2]. Catalysts (0.01-0.03 g) were first treated in a 5% $O_2$ / 95% He mixture (16.7 $cm^3$ $g^{-1}$ $s^{-1}$, 99.999%, Praxair) at 803 K (0.0167 K $s^{-1}$) for 2 h and then in pure He flow (16.7 $cm^3$ $g^{-1}$ $s^{-1}$, 99.999%, Praxair) for 0.5 h, while isobutane reactants (10% *i*-$C_4H_{10}$, 5% Ar, 85% He, Praxair, 99.5% purity) were transferred via heated lines (423 K) to a gas chromatograph (Agilent HP-6890GC) for calibration purposes. Flame ionization and thermal conductivity detection were used to measure reactants and products, which were separated chromatographically using GS-AL\KCl capillary (0.530 mm ID x 50 m; Agilent) and HayeSep DB packed (100-120 mesh, 10 ft.; Sigma-Aldrich) columns. Reactants were mixed with He (99.999%, Praxair) to vary *i*-$C_4H_{10}$ pressures (1-5 kPa) and molar rates ($10^{-4}$-$10^{-3}$ mol alkane $g^{-1}$ $s^{-1}$). Equimolar $C_3/C_1$ product ratios were observed at all space velocities; taken together with the absence of $C_{5+}$ products, these data confirm that bimolecular or secondary pathways do not contribute to the products formed. Activation energies and pre-exponential factors were determined from rate constants measured as a function of temperature (703-778 K). Rates and selectivities measured after ~10 h on stream were similar (within 5%) to their initial values on all catalysts, indicating that deactivation did not influence kinetic data.

## 4.3 Acknowledgements

The authors acknowledge with thanks the financial support from the Chevron Energy Technology Company. We also thank Dr. Stacey I. Zones (Chevron) and Prof. Matthew Neurock (University of Virginia) for valuable technical discussions.

## 4.4 Supporting Information

### *4.4.1 Preferential Isobutane Cracking and Dehydrogenation on 8-MR Acid Sites at 718 K and 733 K*

Both monomolecular isobutane cracking and dehydrogenation occurred preferentially on 8-MR acid sites at 748 K; isobutane cracking showed a stronger specificity for such locations, resulting in cracking-to-dehydrogenation rate ratios that increased systematically with increasing 8-MR $H^+$ content. These trends persisted throughout the temperature range studied (700-780 K). We supplement the data shown in the text at 748 K, with isobutane cracking and dehydrogenation rate constants (per total $H^+$) and their rate ratios at 718 K (Fig. 4.5) and 733 K (Fig. 4.6), all of which increase systematically with increasing 8-MR $H^+$ fractions.

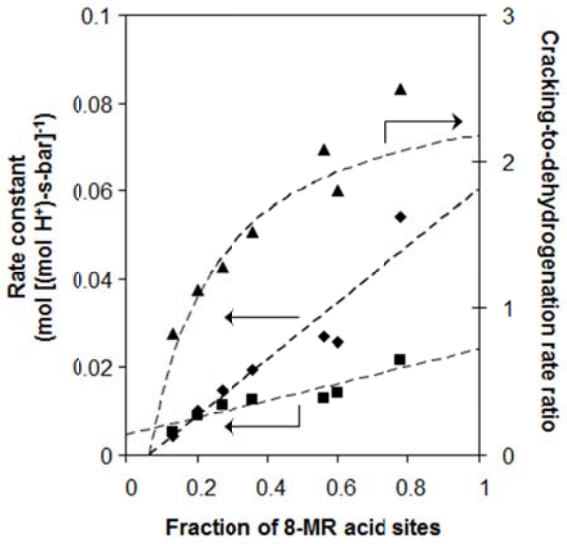


**Figure 4.5.** Isobutane cracking (◆) and dehydrogenation (■) rate constants and cracking-to-dehydrogenation rate ratios (▲) at 718 K plotted against the fraction of Brønsted acid sites in the 8-MR pockets of MOR catalysts.

### *4.4.2 Estimation of Rate Constants for Isobutane Cracking and Dehydrogenation at Each MOR Location Using Linear Regression Methods*

Overall rate constants were expressed by weighing rate constants for 8-MR ($k_{8\text{-}MR}$) and 12-MR ($k_{12\text{-}MR}$) acid sites by the fraction of OH groups ($X_{8\text{-}MR}$, $X_{12\text{-}MR}$) within each environment:

$$k = k_{8-MR} \cdot X_{8-MR} + k_{12-MR} \cdot X_{12-MR}. \tag{4.4}$$

The location-specific rate constant for a given reaction and temperature was estimated by a least-squares regression of rate data on seven MOR catalysts with varying 8-MR $H^+$ fraction (10-80%), as a result of partial $Na^+$ exchange and their different provenance;[S1] uncertainties in regressed rate constants are reported as the standard deviation.

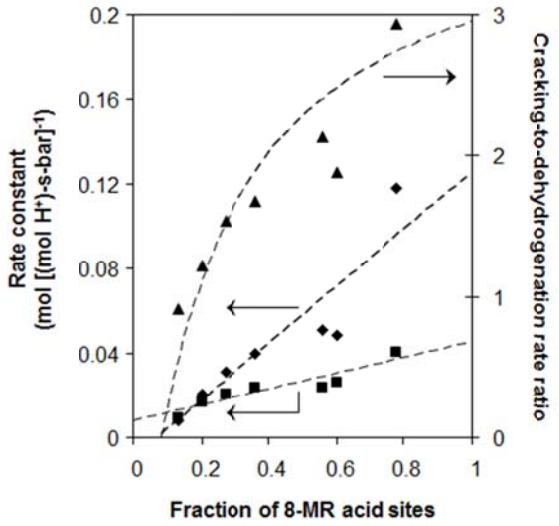


**Figure 4.6.** Isobutane cracking (◆) and dehydrogenation (■) rate constants and cracking-to-dehydrogenation rate ratios (▲) at 733 K plotted against the fraction of Brønsted acid sites in the 8-MR pockets of MOR catalysts.

Regressed rate constants at 748 K are shown in Table 4.2 of the text and indicate that cracking rate constants were negligible on 12-MR sites, within experimental detection limits. Indeed, cracking rates (per g) depended linearly on the number of OH groups (per g) within 8-MR pockets, but not on the number of OH groups located within 12-MR channels (Fig. 4.7). Dehydrogenation rate constants at 748 K were ~7 times larger on 8-MR acid sites than on 12-MR sites; dehydrogenation rates (per g) also depend linearly on the number of 8-MR sites, but the observed non-zero intercept reflects small but detectable dehydrogenation rates on 12-MR sites (Fig. 4.8). Measured isobutane dehydrogenation rates (per g) become strictly proportional to the number of 8-MR sites upon correction for these contributions from 12-MR channels (Fig. 4.8).

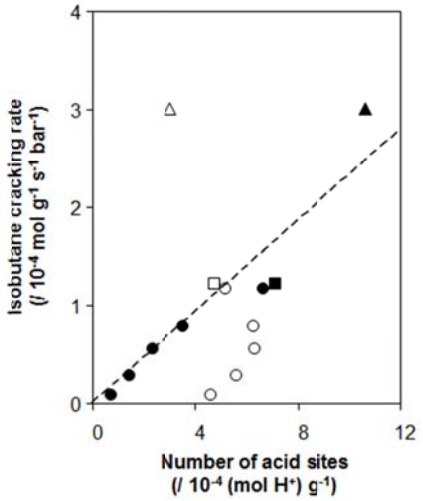


**Figure 4.7.** Isobutane cracking rates (per g) at 748 K in H-MOR and $Na^+$-exchanged MOR samples (MOR-Z: ●, MOR-S: ■, MOR-T: ▲) plotted against the density of Brønsted acid sites (per g) in the 8-MR pockets of MOR (closed symbols) and 12-MR channels of MOR (open symbols).

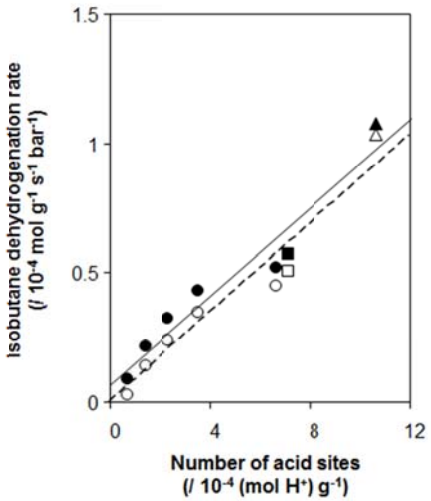


**Figure 4.8.** Measured isobutane dehydrogenation rates (per g) (closed symbols) and residual dehydrogenation rates after correction for the contribution from 12-MR sites (per g) (open symbols) at 748 K in H-MOR and $Na^+$-exchanged MOR samples (MOR-Z: ●, MOR-S: ■, MOR-T: ▲) plotted against the density of Brønsted acid sites (per g) in 8-MR pockets.

### *4.4.3 Transition State Treatments of Monomolecular Reaction Rate Laws*

A more detailed derivation of rate laws and kinetic parameters for monomolecular alkane reactions in zeolites using transition state treatments for thermodynamically non-ideal systems can be found elsewhere [2]; here we include a highly abridged version to supplement the discussion relevant to this manuscript.

Alkanes crack and dehydrogenate on acidic zeolites via monomolecular C-C and C-H activation routes at high temperatures and low pressures and conversions; these reactions involve carbonium ion-like transition states [11,12] formed from Brønsted acid sites ($H^+$) and adsorbed reactants ($A_z$) that are quasi-equilibrated with the gas phase ($A_g$) (Scheme 4.2). At the temperatures required for protonation of C-C and C-H bonds in alkanes, intrazeolite alkane concentrations are low and lead to reaction rates given by:

$$r = k_{int} \cdot K_A \cdot P_A, \text{ and} \tag{4.5}$$

$$k_{meas} = k_{int} \cdot K_A, \tag{4.6}$$

where $k_{int}$ and $k_{meas}$ are intrinsic and measured rate constants, respectively, $P_A$ is the alkane pressure and $K_A$ is the adsorption equilibrium constant [2]. The temperature dependences of $k_{int}$ and $K_A$ are:

$$k_{int} = \exp\left(-\Delta G_{int} / RT\right) = \exp\left(-\left(\Delta G^\circ_{\dagger} - \Delta G^\circ_{Az}\right) / RT\right), \tag{4.7}$$

$$K_A = \exp\left(-\Delta G_{ads} / RT\right) = \exp\left(-\left(\Delta G^\circ_{Az} - \Delta G^\circ_{Ag}\right) / RT\right). \tag{4.8}$$

Therefore, $k_{meas}$ depends on the free energy difference between transition states stabilized within zeolite channels and alkane reactants in the gas phase:

$$k_{meas} = \exp\left(-\Delta G_{meas} / RT\right) = \exp\left(-\left(\Delta G°_{\dagger} - \Delta G°_{Ag}\right) / RT\right). \quad (4.9)$$

Thus, the ratio of cracking (C) and dehydrogenation (D) rate constants reflects free energy differences in their respective transition states:

$$k_{meas,C} / k_{meas,D} = \exp\left(-\left(\Delta G°_{\dagger,C} - \Delta G°_{\dagger,D}\right) / RT\right). \quad (4.10)$$

The free energies (Eq. 4.9) can be further decomposed into enthalpy and entropy components; thus, the measured activation energy ($E_{meas}$) is given by:

$$E_{meas} = E_{\text{int}} + \Delta H_{ads}, \quad (4.11)$$

where $\Delta H_{ads}$ is the adsorption enthalpy and $E_{int}$ is the intrinsic activation energy.

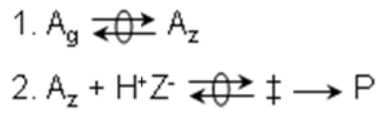


**Scheme 4.2.** Monomolecular alkane (A) activation on Brønsted acid sites located within zeolite channels ($H^+Z^-$) to form products (P); adapted from [2].

### *4.4.4 Assessment of Activation Energies Using Born-Haber Thermochemical Cycles*

Measured activation barriers ($E_{meas}$) for monomolecular alkane reactions on acidic zeolites reflect the stability of carbonium ion-like transition states within zeolite channels with respect to gas-phase alkane reactants. A thermochemical cycle (Scheme 4.3) can be used to relate enthalpies of gaseous reactants and these transition states via hypothetical path-independent steps. In this scheme, measured activation barriers depend on the zeolite deprotonation enthalpies (DPE), on the proton affinities for gas-phase alkanes (PA), and on the transition state stabilization energies ($E_{stab}$), resulting in the following relationship:

$$E_{meas} = DPE + PA + E_{stab}. \quad (4.12)$$

Here, we discuss the specific case of parallel reaction paths of the same reactant and within the same zeolite in order to compare activation energies for monomolecular isobutane cracking and dehydrogenation on H-MOR; a more comprehensive analysis of activation barriers using a thermochemical cycle can be found elsewhere [2].

Differences in measured activation barriers for parallel monomolecular reaction paths on the same zeolite reflect only properties of reactants and transition states, because DPE values

rigorously cancel. DPE values for various T-sites in a zeolite and even for different zeolites lie within a very narrow range (e.g., 1230-1235 kJ $mol^{-1}$ for the four T-sites in H-MOR) [28]. This reflects the predominant stabilization of protons by long-range electrostatic interactions with the zeolite framework and allows sites in zeolites to be considered uniform in acid strength [28].

Transition state stabilization energies contain contributions from both electrostatic interactions between the gas-phase cation and anionic zeolite frameworks and van der Waals contacts between the organic cation and zeolite channels. The electrostatic component of this stabilization is similar for both monomolecular isobutane cracking and dehydrogenation transition states, which are late ion pairs with nearly full positive charges (+0.8-0.9e) that are highly localized within the alkyl fragments [22,25,26]. Furthermore, the van der Waals contacts are nearly commensurate in monomolecular transition states and adsorbed alkane reactants, and therefore cancel when the transition states are identical except for the location of the proton.

We conclude that differences in activation barriers for monomolecular isobutene cracking and dehydrogenation (14-19 kJ $mol^{-1}$) reflect primarily enthalpy differences in gas-phase *i*-$C_4H_{11}^+$ cations formed upon protonation at C-C and tertiary C-H bonds in gas-phase isobutene, respectively. Theory indeed suggests that the former gas-phase *i*-$C_4H_{11}^+$ cations are ~14 kJ $mol^{-1}$ more stable than the latter [9].

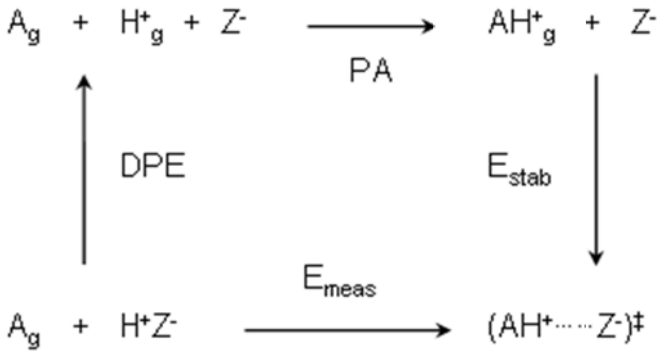


**Scheme 4.3.** A thermochemical cycle for monomolecular alkane reactions on acidic zeolites that relates measured activation barriers ($E_{meas}$) to zeolite deprotonation enthalpies (DPE), gas-phase alkane proton affinities (PA) and transition state stabilization energies within zeolite channels ($E_{stab}$); adapted from [2].

### *4.4.5 Estimation of Gas-Phase Proton Affinities for Propane, n-Butane and Isobutane*

Mota et al. have reported structures and energies for gas-phase carbonium ions (proponium [4]; *n*-butonium [5]; *i*-butonium [9]) using *ab initio* quantum chemical methods at the MP4SDTQ(fc)/6-311++G**//MP2(full)/6-31G** level. In the context of this treatment, the proton affinity is defined as the enthalpy change in the following gas-phase reaction:

$$B + H^+ \longrightarrow BH^+ . \tag{4.13}$$

The difference in C-H and C-C bond proton affinities for each alkane is given by:

$$\Delta PA = PA(C-H-H)^{+} - PA(C-C-H)^{+}. \quad (4.14)$$

Here, we describe methods to estimate the difference in gas-phase proton affinities of alkane C-C and C-H bonds using values calculated by theory [4,5,9].

The most stable $C_3H_9^+$ cation is the carbonium ion formed upon protonation of the C-C bond in gas-phase $C_3H_8$ (-627 kJ mol$^{-1}$). Less stable carbonium ions are formed from protonation at primary C-H bonds (-583 kJ mol$^{-1}$) and secondary C-H bonds (-598 kJ mol$^{-1}$). We estimate the proton affinity of the average C-H bond in propane (-587 kJ mol$^{-1}$) as the proton affinity for each individual C-H bond, weighted by the number of such bonds in propane (six primary C-H; two secondary C-H). Using this method, we obtain a ΔPA value of 40 kJ mol$^{-1}$ for propane.

The most stable *n*-$C_4H_{11}^+$ cations are the carbonium ions formed upon protonation of the secondary C-C bond (-655 kJ mol$^{-1}$) and the primary C-C bond (-636 kJ mol$^{-1}$); we estimate the proton affinity of the average C-C bond in *n*-butane (-642 kJ mol$^{-1}$) by weighing these values by the respective abundance of their bonds in the molecule (two primary C-C; one secondary C-C). Less stable carbonium ions result from protonation at primary C-H bonds (-588 kJ mol$^{-1}$) and secondary C-H bonds (-606 kJ mol$^{-1}$); we estimate the proton affinity of the average C-H bond in *n*-butane (-595 kJ mol$^{-1}$) from these values after weighting by the number of each bond in *n*-butane (six primary C-H; four secondary C-H). Therefore, we estimate that ΔPA = 47 kJ mol$^{-1}$ for *n*-butane.

The most stable *i*-$C_4H_{11}^+$ cation resembles a van der Waals complex between $H_2$ and a *tert*-$C_4H_9^+$ cation, which is formed upon protonation of the tertiary C-H bond (-696 kJ mol$^{-1}$) in gas-phase isobutane. Protonation at the C-C bond in isobutane forms a less stable van der Waals complex between $CH_4$ and a *sec*-$C_3H_7^+$ cation (-682 kJ mol$^{-1}$). Therefore, we estimate that ΔPA = -14 kJ mol$^{-1}$ for isobutane.

Relative differences in these gas-phase proton affinities lead to commensurate differences in monomolecular alkane dehydrogenation and cracking barriers (Fig. 4.4). These effects result in cracking-to-dehydrogenation rate ratios for linear (propane, *n*-butane) and branched (isobutane) alkanes that respectively decrease and increase with increasing temperature (Fig. 4.3). The higher energy pathways involve later and looser transition states that are more sensitive to the entropy benefits upon partial confinement, leading, in turn to cracking-to-dehydrogenation rate ratios that decrease and increase with increasing 8-MR OH content in MOR for linear and branched alkanes, respectively (Fig. 4.2).

## 4.5 References


(1) Bhan, A.; Iglesia, E. *Acc. Chem. Res.* **2008**, *41*, 559.
(2) Gounder, R.; Iglesia, E. *J. Am. Chem. Soc.* **2009**, *131*, 1958.
(3) Bhan, A.; Allian, A. D.; Sunley, G. J.; Law, D. J.; Iglesia, E. *J. Am. Chem. Soc.* **2007**, *129*, 4919.
(4) Esteves, P. M.; Mota, C. J. A.; Ramírez-Solís, A.; Hernández-Lamoneda, R. *J. Am. Chem. Soc.* **1998**, *120*, 3213.
(5) Esteves, P. M.; Alberto, G. G. P.; Ramírez-Solís, A.; Mota, C. J. A. *J. Phys. Chem. A* **2000**, *104*, 6233.
(6) Horiuti, J.; Polanyi, M. *Acta Physicochim.* **1935**, *2*, 505.
(7) Bell, R. P. *The Proton in Chemistry*; Chapman and Hall: London, **1973**.
(8) Marcus, R. A. *Annu. Rev. Phys. Chem.* **1964**, *15*, 155.
(9) Mota, C. J. A.; Esteves, P. M.; Ramirez Solis, A.; Hernandez Lamoneda, R. *J. Am. Chem. Soc.* **1997**, *119*, 5193.
(10) Samples are labeled according to their fractional $H^+$ and $Na^+$ content and appended with a letter denoting their origin: Zeolyst (-Z), Sud-Chemie (-S), Tosoh (-T).
(11) Haag, W. O.; Dessau, R. M. In *Proc. 8th Int. Congr. Catalysis, Berlin* **1984**; Vol. 2, p 305.
(12) Kotrel, S.; Knözinger, H.; Gates, B. C. *Microporous Mesoporous Mater.* **2000**, *35-6*, 11.
(13) Narbeshuber, T. F.; Vinek, H.; Lercher, J. A. *J. Catal.* **1995**, *157*, 388.
(14) Haag, W. O. *Stud. Surf. Sci. Catal.* **1994**, *84*, 1375.
(15) van Bokhoven, J. A.; Williams, B. A.; Ji, W.; Koningsberger, D. C.; Kung, H. H.; Miller, J. T. *J. Catal.* **2004**, *224*, 50.
(16) Babitz, S. M.; Williams, B. A.; Miller, J. T.; Snurr, R. Q.; Haag, W. O.; Kung, H. H. *Appl. Catal. A* **1999**, *179*, 71.
(17) Lombardo, E. A.; Hall, W. K. *J. Catal.* **1988**, *112*, 565.
(18) Stefanadis, C.; Gates, B. C.; Haag, W. O. *J. Mol. Catal.* **1991**, *67*, 363.
(19) Narbeshuber, T. F.; Brait, A.; Seshan, K.; Lercher, J. A. *J. Catal.* **1997**, *172*, 127.
(20) Corma, A.; Miguel, P. J.; Orchilles, A. V. *J. Catal.* **1994**, *145*, 171.
(21) Yaluris, G.; Rekoske, J. E.; Aparicio, L. M.; Madon, R. J.; Dumesic, J. A. *J. Catal.* **1995**, *153*, 54.
(22) Milas, I.; Nascimento, M. A. C. *Chem. Phys. Lett.* **2003**, *373*, 379.
(23) Zygmunt, S. A.; Curtiss, L. A.; Zapol, P.; Iton, L. E. *J. Phys. Chem. B* **2000**, *104*, 1944.
(24) Frash, M. V.; van Santen, R. A. *Top. Catal.* **1999**, *9*, 191.
(25) Kazansky, V. B.; Frash, M. V.; van Santen, R. A. *Appl. Catal. A* **1996**, *146*, 225.
(26) Zheng, X. B.; Blowers, P. *J. Phys. Chem. A* **2006**, *110*, 2455.
(27) a) The kinetic diameter of isobutane is 0.50 nm and of a methyl group is 0.38 nm (D. W. Breck, *Zeolite Molecular Sieves*, Wiley, New York, **1974**, pp. 633 – 641); b) the 8-MR pocket diameter is 0.41 nm and depth is 0.37 nm (R. Gounder, E. Iglesia, *J. Am. Chem. Soc.* **2009**, *131*, 1958).
(28) Brändle, M.; Sauer, J. *J. Am. Chem. Soc.* **1998**, *120*, 1556.
(29) Bhan, A.; Gounder, R.; Macht, J.; Iglesia, E. *J. Catal.* **2008**, *253*, 221.
(30) van Santen, R. A.; Neurock, M. *Molecular Heterogeneous Catalysis*; Wiley-VCH: Weinheim, **2006**.

# CHAPTER FIVE

## The Roles of Entropy and Enthalpy in Stabilizing Ion-Pairs at Transition States in Zeolite Acid Catalysis

### Conspectus

The confinement of reactive intermediates and transition states within voids of molecular dimensions involves van der Waals interactions, which mediate chemical reactions on zeolitic solid acids in a manner reminiscent of the solvation effects of enzyme pockets and with analogous consequences for catalytic specificity. Voids provide the "right fit" for certain transition states, as reflected in their lower free energies, thus extending the catalytic diversity of zeolites beyond their ability to discriminate molecules and their chemical pathways by excluding moieties of a certain size. This diversity is all the more remarkable because acid strength is unaffected by confinement and similar amongst known crystalline aluminosilicates. In this Account, we discuss the factors that determine the "right fit" for a specific chemical reaction and explore predictive criteria that extend the prevailing discourse based on size and shape; in doing so, we link the respective structures of reactants, transition states, and voids to chemical reactivity and selectivity.

Confinement mediates enthalpy-entropy trade-offs that determine Gibbs free energies of transition states and relevant reactants; the resulting activation free energies determine turnover rates in the context of transition state theory. At low temperatures (400-500 K), dimethyl ether carbonylation occurs with high specificity within small eight-membered ring (8-MR) voids in FER and MOR, but at undetectable rates within larger voids (MFI, BEA, FAU, $SiO_2$-$Al_2O_3$). More effective van der Waals stabilization within 8-MR voids leads to ion-pair transition states with lower enthalpies but also with lower entropies, which taken together decrease carbonylation activation free energies. The "right fit" is a "tight fit" at low temperatures, a natural consequence of how temperature appears in the defining equation for Gibbs free energy.

In contrast, entropy effects become dominant in catalytic reactions of small alkanes at higher temperatures (700-800 K) where the "right fit" becomes a "looser fit"; yet, alkane activation turnovers are also faster on 8-MR protons in MOR. These transition states are confined only *partially* within shallow 8-MR pockets and retain higher entropies, at the expense of enthalpic stability, than ion-pairs confined fully within 12-MR channels. The selectivities toward n-alkane dehydrogenation (relative to cracking) and iso-alkane cracking (relative to dehydrogenation) are higher on 8-MR than 12-MR sites because partial confinement preferentially stabilizes ion-pair structures that are looser; such structures occur later along reaction coordinates and are higher in energy, consistent with Marcus theory for charge-transfer reactions. Enthalpy differences between cracking and dehydrogenation ion-pairs of a given reactant are independent of zeolite structure (FAU, FER, MFI, MOR) and reflect gas-phase proton affinity differences between alkane C-C and C-H bonds, as expected from Born-Haber thermochemical cycles. These thermochemical relations, together with statistical mechanics treatments, also show how rotational entropy differences between intact reactants and ion-pair transition states cause cracking turnover rates to increase with n-alkane size. Through these

illustrative examples, our Account highlights the effects of reactant and catalyst structures on ion-pair transition state enthalpies and entropies, while underscoring the role of temperature to mediate enthalpic and entropic contributions to free energies and, in turn, to turnover rates and selectivities in solid acid catalysis.

## 5.1 Introduction

Zeolites are used in refining and petrochemical processes as Brønsted acid catalysts that target specific products based on the size and shape of the molecules and confining voids [1-3]. Cracking, alkylation, and hydride transfer reactions require that ion-pairs form at transition states from relatively uncharged physisorbed reactants or bound alkoxides [3-7]. Activation barriers decrease as ion-pairs become more stable with increasing acid strength, reflected in smaller deprotonation energies ($\Delta E_{DP}$), and with smaller cation-anion distances [5-7]. In contrast, activation barriers for steps involving more neutral transition states that are predominantly stabilized by covalent interactions, such as H-D exchange and alkene adsorption, depend weakly on acid strength [5-7].

Brønsted acid sites within aluminosilicates are weaker ($\Delta E_{DP}$ ~1200 kJ/mol), than in Brønsted-Lewis superacids (HF-$SbF_5$; $\Delta E_{DP}$ ~1000 kJ/mol) [8], polyoxometalates or anion-modified oxides ($\Delta E_{DP}$ ~1050-1150 kJ/mol) [9]. Theoretical treatments of structural and electrostatic effects in zeolite frameworks indicate that $\Delta E_{DP}$ values are similar for isolated protons (within ~10 kJ/mol) at all locations within MFI [10] and MOR [11], and for the most stable locations in other frameworks [12]. Even though acid sites in zeolites are weaker and less diverse in composition and strength than in mesoporous or liquid acids, turnover rates are often higher than on stronger acids and depend sensitively on the geometry of both the microporous voids and the reacting molecules [13-16].

Confinement causes ubiquitous compromises between entropy and enthalpy because dispersion forces restrict mobility. Smaller channels confine alkanes (and transition states by extension) more strongly *as long as they fit*, because more effective van der Waals contacts with framework O-atoms make adsorption enthalpies and entropies more negative [17-20]. Chemical reaction rates depend on the Gibbs free energies of transition states ($\Delta G^o_{\ddagger}$) with respect to the relevant reactants.

$$\Delta G^\circ_{\ddagger} = \Delta H^\circ_{\ddagger} - T\Delta S^\circ_{\ddagger}. \tag{5.1}$$

Thus, trade-offs between enthalpy ($\Delta H^o_{\ddagger}$) and entropy ($\Delta S^o_{\ddagger}$) upon confinement determine reactivity. Enthalpic contributions tend to dominate at low temperatures, for which the first term in Eq. (5.1) prevails, while entropic effects become important at higher temperatures. In turn, we expect that stronger solvation and a tighter fit will benefit chemical reactivity at low temperatures, but that a looser fit will do so at higher temperatures. We illustrate these trends for alkane cracking and dehydrogenation at high temperatures (700-800 K), where entropy effects prevail and vary predictably with alkane structure and with the lateness of transition states along reaction coordinates. In sharp contrast, enthalpic considerations dominate free energies at the low temperatures (400-500 K) of dimethyl either (DME) carbonylation.

## 5.2 Results and Discussion

### *5.2.1 Enthalpic Stabilization and "Tighter Fits" in Carbonylation Catalysis*

DME carbonylation under anhydrous conditions selectively (>99%) forms methyl acetate on acidic zeolites at 400-500 K via kinetically-relevant addition of CO to bound $CH_3$ groups [21-23]. Turnover rates are much higher on zeolites containing eight-membered ring (8-MR) structures (FER, MOR) than on materials with larger voids (MFI, BEA, FAU, $SiO_2$-$Al_2O_3$) [23]. Carbonylation rates are strictly proportional to the number of $H^+$ within 8-MR structures in FER and MOR, which varied with $Na^+$ content and sample provenance and was measured by deconvolution of OH infrared bands and by titration of 12-MR $H^+$ with large molecules (n-hexane, pyridine, 2,6-lutidine) [23]. Carbonylation rates were independent of the number of protons within 10-MR or 12-MR structures, in spite of acid strengths ($\Delta E_{DP}$) that do not depend on location [11].

Thus, the preferential stabilization of carbonylation transition states within 8-MR voids cannot reflect the electrostatic component of ion-pair energies. Theoretical estimates of barriers for CO addition to bound $CH_3$ are similar at all four Al T-site locations within MOR when the methods used account for electrostatic but not attractive dispersion forces, but become ~30 kJ/mol lower within 8-MR voids using *ab initio* [24] or DFT-based methods [25] that account for dispersion. More effective van der Waals interactions within smaller voids decrease the enthalpy of transition states, as long as they fit, relative to larger voids. Although tighter confinement causes entropy losses, activation free energies are smaller and turnover rates larger within 8-MR voids at the low temperatures of DME carbonylation catalysis.

### *5.2.2 Entropic Benefits of Partial Confinement in Catalysis at High Temperatures*

Monomolecular alkane cracking and dehydrogenation prevail at high temperatures (>623 K) and low pressures of alkene products [26]. They involve cations with $(C\text{-}C\text{-}H)^+$ or $(C\text{-}H\text{-}H)^+$ character that mediate kinetically-relevant C-C or C-H bond scissions (Scheme 5.1) and form via proton transfer to physisorbed alkanes present at low intrazeolite concentrations ($C_{A(z)}$) during catalysis [14]. Turnover rates (per $H^+$) are given by:

$$r = k_{int} \cdot C_{A(z)} = k_{int} \cdot K_{ads} \cdot P_A = k_{meas} \cdot P_A, \tag{5.2}$$

where $K_{ads}$ is the alkane adsorption equilibrium constant and $k_{int}$ is the rate constant for C-C or C-H scission steps (Scheme 5.1). Measured rate constants ($k_{meas}$) reflect free energy differences between transition states stabilized within voids and gaseous alkanes:

$$k_{meas} = \left(k_B T/h\right)\exp\left(-\left(\Delta G^\circ_{\ddagger} - \Delta G^\circ_{A(g)} - \Delta G^\circ_{H^+Z^-}\right)/RT\right). \tag{5.3}$$

Measured activation energies ($E_{meas}$) depend on intrinsic activation barriers ($E_{int}$) and adsorption enthalpies ($\Delta H_{ads}$):

$$E_{meas} = E_{int} + \Delta H_{ads} = \Delta H^{\circ}_{\ddagger} - \Delta H^{\circ}_{H^+Z^-} - \Delta H^{\circ}_{A(g)}. \quad (5.4)$$

and reflect enthalpy differences between transition states and gaseous alkanes. Analogous relations hold for activation entropies ($\Delta S_{meas}$) derived from pre-exponential factors:

$$\Delta S_{meas} = \Delta S_{int} + \Delta S_{ads} = \Delta S^{\circ}_{\ddagger} - \Delta S^{\circ}_{H^+Z^-} - \Delta S^{\circ}_{A(g)}. \quad (5.5)$$

Monomolecular cracking and dehydrogenation rate constants were larger (by factors of >3-17; 748 K) on 8-MR than 12-MR protons in MOR for propane, n-butane and isobutane reactants [14,15], as also found for DME carbonylation [23]. These alkanes (~0.65-0.83 nm in length), however, cannot be fully contained within shallow 8-MR pockets (~0.37 nm deep); indeed, 8-MR $H^+$ sites preferentially cleave the terminal C-C bonds in n-butane [14]. Activation energies ($E_{meas}$) were larger and activation entropies ($\Delta S_{meas}$) less negative for propane cracking in 8-MR than 12-MR locations (Table 5.1). Partial containment precludes effective van der Waals contacts between pore walls and organic cations at the transition state, causing them to retain larger amounts of gaseous reactant entropy at the expense of enthalpic stability. Turnover rates are higher when cations are partially-confined because entropy becomes a dominant term in activation free energies at the high temperatures of alkane activation.

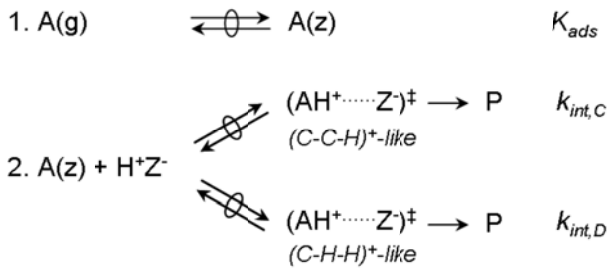


**Scheme 5.1.** Monomolecular alkane activation on Brønsted acid sites ($H^+Z^-$). (1) Gaseous alkanes (A(g)) and those adsorbed onto acid sites within zeolite voids (A(z)) are quasi-equilibrated. (2) Kinetically-relevant cracking or dehydrogenation via carbonium-ion-like transition states to form products (P) depicted using transition state theory formalism.

**Table 5.1.** Measured rate constants, activation energies, entropies and free energies (748 K) for monomolecular propane cracking on 8-MR and 12-MR $H^+$ sites of MOR zeolites [14].

| Location | $k_{meas}$ ($/10^{-3}$) (mol (mol($H^+$)–s–bar)$^{-1}$) | $E_{meas}$ (kJ mol$^{-1}$) | $\Delta S_{meas}$ (J mol$^{-1}$ K$^{-1}$) | $\Delta G_{meas}$ (kJ mol$^{-1}$) |
|---|---|---|---|---|
| 8-MR | 2.0 ± 0.5 | 164 ± 5 | -91 ± 9 | 227 ± 2 |
| 12-MR | 0.7 ± 0.4 | 151 ± 5 | -117 ± 14 | 234 ± 3 |

*5.2.3 Partial Confinement Effects on Alkane Cracking and Dehydrogenation Selectivities*

As the fraction of sites in 8-MR MOR pockets increased, cracking-to-dehydrogenation ratios *decreased* for propane and n-butane but *increased* for isobutane (Fig. 5.1), despite analogous elementary steps for all reactants. For a given alkane, cracking-to-dehydrogenation ratios solely reflect differences in stability between the two transition states:

$$k_{meas,C} / k_{meas,D} = \exp\left(-\left(\Delta G^{\circ}_{\ddagger,C} - \Delta G^{\circ}_{\ddagger,D}\right) / RT\right). \tag{5.6}$$

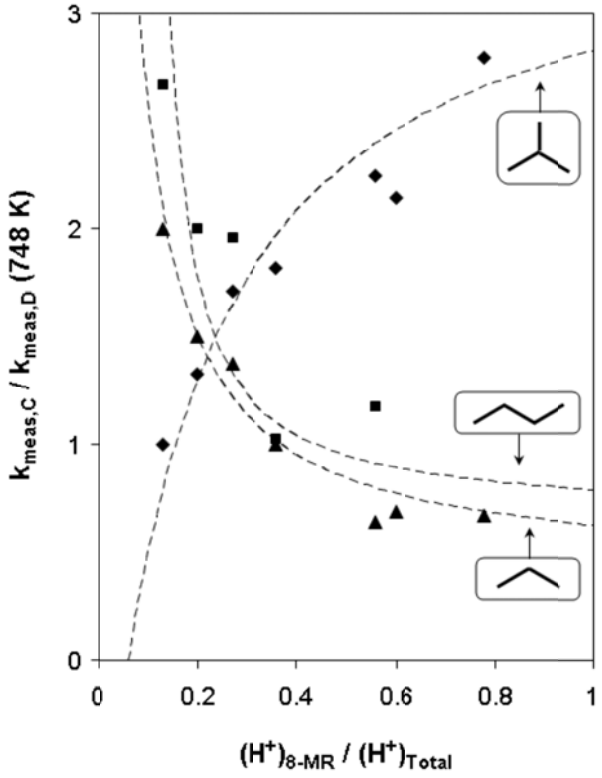


**Figure 5.1.** Monomolecular cracking-to-dehydrogenation rate constant ratios (748 K) for propane (▲), n-butane (■) and isobutane (◆) versus 8-MR $H^+$ fraction in MOR. Dashed curves represent ratios expected from 8-MR and 12-MR rate constants reported elsewhere [14,15].

Thus, partial confinement preferentially stabilizes transition states for n-alkane dehydrogenation (relative to n-alkane cracking) and isobutane cracking (relative to isobutane dehydrogenation). The location of protons within different voids of the same zeolite structure influences turnover rates for monomolecular reactions of a given alkane (Table 5.1), but to different extents as these ratios show (Fig. 5.1).

Kinetic preferences for 8-MR MOR pockets of cracking and dehydrogenation depend on alkane structure and enable changes in reaction selectivity, but on a phenomenological basis that prevents predictions for other alkanes or void structures. Why do transition states so similar in structure sense confinement so differently and why does this sensitivity depend so strongly on

whether alkanes are linear or branched? While rate constant ratios depend only on free energy differences between the two transition states involved (Eq. (5.6)), each contain enthalpy and entropy terms that can be independently obtained from temperature effects on cracking and dehydrogenation rates. The catalytic consequences of enthalpy-entropy trade-offs imposed by confinement differ for two transition states accessible to each reactant because of how late they occur along their reaction coordinates, a property that is reflected in their respective activation barriers, as we discuss next.

### *5.2.4 Relations Between Ion-Pair Enthalpy and Entropy*

Figure 5.2 shows differences in activation *energy* between dehydrogenation and cracking versus activation *entropy* differences for each alkane (propane, n-butane, isobutane) on each zeolite (FER, MFI, MOR, USY, CD-USY (chemically-dealuminated-USY using $(NH_4)_2SiF_6$)). For a given alkane and zeolite, $E_{meas}$ (or $\Delta S_{meas}$) values for dehydrogenation and cracking differ only because their transition states differ in enthalpy (or entropy):

$$E_{meas,D} - E_{meas,C} = \Delta H^{\circ}_{\ddagger,D} - \Delta H^{\circ}_{\ddagger,C} \,. \tag{5.7}$$

Barriers were *larger* for dehydrogenation than cracking for propane and n-butane, but *smaller* for isobutane (Fig. 5.2). Thus, n-alkane dehydrogenation ion-pairs are higher in enthalpy than for cracking, but the opposite applies to isobutane. n-Alkane dehydrogenation and isobutane cracking also gave larger $\Delta S_{meas}$ values than their respective counterparts (Fig. 5.2), in turn, indicating that higher enthalpy ion-pairs also have larger entropies.

These data and their implications for ion-pair enthalpy-entropy tradeoffs are consistent with charge transfer reaction coordinates based on reactant and product potentials (Scheme 5.2) [27,28]. In this approach, paths from one reactant to several products differ only because of product energies. Transition states for the higher barrier path occur later along reaction coordinates and more closely resemble products. For monomolecular alkane activation, products contain one more molecule than reactants, and later transition states become looser and higher in entropy. As a result, ion-pairs that are higher in enthalpy are also higher in entropy.

For each alkane, rates of the higher barrier reaction selectively increased when transition states were partially confined within 8-MR MOR pockets (Fig. 5.1), despite their weaker enthalpic stabilization compared with full confinement within 12-MR channels. The different kinetic preferences of cracking and dehydrogenation predominantly reflect entropic effects of partial confinement, which become more consequential for stability with increasing temperature and for looser transition states. Enthalpy and entropy differences between cracking and dehydrogenation transition states reflect differences in structure between $(C\text{-}C\text{-}H)^+$ and $(C\text{-}H\text{-}H)^+$ cations formed as C-C and C-H bonds acquire positive charge. These differences are intrinsic to reactant molecules and independent of zeolite structure (Fig. 5.2). We examine next how reactant and catalyst properties influence the entropy and enthalpy terms in activation free energies for Brønsted acid catalysis using thermochemical cycles that dissect free energies into their fundamental components.

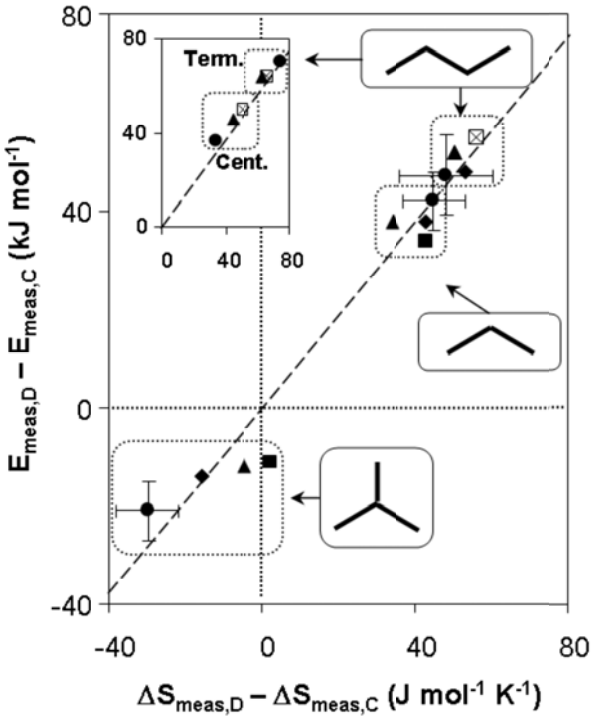


**Figure 5.2.** Differences in measured activation energies ($E_{meas}$) and entropies ($\Delta S_{meas}$) between monomolecular alkane (propane, n-butane, isobutane) dehydrogenation and cracking on MOR (◆), MFI (●), FER (▲), USY (■) and chemically-dealuminated-USY (⊠). Error bars shown for MFI are representative of errors for all samples. Dashed line represents least-squares regression. Inset: n-butane cracking at terminal and central C-C bonds.

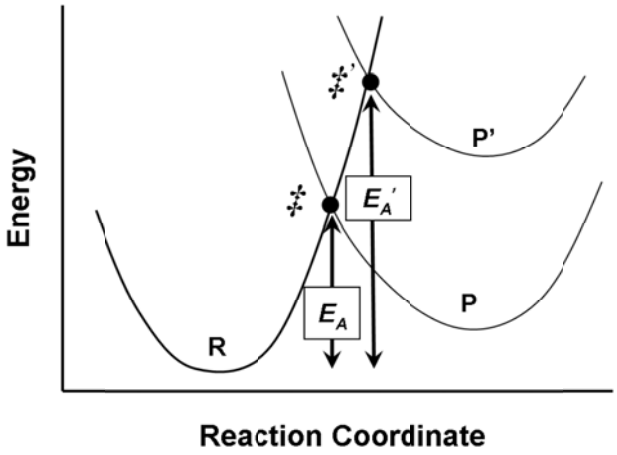


**Scheme 5.2.** Energy diagrams for two reactions of one alkane, adapted from charge transfer reaction coordinates [27,28]. Transition states (‡, ‡') determined from intersections between reactant (R) and product (P, P') potentials. Arrows denote activation barriers ($E_A$, $E_A$').

*5.2.5 Born-Haber Thermochemical Cycles for Monomolecular Alkane Reactions*

Scheme 5.3 depicts a thermochemical cycle that describes energies and entropies of ion-pairs formed from gaseous alkanes ($E_{meas}$, $\Delta S_{meas}$) via adsorption ($\Delta H_{ads}$, $\Delta S_{ads}$) and subsequent proton transfer ($E_{int}$, $\Delta S_{int}$). It includes a hypothetical path to these transition states involving deprotonation of the acid, protonation of C-C or C-H bonds in gaseous alkanes, and electrostatic and van der Waals stabilization of the gaseous cations within zeolite voids. Measured activation energies and entropies are given by:

$$E_{meas} = \Delta E_{DP} + \Delta E_P + \Delta E_{stab}\,, \tag{5.8}$$

$$\Delta S_{meas} = \Delta S_{DP} + \Delta S_P + \Delta S_{stab}\,. \tag{5.9}$$

Here, $\Delta E_{DP}$ is the deprotonation energy, $\Delta E_P$ is gas-phase affinity of alkane C-C or C-H bonds for protonation, and $\Delta E_{stab}$ is the stabilization energy; the analogous $\Delta S$ terms in Eq. (5.9) describe measured activation entropies.

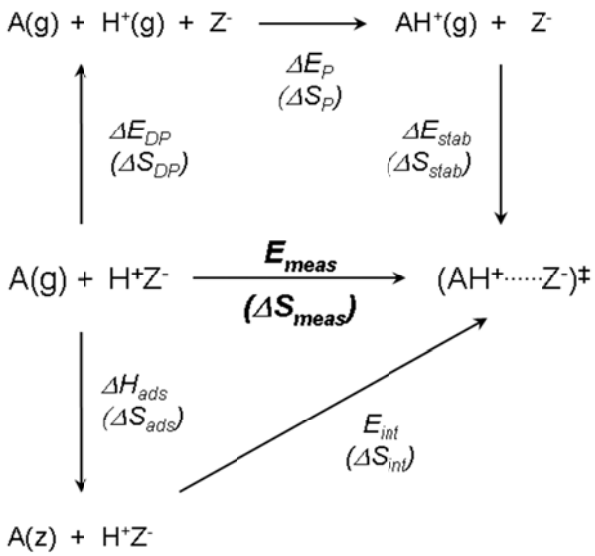


**Scheme 5.3.** Thermochemical cycles of measured activation energies ($E_{meas}$) and entropies ($\Delta S_{meas}$) for monomolecular alkane (A) reactions at zeolitic acid sites ($H^+Z^-$). They depend on quasi-equilibrated alkane adsorption ($\Delta H_{ads}$, $\Delta S_{ads}$) and kinetically-relevant protonation ($E_{int}$, $\Delta S_{int}$) steps and reflect contributions from deprotonation ($\Delta E_{DP}$, $\Delta S_{DP}$), gas-phase alkane protonation ($\Delta E_P$, $\Delta S_P$), and stabilization of gaseous cations within zeolite voids ($\Delta E_{stab}$, $\Delta S_{stab}$).

Acid site deprotonation reflects only catalyst properties and requires that ZO-H bonds cleave heterolytically and $H^+$ and $ZO^-$ fragments separate to non-interacting distances; $\Delta E_{DP}$ [10-12] and $\Delta S_{DP}$ values are independent of active site location. Gas-phase protonation of alkane C-C or C-H bonds forms carbonium-ion-like complexes, with $\Delta E_P$ and $\Delta S_P$ values that depend on proton location within the cation but not on any catalyst properties. The confinement of gaseous

cations or reactants within voids depends on both catalyst and reactant properties. Cations are stabilized ($\Delta E_{stab}$, $\Delta S_{stab}$) via electrostatic interactions with the anionic framework and, to a lesser extent, via van der Waals forces, while neutral alkanes are predominantly stabilized by the latter ($\Delta H_{ads}$, $\Delta S_{ads}$ ) [17-19] .

### *5.2.6 Gas-Phase Alkane Proton Affinities Determine Monomolecular Activation Barriers*

Differences in cracking and dehydrogenation barriers (Eq. (5.8)) are given by:

$$E_{meas,D} - E_{meas,C} = \left(\Delta E_{DP,D} + \Delta E_{P,D} + \Delta E_{stab,D}\right) - \left(\Delta E_{DP,C} + \Delta E_{P,C} + \Delta E_{stab,C}\right). \quad (5.10)$$

$\Delta E_{DP}$ terms rigorously cancel when both reactions occur on the same acid. Confinement stabilizes gaseous analogs of both transition states to similar extents ($\Delta E_{stab}$), because of their similar charge (+0.8-0.9e) and its distribution [5-7,29], which determine electrostatic effects, and their similar size, which defines van der Waals contacts. Thus, cracking and dehydrogenation barriers for a given alkane and zeolite differ predominantly because C-C and C-H bond proton affinities are different:

$$E_{meas,D} - E_{meas,C} = \Delta E_{P,D} - \Delta E_{P,C}. \quad (5.11)$$

The carbonium-ions formed upon protonation of gaseous alkanes decompose without detectable barriers to form complexes containing a neutral fragment (smaller alkane or $H_2$) and a carbenium ion interacting via van der Waals forces with each other [30-33], similar to the late transition state structures identified by theory [29,34-36].

Indeed, differences between cracking and dehydrogenation barriers for each alkane agree with proton affinity differences between their respective C-C and C-H bonds (Fig. 5.3), properly weighed by the number of each bond (details in Supporting Information) [15]. Activation energies were higher for terminal than central C-C cleavage in n-butane (Fig. 3 inset), consistent with the higher energy $(C\text{-}C\text{-}H)^+$ cations formed at terminal locations (by 20-25 kJ/mol) as determined by *ab initio* methods [32,37]. Activation entropies are also higher for terminal than central cracking (Fig. 2 inset), consistent with the higher enthalpy ion-pairs for terminal scission being later and looser (Scheme 5.2). Next, we examine how the structures of alkanes influence the entropies of their cracking transition states and cause differences between terminal and central bonds of n-butane and among $C_3$-$C_6$ n-alkanes.

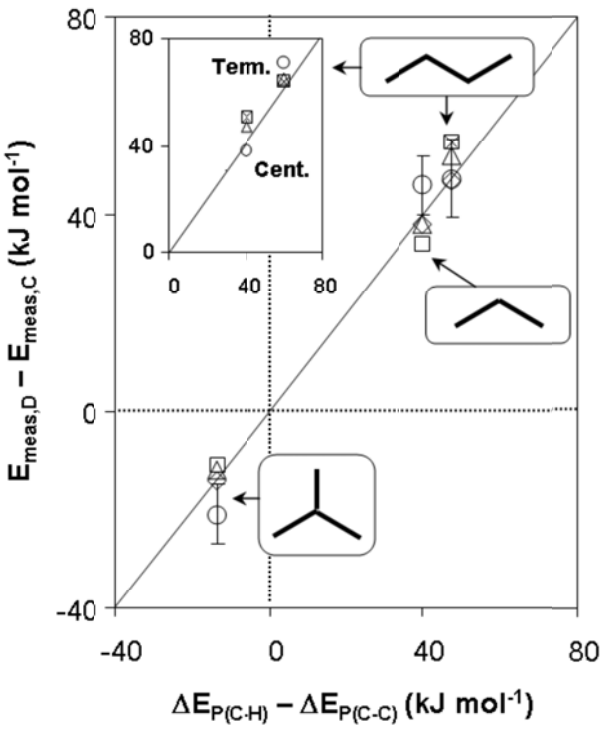


**Figure 5.3.** Difference between measured activation energies ($E_{meas}$) for monomolecular alkane dehydrogenation and cracking on MOR (◇), MFI (○), FER (△), USY (□) and chemically-dealuminated-USY (⊠) versus the difference between bond-averaged gas-phase C-H and C-C proton affinities ($\Delta E_P$) of propane, n-butane, and isobutane. Error bars shown for MFI are representative of errors for all samples. Eq. (5.11) plotted as solid line. Inset: n-butane cracking at terminal and central C-C bonds.

### *5.2.7 Effects of n-Alkane Size on Monomolecular Cracking Turnover Rates*

Measured rate constants (773 K) for monomolecular cracking of $C_3$-$C_6$ n-alkanes increase markedly (>100-fold) with chain size; these rate constants combine cracking events for, and thus reflect a reactivity-average of, all C-C bonds in the reactant [38]. n-Alkane adsorption constants ($K_{ads}$) at reaction temperatures can be estimated from adsorption enthalpies and entropies, which depend weakly on temperature [39-41]:

$$K_{ads} = \exp\left(-\left(\Delta H_{ads} - T\Delta S_{ads}\right)/RT\right). \tag{5.12}$$

Adsorption constants (773 K) [39], from Eq. (5.12) and $\Delta H_{ads}$ and $\Delta S_{ads}$ values (measured at 353 K) [18,19], vary less than two-fold among $C_3$-$C_6$ n-alkanes. *Ab initio*-statistical thermodynamics methods (<five-fold) [40] and configurational-bias Monte Carlo simulations (<two-fold) [42,43] give a similar range of values.

Intrinsic rate constants (773 K), determined from these adsorption constants and Eq. (5.2) and corrected for the number of C-C bonds, increased monotonically with alkane size and were ~50 times larger for n-hexane than for propane [39], Intrinsic activation barriers, which reflect

energy differences between transition states and physisorbed alkanes, depend on energies for the corresponding hypothetical steps in Scheme 5.3:

$$E_{int} = \Delta E_{DP} + \Delta E_P + \Delta E_{stab} - \Delta H_{ads} \,. \tag{5.13}$$

Dispersive interactions stabilize reactants and transition states, which differ only in the presence of a single proton, to similar extents. They account for the effects of alkane size on $\Delta H_{ads}$ and $E_{meas}$ (via $\Delta E_{stab}$); both terms decrease in parallel for $C_3$-$C_6$ n-alkanes in H-MFI (12-16 kJ/mol per $CH_2$ group; Fig. 5.4a). Alkane size does not affect $\Delta E_{DP}$ and its influence on $\Delta E_P$, for which there are small differences with C-C bond position [37], is attenuated because $E_{meas}$ values reflect reactivity-averaged C-C scission events. Differences in n-alkane (or channel) size predominantly influence the number (or strength) of van der Waals contacts with pore walls, but in a commensurate manner for both reactants and transition states; thus, intrinsic barriers are similar for $C_3$-$C_6$ n-alkanes (194-198 kJ/mol; Fig. 5.4a) on H-MFI [38] and insensitive to zeolite structure for $C_3H_8$ cracking [14,44].

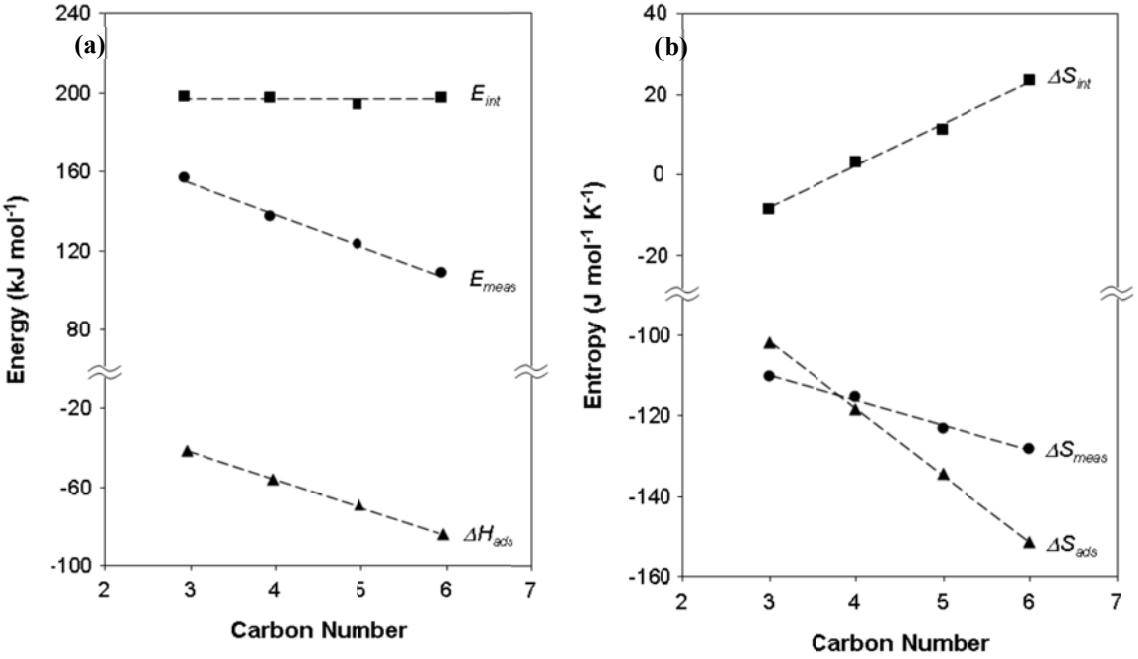


**Figure 5.4.** (a) Energy and (b) entropy terms in adsorption constants [18,19] (▲), and measured [38] (●) and intrinsic (■) rate constants for monomolecular cracking of n-alkanes on MFI.

The higher intrinsic rate constants for larger n-alkanes reflect higher transition state entropies relative to alkanes physisorbed on acid sites ($\Delta S_{int}$; Fig. 5.4b) [39,40]. This increase reflects $\Delta S_{ads}$ and $\Delta S_{meas}$ terms that, in contrast with $\Delta H_{ads}$ and $E_{meas}$ (Fig. 5.4a), decrease to different extents with increasing alkane size (~17 and ~6 J/mol-K per $CH_2$ group in H-MFI, respectively; Fig. 5.4b). Intrinsic activation entropies can be described using the hypothetical steps in Scheme 5.3:

$$\Delta S_{int} = \Delta S_{DP} + \Delta S_P + \Delta S_{stab} - \Delta S_{ads} \,. \tag{5.14}$$

Confinement causes entropy losses because attractive van der Waals interactions restrict mobility. We *surmise* that dispersive interactions similarly influence entropies of n-alkanes ($\Delta S_{ads}$) and their transition states ($\Delta S_{stab}$), in view of their similar size, using arguments similar to those that account for the similar van der Waals contributions to their enthalpies. Confinement *may* cause entropy differences between charged transition states and neutral reactants *if* electrostatic interactions with the anionic framework change the amount or distribution of charge in the cation. Such perturbations seem inconsistent with nearly-full proton transfer (+0.8-0.9e) and with the local nature of this charge in both transition state [5-7,29,30] and gaseous [30-33] complexes; in turn, these entropy changes (contained within $\Delta S_{stab}$) are small and insensitive to n-alkane size. Chain length must therefore cause differences in the entropy gained upon protonation of C-C bonds in gaseous alkanes ($\Delta S_P$), even in the absence of concomitant effects on protonation enthalpies ($\Delta E_P$) [37]. These entropy gains reflect the emergence of frustrated rotational and translational modes accessible at late transition states, but not in intact neutral alkanes.

### *5.2.8 Entropic Consequences of Chain Size in Monomolecular Alkane Cracking*

*Ab initio* treatments indicate that low-frequency vibrations in alkanes physisorbed at intrazeolitic protons represent frustrated translations and rotations relative to the confining walls [40,41]. The entropies of these modes were estimated by statistical mechanics formalisms that treat alkane translation on a plane perpendicular to the O-H bond axis (2D free translation) and rotation about their center axis (1D free rotation); rotation can also occur about an axis perpendicular to the zeolite surface (2D free rotation) when void spaces permit [40,41]. Late cracking transition states resemble van der Waals complexes formed by charge separation and C-C bond lengthening [5,29,34]. Distortion of internal bond lengths and angles in these complexes represent hindered rotations and rocking vibrations of two fragments stabilized weakly by dispersion forces; these motions are essentially barrierless compared to the much larger reaction barriers that predominantly reflect the energies required for charge separation [6,7,29,45-50]. We expect the statistical thermodynamic treatments used for confined alkanes [40,41] would also accurately estimate entropies for late transition states, in which the two products are nearly formed.

Entropy gains along the path from n-alkanes to two molecules were calculated for each C-C bond cleavage event, separately for one and two degrees of free translational and rotational freedom (details in Supporting Information); bond-averaged values are shown in Figure 5.5 as a function of chain size. The formation of two molecules causes large translational entropy gains (~37 (1D), ~66 (2D) J/mol-K) that are, however, affected only *weakly* by alkane size (4 J/mol-K per $CH_2$ group (2D)). In sharp contrast, rotational entropy gains depend *strongly* on chain size (~22 (1D), ~30 (2D) J/mol-K per $CH_2$ group). Entropy gains from 1D free rotation (Fig. 5.5) are similar to $\Delta S_{int}$ values for each n-alkane (Fig. 5.4b); they are also higher for terminal than central C-C cleavage in n-butane (by 8 J/mol-K), consistent with the higher activation entropies measured for terminal cracking (Fig 5.2 inset). The quantitative agreement between these data suggest that *if* fragments at late transition states rotate freely relative to one another, other

translation and rotational modes do not significantly contribute to $\Delta S_{int}$ values. Irrespective of the detailed modes and their specific barriers at transition states, new rotational modes appear to cause the increases in $\Delta S_{int}$ and $k_{int}$ values with n-alkane size. These effects resemble those for protonation [51] and radical dissociation [52] of gaseous hydrocarbons, which disrupt internal symmetry and create new rotations that cause entropy gains.

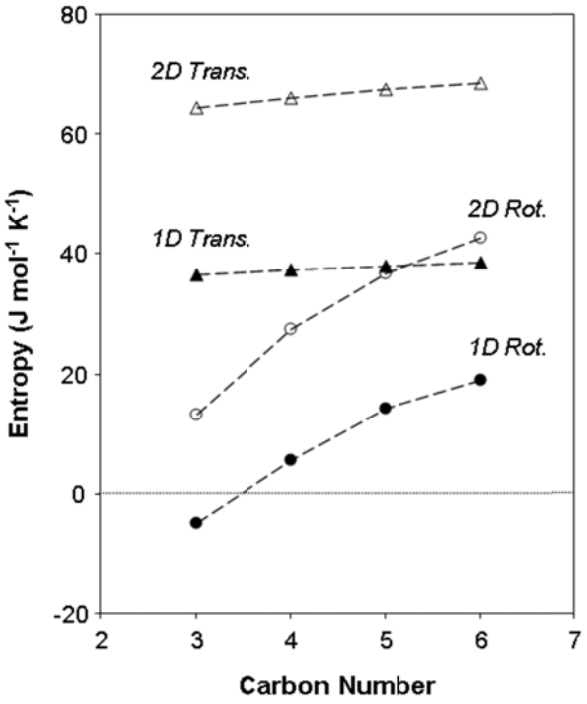


**Figure 5.5.** Entropy differences between transition states and physisorbed reactants in n-alkane cracking caused by 1D (●) and 2D (○) rotation and 1D (▲) and 2D (△) translation; estimated using statistical mechanics for scission of individual C-C bonds and weighted for the number of such bonds in each n-alkane.

Thermochemical relations provide predictive insights into chemical reactivity and selectivity by rigorously connecting thermodynamic properties of transition states to those of reactants and catalysts. As n-alkanes become larger in size, reactant rotational entropies and cracking turnover rates increase concomitantly. Proton affinity differences between alkane C-C and C-H bonds vary with reactant size and structure, leading to commensurate enthalpy differences between monomolecular cracking and dehydrogenation transition states. The selectivity toward breaking these bonds, in turn, depends on local void structure; higher energy ion-pairs, which are also later and looser, are preferentially stabilized within voids that confine them partially. Tighter confinement results in larger enthalpy gains, at the expense of entropy, and benefits DME carbonylation transition states at low temperatures (400-500 K); however, looser confinement and larger entropies, at the expense of enthalpy, benefit late monomolecular alkane transition states at high temperatures (700-800 K). In contrast to monomolecular routes, bimolecular alkene reactions (alkylation, hydrogenation, oligomerization) require that two reactants *lose* entropy to form loosely-bound ion-pairs at *early* transition states, yet, the entropic

gains associated with partial ion-pair confinement are similarly consequential for turnover rates of these reactions at high temperatures [53,54].

### 5.3 Outlook

These ubiquitous principles for catalysis within confined spaces generate research inquiries accessible to theory and experiment. Opportunities emerge for designing catalytic materials with active sites located within voids that provide the "right fit" for a given chemical transformation. Active site distributions can be modified by post-synthetic treatments, but how do we synthesize materials with sites already in desired locations? Recent studies of FER zeolites have demonstrated precise control of Al siting at specific framework locations using structure-directors that template different voids during synthesis [55,56]. These findings offer promise for the development of related strategies to control heteroatom siting in other microporous frameworks.

Determining proton location within different voids of a given structure, even before and after catalytic reactions, remains a state-of-the-art process. Proton location can be accurately determined when OH groups differ in infrared vibrational frequencies, in their ability to interact with titrants of different size, and in their preference for exchange with other cations [23]. These methods provide unclear inferences for structures with many different Al T-sites within voids that differ only slightly in size, such as MFI. Nuclear magnetic resonance spectroscopic methods can resolve Al atoms with different isotropic chemical shifts in MFI, but the specific assignment to unique T-site locations remains uncertain [57]. Methods to characterize Al or OH location with increasing accuracy will require synergistic approaches based on experiment and theory, in which theoretical methods treat spectral features more definitively and help guide experimental design.

Theoretical chemistry can probe how and why voids solvate intermediates and transition states. Attractive dispersion forces largely account for catalytic enhancements caused by confinement and for reactivity differences among zeolites with diverse void structures but acid sites of similar strength. Thus, *ab initio* [24,40,41] and DFT-based methods that account for dispersion [50] are essential to describe reaction coordinate and *potential energy* surfaces within confined spaces. These reaction coordinates exist, however, within *free energy* surfaces; therefore, entropies of confined species need also be determined accurately to predict reactivity. Classical mechanics seem unable to accurately describe low-frequency vibrations, such as hindered rotations [46,47], which are essential to describe entropy differences between intact molecules and ion-pairs at transition states. Treatment of low-frequency vibrations instead as free rotational and translational modes using statistical thermodynamics formalisms has estimated entropies of physisorbed alkanes that resemble experimentally-determined values [40,41,58].

The choice and design of microporous voids for specific catalytic targets typically relies on criteria based on size exclusion, despite the strong consequences of confinement for transition state stability. This reflects our emerging knowledge about the specific catalyst and reactant properties that influence turnover rates and selectivities. These insights become increasingly

important as we expand the ranges of materials used and of the reactions they catalyze. Predictive guidance based on rigorous mechanistic interpretation can replace phenomenological considerations of void geometry and topology and enable the design of inorganic structures that mimic biological catalysts in their ability to confine specific transition states and selectively catalyze the chemical reactions that they mediate.

## 5.4 Summary

Turnover rates and selectivities in zeolite acid catalysis depend predominantly on enthalpic and entropic stabilities of ion-pair transition states at low and high temperatures, respectively. The catalytic consequences of reactant and void structure are identified using thermochemical cycles that separate activation energies and entropies into terms that depend differently on reactant and catalyst identity. These findings provide insight into the high specificity of both DME carbonylation (400-500 K) and monomolecular alkane activation (700-800 K) turnovers for 8-MR MOR pockets, the higher selectivities to n-alkane dehydrogenation but isoalkane cracking in such locations, and the marked increase in cracking turnover rates with n-alkane size.

## 5.5 Acknowledgements

Financial support from the Chevron Energy Technology Company is acknowledged.

## 5.6 Supporting Information

### *5.6.1 Estimation of Gas-Phase C-C and C-H Bond Proton Affinities for Propane, n-Butane and Isobutane*

The proton affinity ($\Delta E_P$) is defined as the enthalpy change in the following gas-phase reaction:

$$B + H^+ \longrightarrow BH^+, \tag{5.15}$$

where *B* denotes a base (proton acceptor). Proton affinity values become more negative, and enthalpy changes for the reaction in Eq. (5.15) more exothermic, as the gaseous cations formed become more stable.

Protonation of alkanes can occur either at C-C or C-H bonds to form carbonium-like ions. The structures and energies for stable intermediates and transition states involved in gas-phase protonation of alkanes ($C_3H_8$;[31] n-$C_4H_{10}$;[32] i-$C_4H_{10}$[33]) at different C-C and C-H bonds were calculated by Mota et al. using *ab initio* quantum chemical calculations at the MP4SDTQ(fc)/6-311++G**//MP2(full)/6-31G** level. Here, we describe how these values were used to estimate differences in gas-phase proton affinities for individual or weighted-average alkane C-C and C-H bonds, which are plotted in Figure 5.3.

Gaseous $C_3H_9^+$ carbonium-ions formed upon protonation at the C-C bond in $C_3H_8$ are more stable (-627 kJ/mol) than those formed upon protonation at primary C-H bonds (-583 kJ/mol) and secondary C-H bonds (-598 kJ/mol).[31] We estimate the proton affinity of the average C-H bond in $C_3H_8$ (-587 kJ/mol) by weighting the proton affinity for each individual C-H bond by the relative numbers of such bonds (six primary C-H and two secondary C-H). Thus, we estimate the difference in proton affinities between an average C-H bond and the C-C bond in $C_3H_8$ ($\Delta E_{P(C-H)}$- $\Delta E_{P(C-C)}$) to be 40 kJ/mol.

Gaseous n-$C_4H_{11}^+$ carbonium-ions formed upon protonation at secondary C-C bonds in n-$C_4H_{10}$ (-655 kJ/mol) are more stable than those formed upon protonation at primary C-C bonds (-636 kJ/mol) by ~20 kJ/mol.[32] The proton affinity of an average C-C bond in n-$C_4H_{10}$ (two primary C-C and one secondary C-C) is -642 kJ/mol. Less stable carbonium-ions are formed upon protonation at primary C-H bonds (-588 kJ/mol) and secondary C-H bonds (-606 kJ/mol)[32] and indicate that the average n-$C_4H_{10}$ C-H bond proton affinity is -595 kJ/mol (six primary C-H and four secondary C-H). These values can be used to calculate proton affinity differences between an average C-H bond and either an average (47 kJ/mol), primary (41 kJ/mol) or secondary (60 kJ/mol) C-C bond in n-$C_4H_{10}$.

The most stable gaseous i-$C_4H_{11}^+$ cation is formed upon protonation at the tertiary C-H bond (-696 kJ/mol) in i-$C_4H_{10}$; this cation resembles a van der Waals complex between $H_2$ and a tert-$C_4H_9^+$ cation.[33] Protonation at i-$C_4H_{10}$ C-C bonds form a less stable van der Waals complex between $CH_4$ and a *sec*-$C_3H_7^+$ cation (-682 kJ/mol).[33] These proton affinities give a $\Delta E_{P(C-H)}$- $\Delta E_{P(C-C)}$ value of -14 kJ/mol.

### *5.6.2 Estimation of Intrinsic Activation Entropies of Monomolecular Alkane Cracking using Statistical Mechanics*

According to the mechanism shown in Scheme 5.1, intrinsic activation entropies of monomolecular alkane cracking ($\Delta S_{int,C}$) reflect entropy differences between transition states and alkanes adsorbed onto acid sites, both of which are contained within zeolite voids:

$$\Delta S_{int} = \Delta S^\circ_{\ddagger} - \left(\Delta S^\circ_{H^+Z^-} + \Delta S^\circ_{A(z)}\right). \tag{5.16}$$

Entropies for adsorbed alkanes have been estimated by De Moor et al.[40,41] using statistical mechanics formalisms that treat alkane translation on a plane perpendicular to the O-H bond axis (2D free translation) and rotation about their center axis (1D free rotation) and about an axis perpendicular to the zeolite surface (2D free rotation) when void spaces permit. Transition states for monomolecular cracking are late and resemble van der Waals complexes of two fragments formed by charge separation and C-C bond lengthening,[5,29,34] approaching the limit in which both cracking product fragments are fully-formed. In this limit, we expect that transition state entropies can be estimated from entropies of products determined by the same statistical mechanics treatments used for adsorbed alkane reactants. Here, we describe how entropies of adsorbed molecules depend individually on translational and rotational contributions, how entropy values were estimated for a given C-C scission event, and how these values were averaged to determine the $\Delta S_{int,C}$ values for $C_3$-$C_6$ n-alkanes in H-MFI plotted in Figure 5.5.

The following expressions, derived using statistical mechanics,[59] were used to evaluate molecular entropies arising from 1D translation (Eq. (5.17)), 2D translation (Eq. (5.18)), 1D rotation (Eq. (5.19)) and 2D rotation (Eq. (5.20)):

$$S^\circ_{1D-trans} = R\left\{\ln\left[\left(\frac{2\pi M k_B T}{h^2}\right)^{1/2}\frac{L^o}{N_A}\right]+\frac{3}{2}\right\} \tag{5.17}$$

$$S^\circ_{2D-trans} = R\left\{\ln\left[\left(\frac{2\pi M k_B T}{h^2}\right)\frac{A^o}{N_A}\right]+2\right\} \tag{5.18}$$

$$S^\circ_{1D-rot} = R\left\{\ln\left[\frac{\sqrt{\pi I_A}}{\sigma}\left(\frac{8\pi^2 k_B T}{h^2}\right)^{1/2}\right]+\frac{1}{2}\right\} \tag{5.19}$$

$$S^\circ_{2D-rot} = R\left\{\ln\left[\frac{\sqrt{\pi I_A I_B}}{\sigma}\left(\frac{8\pi^2 k_B T}{h^2}\right)\right]+1\right\} \tag{5.20}$$

In these expressions, $R$ is the universal gas constant, $k_B$ is the Boltzmann constant, and $h$ is the Planck constant. Translational entropies (Eqs. (5.17)-(5.18)) depend on the molecular mass ($M$) and the surface area ($A^o/N_A$) or distance ($L^o/N_A$) available for translation near the acid site in two or one dimensions, respectively. The molecular surface area ($A^o/N_A$) available for translation in MFI was taken as 200 x 600 pm (1.2 x $10^{-19}$ $m^2$), as reported by De Moor et al.,[41] and $L^o/N_A$ was estimated as $(A^o/N_A)^{1/2}$. Rotational entropies (Eqs. (5.19)-(5.20)) depend on principal moments of inertia ($I_A$, $I_B$) and the external symmetry number ($\sigma$) of the molecule. Moments of inertia were taken from the NIST Computational Chemistry Comparison and Benchmark Database,[60] calculated at the coupled-cluster doubles (CCD) level of theory with the 6-31G* basis set.

These molecular properties ($M$, $I_A$, $I_B$, $\sigma$) are summarized in Table 5.2 for all molecules that are reactants or products of monomolecular cracking routes of $C_3$-$C_6$ n-alkanes. Entropies of these molecules arising from translation and rotation in one and two dimensions were determined from values in Table 5.2 and Eqs. (5.17)-(5.20); these values are summarized in Table 5.3.

Entropy changes for the following cracking reactions are summarized in Table 5.4:

$$C_3H_8 \longrightarrow CH_4 + C_2H_4 \tag{5.21}$$

$$nC_4H_{10} \longrightarrow CH_4 + C_3H_6 \tag{5.22}$$

$$nC_4H_{10} \longrightarrow C_2H_6 + C_2H_4 \tag{5.23}$$

$$nC_5H_{12} \longrightarrow CH_4 + 1C_4H_8 \tag{5.24}$$

$$nC_5H_{12} \longrightarrow C_2H_6 + C_3H_6 \tag{5.25}$$

$$nC_5H_{12} \longrightarrow C_3H_8 + C_2H_4 \tag{5.26}$$

$$nC_6H_{14} \longrightarrow CH_4 + 2C_5H_{10} \tag{5.27}$$

$$nC_6H_{14} \longrightarrow C_2H_6 + 1C_4H_8 \tag{5.28}$$

$$nC_6H_{14} \longrightarrow C_3H_8 + C_3H_6 \tag{5.29}$$

$$nC_6H_{14} \longrightarrow nC_4H_{10} + C_2H_4 \tag{5.30}$$

The entropy changes for cracking of a given alkane (summarized in Table 5.5, plotted in Fig. 5.5) were estimated by weighing entropy changes for individual C-C scission events (Eqs. (5.21)-(5.30)) by the number of such events expected statistically based on the alkane structure. For a $C_n$ alkane, cracking at terminal C-C bonds was assumed to form $CH_4$ and the corresponding $C_{n-1}$ alkene, while cracking at non-terminal C-C bonds was assumed to form the $C_m$ alkane + $C_{n-m}$ alkene (m<n) and the $C_m$ alkene + $C_{n-m}$ alkane products with equal probability (Eqs. (5.31)-(5.34)).

$$\Delta S_{C_3H_8} = \Delta S_{Eq.\ S.7} \tag{5.31}$$

$$\Delta S_{nC_4H_{10}} = (2/3)\Delta S_{Eq.\ S.8} + (1/3)\Delta S_{Eq.\ S.9} \tag{5.32}$$

$$\Delta S_{nC_5H_{12}} = (2/4)\Delta S_{Eq.\ S.10} + (1/4)\Delta S_{Eq.\ S.11} + (1/4)\Delta S_{Eq.\ S.12} \tag{5.33}$$

$$\Delta S_{nC_6H_{14}} = (2/5)\Delta S_{Eq.\ S.13} + (1/5)\Delta S_{Eq.\ S.14} + (1/5)\Delta S_{Eq.\ S.15} + (1/5)\Delta S_{Eq.\ S.16} \tag{5.34}$$

**Table 5.2.** Molecular masses ($M$), principal moments of inertia ($I_A$, $I_B$) and external symmetry numbers ($\sigma$).

| Molecule | $M$ (/ $10^{-26}$ kg) | $I_A$ (/ $10^{-47}$ kg m$^2$) | $I_B$ (/ $10^{-47}$ kg m$^2$) | $\sigma$ |
|---|---|---|---|---|
| $CH_4$ | 2.7 | 5.3 | 5.3 | 12 |
| $C_2H_4$ | 4.6 | 5.7 | 28.1 | 4 |
| $C_2H_6$ | 5.0 | 10.5 | 42.1 | 6 |
| $C_3H_6$ | 7.0 | 18.1 | 90.5 | 1 |
| $C_3H_8$ | 7.3 | 28.6 | 99.6 | 2 |
| 1-$C_4H_8$ | 9.3 | 37.3 | 203 | 1 |
| n-$C_4H_{10}$ | 9.6 | 63.5 | 177 | 2 |
| 2-$C_5H_{10}$ | 11.6 | 62.8 | 342 | 1 |
| n-$C_5H_{12}$ | 12.0 | 49.4 | 433 | 2 |
| n-$C_6H_{14}$ | 14.3 | 57.5 | 738 | 2 |

**Table 5.3.** Entropies (J mol$^{-1}$ K$^{-1}$) of adsorbed molecules from translation and rotation in one and two dimensions.

| Molecule | $S^o_{1D\text{-}trans}$ | $S^o_{2D\text{-}trans}$ | $S^o_{1D\text{-}rot}$ | $S^o_{2D\text{-}rot}$ |
|---|---|---|---|---|
| $CH_4$ | 38 | 68 | 7 | 31 |
| $C_2H_4$ | 41 | 73 | 17 | 47 |
| $C_2H_6$ | 41 | 73 | 16 | 48 |
| $C_3H_6$ | 42 | 76 | 33 | 68 |
| $C_3H_8$ | 42 | 76 | 29 | 65 |
| 1-$C_4H_8$ | 43 | 78 | 36 | 75 |
| n-$C_4H_{10}$ | 44 | 79 | 33 | 71 |
| 2-$C_5H_{10}$ | 44 | 80 | 38 | 79 |
| n-$C_5H_{12}$ | 44 | 81 | 32 | 73 |
| n-$C_6H_{14}$ | 45 | 82 | 32 | 76 |

**Table 5.4.** Reaction entropy changes (J mol$^{-1}$ K$^{-1}$) calculated using values in Table 5.3.

| Reaction | $\Delta S_{1D\text{-}trans}$ | $\Delta S_{2D\text{-}trans}$ | $\Delta S_{1D\text{-}rot}$ | $\Delta S_{2D\text{-}rot}$ |
|---|---|---|---|---|
| S.7 | 36 | 64 | -5 | 13 |
| S.8 | 37 | 65 | 8 | 29 |
| S.9 | 38 | 67 | 0 | 25 |
| S.10 | 37 | 66 | 12 | 32 |
| S.11 | 39 | 69 | 18 | 43 |
| S.12 | 38 | 69 | 15 | 39 |
| S.13 | 37 | 66 | 14 | 34 |
| S.14 | 39 | 70 | 20 | 47 |
| S.15 | 39 | 71 | 30 | 57 |
| S.16 | 39 | 69 | 17 | 42 |

**Table 5.5.** Entropy changes (J mol$^{-1}$ K$^{-1}$) upon cracking of $C_3$-$C_6$ n-alkanes calculated using values in Table 5.4.

| Reactant | $\Delta S_{1D\text{-}trans}$ | $\Delta S_{2D\text{-}trans}$ | $\Delta S_{1D\text{-}rot}$ | $\Delta S_{2D\text{-}rot}$ |
|---|---|---|---|---|
| $C_3H_8$ | 36 | 64 | -5 | 13 |
| n-$C_4H_{10}$ | 37 | 66 | 5 | 27 |
| n-$C_5H_{12}$ | 38 | 67 | 14 | 37 |
| n-$C_6H_{14}$ | 38 | 68 | 19 | 43 |

## 5.7 References


(1) Degnan, T. F. *J. Catal.* **2003**, *216*, 32.
(2) Venuto, P. B. *Microporous Mater.* **1994**, *2*, 297.
(3) Corma, A. *Chem. Rev.* **1995**, *95*, 559.
(4) Kazansky, V. B. *Acc. Chem. Res.* **1991**, *24*, 379.
(5) van Santen, R. A.; Kramer, G. J. *Chem. Rev.* **1995**, *95*, 637.
(6) Rigby, A. M.; Kramer, G. J.; van Santen, R. A. *J. Catal.* **1997**, *170*, 1.
(7) Frash, M. V.; van Santen, R. A. *Top. Catal.* **1999**, *9*, 191.
(8) Koppel, I. A.; Burk, P.; Koppel, I.; Leito, I.; Sonoda, T.; Mishima, M. *J. Am. Chem. Soc.* **2000**, *122*, 5114.
(9) Macht, J.; Carr, R. T.; Iglesia, E. *J. Catal.* **2009**, *264*, 54.
(10) Eichler, U.; Brändle, M.; Sauer, J. *J. Phys. Chem. B* **1997**, *101*, 10035.
(11) Brändle, M.; Sauer, J. *J. Am. Chem. Soc.* **1998**, *120*, 1556.
(12) Sauer, J.; Sierka, M. *J. Comput. Chem.* **2000**, *21*, 1470.
(13) Bhan, A.; Iglesia, E. *Acc. Chem. Res.* **2008**, *41*, 559.
(14) Gounder, R.; Iglesia, E. *J. Am. Chem. Soc.* **2009**, *131*, 1958.
(15) Gounder, R.; Iglesia, E. *Angew. Chem., Int. Ed.* **2010**, *49*, 808.
(16) Carr, R. T.; Neurock, M.; Iglesia, E. *J. Catal.* **2011**, *278*, 78.
(17) Eder, F.; Lercher, J. A. *J. Phys. Chem. B* **1997**, *101*, 1273.
(18) Eder, F.; Lercher, J. A. *Zeolites* **1997**, *18*, 75.
(19) Eder, F.; Stockenhuber, M.; Lercher, J. A. *J. Phys. Chem. B* **1997**, *101*, 5414.
(20) Savitz, S.; Siperstein, F.; Gorte, R. J.; Myers, A. L. *J. Phys. Chem. B* **1998**, *102*, 6865.
(21) Cheung, P.; Bhan, A.; Sunley, G. J.; Iglesia, E. *Angew. Chem., Int. Ed.* **2006**, *45*, 1617.
(22) Cheung, P.; Bhan, A.; Sunley, G. J.; Law, D. J.; Iglesia, E. *J. Catal.* **2007**, *245*, 110.
(23) Bhan, A.; Allian, A. D.; Sunley, G. J.; Law, D. J.; Iglesia, E. *J. Am. Chem. Soc.* **2007**, *129*, 4919.
(24) Neurock, M. *Ind. Eng. Chem. Res.* **2010**, *49*, 10183.
(25) Boronat, M.; Martinez, C.; Corma, A. *Phys. Chem. Chem. Phys.* **2011**, *13*, 2603.
(26) Haag, W. O.; Dessau, R. M. *Proc. 8th Int. Congr. Catalysis, Berlin* **1984**, *2*, 305.
(27) Marcus, R. A. *Annu. Rev. Phys. Chem.* **1964**, *15*, 155.
(28) Bell, R. P. *The Proton in Chemistry*; Chapman and Hall: London, **1973**.
(29) Zygmunt, S. A.; Curtiss, L. A.; Zapol, P.; Iton, L. E. *J. Phys. Chem. B* **2000**, *104*, 1944.
(30) Collins, S. J.; O'Malley, P. J. *Top. Catal.* **1998**, *6*, 151.
(31) Esteves, P. M.; Mota, C. J. A.; Ramírez-Solís, A.; Hernández-Lamoneda, R. *J. Am. Chem. Soc.* **1998**, *120*, 3213.
(32) Esteves, P. M.; Alberto, G. G. P.; Ramírez-Solís, A.; Mota, C. J. A. *J. Phys. Chem. A* **2000**, *104*, 6233.
(33) Mota, C. J. A.; Esteves, P. M.; Ramírez-Solís, A.; Hernández-Lamoneda, R. *J. Am. Chem. Soc.* **1997**, *119*, 5193.
(34) Zheng, X. B.; Blowers, P. *J. Phys. Chem. A* **2005**, *109*, 10734.
(35) Zheng, X. B.; Blowers, P. *J. Phys. Chem. A* **2006**, *110*, 2455.
(36) Kazansky, V. B.; Frash, M. V.; van Santen, R. A. *Appl. Catal. A* **1996**, *146*, 225.
(37) Hunter, K. C.; East, A. L. L. *J. Phys. Chem. A* **2002**, *106*, 1346.
(38) Narbeshuber, T. F.; Vinek, H.; Lercher, J. A. *J. Catal.* **1995**, *157*, 388.
(39) Bhan, A.; Gounder, R.; Macht, J.; Iglesia, E. *J. Catal.* **2008**, *253*, 221.

(40) De Moor, B. A.; Reyniers, M. F.; Gobin, O. C.; Lercher, J. A.; Marin, G. B. *J. Phys. Chem. C* **2011**, *115*, 1204.
(41) De Moor, B. A.; Reyniers, M. F.; Marin, G. B. *Phys. Chem. Chem. Phys.* **2009**, *11*, 2939.
(42) Maesen, T. L. M.; Beerdsen, E.; Calero, S.; Dubbeldam, D.; Smit, B. *J. Catal.* **2006**, *237*, 278.
(43) Swisher, J. A.; Hansen, N.; Maesen, T.; Keil, F. J.; Smit, B.; Bell, A. T. *J. Phys. Chem. C* **2010**, *114*, 10229.
(44) Xu, B.; Sievers, C.; Hong, S. B.; Prins, R.; van Bokhoven, J. A. *J. Catal.* **2006**, *244*, 163.
(45) Janik, M. J.; Davis, R. J.; Neurock, M. *J. Catal.* **2006**, *244*, 65.
(46) Bucko, T.; Benco, L.; Dubay, O.; Dellago, C.; Hafner, J. *J. Chem. Phys.* **2009**, *131*, 214508.
(47) Bucko, T.; Hafner, J. *J. Phys. Cond. Matter* **2010**, *22*, 384201.
(48) Li, Q. B.; Hunter, K. C.; Seitz, C.; East, A. L. L. *J. Chem. Phys.* **2003**, *119*, 7148.
(49) East, A. L. L.; Bucko, T.; Hafner, J. *J. Chem. Phys.* **2009**, *131*, 104314.
(50) Mullen, G. M.; Janik, M. J. *ACS Catal.* **2011**, *1*, 105.
(51) East, A. L. L.; Smith, B. J.; Radom, L. *J. Am. Chem. Soc.* **1997**, *119*, 9014.
(52) Benson, S. W. *Thermochemical Kinetics*; John Wiley & Sons, Inc.: New York, **1976**.
(53) Gounder, R.; Iglesia, E. *J. Catal.* **2011**, *277*, 36.
(54) Gounder, R.; Iglesia, E. *ChemCatChem* **2011**, *3*, 1134.
(55) Pinar, A. B.; Márquez-Álvarez, C.; Grande-Casas, M.; Pérez-Pariente, J. *J. Catal.* **2009**, *263*, 258.
(56) Román-Leshkov, Y.; Moliner, M.; Davis, M. E. *J. Phys. Chem. C* **2011**, *115*, 1096.
(57) Sklenak, S.; Dedecek, J.; Li, C.; Wichterlová, B.; Gábová, V.; Sierka, M.; Sauer, J. *Phys. Chem. Chem. Phys.* **2009**, *11*, 1237.
(58) De Moor, B. A.; Ghysels, A.; Reyniers, M. F.; Van Speybroeck, V.; Waroquier, M.; Marin, G. B. *J. Chem. Theory Comput.* **2011**, *7*, 1090.
(59) Cramer, C. J. *Essentials of Computational Chemistry: Theories and Models*; John Wiley & Sons, Ltd.: Chichester, **2002**.
(60) NIST Webbook Chemistry, http://webbook.nist.gov/chemistry/

# CHAPTER SIX

# Catalytic Hydrogenation of Alkenes on Acidic Zeolites: Mechanistic Connections to Monomolecular Alkane Dehydrogenation Reactions


## Abstract

Brønsted acid sites in zeolites (H-FER, H-MFI, H-MOR) selectively hydrogenate alkenes in excess $H_2$ at high temperatures (>700 K) and at rates proportional to alkene and $H_2$ pressures. This kinetic behavior and the De Donder equations for non-equilibrium thermodynamics show that, even away from equilibrium, alkene hydrogenation and monomolecular alkane dehydrogenation occur on predominantly uncovered surfaces via microscopically reverse elementary steps, which involve kinetically-relevant $(C\text{-}H\text{-}H)^+$ carbonium-ion-like transition states in both directions. As a result, rate constants, activation energies and activation entropies for these two reactions are related by the thermodynamics of the overall stoichiometric gas-phase reaction. The ratios of rate constants for hydrogenation and dehydrogenation reactions do not depend on the identity or reactivity of active sites; thus, sites within different zeolite structures (or at different locations within a given zeolite) that favor alkane dehydrogenation reactions, because of their ability to stabilize the required transition states, also favor alkene hydrogenation reactions to the exact same extent. These concepts and conclusions also apply to monomolecular alkane cracking and bimolecular alkane-alkene reaction paths on Brønsted acids and, more generally, to any forward and reverse reactions that proceed via the same kinetically-relevant step on vacant surfaces in the two directions, even away from equilibrium. The evidence shown here for the sole involvement of Brønsted acids in the hydrogenation of alkoxides with $H_2$ is unprecedented in its mechanistic clarity and thermodynamic rigor. The scavenging of alkoxides via direct H-transfer from $H_2$ indicates that $H_2$ can be used to control the growth of chains and the formation of unreactive deposits in alkylation, oligomerization, cracking, and other acid-catalyzed reactions.


## 6.1 Introduction

The catalytic cracking and dehydrogenation of alkanes on Brønsted acid sites within zeolites have been shown by experiment [1-5] and theory [6-9] to occur via monomolecular routes at high temperatures (>623 K) and low conversions (<2%) [10]. These paths involve protonation at C-C or C-H bonds in alkanes, respectively, to form $(C\text{-}C\text{-}H)^+$ or $(C\text{-}H\text{-}H)^+$ carbonium-ion-like transition states in their respective kinetically-relevant bond scission steps [2]. Cracking and dehydrogenation of alkanes ($C_3H_8$, n-$C_4H_{10}$, i-$C_4H_{10}$) via monomolecular routes at these conditions occur exclusively on Brønsted acid sites in H-FER, H-MFI, and H-MOR, consistent with rates proportional to the proton density in these materials but not with the number of metal or Lewis acid impurity sites [2,3]. On all zeolites, the differences between cracking and dehydrogenation activation energies of a given alkane equal the difference in gas-phase proton affinities of its C-C and C-H bonds, as expected from thermochemical cycle analyses of transition state ion-pairs for cracking and dehydrogenation paths catalyzed by Brønsted acids (Section 6.7.1, Supporting Information) [2,3].

The hydrogenation of alkenes by $H_2$ on acidic zeolites, however, is typically attributed to metals [11-16] or cations [17,18] introduced deliberately or present as adventitious impurities [19,20]. Yet, the reactivity of Brønsted acid sites in monomolecular alkane dehydrogenation would make such sites plausible candidates as catalysts for alkene hydrogenation with $H_2$ via carbonium-ion-like transition states, as proposed, but not shown unequivocally, on liquid superacids [21-23] and solid acids [18,24,25]. This expectation would be justified rigorously for any general chemical reaction only *at equilibrium*, conditions at which reactions occur via identical mechanistic sequences in forward and reverse directions, as dictated by the principle of microscopic reversibility [26,27]. Such requirements hold even *away from equilibrium* for elementary steps, because they involve a single energy barrier that must be surmounted in both directions along the reaction coordinate.

We provide evidence here that Brønsted acid sites in zeolites catalyze alkene hydrogenation with $H_2$, even at conditions far away from equilibrium, via the microscopic reverse of monomolecular alkane dehydrogenation paths and at rates constrained by the thermodynamics of the stoichiometric gas-phase reaction. Rate constants, activation energies and activation entropies for propene hydrogenation and monomolecular propane dehydrogenation are interpreted rigorously using common elementary steps and De Donder relations that describe the rates of elementary steps as a function of their chemical affinity, the relevant metric for their distance from equilibrium. We use these mechanistic insights to show that intrazeolite locations and channel structures that lead to more active Brønsted acid sites do so to the same extent for monomolecular propane dehydrogenation and propene hydrogenation reactions, regardless of their respective distances from equilibrium. These conclusions would seem at first glance to extend the principle of microscopic reversibility beyond its intended description of chemical reactions at equilibrium, but represent, in fact, a not altogether uncommon example of chemical reactions that involve a single kinetically-relevant elementary step on predominantly vacant surfaces, for which such principles apply at all distances from equilibrium.

## 6.2 Methods

### *6.2.1 Catalyst Synthesis and Characterization*

$NH_4^+$-zeolites were treated in flowing dry air (2.5 $cm^3$ $g^{-1}$ $s^{-1}$, zero grade, Praxair) by heating to 773 K (0.0167 K $s^{-1}$) and holding for 4 h to prepare H-zeolites, which were then pelleted, crushed, and sieved to retain 180-250 μm (60-80 mesh) aggregates. The zeolite samples used are described in Table 6.1 together with the relevant characterization data. The notation describes their fractional $H^+$ and $Na^+$ content at exchange sites, their framework structure, and their provenance. Methods to prepare $Na^+$-exchanged zeolites, measure elemental composition, and collect $^{27}$Al-NMR and infrared spectra have been reported elsewhere [2]. The number of Brønsted acid sites in $Na^+$-exchanged samples was determined by the difference in the number of framework Al atoms and exchanged $Na^+$ cations.

**Table 6.1.** Characterization of zeolite samples used in this study.

| Zeolite | Source | Si/Al Ratio[a] | Na/Al Ratio[a] | $Al_{EF}$[b] (%) | $X_{8\text{-}MR}$[c] | $X_{12\text{-}MR}$[c] |
|---|---|---|---|---|---|---|
| $H_{100}Na_0$-FER-Z | Zeolyst | 10.3 | 0.002 | 15 | - | - |
| $H_{100}Na_0$-MFI-Z | Zeolyst | 16.5 | 0.004 | 12 | - | - |
| $H_{100}Na_0$-MOR-T | Tosoh | 8.9 | 0.001 | 19 | 0.78 | 0.22 |
| $H_{100}Na_0$-MOR-S | Sud-Chemie | 10.1 | 0.001 | 21 | 0.60 | 0.40 |
| $H_{100}Na_0$-MOR-Z | Zeolyst | 10.0 | 0.001 | 22 | 0.56 | 0.44 |
| $H_{83}Na_{17}$-MOR-Z | Zeolyst | 10.0 | 0.17 | 22 | 0.36 | 0.64 |
| $H_{73}Na_{27}$-MOR-Z | Zeolyst | 10.0 | 0.27 | 22 | 0.27 | 0.73 |
| $H_{59}Na_{41}$-MOR-Z | Zeolyst | 10.0 | 0.41 | 22 | 0.20 | 0.80 |
| $H_{38}Na_{62}$-MOR-Z | Zeolyst | 10.0 | 0.62 | 22 | 0.17 | 0.83 |

[a] Determined from elemental analysis (ICP-OES; Galbraith Laboratories).
[b] Extra-framework Al content ($Al_{EF}$) determined from $^{27}Al$ MAS NMR spectra; details in [2].
[c] Fraction of $H^+$ sites in 8-MR or 12-MR locations on MOR samples determined from infrared spectral band deconvolution (Section 6.7.3, Supporting Information).

### *6.2.2 Catalytic Rate Measurements*

Procedures for measuring monomolecular alkane dehydrogenation rates have been reported elsewhere [2]. Alkene hydrogenation rates were measured in a plug-flow tubular quartz reactor under differential conditions (<5% conversion). Before rate measurements, catalysts (0.01-0.10 g) were treated at 803 K (0.0167 K $s^{-1}$) in a 5% $O_2$ / 95% He mixture (16.7 $cm^3$ $g^{-1}$ $s^{-1}$, 99.999%, Praxair) for 2 h, and then in pure He flow (16.7 $cm^3$ $g^{-1}$ $s^{-1}$, 99.999%, Praxair) for 0.5 h while propene (1% $C_3H_6$, 5% Ar, 94% He, Praxair, 99.5% purity) and $H_2$ (99.999%, Praxair) reactants were transferred to a gas chromatograph (Agilent HP-6890GC) via heated lines (423 K) for calibration purposes. Reactants and products were separated using GS-AL\KCl capillary (0.530 mm ID x 50 m; Agilent) and HayeSep DB packed (100-120 mesh, 10 ft.; Sigma-Aldrich) columns and detected using flame ionization and thermal conductivity detection, respectively. Reactants were diluted with He (99.999%, Praxair) to vary the pressures and molar rates of $C_3H_6$ (0.01-0.05 kPa; $10^{-7}$-$10^{-6}$ (mol $C_3H_6$) $g^{-1}$ $s^{-1}$) and $H_2$ (10-120 kPa; $10^{-4}$-$10^{-3}$ (mol $H_2$) $g^{-1}$ $s^{-1}$) and to maintain high $H_2/C_3H_6$ feed molar ratios (>1000). Rate constants measured between 718 K and 778 K were used to estimate activation energies and pre-exponential factors. On all catalysts, steady-state rates and selectivities measured after ~12 h on stream were similar (within 5%) to their initial values, indicating that kinetic data were unaffected by deactivation.

## 6.3 Results and Discussion

### *6.3.1 Monomolecular Alkane Dehydrogenation on Acidic Zeolites*

Monomolecular alkane dehydrogenation proceeds via quasi-equilibrated adsorption of alkanes within zeolite voids that contain Brønsted acid sites (Step 1, Scheme 6.1), the subsequent formation of $(C\text{-}H\text{-}H)^+$ carbonium-ion-like transition states in kinetically-relevant C-H scission steps (Step 2, Scheme 6.1), and quasi-equilibrated desorption of alkene and $H_2$ products (Steps 3-5, Scheme 6.1) [2]. The temperatures and pressures required for monomolecular alkane activation lead to unoccupied $H^+$ sites as the most abundant surface intermediate (MASI) [2] and to low intrazeolite alkane concentrations that are proportional to gas-phase pressures.

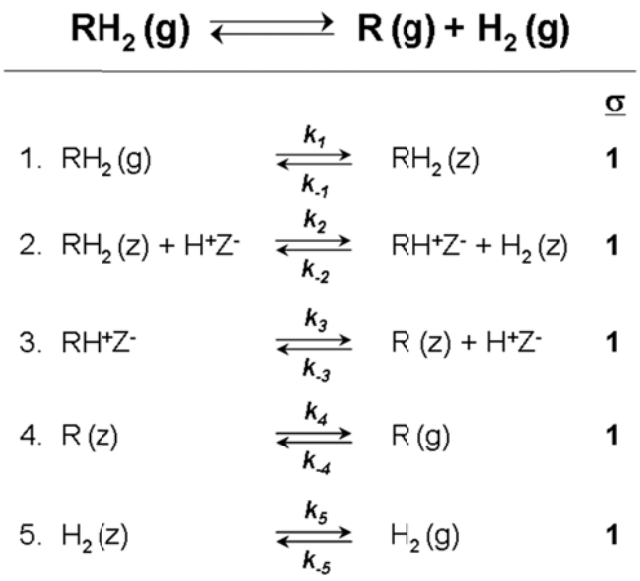


**Scheme 6.1.** Catalytic cycle for monomolecular alkane ($RH_2$) dehydrogenation and for alkene (R) hydrogenation with $H_2$ on acidic zeolites involving gas-phase species (g), adsorbates at framework Al sites ($Z^-$), and species adsorbed within zeolite channels near framework Al sites (z). Stoichiometric numbers ($\sigma$) shown for each elementary step.

Propane dehydrogenation rates (per $H^+$; 718-778 K; <2% conversion) on acidic zeolites (H-FER, H-MFI, H-MOR) are proportional to $C_3H_8$ pressures (Fig. 6.1), consistent with an equation for monomolecular propane dehydrogenation rates (per $H^+$) derived from the mechanistic assumptions described above:

$$\overrightarrow{r_D} = K_1 k_2 P_{C_3H_8} = k_{meas,D} P_{C_3H_8} . \quad (6.1)$$

In this equation, $k_{meas,D}$ is the effective first-order dehydrogenation rate constant, $K_1$ is the equilibrium constant relating intrazeolite $C_3H_8$ concentrations to extrazeolite $C_3H_8$ pressures, and $k_2$ is the rate constant for the step that forms $C_3H_7^+$ and $H_2$ species within zeolites via $(C_3H_9)^+$ carbonium-ion-like transition states. Dehydrogenation rate constants ($k_{meas,D}$) can be expressed in terms of measured activation energies ($E_{meas,D}$) and pre-exponential factors ($A_{meas,D}$):

$$k_{meas,D} = A_{meas,D} \exp\left(-E_{meas,D}/RT\right). \quad (6.2)$$

Temperature effects on $k_{meas,D}$ include contributions from $K_1$ and $k_2$ and $E_{meas,D}$ reflects enthalpy differences between $(C_3H_9)^+$ carbonium-ion-like transition states (Step 2, Scheme 6.1) within zeolite channels and $C_3H_8$ reactants in the extrazeolite fluid phase (as depicted in Scheme 6.2):

$$E_{meas,D} = \Delta H_1 + E_2 = \Delta H^\circ_{\ddagger,2} - \Delta H^\circ_{H^+Z^-} - \Delta H^\circ_{C_3H_8(g)} . \quad (6.3)$$

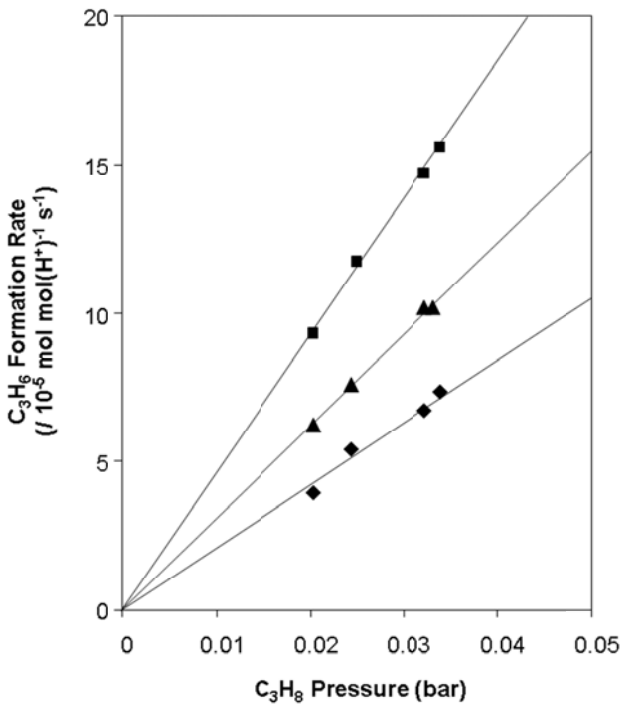


**Figure 6.1.** Dependence of propene formation rates (748 K) on propane pressure on $H_{100}Na_0$-FER-Z (▲), $H_{100}Na_0$-MFI-Z (■), and $H_{100}Na_0$-MOR-Z (◆) during monomolecular propane dehydrogenation reactions.

$A_{meas,D}$ also includes contributions from $K_1$ and $k_2$ and reflects entropy differences between the transition state for step 2 and gaseous $C_3H_8$ reactants. This measured activation entropy ($\Delta S_{meas,D}$), corrected for the number of C-H bonds in the reactant alkane ($n_B$) [2], is given by:

$$\Delta S_{meas,D} = R\left[\ln\left(A_{meas,D}/n_B\right) - \ln\left(k_B T/h\right)\right] = \Delta S^{\circ}_{\ddagger,2} - \Delta S^{\circ}_{H^+Z^-} - \Delta S^{\circ}_{C_3H_8(g)}. \quad (6.4)$$

The measured rate parameters for monomolecular propane dehydrogenation are reported on each sample as $k_{meas,D}$, $E_{meas,D}$, and $\Delta S_{meas,D}$ in Tables 6.2 and 6.3.

**Table 6.2.** Rate constants for monomolecular propane dehydrogenation ($k_{meas,D}$; mol (mol $H^+$)$^{-1}$ $s^{-1}$ (bar $C_3H_8$)$^{-1}$) and for propylene hydrogenation ($k_{meas,H}$; mol (mol $H^+$)$^{-1}$ $s^{-1}$ (bar $C_3H_6$)$^{-1}$ (bar $H_2$)$^{-1}$) and their ratio ($k_{meas,D}/k_{meas,H}$; bar) on acidic zeolites at 748 K. Mean value of $k_{meas,D}/k_{meas,H}$ on all samples is $0.017 \pm 0.001$ bar (95% confidence interval).

| Zeolite | $k_{meas,D}$ | $k_{meas,H}$ | $k_{meas,D}$ / $k_{meas,H}$ |
|---|---|---|---|
| $H_{100}Na_0$-FER-Z | 0.0031 | 0.22 | 0.014 |
| $H_{100}Na_0$-MFI-Z | 0.0046 | 0.26 | 0.018 |
| $H_{100}Na_0$-MOR-T | 0.0029 | 0.17 | 0.018 |
| $H_{100}Na_0$-MOR-S | 0.0018 | 0.10 | 0.018 |
| $H_{100}Na_0$-MOR-Z | 0.0021 | 0.12 | 0.018 |
| $H_{83}Na_{17}$-MOR-Z | 0.0012 | 0.075 | 0.016 |
| $H_{73}Na_{27}$-MOR-Z | 0.00085 | 0.044 | 0.019 |
| $H_{59}Na_{41}$-MOR-Z | 0.00065 | 0.041 | 0.016 |
| $H_{38}Na_{62}$-MOR-Z | 0.00058 | 0.035 | 0.017 |

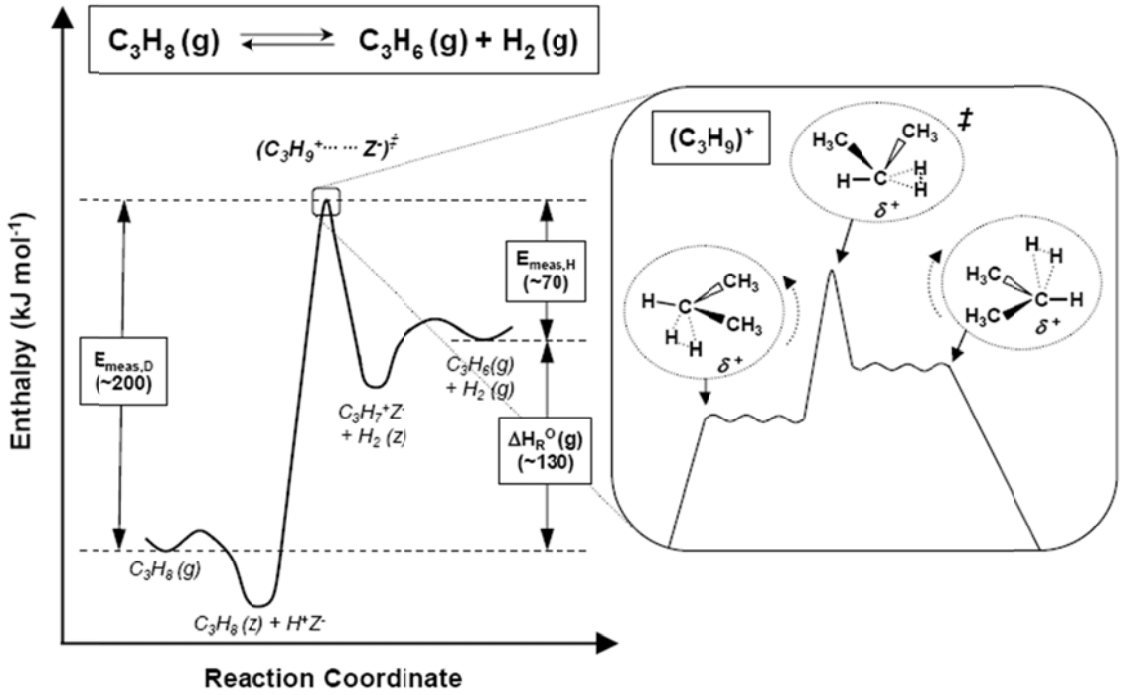


**Scheme 6.2.** Relative enthalpies along the reaction coordinate of molecules in the gas and intrazeolite phases, and of $(C_3H_9)^+$ carbonium-ion-pairs stabilized within zeolite channels. Enthalpy differences are reflected in measured activation barriers for monomolecular propane dehydrogenation ($E_{meas,D}$) and for propene hydrogenation ($E_{meas,H}$), and in the gas-phase reaction enthalpy ($\Delta H_R^O(g)$) (approximate values in parentheses). Plausible carbonium-ion structures involved in the reaction coordinate are also depicted.

### *6.3.2 Catalytic Hydrogenation of Alkenes on Acidic Zeolites*

Reactions of propene with excess $H_2$ ($H_2/C_3H_6$ >2500) at temperatures also used for monomolecular propane dehydrogenation (718-778 K) formed propane with high selectivity (>80%; Fig. 6.2) on H-FER, H-MFI and H-MOR, irrespective of zeolite provenance or $Na^+$ content. Propane formation rates (per $H^+$) increased linearly with $C_3H_6$ and $H_2$ pressures (Fig. 6.3), consistent with rates expected for low intrazeolite $H_2$ and $C_3H_6$ concentrations in equilibrium with their extrazeolite pressures and for kinetically-relevant reactions of $C_3$ intermediates, either as bound alkoxides, carbenium ions or physisorbed alkenes, with intrazeolite $H_2$ species (Step 2, Scheme 6.1):

$$\overleftarrow{r_H} = k_{-2}K_3^{-1}K_4^{-1}K_5^{-1}P_{C_3H_6}P_{H_2} = k_{meas,H}P_{C_3H_6}P_{H_2}\,. \tag{6.5}$$

Here, $k_{meas,H}$ is the effective second-order hydrogenation rate constant, $K_3$, $K_4$, and $K_5$ are equilibrium constants relating intrazeolite concentrations of $C_3H_7^+$, $C_3H_6$ and $H_2$ species to $C_3H_6$ and $H_2$ gas-phase pressures, and $k_{-2}$ is the rate constant for the formation of intrazeolitic $C_3H_8$ species via $(C_3H_9)^+$ carbonium-ion-like transition states. We note that the identity of the $C_3$ intermediate involved in the kinetically-relevant step (Step 2, Scheme 6.1) cannot be determined from kinetic data, which only indicate that $C_3$ species present as alkoxides, carbenium ions or

physisorbed alkenes are in quasi-equilibrium with gaseous $C_3H_6$; we refer to the intermediate involved in step 2 (Scheme 6.1) as an alkoxide to facilitate the discussion that follows.

**Table 6.3.** Measured activation energies ($E_{meas}$; kJ mol$^{-1}$) and entropies ($\Delta S_{meas}$; J mol$^{-1}$ K$^{-1}$) for propane dehydrogenation and for propene hydrogenation on acidic zeolites; uncertainties correspond to a 95% confidence interval. Mean values of ($E_{meas,D}$-$E_{meas,H}$) and ($\Delta S_{meas,D}$-$\Delta S_{meas,H}$) on all samples are 127 ± 8 kJ mol$^{-1}$ and 134 ± 11 J mol$^{-1}$ K$^{-1}$, respectively (95% confidence interval).

| Zeolite | $E_{meas,D}$[a] | $E_{meas,H}$[b] | $E_{meas,D}$ - $E_{meas,H}$ | $\Delta S_{meas,D}$[c] | $\Delta S_{meas,H}$[d] | $\Delta S_{meas,D}$ - $\Delta S_{meas,H}$ |
|---|---|---|---|---|---|---|
| $H_{100}Na_0$-FER-Z | 195 | 76 | 119 | -57 | -180 | 123 |
| $H_{100}Na_0$-MFI-Z | 204 | 90 | 114 | -42 | -160 | 118 |
| $H_{100}Na_0$-MOR-T | 189 | 58 | 131 | -66 | -206 | 140 |
| $H_{100}Na_0$-MOR-S | 192 | 56 | 136 | -66 | -213 | 147 |
| $H_{100}Na_0$-MOR-Z | 198 | 77 | 121 | -56 | -184 | 128 |
| $H_{83}Na_{17}$-MOR-Z | 201 | 71 | 130 | -57 | -195 | 138 |
| $H_{73}Na_{27}$-MOR-Z | 201 | 75 | 126 | -60 | -194 | 134 |
| $H_{59}Na_{41}$-MOR-Z | 196 | 60 | 136 | -69 | -215 | 146 |

[a] ± 7 kJ mol$^{-1}$.
[b] ± 9 kJ mol$^{-1}$.
[c] ± 10 J mol$^{-1}$ K$^{-1}$.
[d] ± 11 J mol$^{-1}$ K$^{-1}$.

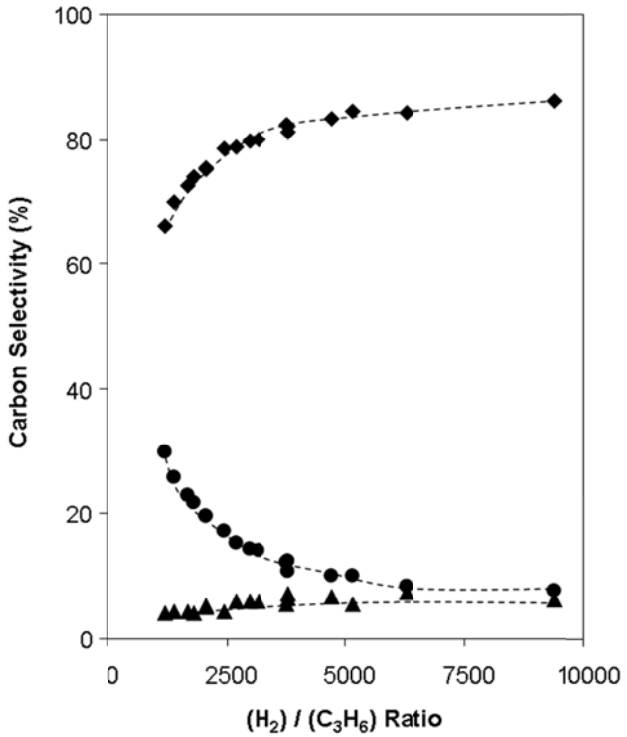


**Figure 6.2.** Carbon selectivity to $C_3H_8$ (◆), $C_2H_4$ (●), and $CH_4$ (▲) products formed during propene hydrogenation with varying $H_2/C_3H_6$ feed ratio at 748 K on $H_{100}Na_0$-MOR-Z.

Rates of propane formation were influenced only weakly by space velocity and gave large values after extrapolation to zero residence time (Fig. 6.4), consistent with its formation via direct hydrogenation of propene. Methane and ethylene were formed in nearly equimolar ratios also as primary products (Fig. 6.4), but with much lower selectivities that decreased with increasing $H_2$ pressure ($H_2/C_3H_6$ >2000; Fig. 6.2). These minority products may form either via monomolecular cracking of propoxide species [28-30] to form $C_2H_4$ and $CH_3^+$ surface species that subsequently react with $H_2$ to form $CH_4$, or via interconversion of $(C\text{-}H\text{-}H)^+$ dehydrogenation-hydrogenation transition states to the $(C\text{-}C\text{-}H)^+$ transition states involved in monomolecular cracking to form $C_2H_4$ and $CH_4$. At lower $H_2$ pressures ($H_2/C_3H_6$ <2000), $C_{4+}$ molecules become detectable and $C_2H_4/CH_4$ ratios become larger than unity, apparently via β-scission of larger chains formed by $C_3H_6$ oligomerization with propoxides or with methyl groups stranded by β-scission reactions of propoxides to form $C_2H_4$ in stoichiometric excess ($C_2H_4/CH_4$>1).

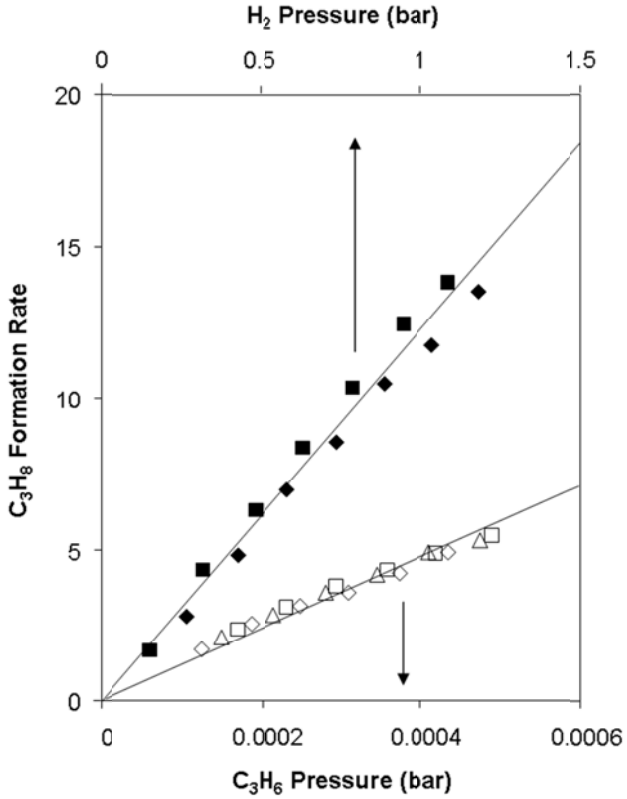


**Figure 6.3.** Dependence of $C_3H_8$ formation rates (748 K) on $C_3H_6$ pressure (x$10^5$ mol (mol $H^+$)$^{-1}$ $s^{-1}$ (bar $H_2$)$^{-1}$; ◇: $P(H_2)$ = 1.2 bar; □: $P(H_2)$ = 0.9 bar; △: $P(H_2)$ = 0.6 bar) and $H_2$ pressure (x$10^2$ mol (mol $H^+$)$^{-1}$ $s^{-1}$ (bar $C_3H_6$)$^{-1}$; ◆: $P(C_3H_6)$ = 0.0003 bar; ■: $P(C_3H_6)$ = 0.0001 bar) on $H_{100}Na_0$-MOR-Z.

Temperature effects on $k_{meas,H}$ reflect enthalpy differences between hydrogenation transition states (Step 2, Scheme 6.1) and alkene and $H_2$ reactants in the external fluid phase:

$$E_{meas,H} = E_{-2} - \Delta H_3 - \Delta H_4 - \Delta H_5 = \Delta H^\circ_{\ddagger,-2} - \Delta H^\circ_{H^+Z^-} - \Delta H^\circ_{C_3H_6(g)} - \Delta H^\circ_{H_2(g)}, \quad (6.6)$$

as also shown in Scheme 6.2 when the same transition state is involved in propane dehydrogenation and propene hydrogenation, because the kinetically-relevant step is the same (albeit in reverse directions) for these two reactions. The same approach leads to expressions for measured activation entropies for hydrogenation ($\Delta S_{meas,H}$), which reflect entropy differences between the hydrogenation transition state (Step 2, Scheme 6.1) and extrazeolite $C_3H_6$ and $H_2$ reactants:

$$\Delta S_{meas,H} = R\left[\ln\left(A_{meas,H}/n_B\right) - \ln\left(k_B T/h\right)\right] = \Delta S^\circ_{\ddagger,-2} - \Delta S^\circ_{H^+Z^-} - \Delta S^\circ_{C_3H_6(g)} - \Delta S^\circ_{H_2(g)}. \quad (6.7)$$

These rate parameters ($k_{meas,H}$, $E_{meas,H}$, $\Delta S_{meas,H}$) for propene hydrogenation on each zeolite catalyst are also shown in Tables 6.2 and 6.3.

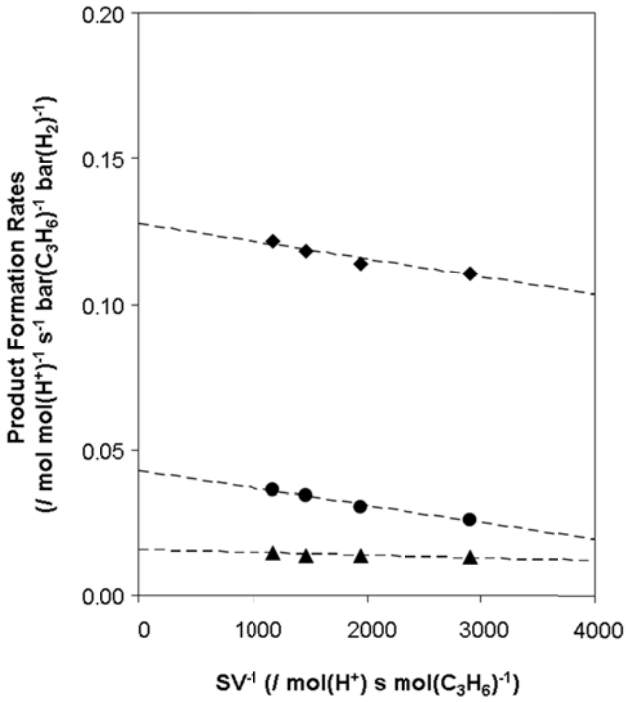


**Figure 6.4.** Rates of formation of $C_3H_8$ (◆), $C_2H_4$ (●), and $CH_4$ (▲) at different $C_3H_6$ space velocities (*SV*) (3-6% $C_3H_6$ conversion) on $H_{100}Na_0$-MOR-Z at 748 K and a 4000/1 $H_2/C_3H_6$ feed ratio.

Monomolecular propane dehydrogenation (Eq. (6.1)) and propene hydrogenation (Eq. (6.5)) rate equations reflect the law of mass action for the stoichiometric reaction in their respective directions (Scheme 6.1). Thus, the ratio of hydrogenation and dehydrogenation rates depends on the same combined pressure terms as in the equilibrium expression for the overall chemical reaction ($(C_3H_6)(H_2)/(C_3H_8)$; Section 6.7.2, Supporting Information). This algebraic resemblance, by itself, is insufficient to establish a mechanistic connection between their respective sequences of elementary steps (i.e., Scheme 6.1) or to relate the measured rate constants ($k_{meas,D}$, $k_{meas,H}$) to specific steps as they appear in Eqs. (6.1) and (6.5), or to the equilibrium constant for the overall reaction, because these rate constants are measured at

different conditions and far from equilibrium in their respective directions. In what follows, we provide evidence that alkane dehydrogenation and alkene hydrogenation paths do, in fact, proceed via the same sequence of elementary steps (Scheme 6.1) by interpreting rate constants in mechanistic terms and using the De Donder relations to connect kinetic parameters ($k_{meas}$, $E_{meas}$, $\Delta S_{meas}$) for these two reactions.

### *6.3.3 The De Donder Formalism for Rates of Elementary Steps and their Sequences*

The net rate of an elementary step ($r_i$) reflects the difference between its forward ($\vec{r}_i$) and reverse ($\overleftarrow{r}_i$) rates:

$$r_i = \vec{r}_i - \overleftarrow{r}_i \,. \tag{6.8}$$

The De Donder equation [31,32] relates forward and reverse rates to chemical affinities ($A_i$) for a given step, which are defined as $(-\partial G/\partial \xi)_{T,P}$ with $G$ denoting the Gibbs free energy and $\xi$ the extent of reaction:

$$\vec{r}_i / \overleftarrow{r}_i = \exp\left(A_i / RT\right). \tag{6.9}$$

Elementary step reaction rates must also obey the law of mass action because they occur as written, and the chemical affinity is given by:

$$A_i = RT \ln\left( K_i \prod_j a_j^{-\nu_j} \right), \tag{6.10}$$

where $a_j$ and $\nu_j$ are the thermodynamic activity and molecularity of the species $j$ involved in step $i$, and where $\nu_j$ is positive for products and negative for reactants. $K_i$ is the equilibrium constant for the step, which is given, in turn, by the ratio of its forward ($\vec{k}_i$) and reverse ($\overleftarrow{k}_i$) rate constants:

$$K_i = \frac{\vec{k}_i}{\overleftarrow{k}_i}. \tag{6.11}$$

The De Donder equation (Eq. (6.9)) accounts rigorously for the consequences of thermodynamic equilibrium and of reactant and product thermodynamic activities on the net rate of any elementary step in a catalytic sequence [33-36]; the sign of $A_i$ prescribes the direction in which the chemical transformation indicated by that step will occur. The net rate of each elementary step is then given by Eqs. (6.8)-(6.10) in terms of the approach to equilibrium parameter for the $i$th step ($\eta_i$) as:

$$r_i = \vec{r}_i \left( 1 - \frac{1}{K_i \prod_j a_j^{-\nu_j}} \right) = \vec{r}_i \left( 1 - \eta_i \right). \tag{6.12}$$

The value of $\eta_i$ approaches zero far away from equilibrium and unity as a step reaches equilibrium.

Catalytic reactions occur, however, via a sequence of elementary steps that form reactive intermediates on active sites, transform them chemically, and ultimately desorb them as products to regenerate sites for subsequent turnovers. The pseudo-steady-state hypothesis (PSSH) for all adsorbed species requires that the net rate of each elementary step be related to that of the overall reaction ($r$) by:

$$\vec{r}_i - \overleftarrow{r}_i = \sigma_i \left( \vec{r} - \overleftarrow{r} \right) = \sigma_i r, \tag{6.13}$$

in which $\sigma_i$ is the stoichiometric number for step $i$, defined as the number of times it must occur to complete one catalytic turnover. Applying Eq. (6.9) to each elementary step in a catalytic sequence allows the De Donder formalism to be extended from elementary steps to single path catalytic sequences [36]:

$$\frac{\vec{r}}{\overleftarrow{r}} = \frac{\prod \vec{r}_i}{\prod \overleftarrow{r}_i} = \exp\left( \sum A_i / RT \right) = \exp\left( A / \bar{\sigma} RT \right), \tag{6.14}$$

where $A$ represents the chemical affinity for the overall reaction sequence:

$$A = \sum_i \sigma_i A_i, \tag{6.15}$$

and $\bar{\sigma}$ is an affinity-averaged stoichiometric number for the catalytic sequence:

$$\bar{\sigma} = \sum_i \sigma_i A_i \Big/ \sum_i A_i. \tag{6.16}$$

The fact that elementary steps are reversible (Eq. (6.9)) implies that a single path catalytic sequence must also occur in both forward and reverse directions at the respective rates given by Eq. (6.14), *at a given set of reaction conditions (T, $P_j$)*. Moreover, forward ($\vec{k}$) and reverse ($\overleftarrow{k}$) rate constants must be related to the equilibrium constant ($K_R$) for the overall reaction [36] by:

$$\vec{k} / \overleftarrow{k} = K_R^{1/\bar{\sigma}}. \tag{6.17}$$

When all kinetically-relevant steps in a catalytic sequence have stoichiometric numbers of unity, as is the case for hydrogenation-dehydrogenation reactions (Scheme 6.1), Eqs. (6.14)

and (6.17) become indistinguishable from those derived for a single elementary step, irrespective of the concentrations of reactants and products relative to their equilibrium values.

### *6.3.4 Mechanistic Connections Between Alkane Dehydrogenation and Alkene Hydrogenation*

The application of Eq. (6.14) to the alkane dehydrogenation sequence in Scheme 6.1 and with forward and reverse rates for elementary steps given by the law of mass action results in:

$$\frac{\overrightarrow{r_D}}{\overleftarrow{r_H}} = \frac{\overrightarrow{r_1}\overrightarrow{r_2}\overrightarrow{r_3}\overrightarrow{r_4}\overrightarrow{r_5}}{\overleftarrow{r_1}\overleftarrow{r_2}\overleftarrow{r_3}\overleftarrow{r_4}\overleftarrow{r_5}} = \frac{k_1 a_{RH_2(g)} k_2 a_{RH_2(z)} a_{H^+Z^-} k_3 a_{RH^+Z^-} k_4 a_{R(z)} k_5 a_{H_2(z)}}{k_{-1} a_{RH_2(z)} k_{-2} a_{RH^+Z^-} a_{H_2(z)} k_{-3} a_{R(z)} a_{H^+Z^-} k_{-4} a_{R(g)} k_{-5} a_{H_2(g)}} . \tag{6.18}$$

The thermodynamic activity of any given surface intermediate appearing in the forward and reverse rate expressions in Eq. (6.18) is identical for a fixed set of reaction conditions (T, $P_j$). These terms cancel in such cases, and replacing activities for ideal gases with pressures results in:

$$\frac{\overrightarrow{r_D}}{\overleftarrow{r_H}} = \frac{k_1 P_{RH_2} k_2 k_3 k_4 k_5}{k_{-1} k_{-2} k_{-3} k_{-4} P_R k_{-5} P_{H_2}} . \tag{6.19}$$

The isolation of dehydrogenation and hydrogenation rate parameters in the numerator and denominator, respectively, then gives:

$$\frac{\overrightarrow{r_D}}{\overleftarrow{r_H}} = \frac{K_1 k_2 P_{RH_2}}{k_{-2} K_3^{-1} K_4^{-1} K_5^{-1} P_R P_{H_2}} = \frac{k_{meas,D} P_{RH_2}}{k_{meas,H} P_R P_{H_2}} . \tag{6.20}$$

Thus, the ratio of measured rate constants for alkane dehydrogenation ($k_{meas,D}$) and alkene hydrogenation ($k_{meas,H}$), as given by Eq. (6.20), equals the equilibrium constant for the interconversion of the gaseous molecules, as given by Eq. (6.17), but only when the surface coverage of each species is identical in both directions. This requirement is rigorously met *only for a fixed set of reaction conditions (T, $P_j$)*, however, the reaction rate in the direction opposing equilibrium cannot be measured directly in such cases.

Turnover rates for monomolecular propane dehydrogenation and bimolecular propene hydrogenation were measured at different pressures so as to ensure unidirectional reactions in their respective directions ($\eta_i < 0.001$). Propene hydrogenation rates depend linearly on both $C_3H_6$ and $H_2$ pressures (Fig. 6.3), consistent with the rate expression derived when propoxide formation (Step 3, Scheme 6.1) is quasi-equilibrated but inconsistent with the zero-order $H_2$ dependence in the expression derived when step 2 (Scheme 6.1) is assumed to be quasi-equilibrated instead (derivation in Section 6.6). The mean value of $k_{meas,D}/k_{meas,H}$ at 748 K for all zeolites tested is $0.017 \pm 0.001$ bar (Table 6.2), which is identical, within experimental accuracy, to the equilibrium constant ($K_R$) for the stoichiometric propane dehydrogenation reaction at 748 K (0.017 bar; Section 6.7.2, Supporting Information). This remarkable agreement is consistent

with Eq. (6.17) for $\overline{\sigma}$=1 (evident from the elementary steps in Scheme 6.1), as if stoichiometric dehydrogenation-hydrogenation reactions behaved as a single elementary step.

This thermodynamic consistency between alkane dehydrogenation and alkene hydrogenation rate constants and equations persists at all temperatures (718-778 K; Fig. 6.5), but it is not rigorously required in this case, because De Donder relations apply only when forward and reverse reactions are carried out at the same reactant and product pressures. The ratio of propane dehydrogenation and propene hydrogenation rates, when measured at different conditions (denoted by subscripts *A* and *B*, respectively) and when alkoxide desorption and formation (Step 3, Scheme 6.1) is quasi-equilibrated, is given by (derivation in Section 6.6):

$$\frac{\left(\overrightarrow{r_D}\right)_A}{\left(\overleftarrow{r_H}\right)_B} = \frac{k_{meas,D}\left(P_{RH_2}\right)_A\left(c_{H^+Z^-}\right)_A}{k_{meas,H}\left(P_{H_2}\right)_B\left(P_R\right)_B\left(c_{H^+Z^-}\right)_B}. \tag{6.21}$$

This equation reduces to that describing a fixed set of reaction conditions (Eq. (6.20)) *only* when unoccupied $H^+$ sites are the most abundant species at the different reaction conditions used to measure forward and reverse rates, which is the case for the high temperatures and low hydrocarbon pressures used in this study. Thus, the persistent relevance of the De Donder relation beyond its intended scope reflects a unique situation in which different conditions for forward and reverse catalytic reactions preserve the identity of a *single* most-abundant surface intermediate and of a *single* kinetically-relevant step, which must be unoccupied $H^+$ sites and step 2 (Scheme 6.1), respectively, for the dehydrogenation-hydrogenation reactions described in this study (Section 6.6). In such cases, forward and reverse directions of the kinetically-relevant step, and consequently of a multi-step chemical reaction sequence even far away from equilibrium, must obey the principle of microscopic reversibility. This unique situation, not all that infrequent in heterogeneous catalysis, allows the rigorous prediction of the rate in one direction from thermodynamic data and the rate in the opposite direction by using Eq. (6.17), for any active site or catalyst, irrespective of its reactivity or structure.

Measured activation barriers for monomolecular propane dehydrogenation (Eq. (6.3)) and for propene hydrogenation (Eq. (6.6)) depend on zeolite channel structure because they each reflect enthalpy differences between the same transition state (Step 2, Scheme 6.1) solvated by channel environments and their respective reactants in the extrazeolitic gas phase. The difference between $E_{meas,D}$ and $E_{meas,H}$ on a given site is:

$$E_{meas,D} - E_{meas,H} = \Delta H^\circ_{C_3H_6(g)} + \Delta H^\circ_{H_2(g)} - \Delta H^\circ_{C_3H_8(g)} = \Delta H_R{}^\circ_{(g)}, \tag{6.22}$$

in which the enthalpy of the bare proton and of the transition state cancel rigorously. The differences between measured $E_{meas,D}$ and $E_{meas,H}$ are very similar on all zeolites ($127 \pm 8$ kJ mol$^{-1}$; Table 6.3) and identical, within experimental accuracy, to the enthalpy for the stoichiometric propane dehydrogenation reaction ($\Delta H_{R(g)}$ = 129 kJ mol$^{-1}$; Section 6.7.2, Supporting Information), consistent with the relation expected (Eq. (6.22)) when the same elementary step (Step 2, Scheme 6.1) is kinetically-relevant in both forward and reverse directions.

Theoretical studies indicate that monomolecular alkane dehydrogenation requires late transition states, with a nearly full positive charge localized at the alkyl cations and activation barriers that reflect predominantly electrostatic interactions of the fully-formed ion-pairs [6,7,37,38]. We conclude from the thermodynamic consistency of the rate parameters for monomolecular alkane dehydrogenation and alkene hydrogenation that they occur via a common transition state, however, the initial carbonium-ions formed in these two reactions are likely to differ in structure (as depicted qualitatively in Scheme 6.2). This requires, in turn, that the incipient $(C\text{-}H\text{-}H)^+$ carbonium-ions formed in forward and reverse directions of step 2 (Scheme 6.1) interconvert via rotations that involve kinetically-insignificant energy barriers, which has been shown by theory for the cationic intermediates and transition states involved in hydride transfer and dehydrogenation reactions of hydrocarbons on heteropolyacids [39,40]. These data and interpretations provide the first experimental evidence for the facile rotation of cationic species at transition states, which appears to be ubiquitous in catalysis on solid acids.

The reaction coordinate for the overall catalytic reaction contains free energy barriers for the other elementary steps in Scheme 6.1, but they are small enough in both directions to make these steps quasi-equilibrated. As a consequence, monomolecular alkane dehydrogenation and alkene hydrogenation reactions proceed via the same kinetically-relevant transition state and differences in their measured activation energies merely reflect the enthalpy for the overall chemical reaction (Eq. (6.22)). This relation between activation energies in the forward and reverse direction and the reaction enthalpy (shown in Scheme 6.2) holds rigorously for any elementary step, but is unexpected in general for rates and barriers arising from the sequence of elementary steps required to complete a catalytic turnover. These same arguments apply for differences in measured activation entropies for the catalytic reaction in forward and reverse directions, which causes differences between $\Delta S_{meas,D}$ and $\Delta S_{meas,H}$ on all zeolites tested ($134 \pm 11$ J mol$^{-1}$ K$^{-1}$; Table 6.3) to equal, within experimental error, the gas-phase reaction entropy for propane dehydrogenation ($\Delta S_{R(g)}$ = 138 J mol$^{-1}$ K$^{-1}$; Section 6.7.2, Supporting Information) because the transition state entropy also cancels when evaluating this difference:

$$\Delta S_{meas,D} - \Delta S_{meas,H} = \Delta S^{\circ}_{C_3H_6(g)} + \Delta S^{\circ}_{H_2(g)} - \Delta S^{\circ}_{C_3H_8(g)} = \Delta S_{R}{}^{\circ}{}_{(g)}\,. \tag{6.23}$$

Temperature effects on $k_{meas,D}/k_{meas,H}$ ratios depend only on the thermodynamics of the overall reaction (Eq. (6.22); Fig. 6.5); therefore, they must be identical on all catalysts, irrespective of the structure or reactivity of the active sites or of any confinement effects provided by the spatial constraints within zeolite structures, as long as $H^+$ remains the single MASI and step 2 (Scheme 6.1) remains the sole kinetically-relevant step at the different conditions used to measure forward and reverse reaction rates. As a result, the rate of the reverse reaction at any given temperature and at any reactant and product concentrations can be determined rigorously from the rate of the forward reaction determined at that temperature but at different reactant concentrations. In the same manner, activation energies and entropies for a reaction can be estimated accurately from thermodynamic data and their values for the reaction in the opposite direction, as long as these requirements are met, as they are in this case for propane-propene interconversions.

*6.3.5 Preferences of Mechanistically-Related Paths for Specific Intrazeolite Locations*

Each elementary step occurring on acid sites in zeolites, and on catalytic sites in general, must proceed via a single reversible barrier and thus via identical transition states in its forward and reverse directions. As a result, an active site that preferentially catalyzes a given elementary step by stabilizing its transition state must also do so with equal preference and to the same extent in the reverse direction. This must also be true, by extension, for entire catalytic sequences even away from equilibrium at fixed reaction conditions (T, $P_j$) as indicated by Eq. (6.20), and even at different reaction conditions as long as the kinetically-relevant step remains the same and unoccupied sites are the most abundant surface species, as indicated by Eq. (6.21). In contrast, when surfaces are predominantly covered by species other than empty sites at the different reaction conditions used for the forward and reverse directions of a catalytic sequence, the coverage of intermediates is given by terms of different magnitude in the respective denominators of the forward and reverse rate expressions, which therefore do not cancel in the ratio of forward and reverse rates; in such cases (e.g., $NH_3$ synthesis and decomposition [41]), surfaces that preferentially catalyze the reaction in the forward direction do not necessarily do so in the reverse direction.

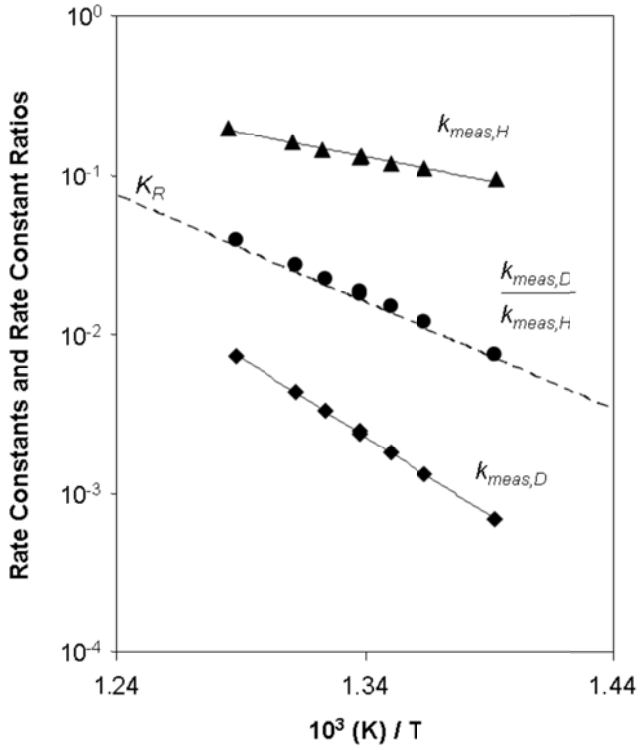


**Figure 6.5.** Rate constants for monomolecular propane dehydrogenation ($k_{meas,D}$; mol (mol $H^+$) $s^{-1}$ (bar $C_3H_8$)$^{-1}$; ◆) and propene hydrogenation ($k_{meas,H}$; mol (mol $H^+$) $s^{-1}$ (bar $C_3H_6$)$^{-1}$ (bar $H_2$)$^{-1}$; ▲) and their ratio ($k_{meas,D}/k_{meas,H}$ bar; ●) from 718-778 K on $H_{100}Na_0$-MOR-T. The equilibrium constant for the gas-phase reaction ($K_R$; bar) is given by the dashed line.

A given catalytic solid contains a range of active sites differing in structure, binding properties and spatial environment, and therefore also in catalytic reactivity, even for regular crystalline materials such as zeolites. As a result, turnover rates for monomolecular alkane activation differ among protons present at different locations within a given zeolite (e.g. 8-member and 12-member rings in H-MOR) [2,3], and the ensemble-averaged reactivity of protons in a given zeolite also varies with channel structure (e.g. H-FER, H-MFI, H-MOR) [2,42]. Thus, it seems reasonable to conclude that the aforementioned irrelevance of the catalyst identity for $k_{meas,D}/k_{meas,H}$ ratios and their exclusive thermodynamic origins can be extended to sites of different reactivity within a given catalyst. If indeed so, site properties that affect reactivity would do so with the exact proportional effects on the rates of the forward and reverse reaction, even when the rates for these reactions are measured at different conditions and each far away from its respective equilibrium, as long as such conditions preserve the identity of the single MASI (unoccupied $H^+$) and the single kinetically-relevant step (Step 2, Scheme 6.1).

Turnover rates for the monomolecular cracking and dehydrogenation of linear ($C_3H_8$, n-$C_4H_{10}$) [2] and branched (i-$C_4H_{10}$) [3] alkanes are significantly larger on protons located within eight-membered ring (8-MR) pockets in H-MOR than on protons with similar acid strength [43] but present within larger and more accessible 12-MR channels. The required transition states for alkane protonation at C-C and C-H bonds (Step 2, Scheme 6.1) are confined only partially within the shallow 8-MR pockets, leading to structures with higher entropy and lower free energy and to rate constants significantly larger on 8-MR than 12-MR protons for both dehydrogenation and cracking reactions [2]. Alkene hydrogenation proceeds via the same kinetically-relevant step and transition state as monomolecular alkane dehydrogenation; thus, hydrogenation turnover rates must also be larger, to the same exact extent, on 8-MR than on 12-MR protons in H-MOR.

**Table 6.4.** Rate constants for monomolecular propane dehydrogenation ($k_{meas,D}$; mol (mol $H^+$)$^{-1}$ $s^{-1}$ (bar $C_3H_8$)$^{-1}$) and for propylene hydrogenation ($k_{meas,H}$; mol (mol $H^+$)$^{-1}$ $s^{-1}$ (bar $C_3H_6$)$^{-1}$ (bar $H_2$)$^{-1}$) at 748 K on 8-MR and 12-MR $H^+$ of MOR.

| Rate Constant | 8-MR $H^+$ | 12-MR $H^+$ | 8-MR $H^+$ / 12-MR $H^+$ |
|---|---|---|---|
| $k_{meas,D}$[a] | 0.0036 ± 0.0004 | n.d.[b] | >10[c] |
| $k_{meas,H}$[a] | 0.20 ± 0.03 | n.d.[b] | >17[c] |
| $k_{meas,D}$ / $k_{meas,H}$ | 0.018 ± 0.004 | n.d.[b] | |

[a] Rate constants determined by linear regression methods (Section 5.7.3, Supporting Information).
[b] n.d., not detected.
[c] Lower bounds on 8-MR-to-12-MR rate constant ratios determined by assuming maximum values for 12-MR rate constants were upper bounds of confidence intervals containing one standard deviation, because 12-MR rate constants were undetectable, within the accuracy of regression.

Infrared spectral band deconvolution methods (Section 6.7.3, Supporting Information) showed that H-MOR samples of varying provenance or extent of $Na^+$ exchange contain very different distributions of protons between 8-MR side pockets (0.10-0.80 fraction; Table 6.1) and 12-MR channels [2]. As in the case of propane dehydrogenation, rate constants for propene hydrogenation (per total $H^+$; 748 K; Fig. 6.6) increased linearly as the fraction of the $H^+$ that reside within 8-MR pockets increased, consistent with the preference of both reactions for 8-MR sites. The contributions of 12-MR sites to both measured propane dehydrogenation and propene hydrogenation turnover rates were negligible (Table 6.4; Section 6.7.3, Supporting Information).

On all MOR zeolites, irrespective of their $H^+$ distribution, the $k_{meas,D}/k_{meas,H}$ ratios were equal to the equilibrium constant (Table 6.2, Fig. 6.7; 748 K) and differences between the measured activation energies and entropies for the dehydrogenation and hydrogenation reactions gave the overall reaction enthalpy and entropy, respectively (Table 6.3). These data are consistent with Eqs. (6.17), (6.22) and (6.23), respectively, and with their requirement that the same elementary step (Step 2, Scheme 6.1) remains the sole kinetically-relevant step and that the unoccupied sites persist as the most abundant surface species at the conditions used for alkane dehydrogenation and alkene hydrogenation reactions. Therefore, Brønsted sites within a given zeolite structure that stabilize transition states more effectively and give higher turnover rates for alkane dehydrogenation (e.g., 8-MR $H^+$ in MOR) also do so for alkene hydrogenation, even at the very different reactant and product concentrations used to measure turnovers rates in the two reaction directions.

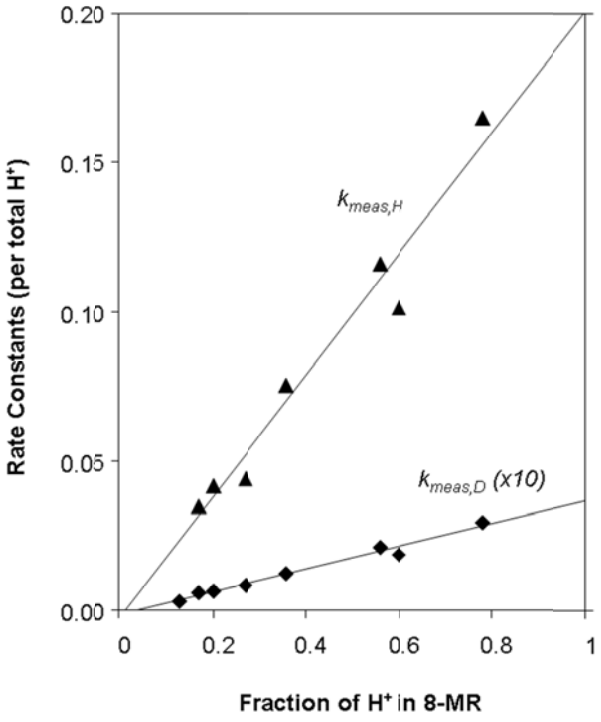


**Figure 6.6.** Dependence of rate constants (per total $H^+$) for monomolecular propane dehydrogenation ($k_{meas,D}$; x10 mol (mol $H^+$) $s^{-1}$ (bar $C_3H_8)^{-1}$; ◆) and propene hydrogenation ($k_{meas,H}$; mol (mol $H^+$) $s^{-1}$ (bar $C_3H_6)^{-1}$ (bar $H_2)^{-1}$; ▲) on the fraction of 8-MR $H^+$ in MOR catalysts.

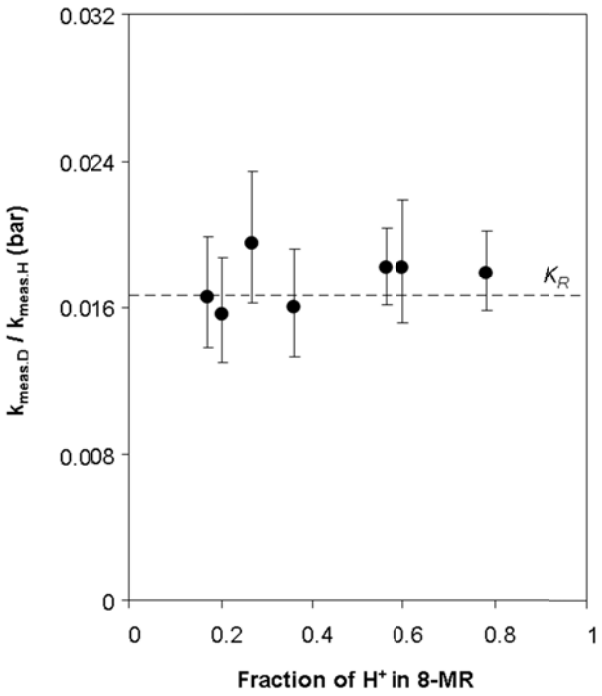


**Figure 6.7.** Dependence of monomolecular propane dehydrogenation-to-propene hydrogenation rate constant ratios ($k_{meas,D}/k_{meas,H}$; bar; ●) at 748 K on the fraction of 8-MR $H^+$ in MOR catalysts. The equilibrium constant for the gas-phase reaction ($K_R$ = 0.017 bar; 748 K) is given by the dashed line.

## 6.4. Conclusions

Brønsted acid sites within zeolite channels catalyze alkane dehydrogenation via monomolecular routes involving $(C\text{-}H\text{-}H)^+$ carbonium-ion-like transition states for kinetically-relevant C-H bond scission steps. The De Donder relations for non-equilibrium thermodynamics indicate that such sites must also catalyze the reverse reaction, alkene hydrogenation with $H_2$, at a fixed set of reaction conditions (T, $P_j$), even away from equilibrium. We show here that propene-$H_2$ reactions on acidic zeolites (H-FER, H-MFI, H-MOR) indeed led to the selective formation of propane, but at reactant and product concentrations that differ from those used for monomolecular alkane dehydrogenation. Moreover, the ratio of rate constants for the forward and reverse reactions was independent of catalyst identity or Brønsted acid site reactivity and depended only on the standard enthalpy and entropy of the overall reaction.

The thermodynamic origin of the ratio of rate constants measured at different conditions, possibly reflecting different mechanisms, most abundant surface intermediates or kinetically-relevant steps, is surprising and not required rigorously by non-equilibrium thermodynamic treatments of reaction rates developed by De Donder and used by Boudart. The fortuitous success of the De Donder equation in enforcing these thermodynamic constraints reflects surfaces that remain predominantly vacant and elementary steps that remain kinetically-relevant at the different conditions used to measure forward and reverse rates. In this case, propene hydrogenation proceeds via elementary steps identical (but reverse) to those required for monomolecular alkane dehydrogenation; these steps involve quasi-equilibrated adsorption of

alkenes to form alkoxides and their reaction with $H_2$ via the same kinetically-relevant $(C\text{-}H\text{-}H)^+$ carbonium-ion-like transition states (Step 2, Scheme 6.1) as required for monomolecular dehydrogenation of alkanes on Brønsted acid sites. Thus, differences in catalytic reactivity among zeolitic materials, which are influenced by confinement, binding energy, and acid strength, must influence to the same proportional extent the rates of the forward and reverse reactions in general, even when the reactant and product concentrations differ in the measurement of the two rates, as long as the conditions required for the De Donder relations to hold are maintained. Within the specific context of zeolite catalysis by Brønsted acids, these concepts can be extended logically to alkylation reactions between alkanes (e.g., $CH_4$, $C_2H_6$) and alkenes (e.g., $C_2H_4$, $C_3H_6$) that proceed via $(C\text{-}C\text{-}H)^+$ carbonium-ion-like transition states [44,45] also involved in monomolecular cracking reactions of linear [2] and branched [3] alkanes.

The ability of $H_2$ to scavenge surface alkoxides directly via hydrogen transfer can guide design and selection strategies for zeolite catalysts that contain Brønsted acid sites, but are devoid of metal or cationic species, for hydrogenation and hydrogen transfer catalysis. These results suggest further that reactions of alkoxides with alkenes in oligomerization reactions can be terminated by hydrogen transfer from $H_2$, in steps analogous to those that transfer hydrogen from alkanes, and at rates that can be estimated from the reverse reaction (alkane dehydrogenation to form the alkoxide species). The incorporation of $H_2$ into Brønsted acid-catalyzed reaction paths indicates its presence during oligomerization, alkylation and cracking processes can influence chain growth selectivities and mitigate the formation of unreactive residues [46,47].

## 6.5 Acknowledgements

The authors acknowledge with thanks financial support from the Chevron Energy Technology Company. We also thank Prof. Matthew Neurock (University of Virginia) for helpful technical discussions.

## 6.6 Appendix: Derivation of Rate Expressions for Alkane Dehydrogenation and Alkene Hydrogenation

### *6.6.1 Temkin Relation for Forward and Reverse Rate Expressions*

The reaction rates in the forward (monomolecular alkane dehydrogenation) and reverse (alkene hydrogenation) directions can be written by considering only steps 2 and 3 in Scheme 6.1, which by themselves comprise a closed sequence and are preceded only by equilibrated steps that relate the activities of the species involved to those in the gas phase, using the following relation [36,48]:

$$\left(\overrightarrow{r_D}\right)_A = \frac{\left(\overrightarrow{r_2}\right)_A \left(\overrightarrow{r_3}\right)_A}{\sigma_2 \left(\overrightarrow{r_3}\right)_A + \sigma_3 \left(\overleftarrow{r_2}\right)_A}, \tag{6.24}$$

$$\left(\overleftarrow{r_H}\right)_B = \frac{\left(\overleftarrow{r_2}\right)_B \left(\overleftarrow{r_3}\right)_B}{\sigma_2 \left(\overrightarrow{r_3}\right)_B + \sigma_3 \left(\overleftarrow{r_2}\right)_B} . \tag{6.25}$$

In these equations, the subscripts *A* and *B* denote the different reaction conditions used to measure rates of dehydrogenation and hydrogenation, respectively. Reaction rates for elementary steps are given by the law of mass action, and Eqs. (6.24) and (6.25) can be rewritten as:

$$\left(\overrightarrow{r_D}\right)_A = \frac{k_2 k_3 \left(a_{RH_2(z)}\right)_A \left(a_{H^+Z^-}\right)_A}{k_3 + k_{-2} \left(a_{H_2(z)}\right)_A}, \tag{6.26}$$

$$\left(\overleftarrow{r_H}\right)_B = \frac{k_{-2} k_{-3} \left(a_{H_2(z)}\right)_B \left(a_{R(z)}\right)_B \left(a_{H^+Z^-}\right)_B}{k_3 + k_{-2} \left(a_{H_2(z)}\right)_B}, \tag{6.27}$$

in which the $a_{RH^+Z^-}$ terms have been cancelled from the numerator and denominator of each equation.

The activity of $H^+$ species ($a_{H^+Z^-}$) can be expressed as the product of their activity coefficient ($\gamma_{H^+Z^-}$) and concentration ($c_{H^+Z^-}$):

$$a_{H^+Z^-} = \gamma_{H^+Z^-} c_{H^+Z^-} . \tag{6.28}$$

We have shown previously [2], using reported adsorption enthalpies and entropies for hydrocarbons on acidic zeolites [49-51], that $H^+$ sites are predominantly unoccupied at the conditions (>700 K, <0.05 bar(hydrocarbon)) relevant for monomolecular alkane dehydrogenation and alkene hydrogenation reactions. In this low coverage limit, both the fractional coverage of and activity coefficients for $H^+$ sites approach unity. Studies of alkane adsorption on acidic zeolites (Si/Al>10) using calorimetry, gravimetry and infrared spectroscopy have shown further that $C_3$-$C_6$ n-alkanes adsorb specifically onto $H^+$ sites with constant adsorption enthalpies, even up to saturation coverages [49-51]. Thus, when framework Al atoms are isolated from each other, as tends to occur when Si/Al>9 in FER, MFI and MOR [52], zeolites behave as Langmuirian ensembles of Brønsted acid sites with uniform binding properties, and in turn, activity coefficients that are independent of surface coverage.

### *6.6.2 Case I: Step 3 is Quasi-Equilibrated*

The assumption of quasi-equilibrium on step 3 results in the following relation:

$$k_3 >> k_{-2} a_{H_2(z)} . \tag{6.29}$$

Eqs. (6.26) and (6.27) can be simplified by using the assumption in Eq. (6.29), by rewriting the activities of $H^+$ using Eq. (6.28), and by relating the activities of intrazeolitic species to gas-phase pressures via steps 1, 4, and 5:

$$\left(\overrightarrow{r_D}\right)_A = K_1 k_2 \left(P_{RH_2}\right)_A \left(\gamma_{H^+Z^-}\right)_A \left(c_{H^+Z^-}\right)_A, \tag{6.30}$$

$$\left(\overleftarrow{r_H}\right)_B = k_{-2} K_3^{-1} K_4^{-1} K_5^{-1} \left(P_R\right)_B \left(P_{H_2}\right)_B \left(\gamma_{H^+Z^-}\right)_B \left(c_{H^+Z^-}\right)_B. \tag{6.31}$$

These rate expressions for monomolecular alkane dehydrogenation and alkene hydrogenation agree with their respective first-order dependences on alkane (Fig. 6.2) and on alkene and $H_2$ pressures (Fig. 6.3). The only rate constants that appear individually and not as a ratio (i.e., an equilibrium constant) in Eqs. (6.30) and (6.31) are for step 2 ($k_2$, $k_{-2}$), indicating that this step, which involves the formation of $(C\text{-}H\text{-}H)^+$ carbonium-ion-like ion-pairs at the transition state, is the sole kinetically-relevant step in both directions. The ratio of forward (Eq. (6.30)) to reverse (Eq. (6.31)) rates, after cancelling $\gamma_{H^+Z^-}$ terms that are independent of coverage, gives:

$$\frac{\left(\overrightarrow{r_D}\right)_A}{\left(\overleftarrow{r_H}\right)_B} = \frac{K_1 k_2 \left(P_{RH_2}\right)_A \left(c_{H^+Z^-}\right)_A}{k_{-2} K_3^{-1} K_4^{-1} K_5^{-1} \left(P_R\right)_B \left(P_{H_2}\right)_B \left(c_{H^+Z^-}\right)_B} = K_R \frac{\left(P_{RH_2}\right)_A \left(c_{H^+Z^-}\right)_A}{\left(P_R\right)_B \left(P_{H_2}\right)_B \left(c_{H^+Z^-}\right)_B}. \tag{6.32}$$

The $c_{H^+Z^-}$ terms in Eq. (6.32) cancel only when surface sites are occupied to the same extent at conditions A and B. This is the case for the range of pressures and temperatures used in this study, which result in $H^+$ sites that are predominantly unoccupied by hydrocarbons, and Eq. (6.32) becomes:

$$\frac{\left(\overrightarrow{r_D}\right)_A}{\left(\overleftarrow{r_H}\right)_B} = K_R \frac{\left(P_{RH_2}\right)_A}{\left(P_R\right)_B \left(P_{H_2}\right)_B}. \tag{6.33}$$

This expression is equivalent to that derived from the De Donder relations (Eq. (6.20)), which apply for a fixed set of reaction conditions, in which case $c_{H^+Z^-}$ values are identical in forward and reverse directions and thus cancel rigorously.

### *6.6.3 Case II: Step 2 is Quasi-Equilibrated*

The following relation holds if, instead, step 2 is quasi-equilibrated:

$$k_{-2} a_{H_2(z)} >> k_3. \tag{6.34}$$

In this case, the rate expressions for alkane dehydrogenation (Eq. (6.26)) and alkene hydrogenation (Eq. (6.27)) simplify to:

$$\left(\overrightarrow{r_D}\right)_A = \frac{K_2 k_3 \left(a_{RH_2(z)}\right)_A \left(a_{H^+Z^-}\right)_A}{\left(a_{H_2(z)}\right)_A}, \tag{6.35}$$

$$\left(\overleftarrow{r_H}\right)_B = k_{-3}\left(a_{R(z)}\right)_B \left(a_{H^+Z^-}\right)_B. \tag{6.36}$$

Expressing $a_{H^+Z^-}$ using Eq. (6.28) and relating the activities of other species to gas-phase pressures via steps 1, 4, and 5 gives:

$$\left(\overrightarrow{r_D}\right)_A = \frac{K_1 K_2 k_3 K_5 \left(P_{RH_2}\right)_A \left(\gamma_{H^+Z^-}\right)_A \left(c_{H^+Z^-}\right)_A}{\left(P_{H_2}\right)_A}, \tag{6.37}$$

$$\left(\overleftarrow{r_H}\right)_B = k_{-3} K_4^{-1} \left(P_R\right)_B \left(\gamma_{H^+Z^-}\right)_B \left(c_{H^+Z^-}\right)_B. \tag{6.38}$$

In these rate expressions, the only rate constants that appear individually are for step 3 ($k_3$, $k_{-3}$), indicating that this step, which corresponds to alkoxide desorption and formation, must be kinetically-relevant in forward and reverse directions. Eqs. (6.37) and (6.38), however, are not supported by the experimental data and the first-order dependence of hydrogenation rates on $H_2$ pressure (Fig. 6.3).

We note, however, that the ratio of Eqs. (6.37) and (6.38), after cancelling $\gamma_{H^+Z^-}$ terms, gives an expression that resembles Eq. (6.32):

$$\frac{\left(\overrightarrow{r_D}\right)_A}{\left(\overleftarrow{r_H}\right)_B} = \frac{K_1 K_2 k_3 K_5 \left(P_{RH_2}\right)_A \left(c_{H^+Z^-}\right)_A}{k_{-3} K_4^{-1} \left(P_{H_2}\right)_A \left(P_R\right)_B \left(c_{H^+Z^-}\right)_B} = K_R \frac{\left(P_{RH_2}\right)_A \left(c_{H^+Z^-}\right)_A}{\left(P_{H_2}\right)_A \left(P_R\right)_B \left(c_{H^+Z^-}\right)_B}. \tag{6.39}$$

The consistency between Eq. (6.39), Eq. (6.32) (derived for step 3 quasi-equilibrated) and Eq. (6.20) (the De Donder relation) reflects solely the fact that the same step is kinetically-relevant in both forward and reverse directions. Eqs. (6.32) and (6.39) are equivalent to Eq. (6.20) only when unoccupied $H^+$ sites are the most abundant species for the different reaction conditions used to obtain kinetic measurements in forward and reverse directions.

## 6.7. Supporting Information

### *6.7.1 Thermochemical Cycle for Monomolecular Alkane Activation on Acidic Zeolites*

Previous studies of monomolecular cracking and dehydrogenation of linear ($C_3H_8$, n-$C_4H_{10}$) [2] and branched (i-$C_4H_{10}$) [3] alkanes showed that measured barriers for dehydrogenation, relative to cracking, are higher for linear alkanes but lower for branched alkanes. Differences in dehydrogenation and cracking activation barriers reflect differences in the gas-phase affinities for protonation of alkane C-H or C-C bonds, respectively, (Fig. 6.8) consistent with thermochemical relations relevant to Brønsted acid catalysis [3]. Here, we review briefly a thermochemical cycle (Scheme 6.3) for monomolecular alkane ($RH_2$) activation on Brønsted acid sites within zeolite channels ($H^+Z^-$) that relates measured activation barriers to reactant and catalyst properties and apply these relations to parallel monomolecular cracking and dehydrogenation paths of the same reactant and within the same zeolite. A more detailed analysis of activation barriers for monomolecular alkane activation using a thermochemical cycle can be found elsewhere [2].

In this thermochemical cycle (Scheme 6.3), measured activation barriers for monomolecular alkane activation ($E_{meas}$) depend on zeolite deprotonation enthalpies (*DPE*), on proton affinities for gaseous alkanes (*PA*), and on transition state stabilization energies ($E_{stab}$):

$$E_{meas} = DPE + PA + E_{stab} \,. \tag{6.40}$$

Measured activation barrier differences for cracking and dehydrogenation of the same alkane on the same zeolite reflect only properties of reactants and transition states, because DPE values cancel rigorously. DPE values for isolated framework Al atoms at various T-sites within a zeolite and even among different zeolites are similar (e.g., 1230-1235 kJ mol$^{-1}$ for the four T-sites in H-MOR) [43]. This reflects the predominant stabilization of $H^+$ by long-range electrostatic interactions with the zeolite framework, suggesting that isolated acid sites in zeolites are approximately uniform in acid strength [43].

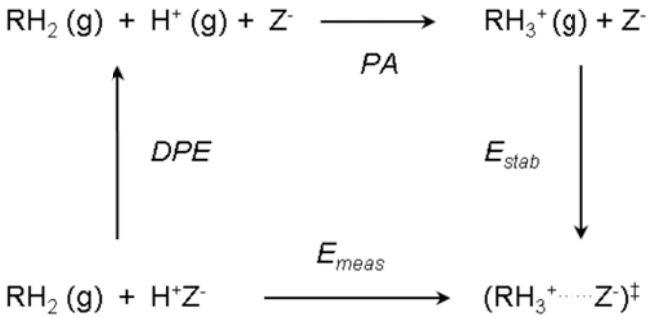


**Scheme 6.3.** A thermochemical cycle for monomolecular alkane ($RH_2$) reactions on zeolitic Brønsted acid sites ($H^+Z^-$) relating measured activation barriers ($E_{meas}$) to zeolite deprotonation enthalpies (*DPE*), gas-phase alkane proton affinities (*PA*) and transition state stabilization energies ($E_{stab}$); adapted from [2,3].

Transition states are stabilized by both electrostatic interactions between the gas-phase cation ($RH_3^+$) and anionic zeolite frameworks ($Z^-$) and van der Waals interactions between the organic cation and zeolite channels. The electrostatic component of this stabilization is similar for the late ion-pairs formed at both monomolecular alkane cracking and dehydrogenation transition states, which contain nearly full positive charges that are localized within the alkyl fragments [6,7,37,38,53]. The van der Waals contacts are also nearly commensurate in monomolecular transition states and adsorbed alkane reactants, which differ in composition by a proton, and are therefore similar for cracking and dehydrogenation transition states that differ primarily in the location of this proton.

Thus, we conclude that differences in activation barriers for alkane cracking and dehydrogenation reflect predominantly enthalpy differences in carbonium ions formed upon protonation at C-C and C-H bonds, respectively, in gas-phase alkanes (Fig. 6.8) [2,3], consistent with monomolecular routes that form carbonium-ion-like transition states within zeolite channels.

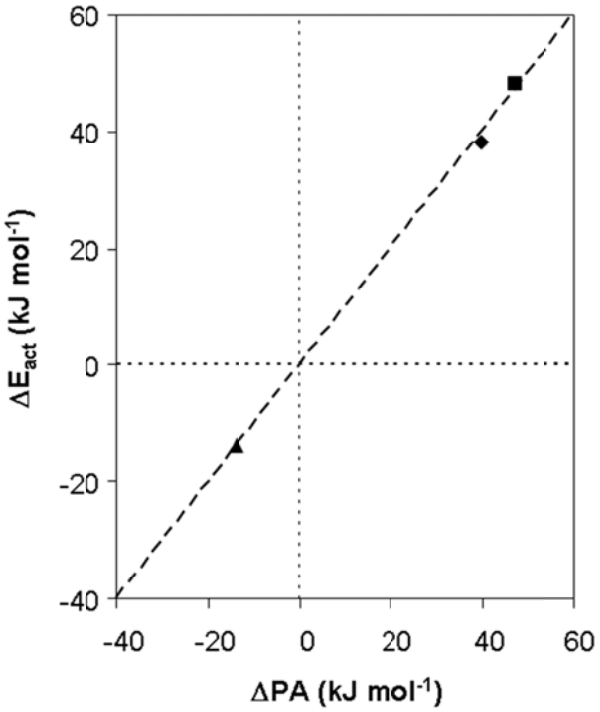


**Figure 6.8.** Relationship between the difference in dehydrogenation and cracking activation barriers ($\Delta E_{meas}$) measured on $H_{100}Na_0$-MOR-Z for propane (◆), *n*-butane (■) and isobutane (▲) and the difference in gas-phase proton affinities of their C-H and C-C bonds ($\Delta PA$); adapted from [3].

*6.7.2 Estimation of Thermochemical Properties of Gas-Phase Reactions*

The reaction enthalpy, entropy and Gibbs free energy change at a given temperature, *T*, for the following gas-phase reaction:

$$C_3H_8 \rightleftarrows C_3H_6 + H_2\,, \tag{6.41}$$

were calculated using thermochemical data [54], the ideal gas assumption, and the following equations:

$$\Delta H_R^{\circ}(T) = \sum_i \nu_i \Delta H_{f,i}^{\circ}(T) = \Delta H_{f,C_3H_6}^{\circ}(T) + \Delta H_{f,H_2}^{\circ}(T) - \Delta H_{f,C_3H_8}^{\circ}(T)\,, \tag{6.42}$$

$$\Delta S_R^{\circ}(T) = \sum_i \nu_i \Delta S_{f,i}^{\circ}(T) = \Delta S_{f,C_3H_6}^{\circ}(T) + \Delta S_{f,H_2}^{\circ}(T) - \Delta S_{f,C_3H_8}^{\circ}(T)\,, \tag{6.43}$$

$$\Delta G_R^{\circ}(T) = \sum_i \nu_i \Delta G_{f,i}^{\circ}(T) = \Delta G_{f,C_3H_6}^{\circ}(T) + \Delta G_{f,H_2}^{\circ}(T) - \Delta G_{f,C_3H_8}^{\circ}(T)\,. \tag{6.44}$$

The dimensionless equilibrium constant, *K*, for this reaction is related to $\Delta G_R^o(T)$:

$$K(T) = \exp(-\Delta G_R^{\circ}(T)/RT) = \frac{a_{C_3H_6} a_{H_2}}{a_{C_3H_8}}\,, \tag{6.45}$$

and the equilibrium constant in pressure units, $K_R$, is given by:

$$K_R(T) = K(T)\left(\frac{P_{C_3H_6}{}^o P_{H_2}{}^o}{P_{C_3H_8}{}^o}\right) = \frac{P_{C_3H_6} P_{H_2}}{P_{C_3H_8}}\left[=\right] bar\,, \tag{6.46}$$

where $P_i^o$ is the standard state pressure of 1 bar.

The following calculations are shown at 748 K as an example:

$$\Delta H_R^{\circ}(748K) = 4.3 + 0 - \left(-124.7\right) = 129 kJ/mol\,, \tag{6.47}$$

$$\Delta S_R^{\circ}(748K) = -177 + 0 - \left(-315\right) = 138 J/molK\,, \tag{6.48}$$

$$\Delta G_R^{\circ}(748K) = 136.4 + 0 - 110.9 = 25.5 kJ/mol\,, \tag{6.49}$$

$$K_R(748K) = \exp\left(-25500/\left(8.3145 * 748\right)\right) = 0.017 bar\,. \tag{6.50}$$

The equilibrium constant for the stoichiometric propane dehydrogenation reaction (Eq. (6.41)), when written in the reverse direction, is given by the inverse of Eq. (6.50):

$$K_R^{-1}(748K) = 60bar^{-1}. \tag{5.51}$$

### *6.7.3 Determination of 8-MR and 12-MR $H^+$ Distribution in MOR and Estimation of Location-Specific Rate Constants*

The infrared spectra of H-MOR samples show an asymmetric OH stretch band (~3550-3650 $cm^{-1}$) arising from the overlapping contribution of Brønsted-acidic Si(OH)Al groups vibrating within 8-MR side pockets (~3592 $cm^{-1}$) and within 12-MR channels (~3611 $cm^{-1}$) [55]. Principal component bands for 8-MR and 12-MR OH groups were obtained using singular value decomposition methods reported previously [55]. The contribution of each pure component to composite OH bands was determined by least-squares regression methods, allowing pure component band centers to shift up to 3 $cm^{-1}$ and assuming identical molar extinction coefficients.

The distribution of sites between 8-MR and 12-MR locations on the MOR samples used in this study varied widely as a result of differing $Na^+$ content and provenance (Table 6.1). The deconvoluted infrared spectra for these samples are reported elsewhere [2,55], along with methods and data used to verify acid site distributions by titration of OH groups with probes of varying size.

Rate constants for propylene hydrogenation measured on a given MOR sample were expressed as the additive contributions of 8-MR ($X_{8\text{-}MR}$) and 12-MR ($X_{12\text{-}MR}$) acid sites, weighed by their respective rate constants ($k_{8\text{-}MR}$, $k_{12\text{-}MR}$):

$$k = k_{8-MR} \cdot X_{8-MR} + k_{12-MR} \cdot X_{12-MR}. \tag{6.52}$$

The location-specific rate constant for propylene hydrogenation at a given temperature was determined by least-squares regression of rate data collected on the seven MOR samples, with uncertainties in regressed rate constants reported as the standard deviation.

## 6.8 References


(1) Haag, W. O.; Dessau, R. M. In *Proc. 8th Int. Congr. Catalysis, Berlin* **1984**; Vol. 2, p 305.
(2) Gounder, R.; Iglesia, E. *J. Am. Chem. Soc.* **2009**, *131*, 1958.
(3) Gounder, R.; Iglesia, E. *Angew. Chem. Int. Ed.* **2010**, *49*, 808.
(4) Narbeshuber, T. F.; Brait, A.; Seshan, K.; Lercher, J. A. *J. Catal.* **1997**, *172*, 127.
(5) Xu, B.; Sievers, C.; Hong, S. B.; Prins, R.; van Bokhoven, J. A. *J. Catal.* **2006**, *244*, 163.
(6) van Santen, R. A.; Kramer, G. J. *Chem. Rev.* **1995**, *95*, 637.
(7) Frash, M. V.; van Santen, R. A. *Top. Catal.* **1999**, *9*, 191.
(8) Blaszkowski, S. R.; van Santen, R. A. *Top. Catal.* **1997**, *4*, 145.
(9) Lercher, J. A.; van Santen, R. A.; Vinek, H. *Catal. Lett.* **1994**, *27*, 91.
(10) Kotrel, S.; Knözinger, H.; Gates, B. C. *Microporous Mesoporous Mater.* **2000**, *35-6*, 11.
(11) Gates, B. C. *Chem. Rev.* **1995**, *95*, 511.
(12) Uzun, A.; Gates, B. C. *J. Am. Chem. Soc.* **2009**, *131*, 15887.
(13) Weber, W. A.; Zhao, A.; Gates, B. C. *J. Catal.* **1999**, *182*, 13.
(14) Choi, M.; Wu, Z. J.; Iglesia, E. *J. Am. Chem. Soc.* **2010**, *132*, 9129.
(15) Zhan, B. Z.; Iglesia, E. *Angew. Chem. Int. Ed.* **2007**, *46*, 3697.
(16) Simon, L. J.; van Ommen, J. G.; Jentys, A.; Lercher, J. A. *Catal. Today* **2002**, *73*, 105.
(17) Minachev, K. M.; Garanin, V. I.; Kharlamov, V. V.; Isakova, T. A. *Kinet. Katal.* **1972**, *13*, 1101.
(18) Kanai, J.; Martens, J. A.; Jacobs, P. A. *J. Catal.* **1992**, *133*, 527.
(19) Heylen, C. F.; Jacobs, P. A.; Uytterhoeven, J. B. *J. Catal.* **1976**, *43*, 99.
(20) Jacobs, P. A.; Uytterhoeven, J. B. *J. Catal.* **1977**, *50*, 109.
(21) Olah, G. A.; Halpern, Y.; Shen, J.; Mo, Y. K. *J. Am. Chem. Soc.* **1971**, *93*, 1251.
(22) Olah, G. A.; Halpern, Y.; Shen, J.; Mo, Y. K. *J. Am. Chem. Soc.* **1973**, *95*, 4960.
(23) Hogeveen, H.; Gaasbeek, C. J.; Bickel, A. F. *Recl. Trav. Chim. Pays-Bas.* **1969**, *88*, 703.
(24) Sano, T.; Hagiwara, H.; Okabe, K.; Okado, H.; Saito, K.; Takaya, H. *Sekiyu Gakkaishi* **1986**, *29*, 89.
(25) Corma, A.; Sánchez, J.; Tomás, F. *J. Mol. Catal.* **1983**, *19*, 9.
(26) Tolman, R. C. *Phys. Rev.* **1924**, *23*, 693.
(27) Tolman, R. C. *Proc. Natl. Acad. Sci.* **1925**, *11*, 436.
(28) Krannila, H.; Haag, W. O.; Gates, B. C. *J. Catal.* **1992**, *135*, 115.
(29) Abbot, J.; Wojciechowski, B. W. *Can. J. Chem. Eng.* **1985**, *63*, 462.
(30) Buchanan, J. S.; Santiesteban, J. G.; Haag, W. O. *J. Catal.* **1996**, *158*, 279.
(31) de Donder, T. *L'Affinité*; Gauthier-Villars: Paris, **1927**.
(32) de Donder, T.; van Rysselberghe, P. *Thermodynamic Theory of Affinity: A Book of Principles*; Stanford University Press: Stanford, **1936**.
(33) Denbigh, K. *The Thermodynamics of the Steady State*; Methuen: London, **1951**.
(34) Dumesic, J. A. *J. Catal.* **1999**, *185*, 496.
(35) Holstein, W. L.; Boudart, M. *J. Phys. Chem. B* **1997**, *101*, 9991.
(36) Boudart, M.; Djéga-Mariadassou, G. *Kinetics of Heterogeneous Catalytic Reactions*; Princeton University Press: Princeton, **1984**.
(37) Rigby, A. M.; Kramer, G. J.; van Santen, R. A. *J. Catal.* **1997**, *170*, 1.
(38) Kazansky, V. B.; Frash, M. V.; van Santen, R. A. *Appl. Catal. A* **1996**, *146*, 225.
(39) Janik, M. J.; Davis, R. J.; Neurock, M. *J. Catal.* **2006**, *244*, 65.
(40) Janik, M. J.; Davis, R. J.; Neurock, M. *Catal. Today* **2006**, *116*, 90.

(41) Boisen, A.; Dahl, S.; Nørskov, J. K.; Christensen, C. H. *J. Catal.* **2005**, *230*, 309.
(42) Bhan, A.; Iglesia, E. *Acc. Chem. Res.* **2008**, *41*, 559.
(43) Brändle, M.; Sauer, J. *J. Am. Chem. Soc.* **1998**, *120*, 1556.
(44) Olah, G. A.; Felberg, J. D.; Lammertsma, K. *J. Am. Chem. Soc.* **1983**, *105*, 6529.
(45) Siskin, M. *J. Am. Chem. Soc.* **1976**, *98*, 5413.
(46) Meusinger, J.; Liers, J.; Mosch, A.; Rescheitilowski, W. *J. Catal.* **1994**, *148*, 30.
(47) Meusinger, J.; Corma, A. *J. Catal.* **1995**, *152*, 189.
(48) Temkin, M. I. *Adv. Catal.* **1979**, *28*, 173.
(49) Eder, F.; Stockenhuber, M.; Lercher, J. A. **1997**, *101*, 5414.
(50) Eder, F.; Lercher, J. A. *J. Phys. Chem. B* **1997**, *101*, 1273.
(51) Eder, F.; Lercher, J. A. *Zeolites* **1997**, *18*, 75.
(52) Barthomeuf, D. *Mater. Chem. Phys.* **1987**, *17*, 49.
(53) Zygmunt, S. A.; Curtiss, L. A.; Zapol, P.; Iton, L. E. *J. Phys. Chem. B* **2000**, *104*, 1944.
(54) Stull, D. R.; Westrum, E. F.; Sinke, G. C. *The Chemical Thermodynamics of Organic Compounds*; John Wiley & Sons, Inc.: New York, **1987**.
(55) Bhan, A.; Allian, A. D.; Sunley, G. J.; Law, D. J.; Iglesia, E. *J. Am. Chem. Soc.* **2007**, *129*, 4919.

# CHAPTER SEVEN

# Catalytic Alkylation Routes via Carbonium-Ion-Like Transition States on Acidic Zeolites

## 7.1 Results and Discussion

Brønsted acid sites in zeolites catalyze alkene hydrogenation with $H_2$ via the same kinetically-relevant $(C\text{-}H\text{-}H)^+$ carbonium-ion-like transition states as those involved in monomolecular alkane dehydrogenation [1]. $C_3H_6$-$H_2$ reactions selectively form $C_3H_8$ (>80% carbon basis) at high $H_2/C_3H_6$ ratios (>2500) and temperatures (>700 K) [1]. Ratios of $C_3H_8$ dehydrogenation to $C_3H_6$ hydrogenation rate constants (718-778 K) were identical on H-FER, H-MFI and H-MOR zeolites and equal to the equilibrium constant for the stoichiometric gas-phase reaction, consistent with De Donder non-equilibrium thermodynamic treatments of chemical reaction rates [2-4]. The seemingly fortuitous extension of the principle of microscopic reversibility [5,6] and the De Donder relations beyond their rigorous descriptions of chemical reaction dynamics at equilibrium and far from equilibrium but at identical ($T$, $P_j$), respectively, reflect the persistence of the same single kinetically-relevant step and the prevalence of unoccupied $H^+$ sites at the very different conditions used to measure forward and reverse rates [1].

By inference, larger alkanes should also form via direct alkene-alkane addition steps via the same $(C\text{-}C\text{-}H)^+$ *carbonium-ion-like transition states* involved in monomolecular alkane cracking. These chemical processes differ from alkylation mechanisms prevalent on liquid and solid acids (e.g. HF, $H_2SO_4$, H-zeolites) and superacids (e.g., HF-$SbF_5$, HF-$TaF_5$), which are mediated by *carbenium-ion chain carriers* that terminate as alkanes via hydride transfer [7]. Carbonium-ions contain three-atom/two-electron centers [8,9] and have been posited to mediate the formation of $C_3H_8$ in reactions of $CH_4$-$C_2H_4$ mixtures on superacids at the low temperatures (<573 K) required for favorable alkylation thermodynamics [10-13]. Here, we provide definitive kinetic and isotopic evidence that catalytic $CH_4$-$C_2H_4$ alkylation reactions occur via the same transition states involved in monomolecular alkane cracking, even on zeolitic Brønsted acid sites at high temperatures (>700 K).

Monomolecular alkane cracking routes prevail at high temperatures and low concentrations of alkene products; they involve late $(C\text{-}C\text{-}H)^+$ carbonium-ion-like transition states in kinetically-relevant C-C bond cleavage steps and unoccupied $H^+$ sites as most abundant surface intermediates (MASI) [8,9,14-18]. Minority species adsorbed on $H^+$ sites are in quasi-equilibrium with gas phase reactants and products, leading to monomolecular $C_3H_8$ cracking rates given by:

$$\vec{r_c} = K_1 k_2 P_{C_3H_8} = k_{meas,c} P_{C_3H_8}, \tag{7.1}$$

where $K_1$ is the equilibrium constant for intrazeolite $C_3H_8$ adsorption and $k_2$ is the rate constant for the elementary step that forms $C_2H_5^+Z^-$ and $CH_4$ via $(C_3H_9)^+$ transition states (Scheme 7.1).

Measured monomolecular cracking rate constants ($k_{meas,c}$) reflect free energy differences between these transition states, stabilized within zeolite voids, and reactants in the gas phase (derivation and data in Section 7.4.1, Supp. Info.). As a result, rates are influenced by solvation effects that depend on spatial constraints characteristic of specific zeolite structures (Table 7.1; FER, MFI, MOR) [18].

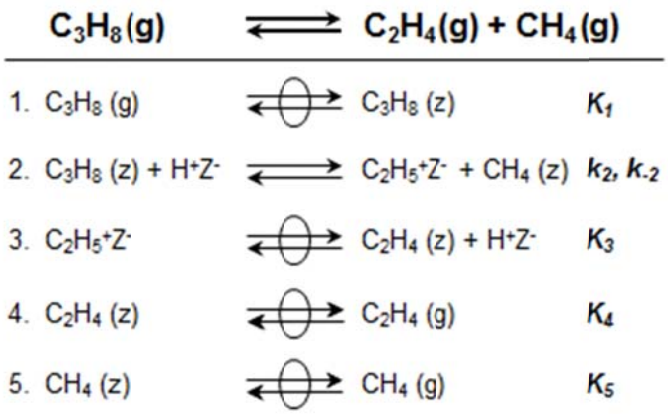


**Scheme 7.1.** Catalytic cycle for monomolecular $C_3H_8$ cracking and $CH_4$-$C_2H_4$ alkylation on Brønsted acid sites ($H^+Z^-$) within zeolites. Species are in the gas phase (g), chemically-bound to oxygens at framework Al sites ($Z^-$), and physisorbed within zeolite channels near acid sites (z). Stoichiometric numbers ($\sigma$) are shown for each elementary step.

**Table 7.1.** Rate constants for monomolecular $C_3H_8$ cracking ($k_{meas,c}$), $CH_4$-$C_2H_4$ alkylation ($k_{meas,alk}$) and $C_2H_4$ dimerization ($k_{meas,dim}$), and rate constant ratios on H-zeolites at 748 K.

| Zeolite | $k_{meas,c}$ (x $10^3$)[a] | $k_{meas,alk}$ (x $10^4$)[b] | $k_{meas,dim}$[c] | $k_{meas,c}$ / $k_{meas,alk}$ (bar) | $k_{meas,alk}$ (x $10^4$) / $k_{meas,dim}$ |
|---|---|---|---|---|---|
| H-FER | 6.4 | 2.1 | 0.48 | 31 ± 6 | 4.3 ± 0.9 |
| H-MFI | 9.2 | 3.8 | 0.99 | 24 ± 5 | 3.8 ± 0.8 |
| H-MOR-56 | 1.4 | 0.55 | 0.63 | 26 ± 5 | 1.2 ± 0.2 |

[a] mol (mol $H^+$)$^{-1}$ $s^{-1}$ (bar $C_3H_8$)$^{-1}$

[b] mol (mol $H^+$)$^{-1}$ $s^{-1}$ (bar $C_2H_4$)$^{-1}$ (bar $CH_4$)$^{-1}$

[c] mol (mol $H^+$)$^{-1}$ $s^{-1}$ (bar $C_2H_4$)$^{-2}$

Rates of the reverse reaction, in which $CH_4$ and $C_2H_4$ react to form $C_3H_8$, were first-order in $CH_4$ and $C_2H_4$ pressures (Fig. 7.1; 748 K; H-MFI) on all zeolites (data in Section 7.4.2, Supp. Info.); no conversion was detected with $CH_4$ as the sole reactant. This kinetic behavior is consistent with Scheme 7.1 when steps 3-5 are quasi-equilibrated and $H^+$ sites are the MASI:

$$\overleftarrow{r_{alk}} = k_{-2}K_3^{-1}K_4^{-1}K_5^{-1}P_{C_2H_4}P_{CH_4} = k_{meas,alk}P_{C_2H_4}P_{CH_4} . \quad (7.2)$$

Here, $k_{-2}$ is the rate constant for the formation of $C_3H_8$ via $(C_3H_9)^+$ transition states and $K_3$, $K_4$, and $K_5$ are the equilibrium constants that relate intrazeolite $CH_4$, $C_2H_4$ and $C_2H_5^+Z^-$ concentrations to $CH_4$ and $C_2H_4$ pressures. As for cracking ($k_{meas,c}$), measured rate constants for alkylation ($k_{meas,alk}$) depend on zeolite structure (Table 7.1), which stabilizes transition states but

not gaseous reactants (derivation and data in Section 7.4.2, Supp. Info.). The $k_{meas,c}/k_{meas,alk}$ ratios, *however*, were the same (within experimental error) on H-FER, H-MFI and H-MOR-56 (24-31 bar; 748 K; Table 7.1) and were equal to the equilibrium constant for the gas-phase reaction in Scheme 7.1 ($K_{R1}$ = 26 bar; 748 K; calculation in Section 7.4.3, Supp. Info.).

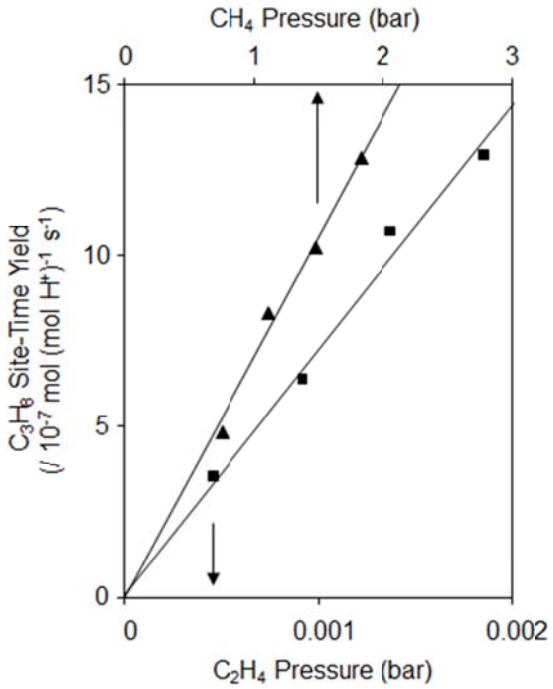


**Figure 7.1.** Dependence of $C_3H_8$ synthesis rates (748 K) on $C_2H_4$ pressure (■; P($CH_4$) = 1.8 bar) and $CH_4$ pressure (▲; P($C_2H_4$) = 0.002 bar) on H-MFI.

Rate constants in forward ($\vec{k}$) and reverse ($\overleftarrow{k}$) directions of a single-path catalytic sequence, at the same thermodynamic activities of all species (i.e. fixed ($T$, $P_j$)), are related to the equilibrium constant for the overall reaction ($K_R$) and the affinity-averaged stoichiometric number ($\overline{\sigma}$ = 1 in Scheme 7.1) by De Donder relations [4]:

$$\vec{k}/\overleftarrow{k} = K_R^{1/\overline{\sigma}}. \tag{7.3}$$

The strict adherence of $\vec{k}$ and $\overleftarrow{k}$ to Eq. (7.3) when the two parameters are measured at *different conditions ($T$, $P_j$)*, however, is not required *unless* the same single elementary step (Step 2, Scheme 7.1) is kinetically-relevant in both directions and the active sites ($H^+$) are predominantly unoccupied at the different reaction conditions (derivation in Section 7.4.4, Supp. Info.) [1]. Thus, the agreement between $k_{meas,c}/k_{meas,alk}$ ratios among all samples (Table 7.1) and their numerical equivalence with $K_{R1}$ indicate that the same kinetically-relevant $(C\text{-}C\text{-}H)^+$ transition state (Step 2, Scheme 7.1) mediates monomolecular alkane cracking and alkane-alkene alkylation reactions, even though the reactant configurations required to form this transition state are quite different in the two directions. In turn, the cations formed incipiently in either direction

differ in structure and orientation, but they must access the same transition state via kinetically-insignificant conformational changes to give transition state free energies (reflected in $k_{meas,c}$ and $k_{meas,alk}$) that are measured with respect to gaseous reactants. These effects are consistent with the facile rotation of cationic species formed during acid-catalyzed hydrocarbon reactions, as shown by theoretical studies [19,20] and as found for alkane dehydrogenation-alkene hydrogenation [1].

Propane formation via paths other than that in Scheme 7.1 (e.g., H-transfer between $CH_4$ and propoxides formed from $C_2H_4$ oligomerization-cracking cycles) may also occur at rates proportional to $CH_4$ pressure, but would require an implausible coincidence of rate constants for monomolecular $C_3H_8$ cracking and the mechanistically-unrelated step so as to give ratios equal to the $C_3H_8$ cracking equilibrium constant. These alternate paths are also ruled out by the isotopologues formed in $^{13}CH_4$-$^{12}C_2H_4$ reactions (Table 7.2; H-MFI; 748 K). $C_3H_8$ molecules predominantly contain one $^{13}C$-atom (91%) and the $C_3H_6$ molecules formed are predominantly unlabeled (88%) and reflect oligomerization-cracking reactions of $^{12}C_2H_4$. These isotopologue distributions, taken together with the linear dependence of $C_3H_8$ synthesis rates on $CH_4$ and $C_2H_4$ pressures and the agreement between $k_{meas,c}/k_{meas,alk}$ ratios and $K_{R1}$ (Table 7.1, Eq. (7.3)) constitute clear and rigorous evidence for direct $CH_4$-$C_2H_4$ alkylation via carbonium-ion-like transition states.

**Table 7.2.** Product isotopologues formed from $^{13}CH_4$-$^{12}C_2H_4$ reactions on H-MFI at 748 K.

| Product | Mole Fraction | | | |
|---|---|---|---|---|
| | *0* $^{13}C$ | *1* $^{13}C$ | *2* $^{13}C$ | *3* $^{13}C$ |
| $C_3H_8$ | 0.09 | 0.91 | 0 | 0 |
| $C_3H_6$ | 0.88 | 0.12 | 0 | 0 |

Reactions of $CH_4$-$C_2H_4$ mixtures on acidic zeolites form $C_3H_8$ as the predominant product only at high $CH_4/C_2H_4$ ratios (>3000; Fig. 7.2); $C_3$, $C_4$ and $C_6$ alkenes are also formed (Fig. 7.2), but with a total selectivity that decreases with increasing $CH_4/C_2H_4$ ratios (data in Section 7.4.2, Supp. Info.). These trends reflect competitive reactions of ethoxides (Scheme 7.2) with $CH_4$ (alkylation to form $C_3H_8$) and $C_2H_4$ (dimerization to form butoxides), consistent with products of $C_2H_4$ reactions on H-zeolites in the absence of $CH_4$ that reflect solely the latter route (data in Section 7.4.5, Supp. Info.). The butoxides formed from $C_2H_4$ dimerization can desorb as butene isomers or react further with $C_2H_4$ to form larger $C_6$ oligomers, which desorb as alkenes, isomerize, undergo β-scission to form predominantly $C_3H_6$ [21-24] or cyclize to form arenes after hydrogen transfer [25-27].

The rates of formation of unsaturated $C_3$-$C_6$ species are related to the rate at which $C_4$ intermediates ($C_4H_9^+Z^-$) are formed (Scheme 7.2) by:

$$r_{dim} = r_{C_4H_9^+Z^-} = r_{C_4H_8} + \sum r_{C_6} + \frac{1}{2}\left(r_{C_3H_6} + r_{C_4H_{10}}\right). \quad (7.4)$$

When $H^+$ sites are the MASI, $C_2H_4$ dimerization rates are second-order in $C_2H_4$ pressure (derivation in Section 7.4.5, Supp. Info.) and alkylation-to-dimerization rate ratios become:

$$\frac{r_{alk}}{r_{dim}} = \frac{k_{meas,alk}\left(P_{CH_4}\right)}{k_{meas,dim}\left(P_{C_2H_4}\right)}, \tag{7.5}$$

consistent with $r_{alk}/r_{dim}$ ratios that are strictly proportional to $CH_4/C_2H_4$ reactant ratios on H-FER, H-MFI and H-MOR-56 (Fig. 7.3). On all samples, rate constants for dimerization are 2000-12000 times larger than for alkylation (Table 7.1; 748 K), reflecting the more effective stabilization of positively-charged transition state fragments ($C_2$ carbenium-ions) by alkenes in dimerization steps ($C_2H_4$) than alkanes in alkylation steps ($CH_4$) [19,20]. Thus, selective alkylation to form $C_3H_8$ (>90%) would require very high $CH_4/C_2H_4$ ratios (>25000) to offset the strong kinetic preference for $C_2H_4$ dimerization.

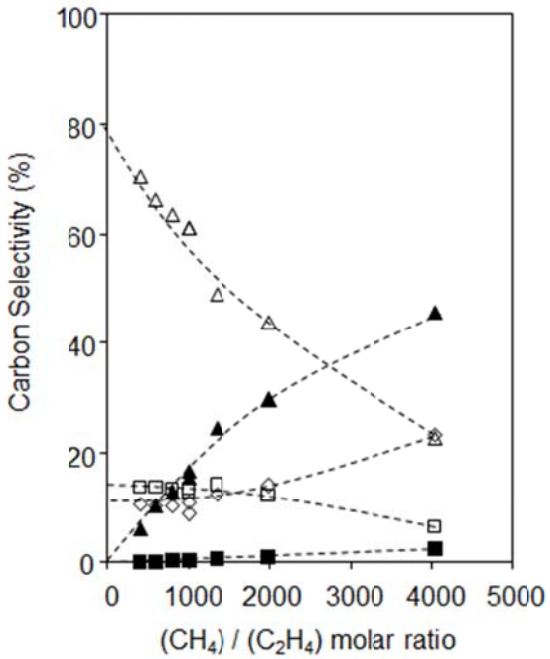


**Figure 7.2.** Carbon selectivity to $C_3H_8$ (▲), n-$C_4H_{10}$ (■), $C_3H_6$ (△), $C_4H_8$ (□), and unsaturated $C_6$ (◇) products formed during $CH_4$-$C_2H_4$ reactions on H-MFI at 748 K with varying $CH_4/C_2H_4$ molar ratio. Dashed curves are included to guide the eye.

Rate constants for $C_2H_4$ dimerization steps can also be used to predict rate constants for the reverse reaction, monomolecular $C_4H_8$ cracking, from the gas-phase equilibrium constant ($K_{R2}$ = 5.4 $bar^{-1}$; 748 K) and Eq. (7.3). Indeed, predicted values on all samples are similar to measured $C_4H_8$ cracking rate constants (Fig. 7.4), despite the different conditions ($T$, $P_j$) used to measure forward and reverse rates (details in Section 7.4.6, Supp. Info.). These data provide yet another demonstration for the applicability of the De Donder relations beyond their intended bounds and even in cases where the observed kinetic behavior reflects complex chemical reaction networks involving multiple elementary steps (e.g., alkene oligomerization).

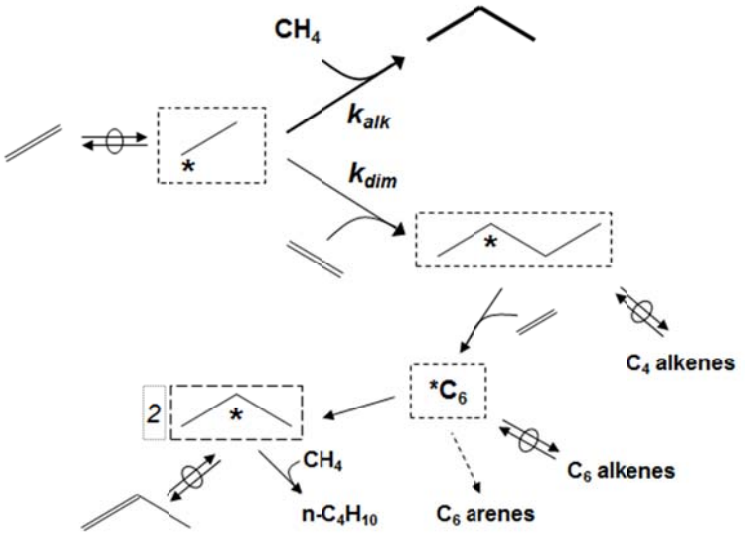


**Scheme 7.2.** Reaction scheme for $CH_4$-$C_2H_4$ alkylation ($k_{alk}$) and $C_2H_4$ dimerization ($k_{dim}$) on acidic zeolites. Surface intermediates (denoted by an asterisk, enclosed in dashed boxes) of a given carbon number are present as quasi-equilibrated alkoxides, carbenium ions and physisorbed alkenes; we refer to these as alkoxides for ease of discussion.

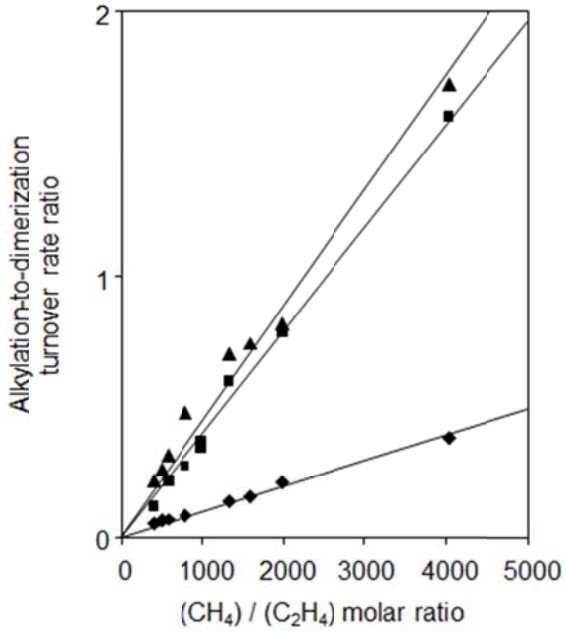


**Figure 7.3.** Alkylation-to-dimerization turnover rate ratios (748 K) with varying $CH_4/C_2H_4$ molar ratio on H-FER (▲), H-MFI (■), and H-MOR-56 (◆).

Alkylation and dimerization transition states are expected to be stabilized differently by specific spatial constraints [28], thus providing a potential strategy to influence selectivity, as found for alkane ($C_3H_8$, *n*-$C_4H_{10}$, *i*-$C_4H_{10}$) cracking and dehydrogenation paths by varying the distribution of $H^+$ between 8-MR side pockets and 12-MR channels (0.10-0.80 fraction in 8-MR) in MOR zeolites [18,29]. Rate constants for $C_2H_4$ dimerization (per total $H^+$) increased and $k_{meas,alk}/k_{meas,dim}$ ratios decreased monotonically with increasing $H^+$ fraction within 8-MR pockets (Fig. 7.5). These data indicate that the kinetic preference for 8-MR $H^+$ is stronger for $C_2H_4$ dimerization than $CH_4$-$C_2H_4$ alkylation, which we *surmise* reflects larger entropy differences, in the former reaction, between transition states confined partially within 8-MR pockets [18,29] and contained fully within 12-MR channels. The higher alkylation selectivity of 12-MR $H^+$ is accompanied by lower turnover rates for both alkylation and dimerization reactions.

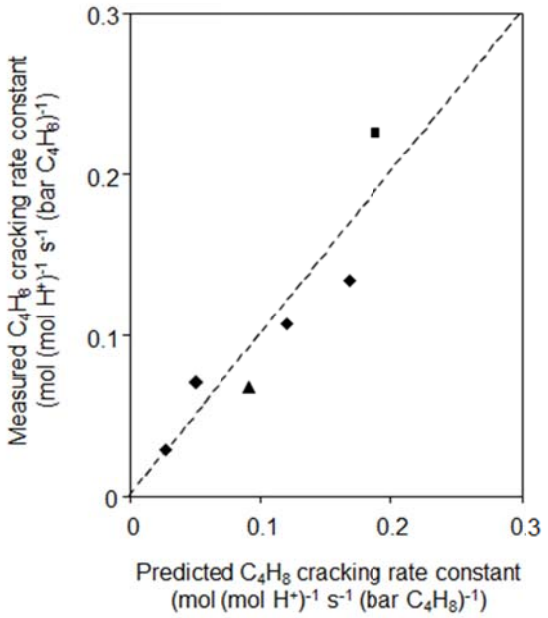


**Figure 7.4.** Monomolecular $C_4H_8$ cracking rate constants measured experimentally and predicted using $C_2H_4$ dimerization rate constants ($k_{meas,dim}$; Table 7.3) and Eq. (7.3) on H-FER (▲), H-MFI (■), and MOR (◆) zeolites. Parity line is indicated by the dashed line.

These data show clearly that Brønsted acids catalyze alkane-alkene alkylation via the same $(C\text{-}C\text{-}H)^+$ carbonium-ion-like transition states required for monomolecular alkane cracking. Unfavorable thermodynamics (>573 K) and alkene dimerization side reactions limit the useful practice of such routes, but alkylation selectivities can be increased by confining $H^+$ sites within structures that preferentially stabilize alkylation transition states. The De Donder relations apply even when reaction conditions differ, as long as the same single step limits rates and active sites remain predominantly unoccupied, enabling the prediction of rate constants in one direction of a catalytic sequence from thermodynamic data and rate constants in the other direction; such is the case for $C_3H_8$ cracking and $CH_4$-$C_2H_4$ alkylation, and for $C_4H_8$ cracking and $C_2H_4$ dimerization.

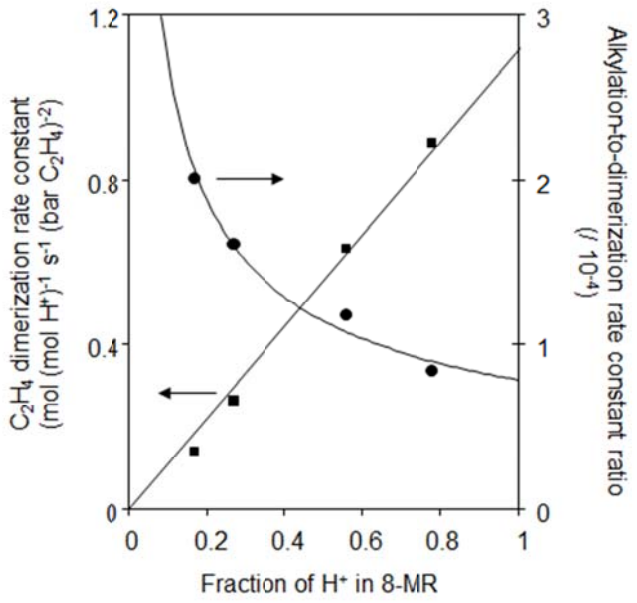


**Figure 7.5.** Dependence of $C_2H_4$ dimerization rate constants (■; $k_{meas,dim}$; per total $H^+$) and alkylation-to-dimerization rate constant ratios (●; $k_{meas,alk}/k_{meas,dim}$) at 748 K on the fraction of $H^+$ in 8-MR pockets of MOR zeolites.

## 7.2 Experimental Section

MFI (Si/Al = 16.5, Zeolyst), FER (Si/Al = 10, Zeolyst) and MOR (Si/Al = 10, Zeolyst; Si/Al = 8.9, Tosoh) were obtained in the $NH_4^+$-form and converted to the $H^+$-form by treatment in flowing dry air (2.5 $cm^3$ $g^{-1}$ $s^{-1}$, zero grade, Praxair) for 4 h at 773 K (0.0167 K $s^{-1}$). MOR samples are denoted by the percentage of $H^+$ in 8-MR pockets, determined by infrared deconvolution methods described together with all characterization data and $Na^+$-exchange protocols elsewhere [18]. Steady-state reaction rates were measured in a plug-flow tubular quartz reactor from product concentrations measured by gas chromatography and flame ionization detection (Agilent HP-6890GC) [18]. $CH_4$ (99.97%), $C_2H_4$ (1% $C_2H_4$ (99.9%), 5% Ar, 94 % He), $C_3H_8$ (10% $C_3H_8$ (99.999%), 5% Ar, 85% He) and $C_4H_8$ (1% 1-$C_4H_8$ (99.9%), 5% Ar, 94 % He) reactants were obtained from Praxair. H-zeolites (0.08-0.50 g; 180-250 μm) were treated in flowing 5% $O_2$ / 95% He (16.7 $cm^3$ $g^{-1}$ $s^{-1}$, 99.999%, Praxair) for 2 h at 803 K (0.0167 K $s^{-1}$) and then in He (16.7 $cm^3$ $g^{-1}$ $s^{-1}$, 99.999%, Praxair) for 0.5 h at 748 K before reaction. Rate constants at the end of each experiment (~12 h time-on-stream) were similar (within 5%) to initial values on all catalysts; thus, deactivation did not corrupt any kinetic data. Uncertainties are reported as 95% confidence intervals. Isotopic studies used $^{13}CH_4$ (99 atom% $^{13}C$, Isotec) and $^{12}C_2H_4$ mixtures (80 kPa $^{13}CH_4$, 0.2 kPa $^{12}C_2H_4$) on H-MFI (0.05 g, 180-250 μm; $1.5x10^{-6}$ (mol carbon) $g^{-1}$ $s^{-1}$) held within a tubular stainless steel reactor (4.6 mm i.d.) with a fritted VCR gasket and quartz wool. Temperatures were maintained by resistive heating (Watlow Series 96 controller) and measured with a K-type thermocouple. Products were measured by chromatography (HP-1 column, 50 m x 0.32 mm; 1.05 μm film; Agilent) using flame ionization and mass selective detectors (HP 5890/HP 5972). Mass spectra and matrix deconvolution methods [30] were used to measure isotopologue distributions.

## 7.3 Acknowledgements

We acknowledge the financial support from the Chevron Energy Technology Company.

## 7.4. Supporting Information

### *7.4.1 Monomolecular Propane Cracking on Acidic Zeolites*

Accepted paths for monomolecular alkane cracking involve the adsorption of alkanes from the gas phase onto Brønsted acid sites within zeolite channels (Step 1, Scheme 7.1) and subsequent C-C bond protonation to form $(C\text{-}C\text{-}H)^+$ carbonium-ion-like transition states that decompose to form smaller alkane and alkoxide species in equimolar amounts (Step 2, Scheme 7.1); protonation can also occur at alkane C-H bonds in monomolecular alkane dehydrogenation paths [8,14,15,18]. Monomolecular routes prevail at high temperatures and low pressures, leading to intrazeolite alkanes present in dilute concentrations ($H^+$ sites are predominantly unoccupied) [18] and in quasi-equilibrium with gaseous alkanes. These mechanistic details result in the following expression for monomolecular cracking rates (a detailed derivation can be found elsewhere) [18]:

$$\vec{r_c} = K_1 k_2 P_{C_3H_8} = k_{meas,c} P_{C_3H_8} . \tag{7.6}$$

Propane cracking rates (748 K) are first-order in $C_3H_8$ pressure (Fig. 7.6) on all zeolites tested (H-FER, H-MFI, H-MOR-56), consistent with the rate equation for monomolecular $C_3H_8$ cracking given by Eq. (7.6). Reactions of $C_3H_8$ led to the formation of $CH_4$ and $C_2H_4$ in equimolar ratios ($C_2H_4/CH_4$ = 0.93-1.00) at all space velocities (Fig. 7.7). Rate constants for $C_3H_8$ cracking and dehydrogenation were invariant with space velocity (Fig. 7.7) and gave non-zero values upon extrapolation to zero residence time, indicating that all products were formed in primary paths and reflect exclusively contributions from monomolecular activation.

The equilibrium and rate constants in Eq. (7.6) can be expressed in terms of the free energies of reactants, products and transition states involved in their respective elementary steps (given in Scheme 7.1):

$$K_1 = \exp\left(-\left(\Delta G^\circ_{C_3H_8(z)} - \Delta G^\circ_{C_3H_8(g)}\right)/RT\right), \tag{7.7}$$

$$k_2 = \left(k_B T/h\right)\exp\left(-\left(\Delta G^\circ_{\ddagger,2} - \Delta G^\circ_{C_3H_8(z)} - \Delta G^\circ_{H^+Z^-}\right)/RT\right). \tag{7.8}$$

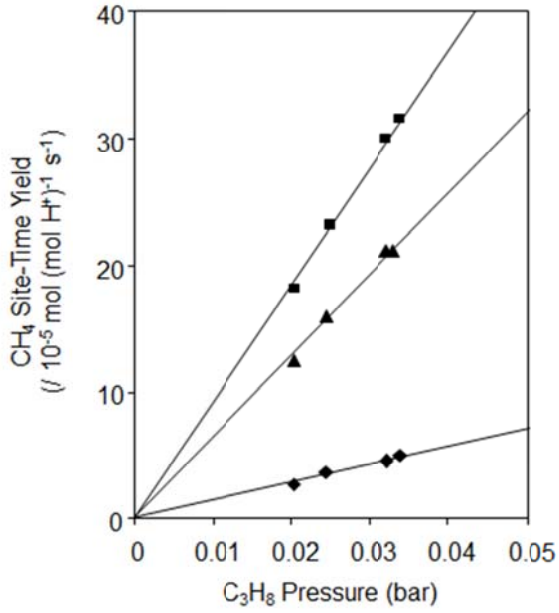


**Figure 7.6.** Dependence of $CH_4$ synthesis rates (748 K) from monomolecular $C_3H_8$ cracking on $C_3H_8$ pressure on H-FER (▲), H-MFI (■), and H-MOR-56 (◆).

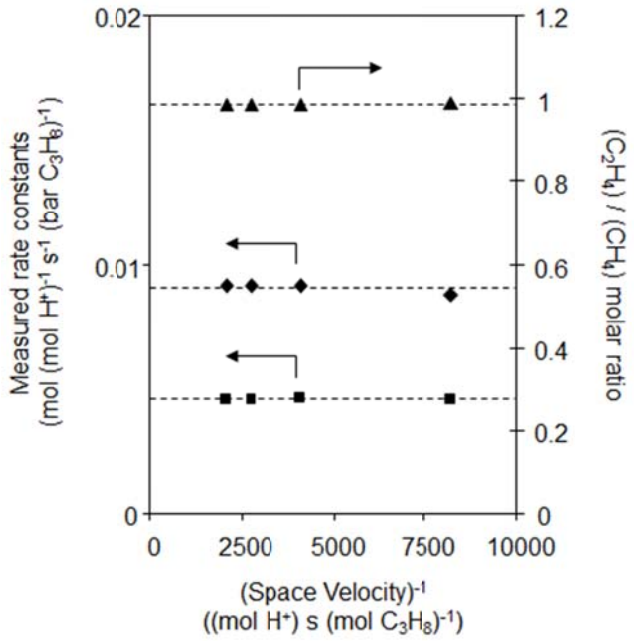


**Figure 7.7.** Dependence of measured rate constants for monomolecular $C_3H_8$ cracking (◆; $k_{meas,c}$) and dehydrogenation (■; $k_{meas,d}$) and of $C_2H_4/CH_4$ product molar ratios (▲) on H-MFI (748 K) on space velocity.

Combining Eqs. (7.7) and (7.8) leads to the following expression for $k_{meas,c}$:

$$k_{meas,c} = \left(k_B T/h\right)\exp\left(-\left(\Delta G^{\circ}_{\ddagger,2} - \Delta G^{\circ}_{C_3H_8(g)} - \Delta G^{\circ}_{H^+Z^-}\right)/RT\right). \quad (7.9)$$

This treatment shows that measured first-order cracking rate constants reflect free energies of (C-C-H)$^+$ carbonium-ion-like transition states solvated by zeolite channels (Step 2, Scheme 7.1) with respect to those of gaseous alkanes. Thus, measured rate constants depend on zeolite structure to the extent that local channel environments differ in their ability to solvate these transition states [28].

### *7.4.2 Methane-Ethene Reactions on Acidic Zeolites*

The elementary steps in Scheme 7.1, in the reverse direction as written, describe the alkylation of $CH_4$ and $C_2H_4$ to form $C_3H_8$ via the same kinetically-relevant (C-C-H)$^+$ carbonium-ion-like transition state as involved in monomolecular $C_3H_8$ cracking. This route involves quasi-equilibrium between gaseous $CH_4$ and $C_2H_4$ and their respective intrazeolitic intermediates that are involved in Step 2. When $H^+$ is the MASI, alkylation reaction rates are given by:

$$\overleftarrow{r_{alk}} = k_{-2}K_3^{-1}K_4^{-1}K_5^{-1}P_{C_2H_4}P_{CH_4} = k_{meas,alk}P_{C_2H_4}P_{CH_4} \; . \tag{7.10}$$

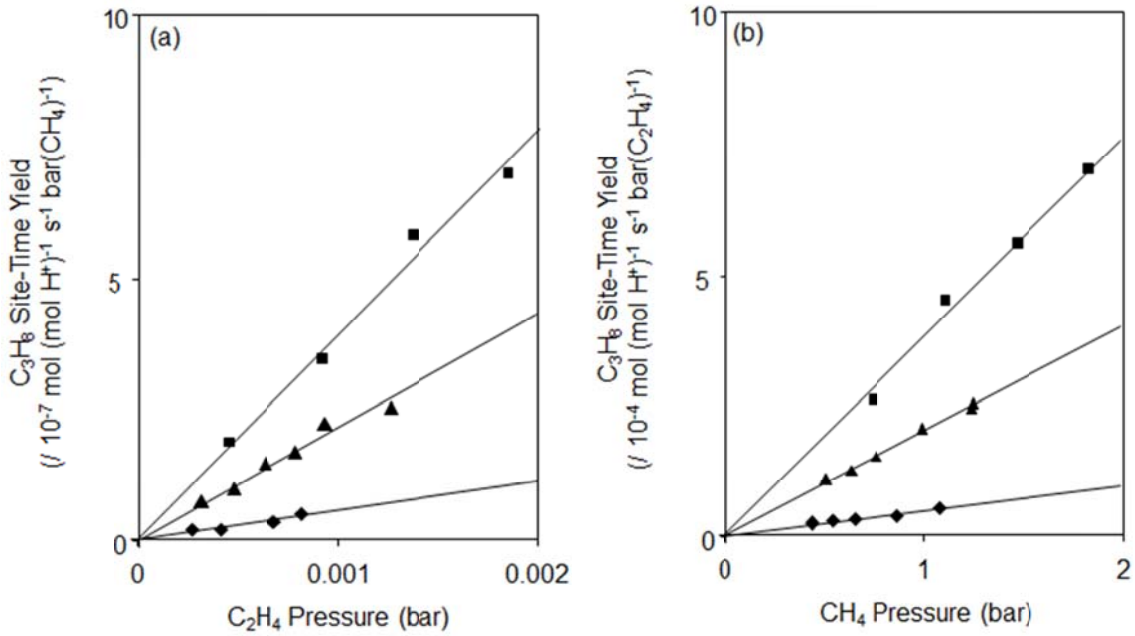


**Figure 7.8.** Dependence of $C_3H_8$ synthesis rates (748 K) from $CH_4$-$C_2H_4$ alkylation on (a) $C_2H_4$ pressure and (b) $CH_4$ pressure on H-FER (▲), H-MFI (■), and H-MOR-56 (◆).

This rate expression is consistent with the first-order dependence of $C_3H_8$ formation rates on $CH_4$ and $C_2H_4$ pressures (Fig. 7.8) on all zeolites tested (H-FER, H-MFI, H-MOR-56). We note that the first-order dependence of alkyation rates on $C_2H_4$ pressure cannot discriminate among $C_2$ intermediates present as chemically-bound ethoxides, carbenium ions or physisorbed alkenes, but only indicate that they are in quasi-equilibrium with each other and with gaseous $C_2H_4$. This distinction, however, is not required for the interpretation and analysis of kinetic data

discussed in this manuscript, and we refer to these intermediates as alkoxides for ease of discussion. $C_3H_8$ was formed as a primary product from $CH_4$-$C_2H_4$ reactions on acidic zeolites (Fig. 7.9) and the selectivity toward saturated products ($C_3H_8$, *n*-$C_4H_{10}$) becomes undetectably small in the absence of $CH_4$ and increases monotonically with $CH_4/C_2H_4$ ratio (Fig. 7.10). These trends are consistent with parallel reactions of ethoxides with $CH_4$ to form $C_3H_8$ and with $C_2H_4$ to form butoxides (Scheme 7.2).

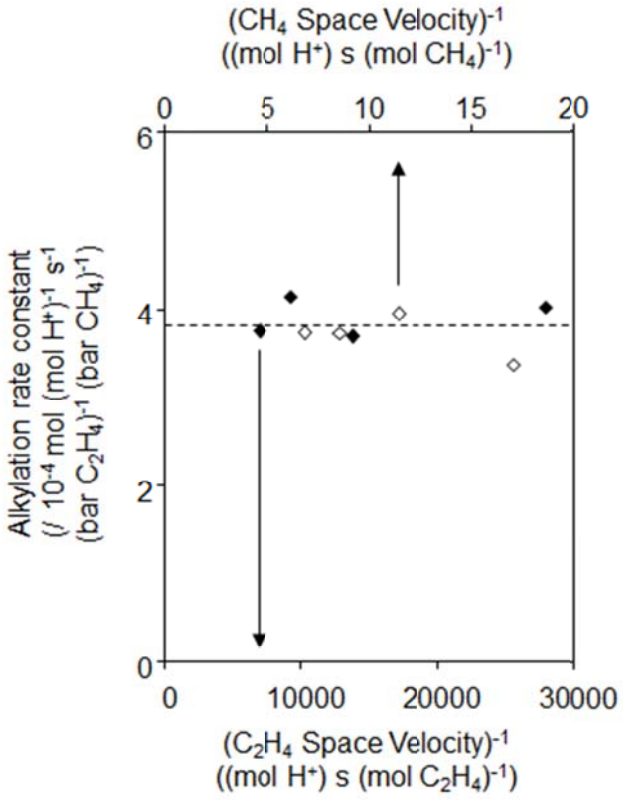


**Figure 7.9.** Dependence of measured alkylation rate constants on H-MFI ($k_{meas,alk}$; 748 K) with varying $C_2H_4$ (◆; $P(CH_4)$ = 1.8 bar) and $CH_4$ (◇; $P(C_2H_4)$ = 0.0002 bar) space velocities.

The equilibrium and rate constants in Eq. (7.10) can be expressed as follows:

$$k_{-2} = \left(k_B T/h\right)\exp\left(-\left(\Delta G^\circ_{\ddagger,-2} - \Delta G^\circ_{CH_4(z)} - \Delta G^\circ_{C_2H_5^+Z^-}\right)/RT\right). \tag{7.11}$$

$$K_3^{-1} = \exp\left(-\left(\Delta G^\circ_{C_2H_5^+Z^-} - \Delta G^\circ_{C_2H_4(z)} - \Delta G^\circ_{H^+Z^-}\right)/RT\right), \tag{7.12}$$

$$K_4^{-1} = \exp\left(-\left(\Delta G^\circ_{C_2H_4(z)} - \Delta G^\circ_{C_2H_4(g)}\right)/RT\right), \tag{7.13}$$

$$K_5^{-1} = \exp\left(-\left(\Delta G^\circ_{CH_4(z)} - \Delta G^\circ_{CH_4(g)}\right)/RT\right), \tag{7.14}$$

Combining Eqs. (7.11)-(7.14) results in the following expression for $k_{meas,alk}$:

$$k_{meas,alk} = \left(k_B T/h\right)\exp\left(-\left(\Delta G^\circ_{\ddagger,-2} - \Delta G^\circ_{C_2H_4(g)} - \Delta G^\circ_{CH_4(g)} - \Delta G^\circ_{H^+Z^-}\right)/RT\right). \quad (7.15)$$

Thus, measured alkylation rate constants reflect free energies of $(C\text{-}C\text{-}H)^+$ carbonium-ion-like transition states stabilized within zeolite channels (Step 2, Scheme 7.1) with respect to those of gas-phase reactants, and depend on local channel environments near $H^+$ sites.

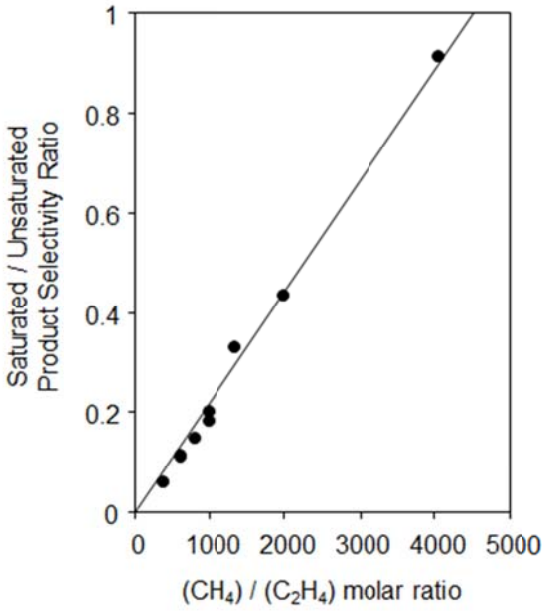


**Figure 7.10.** Saturated-to-unsaturated product selectivity ratio (carbon basis) on H-MFI (748 K) with varying $CH_4/C_2H_4$ molar ratio.

### *7.4.3 Estimation of Thermochemical Properties of Gas-Phase Reactions*

The Gibbs free energy change for the following gas-phase reaction:

$$C_3H_8 \rightleftarrows C_2H_4 + CH_4, \quad (7.16)$$

was calculated using reported thermochemical data [31], the ideal gas assumption, and the following relation:

$$\Delta G_R^\circ(T) = \sum_i \nu_i \Delta G_{f,i}^\circ(T) = \Delta G_{f,C_2H_4}^\circ(T) + \Delta G_{f,CH_4}^\circ(T) - \Delta G_{f,C_3H_8}^\circ(T). \quad (7.17)$$

The dimensionless equilibrium constant ($K$) for this reaction is related to $\Delta G_R^o(T)$ by:

$$K(T) = \exp(-\Delta G_R^\circ(T)/RT) = \frac{a_{C_2H_4}a_{CH_4}}{a_{C_3H_8}}. \quad (7.18)$$

The equilibrium constant in pressure units ($K_R$) is given by:

$$K_R(T) = K(T)\left(\frac{P_{C_2H_4}{}^{o} P_{CH_4}{}^{o}}{P_{C_3H_8}{}^{o}}\right) = \frac{P_{C_2H_4} P_{CH_4}}{P_{C_3H_8}}[=]bar\,, \tag{7.19}$$

in which the standard state pressure ($P_i^o$) is 1 bar.

The following calculations are shown at 748 K as an example:

$$\Delta G_{R1}°(748K) = 98.5 + (-7.8) - 111.0 = -20.3\ \ kJ\ \ mol^{-1}\,, \tag{7.20}$$

$$K_{R1}(748K) = \exp\left(-20300/\left(8.3145 * 748\right)\right) = 26\ \ bar\,. \tag{7.21}$$

*7.4.4 De Donder Treatments of Chemical Reaction Rates*

A more detailed treatment of the De Donder relations and their consequences for chemical reaction rates in forward and reverse directions can be found elsewhere.[1] In this section, we include a highly abridged version relevant to the discussion in this manuscript.

The De Donder equation, which relates the rates of an elementary step in forward ($\vec{r}_i$) and reverse ($\overleftarrow{r}_i$) directions to the chemical affinity ($A_i$) of the step, can be extended to describe forward ($\vec{r}$) and reverse ($\overleftarrow{r}$) rates of single-path catalytic sequences [4]:

$$\frac{\vec{r}}{\overleftarrow{r}} = \frac{\prod \vec{r}_i}{\prod \overleftarrow{r}_i} = \exp\left(\sum A_i / RT\right) = \exp\left(A/\overline{\sigma} RT\right). \tag{7.22}$$

In this equation, the chemical affinity for the overall reaction sequence ($A$) is given by:

$$A = \sum_i \sigma_i A_i\,, \tag{7.23}$$

in which $\overline{\sigma}$ is the affinity-averaged stoichiometric number for the entire catalytic sequence:

$$\overline{\sigma} = \sum_i \sigma_i A_i \Big/ \sum_i A_i\,. \tag{7.24}$$

These treatments also show that forward ($\vec{k}$) and reverse ($\overleftarrow{k}$) rate constants and the equilibrium constant ($K_R$) for the overall reaction must be related by [4]:

$$\vec{k}/\overleftarrow{k} = K_R{}^{1/\overline{\sigma}}\,. \tag{7.25}$$

Equation (7.22) can be applied to the catalytic sequence shown in Scheme 7.1 for $C_3H_8$ cracking and $C_2H_4$-$CH_4$ alkylation:

$$\frac{\vec{r}_c}{\overleftarrow{r_{alk}}} = \frac{\vec{r}_1\vec{r}_2\vec{r}_3\vec{r}_4\vec{r}_5}{\overleftarrow{r}_1\overleftarrow{r}_2\overleftarrow{r}_3\overleftarrow{r}_4\overleftarrow{r}_5} = \frac{k_1 a_{C_3H_8(g)} k_2 a_{C_3H_8(z)} a_{H^+Z^-} k_3 a_{C_2H_5^+Z^-} k_4 a_{C_2H_4(z)} k_5 a_{CH_4(z)}}{k_{-1} a_{C_3H_8(z)} k_{-2} a_{C_2H_5^+Z^-} a_{CH_4(z)} k_{-3} a_{C_2H_4(z)} a_{H^+Z^-} k_{-4} a_{C_2H_4(g)} k_{-5} a_{CH_4(g)}}, \tag{7.26}$$

in which elementary step reaction rates are given by the law of mass action. At fixed reaction conditions ($T$, $P_j$), the thermodynamic activity of a given surface intermediate is constant and will cancel when appearing in both forward and reverse rate expressions, allowing Equation (7.26) to be simplified to:

$$\frac{\vec{r}_c}{\overleftarrow{r_{alk}}} = \frac{k_1 P_{C_3H_8} k_2 k_3 k_4 k_5}{k_{-1} k_{-2} k_{-3} k_{-4} P_{C_2H_4} k_{-5} P_{CH_4}}. \tag{7.27}$$

Rate expressions for cracking (Eq. (7.6)) and alkylation (Eq. (7.10)) can be isolated in numerator and denominator of Eq. (7.27) to give:

$$\frac{\vec{r}_c}{\overleftarrow{r_{alk}}} = \frac{K_1 k_2 P_{C_3H_8}}{k_{-2} K_3^{-1} K_4^{-1} K_5^{-1} P_{C_2H_4} P_{CH_4}} = \frac{k_{meas,c} P_{C_3H_8}}{k_{meas,alk} P_{C_2H_4} P_{CH_4}}. \tag{7.28}$$

Thus, when surface coverages are identical (i.e., fixed ($T$, $P_j$)), the ratio of measured rate constants for $C_3H_8$ cracking ($k_{meas,c}$) and $C_2H_4$-$CH_4$ alkylation ($k_{meas,alk}$), as given by Eq. (7.28) will equal the equilibrium constant for the stoichiometric gas-phase reaction ($K_R$), as given by Eq. (7.19).

When rates in forward and reverse directions are measured at different reaction conditions (denoted by subscripts $A$ and $B$, respectively) as they are in this study, however, their ratio is given by:

$$\frac{\left(\vec{r}_c\right)_A}{\left(\overleftarrow{r_{alk}}\right)_B} = \frac{k_{meas,c}\left(P_{C_3H_8}\right)_A \left(c_{H^+Z^-}\right)_A}{k_{meas,alk}\left(P_{CH_4}\right)_B \left(P_{C_2H_4}\right)_B \left(c_{H^+Z^-}\right)_B}. \tag{7.29}$$

This equation becomes equivalent to Eq. (7.28), which holds rigorously for constant ($T$, $P_j$), *only* when $H^+$ sites are predominantly unoccupied at the different reaction conditions used to measure forward and reverse rates. We conclude from this treatment that the relevance of the De Donder relations beyond their rigorous description of chemical reaction rates at fixed reaction conditions reflects kinetic measurements of the same single kinetically-relevant step (Step 2, Scheme 7.1), albeit in opposite directions, on predominantly vacant surfaces at the different reaction conditions used to measure forward and reverse rates.

*7.4.5 Ethene Dimerization in the Absence of Methane*

$C_2H_4$ dimerization routes, and subsequent reactions of the butoxides they form, are proposed to account for the formation for unsaturated $C_3$-$C_6$ products and to occur in parallel to $CH_4$-$C_2H_4$ alkylation, according to Scheme 7.2. Reactions of $C_2H_4$ on acidic zeolites in the absence of co-fed $CH_4$ reactants formed solely unsaturated $C_3$-$C_6$ products. Steady-state product formation rates can be related to the rate at which $C_4$ intermediates ($C_4H_9^+Z^-$) are formed by $C_2H_4$ dimerization ($r_{dim}$):

$$r_{dim} = r_{C_4H_9^+Z^-} = r_{C_4H_8} + r_{C_6} + \frac{1}{2}\left(r_{C_3H_6} + r_{C_4H_{10}}\right). \tag{7.30}$$

$C_2H_4$ dimerization likely occurs between reactions of intrazeolitic $C_2H_4$ molecules and $C_2$ surface intermediates present as alkoxides or carbenium ions (depicted in Scheme 7.3). The high temperatures and low hydrocarbon pressures used in this study result in predominantly unoccupied $H^+$ sites and quasi-equilibrated adsorption between gaseous $C_2H_4$ and intrazeolitic $C_2$ intermediates. These mechanistic assumptions, along with the assumption that Step 3 (Scheme 7.3) is irreversible, can be used to derive the following rate expression for $C_2H_4$ dimerization:

$$r_{dim} = k_3\left(C_2H_5^+Z^-\right)\left(C_2H_4(z)\right) = k_3K_1K_2P_{C_2H_4}K_1P_{C_2H_4} = k_{meas,dim}\left(P_{C_2H_4}\right)^2. \tag{7.31}$$

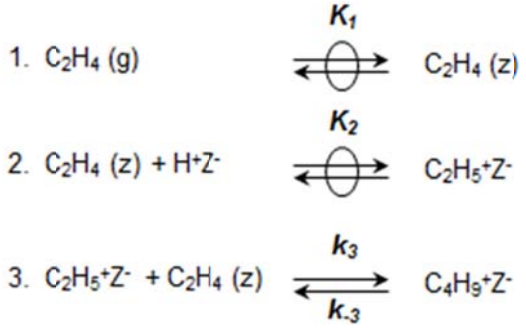


**Scheme 7.3.** Reaction scheme for $C_2H_4$ dimerization on Brønsted acid sites ($H^+Z^-$) within zeolites. Species are in the gas-phase (g), chemically-bound to oxygens at framework Al sites ($Z^-$) and physisorbed within zeolite channels (z).

Thus, effective second-order $C_2H_4$ dimerization rate constants ($k_{meas,dim}$), which are invariant with space velocity (Fig. 7.11), can be measured directly in the absence of $CH_4$ co-reactants. These values are identical, within experimental error, to those determined from $k_{meas,alk}$ values and the dependence of alkylation-to-dimerization turnover rate ratios on $CH_4/C_2H_4$ molar ratios (Table 7.1). For instance, the former and latter methods respectively give $k_{meas,dim}$ values (748 K) of 0.98 $\pm$ 0.10 and 0.97 $\pm$ 0.10 mol (mol $H^+$)$^{-1}$ s$^{-1}$ (bar $C_2H_4$)$^{-2}$ on H-MFI.

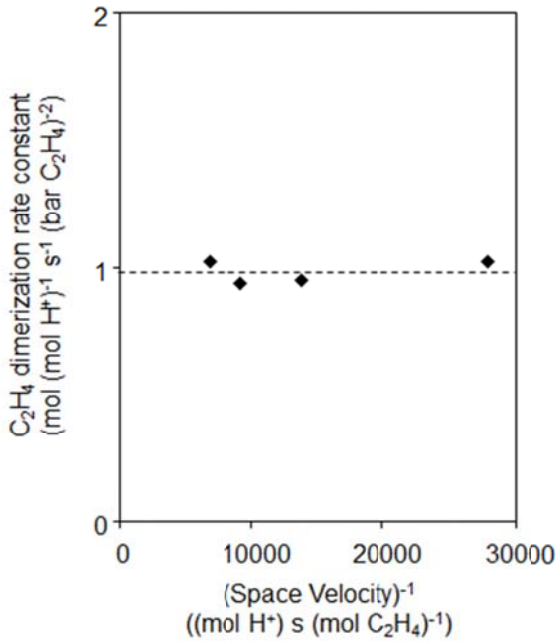


**Figure 7.11.** Dependence of measured second-order $C_2H_4$ dimerization rate constants ($k_{meas,dim}$; 748 K) on H-MFI on space velocity, determined in the absence of $CH_4$ co-reactants.

### *7.4.6 Rate Constants for Monomolecular Butene Cracking*

The stoichiometric reaction for $C_2H_4$ dimerization to form $C_4H_8$ is:

$$2C_2H_4 \rightleftarrows C_4H_8 . \tag{7.32}$$

The equilibrium constant for the gas-phase interconversion of two $C_2H_4$ molecules and $C_4H_8$ (assuming an equilibrium pool of $C_4H_8$ isomers) was calculated using reported thermochemical data [31] and the methods described in Section S.3:

$$K_{R2}(748K) = 5.4\ bar^{-1} . \tag{7.33}$$

Monomolecular $C_4H_8$ cracking rate constants were predicted using Eqs. (7.25) and (7.33) and measured $C_2H_4$ dimerization rate constants ($k_{meas,dim}$; 748 K; Table 7.1).

Steady-state $C_4H_8$ cracking rates on acidic zeolites (748 K) were measured by feeding dilute streams of 1-$C_4H_8$ (0.01-0.04 kPa), which underwent rapid isomerization to give essentially equilibrated $C_4H_8$ mixtures. Rate constants were determined by normalizing $C_4H_8$ cracking rates by the $C_4H_8$ pressure averaged linearly across the catalyst bed. Effective first-order $C_4H_8$ cracking rate constants ($k_{meas,c,C4H8}$) increased systematically with $C_4H_8$ pressure (Fig. 7.12) as a result of increasing contributions from $C_4H_8$ oligomerization-cracking cycles; monomolecular $C_4H_8$ cracking rate constants were taken as the values extrapolated to zero $C_4H_8$ pressure.

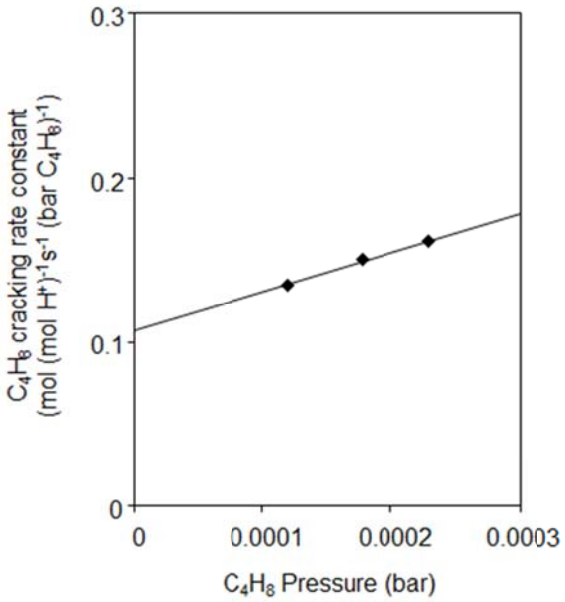


**Figure 7.12.** Dependence of measured first-order $C_4H_8$ cracking rate constants (748 K) on H-MOR-56 on $C_4H_8$ pressure.

## 7.5 References


(1) Gounder, R.; Iglesia, E. *J. Catal.* **2011**, *277*, 36.
(2) de Donder, T. *L'Affinité*; Gauthier-Villars: Paris, **1927**.
(3) de Donder, T.; van Rysselberghe, P. *Thermodynamic Theory of Affinity: A Book of Principles*; Stanford University Press: Stanford, **1936**.
(4) Boudart, M.; Djéga-Mariadassou, G. *Kinetics of Heterogeneous Catalytic Reactions*; Princeton University Press: Princeton, **1984**.
(5) Tolman, R. C. *Phys. Rev.* **1924**, *23*, 693.
(6) Tolman, R. C. *Proc. Natl. Acad. Sci. USA* **1925**, *11*, 436.
(7) Corma, A.; Martinez, A. *Catal. Rev.-Sci. Eng.* **1993**, *35*, 483.
(8) Lercher, J. A.; van Santen, R. A.; Vinek, H. *Catal. Lett.* **1994**, *27*, 91.
(9) Rigby, A. M.; Kramer, G. J.; van Santen, R. A. *J. Catal.* **1997**, *170*, 1.
(10) Olah, G. A.; Felberg, J. D.; Lammertsma, K. *J. Am. Chem. Soc.* **1983**, *105*, 6529.
(11) Siskin, M. *J. Am. Chem. Soc.* **1976**, *98*, 5413.
(12) Scurrell, M. S. *Appl. Catal.* **1987**, *34*, 109.
(13) Sommer, J.; Muller, M.; Laali, K. *Nouv. J. Chim.* **1982**, *6*, 3.
(14) Haag, W. O.; Dessau, R. M. **1984**, *2*, 305.
(15) Kotrel, S.; Knözinger, H.; Gates, B. C. *Microporous Mesoporous Mater.* **2000**, *35-6*, 11.
(16) Narbeshuber, T. F.; Vinek, H.; Lercher, J. A. *J. Catal.* **1995**, *157*, 388.
(17) Xu, B.; Sievers, C.; Hong, S. B.; Prins, R.; van Bokhoven, J. A. *J. Catal.* **2006**, *244*, 163.
(18) Gounder, R.; Iglesia, E. *J. Am. Chem. Soc.* **2009**, *131*, 1958.
(19) Janik, M. J.; Davis, R. J.; Neurock, M. *J. Catal.* **2006**, *244*, 65.
(20) Janik, M. J.; Davis, R. J.; Neurock, M. *Catal. Today* **2006**, *116*, 90.
(21) Buchanan, J. S.; Santiesteban, J. G.; Haag, W. O. *J. Catal.* **1996**, *158*, 279.
(22) Abbot, J.; Wojciechowski, B. W. *Can. J. Chem. Eng.* **1985**, *63*, 462.
(23) Koyama, T.; Hayashi, Y.; Horie, H.; Kawauchi, S.; Matsumoto, A.; Iwase, Y.; Sakamoto, Y.; Miyaji, A.; Motokura, K.; Baba, T. *Phys. Chem. Chem. Phys.* **2010**, *12*, 2541.
(24) Inazu, K.; Koyama, T.; Miyaji, A.; Baba, T. *J. Jpn. Pet. Inst.* **2008**, *51*, 205.
(25) Joshi, Y. V.; Bhan, A.; Thomson, K. T. *J. Phys. Chem. B* **2004**, *108*, 971.
(26) Bhan, A.; Delgass, W. N. *Catal. Rev.* **2008**, *50*, 19.
(27) Bhan, A.; Hsu, S. H.; Blau, G.; Caruthers, J. M.; Venkatasubramanian, V.; Delgass, W. N. *J. Catal.* **2005**, *235*, 35.
(28) Bhan, A.; Iglesia, E. *Acc. Chem. Res.* **2008**, *41*, 559.
(29) Gounder, R.; Iglesia, E. *Angew. Chem. Int. Ed.* **2010**, *49*, 808.
(30) Price, G. L.; Iglesia, E. *Ind. Eng. Chem. Res.* **1989**, *28*, 839.
(31) Stull, D. R.; Westrum, E. F.; Sinke, G. C. *The Chemical Thermodynamics of Organic Compounds*; John Wiley & Sons, Inc.: New York, **1987**.

# CHAPTER EIGHT

## Solvation and Acid Strength Effects on Catalysis by Faujasite Zeolites


### Abstract

Kinetic, spectroscopic and chemical titration data show that small differences in monomolecular isobutane cracking and dehydrogenation and methanol dehydration turnover rates (per $H^+$) among FAU zeolites treated thermally (H-USY) and then chemically with ammonium hexafluorosilicate (CD-HUSY) do not reflect differences in acid strength but instead differences in the size and solvating properties of their supercage voids. The number of protons, measured by their titration with $Na^+$, with $CH_3$ groups via reactions of dimethyl ether, and with 2,6-di-*tert*-butylpyridine *during* methanol dehydration catalysis, was similar for each sample; OH infrared bands indicated these methods selectively counted the number of acidic OH groups. The number of protons, taken as the average of the three titration methods, was significantly smaller than the number of framework Al atoms ($Al_f$) obtained from $^{27}Al$ MAS NMR on H-USY (0.35 $H^+/Al_f$) and CD-HUSY (0.69 $H^+/Al_f$). These data indicate that $Al_f$ sites, ubiquitously used as structural proxies for active $H^+$ sites, are imprecise, apparently because NMR lines assigned to $Al_f$ sites do not always correspond to structures associated with acidic protons. Monomolecular isobutane cracking and dehydrogenation rates, when non-rigorously normalized by the number of $Al_f$ species, decreased with increasing $Na^+$ content on both H-USY and CD-HUSY samples and became undetectable at sub-stoichiometric exchange levels (0.32 and 0.72 $Na^+/Al_f$ ratios, respectively), an unexpected finding inaccurately attributed to the presence of minority 'super-acidic' sites in previous studies. These same rates, when rigorously normalized by the number of residual $H^+$, were independent of $Na^+$ content on both H-USY and CD-HUSY samples, reflecting the stoichiometric replacement of protons that are uniform in reactivity by $Na^+$ cations. Zero-order rate constants for methanol dehydration, which depend on acid strength but not solvation within zeolite voids, were similar (within a factor of 1.1) on H-USY and CD-HUSY, consistent with uniform $H^+$ species of similar reactivity in both samples. First-order rate constants for methanol dehydration and for monomolecular isobutane activation, which depend on both acid strength and solvation effects, were larger on H-USY than on CD-HUSY (by factors of 3.4 and 1.8, respectively). These small differences in reactivity reflect slightly smaller voids in H-USY, apparently because extraframework Al ($Al_{ex}$) residues occlude space within FAU supercages. These findings appear to clarify enduring controversies about the interpretation and mechanistic attribution of the effects of $Na^+$ and $Al_{ex}$ species on the catalytic reactivity of FAU zeolites. They also illustrate the need to normalize rates by the number of active sites, instead of using more convenient but less precise structural proxies for such sites.


### 8.1 Introduction

Faujasite (FAU, Y-zeolite) is used as a solid acid catalyst, often after thermal or chemical treatments render it more stable during catalysis [1-4]. Although FAU zeolites contain only one framework Al ($Al_f$) T-site, isolated $Al_f$ atoms give rise to OH groups with significantly smaller deprotonation energies (DPE; 1161-1166 kJ $mol^{-1}$) than OH groups on $Al_f$ atoms with next-

nearest Al neighbors (1177-1247 kJ $mol^{-1}$) [5]. As a result, isolated *Brønsted acid sites* in FAU zeolites should behave as uniform sites, equal in acid strength as well as solvating environment. This appears to be consistent with rates of alkane cracking (per g) that are proportional to the number of isolated $Al_f$ *atoms* on FAU zeolites treated by a given thermal or chemical protocol [6-10]. Yet, cracking rates (per $Al_f$) differ among FAU zeolites treated by different thermal and chemical methods [6-10], in apparent contradiction to the constant turnover rates expected from a single-site catalyst.

Thermal treatments that convert Y-zeolite to its ultrastable form (USY) [1,4,11,12] create extraframework Al ($Al_{ex}$) moieties by extraction of Al from framework sites and increase cracking rates (per g) of i-$C_4H_{10}$ [7], n-$C_5H_{12}$ [9] and n-$C_6H_{14}$ [6,13,14]. Alkane cracking reactions are fully suppressed upon addition of only small amounts of $Na^+$ to H-USY (0.2-0.3 per $Al_f$) [9,15-17]. These effects have been previously interpreted as the result of a small number of highly reactive and 'super-acidic' Brønsted sites, formed via electronic interactions with $Al_{ex}$ moieties and titrated selectively by $Na^+$ [9,15-17]. Some studies have suggested that higher alkane cracking rates on thermally-treated zeolites reflect the generation of mesopores and of external surfaces that decrease diffusional constraints on bimolecular cracking reactions [13,18-21]. A recent study concluded that monomolecular $C_3H_8$ cracking turnovers occur only on $H^+$ sites at isolated $Al_f$ atoms [10]; yet, this interpretation appears inconsistent with turnover rates (per $H^+$) that vary (up to factors of 3) on FAU zeolites treated with steam, ammonia, or ethylenediaminetetraacetic acid [10] and with the elimination of detectable alkane cracking rates after substoichiometric titration of isolated $Al_f$ with $Na^+$ cations [15-17].

Here, we examine the structural and catalytic properties of FAU zeolites containing different $Al_f$ and $Al_{ex}$ contents, resulting from thermal treatment in water vapor that forms $Al_{ex}$ moieties and from chemical treatments with $(NH_4)_2SiF_6$ that remove these species. The number of $H^+$ was determined directly by their chemical titration with $Na^+$, with dimethyl ether (DME) to form $CH_3$ groups, and with 2,6-di-*tert*-butylpyridine *during* methanol dehydration catalysis. On each sample, proton counts were similar among these methods but much smaller than the number of $Al_f$ atoms, determined by $^{27}Al$ magic angle spinning nuclear magnetic resonance (MAS NMR) and X-ray diffraction (XRD). Yet, $Al_f$ atoms measured by these methods are ubiquitously used as a structural proxy for Brønsted acid sites in the reporting of catalytic reactivity as turnover rates.

Turnover rates (per $H^+$) for isobutane cracking and dehydrogenation (763 K) and methanol dehydration to DME (433 K) were measured at differential conversions in the absence of mass and heat transfer artifacts. These kinetic data provide evidence that $Na^+$ cations stoichiometrically titrate $H^+$ sites that are uniform in reactivity and acid strength within a given sample. These data also indicate that thermal and chemical treatments weakly influence the solvation properties of FAU supercage voids but not the strength of Brønsted acid sites. These findings seem to resolve issues that have persisted for decades regarding the mechanistic origin of the effects of $Na^+$ and $Al_{ex}$ species in catalysis by FAU zeolites. The distractions inherent in using imprecise structural proxies ($Al_f$) for active sites ($H^+$) to normalize reaction rates have led to incorrect interpretations of reactivity in terms of 'super-acid' sites.

## 8.2 Methods

### *8.2.1 Catalyst Synthesis and Preparation*

H-USY (Engelhard, Si/Al = 2.8) and H-BEA (Zeolyst, Si/Al = 11.8) samples were treated in flowing dry air (2.5 $cm^3$ $g^{-1}$ $s^{-1}$, zero grade, Praxair) by heating to 773 K (at 0.0167 K $s^{-1}$) and holding for 4 h. A chemically-dealuminated USY sample (CD-$NH_4$USY, $Si/Al_{tot}$ = 7.5) was prepared by protocols reported in the LZ-210 patent [22]; this procedure has been shown to remove $Al_{ex}$ moieties selectively without significant removal of $Al_f$ atoms [23]. H-USY (Union Carbide, Si/Al = 2.9, 12 kg) was stirred in $H_2O$ (36 L) at 348 K while adding an aqueous 1.5 M $(NH_4)_2SiF_6$ solution (99%, 15 L, 323 K) continuously (at 1.67 g $s^{-1}$). Small batches (1.8 kg) of this treated zeolite slurry were then added to aqueous $Al_2(SO_4)_3$ solutions (0.6 M, 0.8 L) and stirred at 368 K for 24 h to decrease the $F^-$ content in the samples. The resulting solids were filtered and rinsed with 1 L $H_2O$ to yield CD-$NH_4$USY (~0.1 kg per batch). CD-HUSY was obtained by treating CD-$NH_4$USY in flowing dry air (2.5 $cm^3$ $g^{-1}$ $s^{-1}$, zero grade, Praxair) by heating to 773 K (at 0.0167 K $s^{-1}$) and holding for 4 h to convert $NH_4^+$ to $H^+$. H-USY and CD-HUSY samples were exposed to ambient air before structural and functional characterization.

H-USY, $NH_4$-CD-USY and CD-HUSY samples (0.5-2.0 g) were partially-exchanged with $Na^+$ cations by stirring in aqueous $NaNO_3$ (99%, EMD Chemicals) solutions (0.25 or 0.50 L) at 353 K for 12 h. The extent of $Na^+$ exchange was varied by changing the concentration of $NaNO_3$ in the exchange solution (0.001-0.150 M). These $Na^+$-exchanged zeolites were filtered and rinsed with 1 L of deionized water. $Na^+$-zeolites were treated in flowing dry air (2.5 $cm^3$ $g^{-1}$ $s^{-1}$, zero grade, Praxair) by heating to 773 K (at 0.0167 K $s^{-1}$) and holding for 4 h to convert residual $NH_4^+$ cations to $H^+$. Samples were exposed to ambient air before structural and functional characterization studies.

### *8.2.2 Catalyst Characterization*

$Al_f$ and $Al_{ex}$ contents were estimated from XRD and $^{27}Al$ MAS NMR spectroscopy. X-ray diffractograms of zeolite samples, after exposure to ambient air, were obtained using a Siemens D-5000 diffractometer and Cu-K$\alpha$ radiation. Lattice parameters were calculated from (533) reflections and used to estimate $Al_f$ content based on methods reported in the literature [24,25] (diffractograms and additional details in Section 8.6.1, Supporting Information). $^{27}Al$ MAS NMR spectra of zeolites were collected using a Bruker Avance 500 MHz spectrometer in a wide-bore 11.7 Tesla magnet (Caltech Solid State NMR Facility). Samples were held within a 4 mm $ZrO_2$ rotor and hydrated in a desiccator containing 1.0 M KCl for >48 h before sealing the rotor. NMR spectra were measured at 130.35 MHz using a 4 mm cross polarization (CP) MAS probe with the application of strong proton decoupling and with a magic angle spinning rate of 13 kHz. NMR spectra were acquired at ambient temperature from 512 scans with 0.5 μs pulses and a 6 s delay; they were referenced to aqueous 1.0 M $Al(NO_3)_3$ solutions.

The number and types of OH groups remaining after titration with different amounts of $Na^+$ or pyridine were measured from the intensity of OH vibrational bands (3400-3800 $cm^{-1}$) before and after titrant introduction. Infrared (IR) spectra were collected with a Nicolet NEXUS

670 Fourier-transform spectrometer equipped with a Hg-Cd-Te (MCT) detector by averaging 64 scans at 2 $cm^{-1}$ resolution in the 4000-400 $cm^{-1}$ range. Self-supporting wafers (5-15 mg $cm^{-2}$) were sealed within a quartz vacuum cell equipped with NaCl windows, treated in flowing dry air (1.67 $cm^3$ $s^{-1}$, zero grade, Praxair) at 773 K (at 0.033 K $s^{-1}$) and holding for 2 h, evacuated at 773 K for >2 h (<0.01 Pa dynamic vacuum; Edwards E02 diffusion pump), and cooled to 303 K in vacuum before collecting spectra. Acid sites were titrated with pyridine (99.8%, Aldrich) at 298 K and 450 K by incremental dosing without intervening evacuation; infrared spectra were collected after each dose. All infrared spectra were normalized by overtone and combination bands for zeolite framework vibrations (1750-2100 $cm^{-1}$).

Si, Al and Na contents were determined by inductively-coupled plasma optical emission spectroscopy (Galbraith Laboratories).

### *8.2.3 Methylation of OH Groups by Dimethyl Ether*

The number of protons in FAU zeolites was measured by titration with dimethyl ether at 438 K. Samples were placed in a quartz tube (7.0 mm i.d) held at 438 K using a resistively-heated three-zone furnace (Applied Test Systems Series 3210) and Watlow controllers (EZ-ZONE PM Series). Samples (0.10-0.12 g, 180-250μm) were held on a coarse quartz frit; temperatures were measured with a K-type thermocouple contained within a thermowell at the external tube surface.

Samples were treated in a flowing 5% $O_2$/He mixture (8.3 $cm^3$ $g^{-1}$ $s^{-1}$, 99.999%, Praxair) by heating to 773 K (at 0.025 K $s^{-1}$) and holding for 2 h, followed by cooling to 438 K (at 0.083 K $s^{-1}$) in flowing He (16.7 $cm^3$ $g^{-1}$ $s^{-1}$, 99.999%, Praxair). DME reactants (0.30 $cm^3$ $s^{-1}$, 99.8%, Praxair) were treated by passing over $CaH_2$ (99%, Aldrich) at ambient temperature to remove trace amounts of water and mixed with Ar (0.15 $cm^3$ $s^{-1}$, 99.999%, Praxair), used as an inert tracer, before flowing through a sample loop (420 K, 0.250 $cm^3$). This DME/Ar mixture was introduced as pulses onto samples via injection into flowing He (14.2 $cm^3$ $s^{-1}$ $g^{-1}$, 99.999%, Praxair) at 10 s intervals via heated transfer lines (420 K). A heated Si-coated stainless steel capillary (420 K, 0.254 mm i.d., 183 cm length) placed at the end of the quartz frit holding the samples brought the effluent into a mass spectrometer (MKS Spectra Minilab) to measure the concentrations of DME (m/z = 45, 46), $CH_3OH$ (m/z = 32), $H_2O$ (m/z = 18) and Ar (m/z = 40) every 0.7 s.

### *8.2.4 Isobutane Reaction Rates and Selectivities*

Isobutane cracking and dehydrogenation rates were measured at differential conversions (<2%) in a tubular packed-bed quartz reactor (7.0 mm i.d.) with plug-flow hydrodynamics at 763 K. Samples (0.01-0.05 g, 180-250μm) were held on a coarse quartz frit. Temperatures were set by a resistively-heated three-zone furnace (Applied Test Systems Series 3210) and Watlow controllers (96 Series) and measured with a K-type thermocouple held within a thermowell at the external surface of the quartz tube.

Catalysts were treated in 5% $O_2$/He flow (16.7 $cm^3$ $g^{-1}$ $s^{-1}$, 99.999%, Praxair) by heating to 803 K (at 0.0167 K $s^{-1}$) and holding for 2 h. This stream was replaced with He (16.7 $cm^3$ $g^{-1}$ $s^{-1}$, 99.999%, Praxair) for 0.5 h, while isobutane (10% i-$C_4H_{10}$, 5% Ar, 85% He, Praxair, 99.5% purity) was sent to a gas chromatograph (Agilent HP-6890GC) via heated lines (423 K) for calibration purposes. Reactant pressures (0.1-1.0 kPa i-$C_4H_{10}$) and molar rates ($10^{-6}$-$10^{-4}$ (mol $iC_4H_{10}$) $g^{-1}$ $s^{-1}$) were varied by diluting with inert He (99.999%, Praxair). Reactant and product concentrations were measured by flame ionization and thermal conductivity detectors after chromatographic separation (GS-AL\KCl Agilent capillary column, 0.530 mm ID x 50 m; HayeSep DB Sigma-Aldrich packed column, 100-120 mesh, 10 ft.). Rates and selectivities measured after ~12 h on stream were similar (within 5%) to initial steady-state values on all samples, indicating that rate and selectivity data were not affected by changes in the number, reactivity, or accessibility of active sites.

### *8.2.5 Methanol Dehydration Rates and Titration of $H^+$ with 2,6-di-tert-butyl Pyridine During Catalysis*

$CH_3OH$ conversion rates to dimethyl ether were measured at differential conditions (<1% conversion) at 433 K in the reactor setup described in section 2.3. Catalyst samples (0.01-0.05 g, 125-180 μm) were diluted with $SiO_2$ (Cab-o-sil, washed with 1.0 M $HNO_3$, 125-180 μm, >0.1 g total bed weight) and treated in dry air (99.999%, Praxair) by heating to 773 K (at 0.083 K $s^{-1}$) and holding for 2 h. Liquid $CH_3OH$ (Sigma-Aldrich; 99.8%; no additional purification) was evaporated into a stream of He (99.999%, Praxair) using a liquid syringe pump (Cole-Palmer 780200C series). Liquid deionized water was evaporated into a separate stream of He (99.999%, Praxair) using a liquid syringe pump (Cole-Palmer 74900 series) and mixed with the $CH_3OH$ reactant stream in order to examine the inhibition of dehydration rates by water. Reactants were transferred via heated lines (>393 K) to prevent the condensation of liquids. Reactant pressures (0.05-3.0 kPa $CH_3OH$, 0 or 0.6 kPa $H_2O$) and molar rates were changed by varying liquid flow rates. Concentrations of reactants, products, and titrants were determined by gas chromatography (Agilent 6890N GC) using flame ionization detection (DB-Wax capillary column; 0.320 mm ID x 30 m x 0.25 μm film; J&W Scientific) and mass spectrometry (MKS Spectra Minilab). Dimethyl ether and water were the only products observed under all reaction conditions examined. $SiO_2$ (0.1 g) did not lead to detectable product formation at the conditions used in this study. Conditions were periodically returned to a reference condition (0.6 kPa $CH_3OH$, 0.6 kPa $H_2O$, 433 K) to check for catalyst deactivation during kinetic experiments. Rates were similar to initial values at the reference condition (within 5% after 5h time-on-stream) indicating that deactivation was negligible on all samples.

The number of Brønsted acid sites was measured by titration with 2,6-di-*tert*-butyl pyridine during dehydration catalysis in the same reactor setup. Steady-state dehydration rates at 433 K were maintained before the introduction of titrant molecules. 2,6-di-*tert*-Butylpyridine (>97%; Aldrich; CAS #585-48-8) was dissolved in $CH_3OH$ (99.8%; Sigma-Aldrich) reactants and evaporated into a He stream (99.999%, Praxair) using a syringe pump to give their desired concentrations (0.40-0.55 Pa titrant). Titrant adsorption uptakes and dehydration rates were calculated during titrant injection from the concentrations of reactants, products, and titrant in the reactor effluent using the chromatographic protocols described above. The total number of

protons on each sample was calculated by extrapolating cumulative titrant uptake to zero dehydration rates and assuming 1:1 titrant:$H^+$ adsorption stoichiometries [26]. Titrations using pyridine (anhydrous, 99.8%; Aldrich) were conducted using the same protocols over a range of 0.30-3.0 Pa of pyridine.

## 8.3 Results and Discussion

### *8.3.1 Characterization of Aluminum Structure and Coordination in Zeolites*

Catalytic rates on acidic zeolites are often normalized by the number of framework Al atoms, which act as structural surrogates for protons that are assumed to exist in equimolar amounts to balance the framework negative charge. The different $^{27}$Al MAS NMR lines for tetrahedral $Al_f$ and octahedral $Al_{ex}$ atoms (60 and 0 ppm chemical shifts) can be used to distinguish these species, but Al centers in distorted environments give broad lines that often become undetectable [27,28]. $^{27}$Al MAS NMR spectra for H-USY, CD-HUSY and CD-$NH_4$USY, acquired after hydrating samples (section 2.2), are shown in Figure 8.1. CD-HUSY gave much sharper tetrahedral Al lines than H-USY (Fig. 8.1) and the latter, but not the former, showed a line at 0 ppm corresponding to octahedral Al centers. These spectra indicate that treatment of H-USY with $(NH_4)_2SiF_6$ removed Al centers in octahedral and distorted tetrahedral sites or converted them to tetrahedral Al centers through healing of structural defects. An octahedral Al NMR line appears in the spectrum of CD-HUSY (Fig. 8.1) upon removal of $NH_4$ by treatment in dry air at 773 K and subsequent exposure to ambient conditions. This reflects the extraction of some $Al_f$ atoms into $Al_{ex}$ moieties or the presence of Al species that can adopt tetrahedral or octahedral coordination depending on the temperature or the titrants (e.g., water, $NH_3$) with which they interact [29,30].

The fraction of total Al atoms present as $Al_f$ species, estimated from integrated intensities of tetrahedral and octahedral Al NMR lines, is 0.71 on H-USY and 0.75 on CD-HUSY (Table 8.1). The number of $Al_f$ atoms can also be inferred from XRD-derived FAU lattice constants because Al-O bonds are longer than Si-O bonds [24,25]; these methods (details and diffractograms in Section 8.6.1, Supporting Information) gave $Al_f/Al_{tot}$ ratios of 0.46 on H-USY and 0.74 on CD-HUSY (Table 8.1). Estimates of $Al_f$ content may be imprecise, however, because some Al atoms may not be detected in NMR spectra or may reside within distorted tetrahedral locations in extrazeolite phases. The *ex situ* conditions of these measurements, such as the hydration treatments at ambient temperature intended to weaken Al quadrupolar interactions and sharpen NMR lines, may also cause unintended structural changes that may be reversed at the conditions used for catalysis. Ultimately, $Al_f$ atoms are merely a structural surrogate for active sites, which are present as charge-balancing protons ($H^+$); as we show next, these sites can be counted directly and precisely at conditions more relevant to catalysis using chemical titrants.

**Table 8.1.** Elemental composition and structural characterization of zeolite samples.

| Zeolite | $Si/Al_{tot}$[a] | $Al_f/Al_{tot}$ | | $Si/Al_f$[b] | $Al_{ex}$/supercage[c] |
|---|---|---|---|---|---|
| | | *$^{27}$Al MAS NMR* | *XRD* | | |
| H-USY | 2.8 | 0.71 | 0.46 | 6.1 | <3.9 |
| CD-HUSY | 7.5 | 0.75 | 0.74 | 10.1 | <0.76 |
| CD-$NH_4$USY | 7.5 | 0.99 | n.m.* | 7.5 | <0.03 |

[a]Determined from elemental analysis (ICP-OES; Galbraith Laboratories).
[b]Determined from XRD for H-USY and CD-HUSY (details in Section 8.6.1, Supporting Information) and from $^{27}$Al MAS NMR for CD-$NH_4$USY (supporting text in Section 8.3.1).
[c]Upper bound for $Al_{ex}$ content (per supercage) estimated from $Al_f$ (by XRD or NMR) and $Al_{tot}$ (by elemental analysis) contents (details in Section 8.6.1, Supporting Information).
*n.m., not measured.

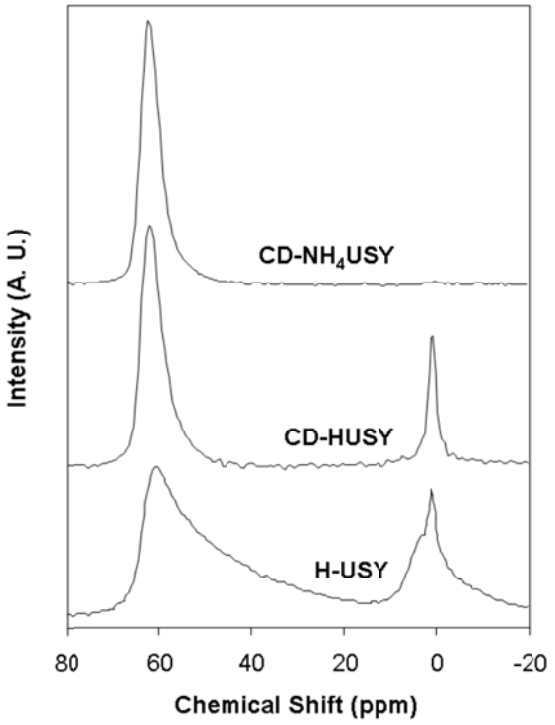


**Figure 8.1.** $^{27}$Al MAS NMR spectra of H-USY, CD-HUSY and CD-$NH_4$USY; chemical shifts referenced to $Al(NO_3)_3$.

*8.3.2 Titration of Brønsted Acid Sites in Zeolites*

The number of protons (or $NH_4^+$) on H-USY, CD-HUSY and CD-$NH_4$USY was determined by equilibrium exchange with $Na^+$ [31] under aqueous conditions at 353 K (section 2.1), according to:

$$Na^+_{aq} + \left[ SiO^- \left( X^+ \right) Al \right] \overset{K_X}{\longleftrightarrow} X^+_{aq} + \left[ SiO^- \left( Na^+ \right) Al \right]. \tag{8.1}$$

$X^+$ denotes the cation initially present ($H^+$ or $NH_4^+$) at anionic framework oxygen sites ($Al_{exch}$). The number of $X^+$ cations replaced as a function of $Na^+$ concentration in solution is described by the isotherm:

$$\theta_{Na^+} = \frac{Na^+}{Al_{tot}} = \left( \frac{Al_{exch}}{Al_{tot}} \right) \frac{K_X \left( Na^+ \right)_{aq} \Big/ \left( X^+ \right)_{aq}}{1 + K_X \left( Na^+ \right)_{aq} \Big/ \left( X^+ \right)_{aq}}, \tag{8.2}$$

in which $K_X$ is the equilibrium constant for the replacement of $X^+$ by $Na^+$ (derivation in Section 8.6.2, Supporting Information). Here, $\theta_{Na^+}$ reflects the $Na^+/Al_{tot}$ ratio after exchange, determined by elemental analysis; these values are plotted for H-USY, CD-HUSY and CD-$NH_4$USY against aqueous-phase $Na^+/X^+$ ratios in Figure 8.2. Saturation $Na^+$ exchange levels ($Al_{exch}/Al_{tot}$) were determined from $Na^+$ exchange data by regression to the form of Eq. (8.2). The difference between saturation $Na^+$ levels and $Na^+$ contents in partially-exchanged samples was taken as the number of residual $H^+$ sites after $Na^+$-exchange.

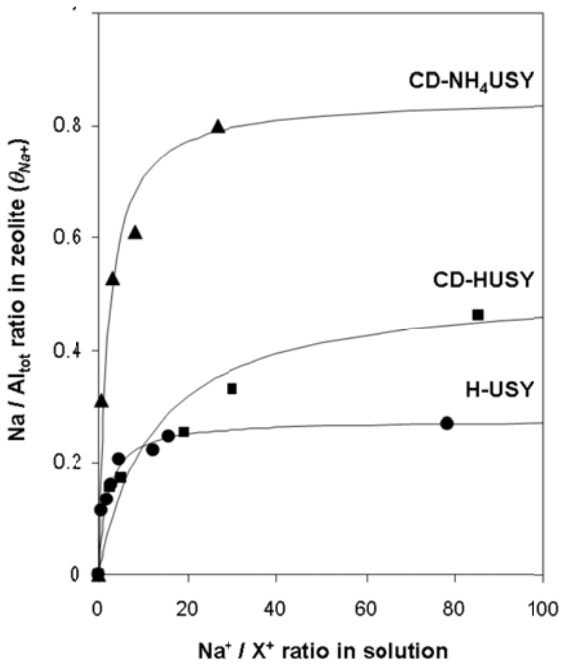


**Figure 8.2.** Aqueous-phase $Na^+$-exchange isotherms (353 K) for H-USY (●), CD-HUSY (■) and CD-$NH_4$USY (▲), where $X^+$ denotes the cation initially present on zeolite samples ($NH_4^+$ or $H^+$). Dashed curves represent the regressed best fits to Eq. (8.2). Saturation $Na^+$ exchange levels listed in Table 8.2.

Saturation $Na^+$ exchange levels (per $Al_{tot}$) were 0.28 on H-USY and 0.51 on CD-HUSY (Table 8.2), indicating that only a fraction of all the Al atoms contain a proton that can be exchanged by $Na^+$. These values were larger for CD-$NH_4$USY (0.85 $Na^+/Al_{tot}$; Table 8.2) than for CD-HUSY, suggesting that $NH_4$ removal by treatment in dry air at 773 K and subsequent exposure to ambient air to form CD-HUSY led to framework dealumination [3,32], which decreased the number of available exchange sites and, in turn, the number of protons available for exchange.

**Table 8.2.** Brønsted acid site titration of zeolite samples.

| **Zeolite** | **$H^+/Al_{tot}$** | | | **$H^+/Al_f$[a]** | **$Na/Al_f$ at zero turnover rate[b]** |
|---|---|---|---|---|---|
| | *Na* | *$CH_3$* | *2,6 di-tert-butylpyridine* | | |
| H-USY | 0.28 | 0.26 | 0.20 | 0.35 | $0.32 \pm 0.04$ |
| CD-HUSY | 0.51 | 0.53 | 0.50 | 0.69 | $0.72 \pm 0.05$ |
| CD-$NH_4$USY | 0.85 | n.m.* | n.m.* | 0.86 | n.m.* |

[a]Calculated from average $H^+$ count determined by the three titration methods and the $Al_f$ count determined by $^{27}Al$ MAS NMR (Table 8.1).
[b]$Na/Al_f$ ratios required for undetectable i-$C_4H_{10}$ cracking and dehydrogenation rates (from Fig. 8.7).
*n.m., not measured.

Infrared spectra of CD-HUSY and two $Na^+$-exchanged CD-HUSY samples are shown in Figure 8.3 (spectra of all CD-HUSY samples in Section 8.6.3, Supporting Information). They showed strong bands at 3630 and 3550 $cm^{-1}$, assigned to acidic OH groups vibrating within supercage and sodalite cages, respectively; weaker bands at 3740 $cm^{-1}$ (silanol OH) and 3675 $cm^{-1}$ (OH associated with $Al_{ex}$ species) were also detected [10,33]. The intensity of the acidic OH bands decreased linearly with increasing $Na^+/Al_{tot}$ ratio (Fig. 8.3 inset) and extrapolated to zero values at 0.56 $Na/Al_{tot}$ ratios, consistent with the maximum ion-exchange capacity of CD-HUSY (0.51 $Na/Al_{tot}$; Table 8.2) and with the complete replacement of $H^+$ by $Na^+$.

The infrared spectra of H-USY and two $Na^+$-exchanged H-USY samples are shown in Figure 8.4 (the other samples are included in Section 8.6.3, Supporting Information). In contrast with CD-HUSY, saturation $Na^+$ levels on H-USY did not fully remove OH bands (3660-3475 $cm^{-1}$), which retained a strong feature at 3600 $cm^{-1}$ (Fig. 8.4). The difference spectrum between H-USY samples before and after $Na^+$-exchange (Fig. 8.4) predominantly shows bands assigned to acidic OH groups centered at 3630 and 3550 $cm^{-1}$ (~90% of total difference spectrum area), indicating that $Na^+$ preferentially titrates $H^+$ sites. These findings sharply contrast previous reports that $Na^+$ selectively replaced 'super-acid' sites (but not isolated OH groups), which were assigned to a perturbed OH band at ~3600 $cm^{-1}$ [16]. We conclude that acidic OH groups are not responsible for the band at 3600 $cm^{-1}$, as also proposed earlier [10]; this band may instead reflect the presence of OH groups on the amorphous extrazeolite phases [23,34] that form during thermal treatment.

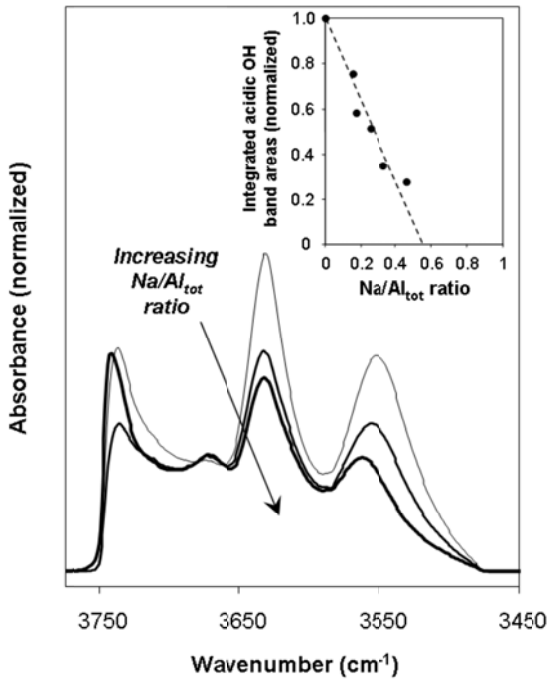


**Figure 8.3.** IR spectra of CD-HUSY samples with increasing $Na/Al_{tot}$ ratio (lighter to darker: 0.00, 0.25, 0.46); absorbance normalized to framework vibrations (1750-2100 $cm^{-1}$). Inset: Integrated acidic OH band areas (3500-3660 $cm^{-1}$) in difference spectra with respect to CD-HUSY (Fig. 8.12) plotted as a function of $Na/Al_{tot}$ ratio; dashed line represents line of best fit through the point at (0, 1) and extrapolates to zero intensity at $Na/Al_{tot} = 0.56$.

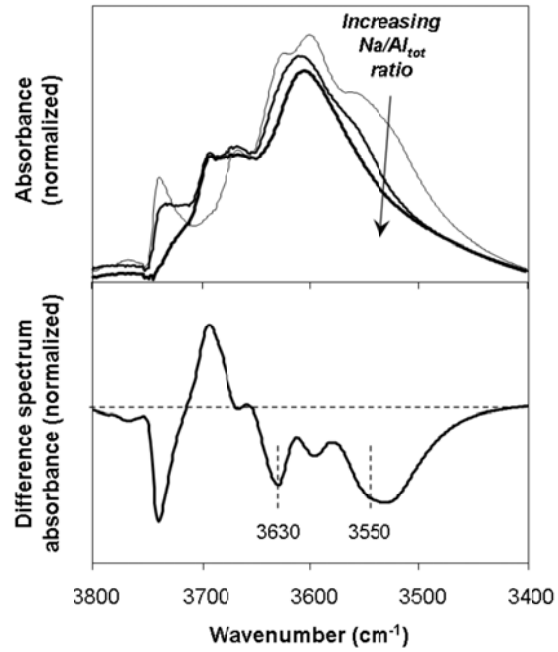


**Figure 8.4.** Top: IR spectra of H-USY samples with increasing $Na/Al_{tot}$ ratio (lighter to darker: 0.00, 0.16, 0.25); absorbance normalized to framework vibrations (1750-2100 $cm^{-1}$). Bottom: Difference spectrum of USY sample with saturation $Na^+$ levels ($Na/Al_{tot} = 0.25$) with respect to H-USY.

The number of protons in H-USY and CD-HUSY was also determined by sequential pulses of DME at 438 K to replace $H^+$ sites with $CH_3$ groups [35]:

$$CH_3OCH_3 + \left[SiO(H)Al\right] \longleftrightarrow \left[SiO(CH_3)Al\right] + CH_3OH\,, \tag{8.3}$$

$$CH_3OH + \left[SiO(H)Al\right] \longleftrightarrow \left[SiO(CH_3)Al\right] + H_2O\,. \tag{8.4}$$

DME and $CH_3OH$ concentrations were undetectable in the reactor effluent during the initial pulses on H-USY and CD-HUSY, consistent with the fast and irreversible nature of these methylation reactions. DME was detected in the effluent only after all protons were replaced by $CH_3$ groups (data in Section 8.6.4, Supporting Information), while methanol was never detected in the effluent stream. DME uptakes (0.5:1 DME:$H^+$; Eqs. (8.3) and (8.4) gave $H^+/Al_{tot}$ ratios of 0.26 and 0.53 on H-USY and CD-HUSY, respectively (Table 8.2). These values were similar, within experimental accuracy, to the respective maximum $Na^+$ exchange capacities of these samples (Table 8.2), but much smaller than expected if all $Al_f$ atoms (from $^{27}$Al MAS NMR spectra) were associated with one proton.

Finally, the number of protons in H-USY and CD-HUSY was measured *during* $CH_3OH$ dehydration catalysis at 433 K by their titration with 2,6-di-*tert*-butylpyridine (i.e. hindered pyridine). This base titrates only Brønsted acid sites because steric constraints around its N-atom prevent coordination to Lewis acid centers [26]. On both H-USY and CD-HUSY, $CH_3OH$ dehydration rates remained constant with time before titrant introduction and then decreased monotonically with increasing titrant uptakes (Fig. 8.5). Detectable rates (~20% of initial rates) persisted on both samples even at maximum uptakes (0.17 and 0.38 titrant per $Al_{tot}$ on H-USY and CD-HUSY, respectively). Titration of CD-HUSY with pyridine, which binds to both Brønsted and Lewis sites, gave larger maximum uptakes (0.66 pyridine per $Al_{tot}$) than with hindered pyridine, but similar residual rates after saturation uptakes (Fig. 8.5), indicating that methanol dehydration occurs at virtually undetectable rates on Lewis acid centers. The infrared spectrum of CD-HUSY after adsorption of 0.71 pyridine titrants (per $Al_{tot}$) at 298 K, showed bands for acidic OH groups vibrating in supercages (3630 $cm^{-1}$) and sodalite cages (3550 $cm^{-1}$) (Fig. 8.6). Bands for both OH groups weakened concurrently with increasing pyridine uptake (Fig. 8.6 inset), even though pyridine titrants cannot enter sodalite cages, because $H^+$ species migrate among the four O-atoms connected to each $Al_f$ atom (further discussion in Section 8.6.5, Supporting Information).

These infrared and kinetic data indicate that residual rates of $CH_3OH$ dehydration at saturation titrant uptakes reflect the presence of acid sites accessible to $CH_3OH$ but not to larger titrants. Thus, the total number of acid sites was determined by extrapolating hindered pyridine uptakes to zero dehydration rates, which gave values of 0.20 and 0.50 $H^+$ (per $Al_{tot}$) for H-USY and CD-HUSY, respectively (Table 8.2). These values are consistent with the number of $H^+$ measured by titration with $Na^+$ and DME (Table 8.2), but they are much smaller than the number of $Al_f$ atoms determined from $^{27}$Al MAS NMR spectra (Table 8.1). Previous studies have also reported that the number of adsorbed amine titrants on chemically-dealuminated FAU was much smaller than the number of $Al_f$ atoms determined from XRD-derived lattice constants [13].

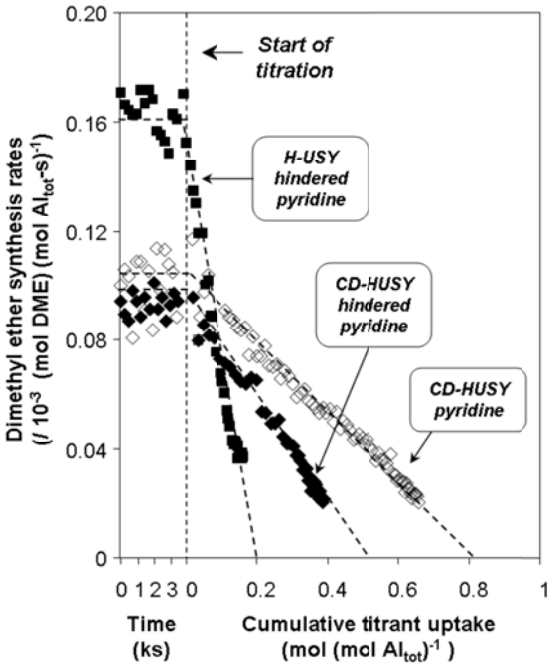


**Figure 8.5.** Dimethyl ether synthesis rates (0.3 kPa $CH_3OH$ and 0 kPa $H_2O$ in feed, 433 K), *per total Al*, as a function time on CD-HUSY (◆) and H-USY (■) before 2,6-di-*tert*-butylpyridine introduction and on CD-HUSY before pyridine introduction (◇), and as a function of cumulative titrant uptake.

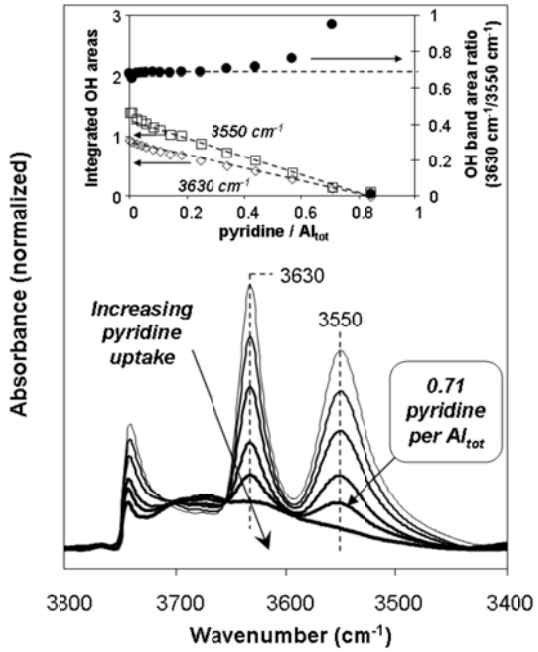


**Figure 8.6.** IR spectra of CD-HUSY with increasing pyridine uptake (lighter to darker) at 298 K. The spectrum corresponding to a pyridine uptake (0.71 pyridine/$Al_{tot}$) near saturation levels during methanol dehydration catalysis (0.66 pyridine/$Al_{tot}$, Fig. 8.5), is indicated. Inset: Integrated areas of acidic OH bands centered at 3630 $cm^{-1}$ (◇) and 3550 $cm^{-1}$ (□) and their ratio (●) plotted as a function of pyridine uptake.

Dehydroxylation and framework dealumination events decrease the number of protons available for titration or catalysis and form non-tetrahedral Al species that are incapable of balancing charge. Yet, $H^+/Al_f$ ratios *decreased* monotonically (Table 8.2) as tetrahedral (60 ppm) lines broadened in $^{27}Al$ MAS NMR spectra (Fig. 8.1), reflecting the presence of Al centers with distorted tetrahedral or five-fold coordination [29,30,32,36] or quadrupolar broadening effects induced by $Al_{ex}$ species proximal to $Al_f$ sites [36,37]. These data suggest that some non-tetrahedral Al sites apparently remain detected as tetrahedral centers and, in turn, that the prevailing interpretations of $^{27}Al$ MAS NMR spectra can lead to imprecise estimates of the number of $Al_f$ atoms. Yet, even precise $Al_f$ counts would preclude rigorous determination of catalytic turnover rates because these atoms are structural proxies for active Brønsted acid sites.

### *8.3.3 Catalytic Consequences of $Na^+$ Titration for Monomolecular Isobutane Activation*

Monomolecular reactions of isobutane over zeolitic Brønsted acid sites prevail at high temperatures and low alkene product pressures, as shown by experiment [38-40] and theory [41-43]. Catalytic sequences involve quasi-equilibrated adsorption of gaseous alkanes (A(g)) within zeolite channels (A(z)) that contain the active sites ($H^+Z^-$) and the subsequent protonation of C-C and C-H bonds in kinetically-relevant steps for cracking and dehydrogenation, respectively (Scheme 8.1) [44]. At the conditions required for monomolecular alkane activation, intrazeolite alkane concentrations are low and proportional to alkane pressures ($P_A$) [44] and rates are given by:

$$r = K_{ads} k_{int} P_A = k_{meas} P_A \,. \tag{8.5}$$

where $K_{ads}$ is the equilibrium constant for alkane adsorption on Brønsted acid sites, $k_{int}$ is the intrinsic rate constant for alkane C-C or C-H bond scission, and $k_{meas}$ is the measured first-order rate constant. Measured rate constants for isobutane cracking and dehydrogenation on H-USY and CD-HUSY did not vary with reactor residence time or with the concomitant changes in alkane conversion. Cracking led to equimolar $CH_4$ and $C_3H_6$ mixtures and dehydrogenation routes formed $H_2$ and isobutene; the latter isomerized to an equilibrated mixture of linear butene isomers with increasing residence time (data in Section 8.6.6, Supporting Information).

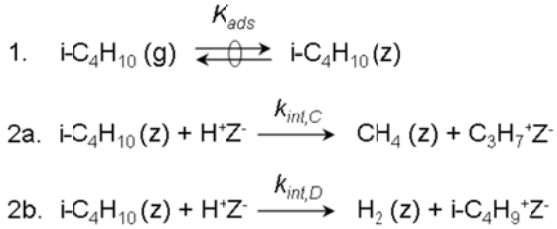


**Scheme 8.1.** Accepted pathways for monomolecular isobutane activation involve quasi-equilibrated adsorption (Step 1) from the gas phase (g) into zeolite channels (z) and subsequent reaction on Brønsted acid sites ($H^+Z^-$) in kinetically-relevant cracking (Step 2a) or dehydrogenation (Step 2b) steps.

Isobutane cracking and dehydrogenation rates, normalized by the number of $Al_f$ atoms (from $^{27}Al$ MAS NMR; Table 8.1), decreased monotonically with increasing $Na^+$ content and extrapolated to zero values at $Na/Al_f$ ratios of 0.32 on H-USY and 0.72 on CD-HUSY (Fig. 8.7). These strong effects of 'sub-stoichiometric' $Na^+$ concentrations led to previous claims that $Na^+$ cations preferentially titrated uniquely active protons in H-USY, purported to become 'super-acidic' as a result of stabilization of the conjugate base by $Al_{ex}$ species acting as Lewis acids [15-17] in a manner analogous to liquid superacids consisting of Brønsted-Lewis pairs. Yet, the $Na/Al_f$ ratios required to fully suppress catalytic rates on both H-USY ($0.32 \pm 0.04$) and CD-HUSY ($0.72 \pm 0.05$) are *identical*, within experimental accuracy, to the $H^+/Al_f$ ratios on these samples (0.35 and 0.69, respectively, Table 8.2) determined from average chemical titration values and $^{27}Al$ MAS NMR spectra.

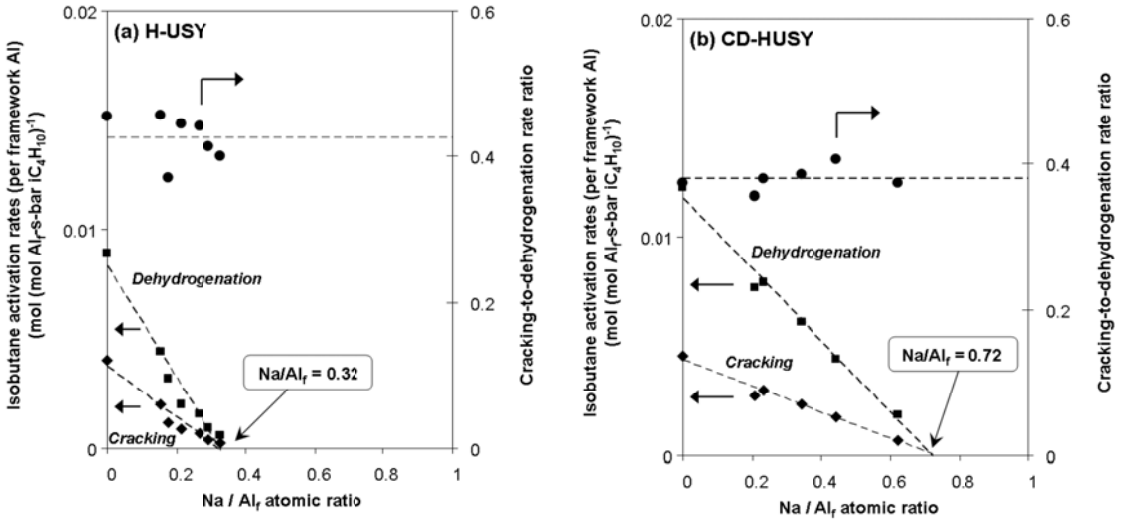


**Figure 8.7.** Monomolecular isobutane cracking (◆) and dehydrogenation (■) rates (763 K), *per framework Al*, and their ratio (●) as a function of $Na/Al_f$ atomic ratio on (a) H-USY and (b) CD-HUSY.

Isobutane cracking and dehydrogenation rates, normalized by the number of residual $H^+$, and the ratio of these rates did not depend on $Na^+$ content on H-USY and CD-HUSY samples (Fig. 8.8). These data indicate that $Na^+$ cations *stoichiometrically* replaced all protons *and that they are uniform in reactivity* within each sample. Isobutane cracking and dehydrogenation rate constants (per $H^+$, 763 K), however, were larger on H-USY than on CD-HUSY (by a factor of 1.8; Table 8.3). These $k_{meas}$ values measure the free energies of their respective monomolecular transition states relative to gaseous isobutane; as a result, $k_{meas}$ values increase as acids become stronger and as zeolite voids decrease in size because transition states are stabilized more effectively by electrostatic or van der Waals forces, respectively. In the section that follows, we use methanol dehydration to assess the independent effects of acid strength and solvation on turnover rates. In contrast with monomolecular alkane activation, Brønsted acid sites need not be predominantly unoccupied for methanol dehydration paths to prevail; in turn, DME formation transition states can be measured with respect to intermediates that are similar to and different from them in charge and size.

**Table 8.3.** First-order rate constants (763 K) for monomolecular isobutane cracking ($k_{meas,C}$) and dehydrogenation ($k_{meas,D}$) and their ratio on H-USY and CD-HUSY (from Fig. 8.8).

| Zeolite | $k_{meas,C}$ | $k_{meas,D}$ | $k_{meas,C}$ / $k_{meas,D}$ |
|---|---|---|---|
| | (mol (mol $H^+$-s-bar $iC_4H_{10}$)$^{-1}$) | | |
| H-USY | 0.012 | 0.029 | 0.43 |
| CD-HUSY | 0.0067 | 0.018 | 0.38 |

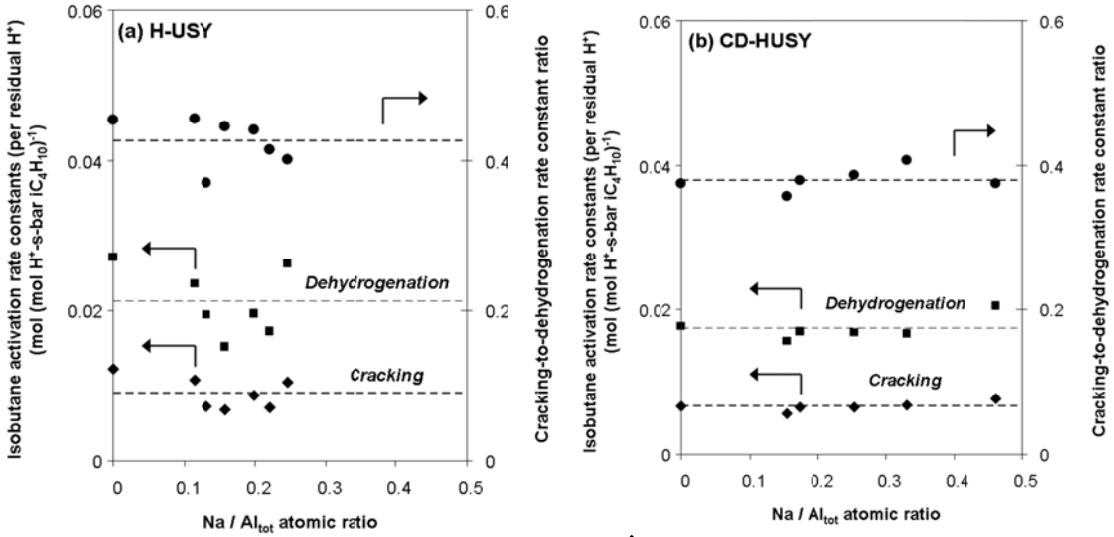


**Figure 8.8.** First-order for monomolecular isobutane cracking (◆) and dehydrogenation (■) rate constants (763 K), *per residual* $H^+$, and their ratio (●) as a function of $Na/Al_{tot}$ atomic ratio on (a) H-USY and (b) CD-HUSY.

### *8.3.4 Assessment of Acid Strength and Solvation Effects Using Methanol Dehydration to Dimethyl Ether*

Brønsted acid sites catalyze $CH_3OH$ dehydration to DME via the sequential quasi-equilibrated adsorption of two $CH_3OH$ molecules to form protonated dimer intermediates; these dimers directly eliminate $H_2O$ and form DME in a concerted kinetically-relevant step (mechanistic details in Section 8.6.7, Supporting Information) [45]. The cationic transition states involved in kinetically-relevant DME formation steps are stabilized by electrostatic interactions with the anionic conjugate base, provided here by the aluminosilicate zeolite framework. The energy of these transition states depends on the deprotonation energy (DPE) of the Brønsted acid sites, which provides a rigorous measure of acid strength. These transition states are also stabilized by van der Waals interactions when confined within microporous zeolite channels, but not when present at tungsten polyoxometalate (POM) Keggin clusters supported on amorphous silica. $CH_3OH$ dehydration rates, normalized by the number of $H^+$ accessible to 2,6-di-*tert*-butylpyridine, on POM clusters of varying central atom (P, Si, Al, Co) and H-BEA are given by [45]:

$$\frac{r}{\left[H^+\right]} = \frac{k_{mono} P_{CH_3OH}}{1 + \left(k_{mono}/k_{dimer}\right) P_{CH_3OH}}. \tag{8.6}$$

in which $k_{mono}$ and $k_{dimer}$ are measured first and zero-order rate constants, respectively. Methanol dehydration rates (433 K) on H-BEA, H-USY and CD-HUSY are shown as a function of $CH_3OH$ pressure in Figure 8.9, along with curves that represent the best fit of these data to the form of Eq. (7).

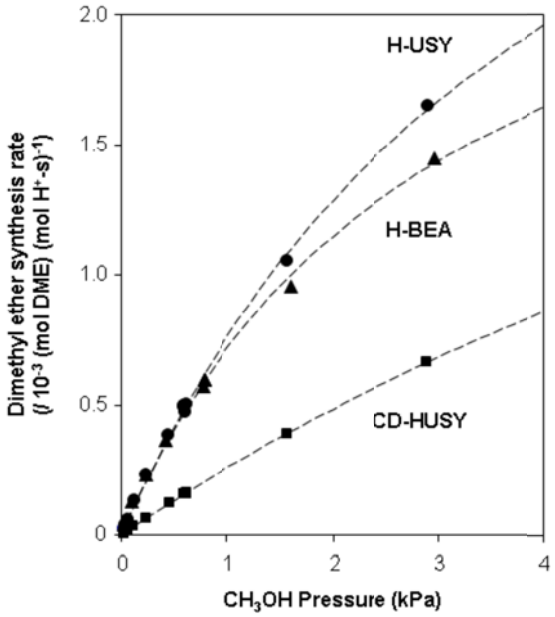


**Figure 8.9.** Dimethyl ether synthesis rates (0.6 kPa $H_2O$ in feed, 433 K), normalized by the number of $H^+$ determined from *in situ* titration of $H^+$ by 2,6-di-*tert*-butylpyridine, as a function of $CH_3OH$ pressure on H-USY (●), CD-HUSY (■) and H-BEA (▲). Dashed curves represent the regressed best fits to Eq. (8.6).

Zero-order methanol dehydration rate constants reflect free energy differences between DME formation transition states and protonated $CH_3OH$ dimer intermediates (Scheme 8.2) [46]. Transition states and dimer precursors are similarly stabilized by van der Waals forces because two methanol molecules are confined within zeolite pores for both species; as a result, the different $k_{dimer}$ values on Keggin POM and H-BEA predominantly reflect differences in their acid strength [45]. Values of $k_{dimer}$ on H-USY and CD-HUSY are similar to each other and to the value measured on H-BEA (within a factor of 1.3; Table 8.4), indicating that acid sites are similar in strength among these zeolites (DPE values within 10 kJ $mol^{-1}$ based on the reactivity-DPE relation found for POM clusters [45]). These data reflect the weak dependence of acid strength on framework structure, as also concluded from the similar DPE values for zeolitic acids (FAU, MFI, MOR, CHA) calculated from theory [5,46,47].

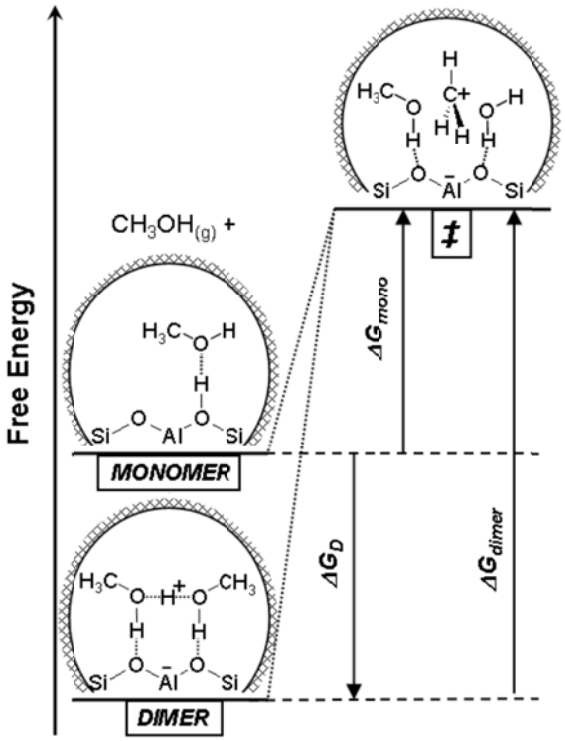


**Scheme 8.2.** Free energy differences between the dimethyl ether formation transition state and either a protonated $CH_3OH$ dimer ($\Delta G_{dimer}$) or one gaseous $CH_3OH$ molecule and one adsorbed $CH_3OH$ monomer ($\Delta G_{mono}$) are reflected in zero-order ($k_{dimer}$) or first-order ($k_{mono}$) methanol dehydration rate constants, respectively (mechanism in Section 8.6.6, Supporting Information).

**Table 8.4.** Zero-order ($k_{dimer}$) and first-order ($k_{mono}$) rate constants for $CH_3OH$ dehydration (433 K) on H-USY, CD-HUSY and H-BEA (from Fig. 8.9).

| **Zeolite** | $\mathbf{k_{dimer}}$ ($/10^{-3}$ (mol DME) (mol $H^+$-s)$^{-1}$) | $\mathbf{k_{mono}}$ ($/10^{-3}$ (mol DME) (mol $H^+$-kPa $CH_3OH$-s)$^{-1}$) |
|---|---|---|
| H-USY | 4.1 | 0.94 |
| CD-HUSY | 3.8 | 0.28 |
| H-BEA | 2.9 | 0.96 |

First-order methanol dehydration rate constants, on the other hand, compare the free energies of DME formation transition states stabilized within zeolite voids to the combined free energies of one adsorbed $CH_3OH$ monomer and one gaseous $CH_3OH$ molecule (Scheme 8.2). Transition states contain an additional $CH_3OH$ moiety than monomer intermediates and are therefore preferentially stabilized by van der Waals interactions with pore walls. Values of $k_{mono}$ depend only on DPE for Keggin POM clusters, for which confinement effects are small and the same for all clusters, but the value for H-BEA is ~100 times larger than predicted for a POM acid of equivalent DPE because of stronger van der Waals interactions [45]. The value of $k_{mono}$ was larger on H-USY than on CD-HUSY (by a factor of 3.4, Table 8.4) indicating that van der Waals interactions are stronger, and supercage void spaces concomitantly smaller [33,48], on H-USY. This appears to contradict the larger supercage voids expected in H-USY from its larger unit cell size (Table 8.5, Supporting Information); however, treatment of H-USY with

$(NH_4)_2SiF_6$ (to form CD-HUSY) increases void size, estimated from $^{129}Xe$ NMR chemical shifts and argon adsorption isotherms [28,49], via the removal of extraframework Al debris that occludes void space. The similar $k_{mono}$ values between H-USY and H-BEA (Table 8.4) appear, at first glance, to reflect similar solvation effects and pore sizes between these samples; however, accounting for the small differences in their $k_{dimer}$ (and therefore DPE) values indicates that solvation effects are stronger in H-BEA (detailed treatment in Section 8.8.8, Supporting Information). Thus, the higher $Al_{ex}$ content in H-USY supercages (Table 8.1) apparently results in void spaces that are smaller than CD-HUSY supercages (~1.3 nm diameter, $Al_{ex}$-free), but larger than H-BEA channels (~0.7 nm diameter).

These findings and their conceptual interpretation seem to resolve issues that have persisted for decades regarding the mechanistic origin of the effects of $Na^+$ and extraframework Al species in catalysis by FAU zeolites. They underscore the requirement that turnover rates be normalized rigorously by the number of active sites before interpreting the origins of reactivity. They also highlight the importance of measuring active sites directly and, if at all possible, during catalysis. In this case, the distractions of using imprecise structural surrogates ($Al_f$) for the active sites ($H^+$) to normalize rates have led to the incorrect attribution of reactivity to 'super-acid' sites.

## 8.4 Conclusions

Kinetic and spectroscopic studies of FAU zeolites treated thermally (H-USY) and then chemically with ammonium hexafluorosilicate (CD-HUSY) were used to examine the effects of extraframework aluminum ($Al_{ex}$) and $Na^+$ species on the number and strength of Brønsted acid sites, and on catalytic rates of isobutane cracking and dehydrogenation (763 K) and of methanol dehydration (433 K). The number of $H^+$ sites on H-USY and CD-HUSY were counted directly by titration with 2,6-di-*tert*-butylpyridine *during* $CH_3OH$ dehydration catalysis (433 K), with dimethyl ether to form $CH_3$ groups (438 K) and with $Na^+$ (353 K). These methods gave similar values for the number of protons on each sample, which were smaller than the number of framework aluminum ($Al_f$) atoms (0.35 and 0.69 $H^+/Al_f$ on H-USY and CD-HUSY, respectively) estimated by $^{27}Al$ MAS NMR. Thus, $Al_f$ atoms are imprecise structural proxies for Brønsted acid sites on FAU zeolites, illustrating the requirement that the number of active sites be measured directly and, when possible, during catalysis.

Turnover rates of monomolecular isobutane cracking and dehydrogenation, normalized rigorously by the number of residual $H^+$ on $Na^+$-exchanged H-USY and CD-HUSY samples, were independent of $Na^+$ content, reflecting the stoichiometric replacement of catalytically-equivalent protons by $Na^+$ cations. These data sharply contrast previous reports [15-17] that claimed $Na^+$ selectively titrated 'super-acidic' $H^+$ sites, formed via electronic interactions with $Al_{ex}$ species. These 'super-acidic' $H^+$ sites, purported to comprise a small fraction of all protons, were invoked to account for artifacts that result from normalizing rates non-rigorously by the number of $Al_f$ atoms.

Zero-order rate constants for methanol dehydration, which depend predominantly on acid strength (DPE), were similar (within a factor of 1.1) on H-USY and CD-HUSY. In contrast, first-

order rate constants for monomolecular isobutane activation and methanol dehydration, which reflect the combined effects of acid strength and solvation, were higher by factors of 1.8 and 3.4, respectively, on H-USY than CD-HUSY. These data reflect stronger van der Waals interactions within H-USY supercages, which are apparently smaller in size because they contain $Al_{ex}$ species that occlude void space. Thermal and chemical treatments of FAU zeolites, which change the distribution of aluminum atoms between framework and extraframework phases and thus the sizes of supercage voids, predominantly influence their solvation properties and not the strength of their Brønsted acid sites.

## 8.5 Acknowledgements

I acknowledge Andrew Jones and Robert Carr for their helpful discussions and their technical and intellectual contributions to this work. We thank Dr. Stacey I. Zones (Chevron) and Prof. Raul F. Lobo (Univ. of Delaware) for helpful technical discussions. We also thank Roger F. Vogel (Chevron) for preparing the CD-USY sample, Dr. Sonjong Hwang (Caltech) for the $^{27}Al$ MAS NMR data and Dr. Jinyi Han (Chevron) for the X-ray diffractograms. We also acknowledge with thanks financial support from the Chevron Energy Technology Company for these studies.

## 8.6 Supporting Information

### *8.6.1 X-ray Diffraction of Zeolite Samples and Estimation of Extraframework Aluminum Content*

The powder X-ray diffractograms of H-USY and CD-HUSY are shown in Figure 8.10. Lattice parameters ($a_o$) determined from (533) reflections were identical, within experimental error, to averaged $a_o$ values determined from individual *hkl* planes between 5-25° 2θ; the lattice parameters (Table 8.5) were 2.449 nm for H-USY and 2.440 nm for CD-HUSY, indicating that unit cells are larger in H-USY. The number of framework Al ($Al_f$) atoms per unit cell ($N_{Alf}$; Table 8.5) on each sample was estimated using correlations reported by Fichtner-Schmittler et al. [50] (Eq. (8.7)) and Sohn et al. [24] (Eq. (8.8)):

$$N_{Alf} = 112.4\left(a_o - 24.233\right). \tag{8.7}$$

$$N_{Alf} = 107.1\left(a_o - 24.238\right). \tag{8.8}$$

$Si/Al_f$ and $Al_f/Al_{tot}$ ratios (Table 8.5) were calculated from $N_{Alf}$ values and total Si/Al ratios determined by elemental analysis. $Al_f$ contents are higher on H-USY ($Si/Al_f$ = 6.1) than CD-HUSY ($Si/Al_f$ = 10.1), but the fraction of total Al within the zeolite framework is lower on H-USY ($Al_f/Al_{tot}$ = 0.46) than CD-HUSY ($Al_f/Al_{tot}$ = 0.74).

**Table 8.5.** The number of framework Al atoms per unit cell ($N_{Alf}$), determined from lattice parameters ($a_o$) and correlations reported by Fichtner-Schmittler et al. (*FS*, [50]) and Sohn et al. (*S*, [24]) on H-USY and CD-HUSY. Corresponding $Si/Al_f$, $Al_f/Al_{tot}$, and $Al_{ex}$/supercage ratios determined from $N_{Alf}$, elemental analysis, and Eqs. (8.9)-(8.11).

| Zeolite | $a_O$ (nm) | $N_{Alf}$ | | $Si/Al_f$ | | $Al_f/Al_{tot}$ | | $Al_{ex}$/supercage | |
|---|---|---|---|---|---|---|---|---|---|
| | | *FS* | *S* | *FS* | *S* | *FS* | *S* | *FS* | *S* |
| H-USY | 2.449 | 28.9 | 27.0 | 5.6 | 6.1 | 0.50 | 0.46 | 0.76 | 0.56 |
| CD-HUSY | 2.440 | 18.8 | 17.4 | 9.2 | 10.1 | 0.81 | 0.74 | 3.94 | 3.62 |

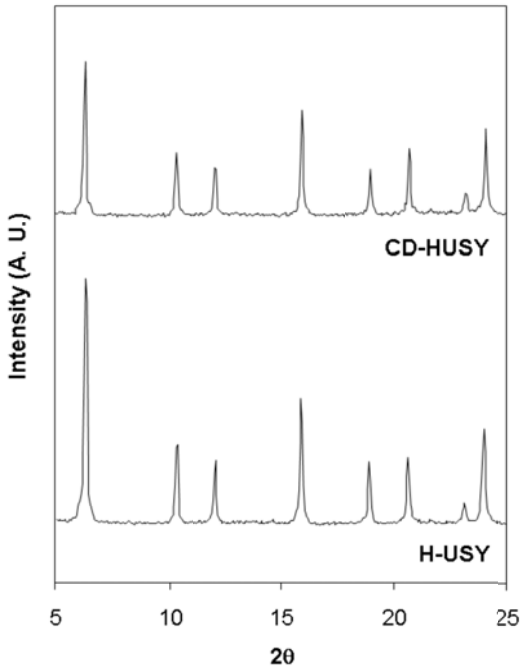


**Figure 8.10.** Powder X-ray diffractograms of H-USY and CD-HUSY.

These data were also used to estimate an upper bound on the number of extraframework ($Al_{ex}$) species present within each supercage in H-USY and CD-HUSY. The $Si/Al_{ex}$ ratio, together with the requirement that all Al must be present in either framework or extraframework phases ($Al_{tot} = Al_f + Al_{ex}$), is given by:

$$\frac{Si}{Al_{ex}} = \left( \left( \frac{Si}{Al_{tot}} \right)^{-1} - \left( \frac{Si}{Al_f} \right)^{-1} \right)^{-1} . \tag{8.9}$$

The number of framework Si atoms ($N_{Sif}$) per FAU unit cell can be determined from the unit cell atomic composition and $N_{Alf}$, estimated by XRD:

$$N_{Sif} = 192 - N_{Alf} . \tag{8.10}$$

Assuming that all Si atoms are contained within the framework, the number of $Al_{ex}$ atoms per unit cell ($N_{Alex}$) can be determined from the $Si/Al_{ex}$ ratio and $N_{Sif}$ by:

$$N_{Alex} = \frac{N_{Sif}}{Si/Al_{ex}}. \tag{8.11}$$

This value for $N_{Alex}$ can be used to estimate the number of $Al_{ex}$ atoms per supercage, of which there are eight per unit cell, assuming that all $N_{Alex}$ species are located within supercage voids. This $Al_{ex}$/supercage ratio is an *upper bound* because some of the $Al_{ex}$ species may be located within sodalite cages or in extracrystalline phases.

The following example calculations are shown for H-USY ($Si/Al_{tot}$ = 2.8; Table 8.1), using XRD-derived values ($N_{Alf}$ = 27.0, $Si/Al_f$ = 6.1; Table 8.5):

$$\frac{Si}{Al_{ex}} = \left( (2.8)^{-1} - (6.1)^{-1} \right)^{-1} = 5.2, \tag{8.12}$$

$$N_{Sif} = 192 - 27 = 165, \tag{8.13}$$

$$N_{Alex} = \frac{165}{5.2} = 31.7, \tag{8.14}$$

which yields an upper bound of 3.9 $Al_{ex}$ species per supercage.

### *8.6.2 Thermodynamics of Aqueous-Phase $Na^+$-exchange of Zeolite Samples*

The total number of Al atoms ($Al_{tot}$) on a given zeolite sample can be expressed as the sum of the number of Al atoms that generate anionic framework oxygen sites capable of ion-exchange ($Al_{exch}$) and the number of those that do not ($Al_{non\text{-}exch}$):

$$Al_{tot} = Al_{non-exch} + \sum_i Al_{exch,i}. \tag{8.15}$$

In Eq. (8.15), each $Al_{exch,i}$ term reflects exchange sites occupied by a distinct monovalent cation *i* (e.g., $H^+$, $NH_4^+$, $Na^+$). For the specific case of $Na^+$ exchange onto H-zeolites, normalizing Eq. (8.15) by $Al_{tot}$ gives:

$$1 = \frac{Al_{non-exch}}{Al_{tot}} + \frac{Al_{exch}}{Al_{tot}} = \frac{Al_{non-exch}}{Al_{tot}} + \frac{Al_{exch,H^+}}{Al_{tot}} + \frac{Al_{exch,Na^+}}{Al_{tot}} = \theta_{Al_{non-exch}} + \theta_{H^+} + \theta_{Na^+}, \tag{8.16}$$

where $\theta_{H^+}$ and $\theta_{Na^+}$ are intrazeolite $H^+$ and $Na^+$ contents (per $Al_{tot}$), respectively. Eq. (8.16) can be rearranged to give an expression for $\theta_{H^+}$ in terms of $\theta_{Na^+}$:

$$\theta_{H^+} = \left(1 - \theta_{Al_{non-exch}}\right) - \theta_{Na^+} = \frac{Al_{exch}}{Al_{tot}} - \theta_{Na^+} . \tag{8.17}$$

The aqueous-phase exchange of $Na^+$ onto H-zeolites (353 K) is described by the following equilibrium reaction:

$$Na^+_{aq} + \left[SiO^-\left(H^+\right)Al\right] \overset{K}{\longleftrightarrow} H^+_{aq} + \left[SiO^-\left(Na^+\right)Al\right] . \tag{8.18}$$

in which the equilibrium constant ($K$), assuming all components behave ideally, is given by:

$$K = \frac{\left[H^+\right]_{aq}}{\left[Na^+\right]_{aq}} \frac{\left[SiO^-\left(Na^+\right)Al\right]}{\left[SiO^-\left(H^+\right)Al\right]} = \frac{\left[H^+\right]_{aq}}{\left[Na^+\right]_{aq}} \frac{\theta_{Na^+}}{\theta_{H^+}} . \tag{8.19}$$

Combining Eqs. (8.17) and (8.19) and rearranging the resulting expression:

$$K \frac{\left[Na^+\right]_{aq}}{\left[H^+\right]_{aq}} = \frac{\theta_{Na^+}}{Al_{exch}/Al_{tot} - \theta_{Na^+}} . \tag{8.20}$$

This equation can be rearranged to obtain a Langmuirian dependence for $\theta_{Na^+}$ on the ratio of $Na^+$ and $H^+$ aqueous-phase concentrations:

$$\theta_{Na^+} = \left(\frac{Al_{exch}}{Al_{tot}}\right) \frac{K\left[Na^+\right]_{aq} \Big/ \left[H^+\right]_{aq}}{1 + K\left[Na^+\right]_{aq} \Big/ \left[H^+\right]_{aq}} . \tag{8.21}$$

This treatment can be used to derive an analogous expression for $Na^+$ exchange onto $NH_4$-zeolites.

### *8.6.3 Infrared Studies of $Na^+$ Titration of $H^+$ Sites*

Infrared spectra of Na-exchanged CD-USY samples and difference spectra (with respect to CD-HUSY) are displayed in Figures 8.11 and 8.12, respectively. These spectra show OH bands at 3630 $cm^{-1}$ (acidic supercage OH), 3550 $cm^{-1}$ (acidic sodalite cage OH ), 3740 $cm^{-1}$ (silanol OH), and 3675 $cm^{-1}$ (OH groups associated with $Al_{ex}$ species) [10,33]. Infrared spectra of Na-exchanged USY samples and difference spectra (with respect to H-USY) are shown in Figures 8.13 and 8.14, respectively. These spectra show an additional band at 3600 $cm^{-1}$, which may reflect OH groups on amorphous extrazeolite phases formed during thermal treatment.

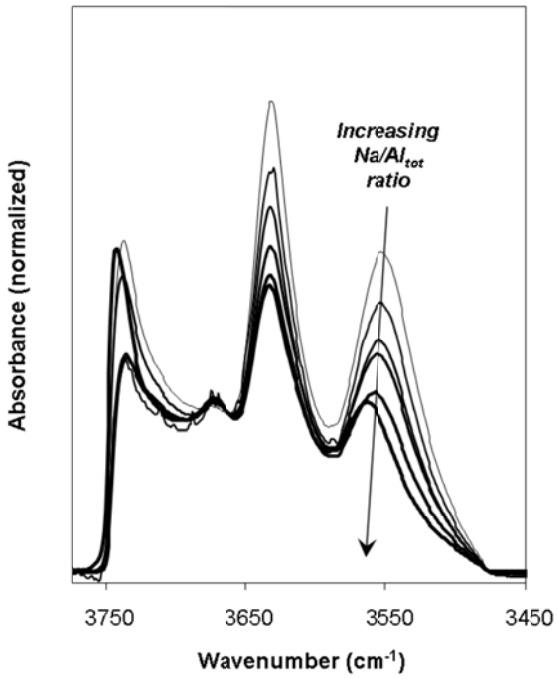


**Figure 8.11.** IR spectra of CD-HUSY samples with increasing $Na/Al_{tot}$ ratio (lighter to darker: 0.00, 0.15, 0.17, 0.25, 0.33, 0.46); absorbance normalized to framework vibrations (1750-2100 $cm^{-1}$).

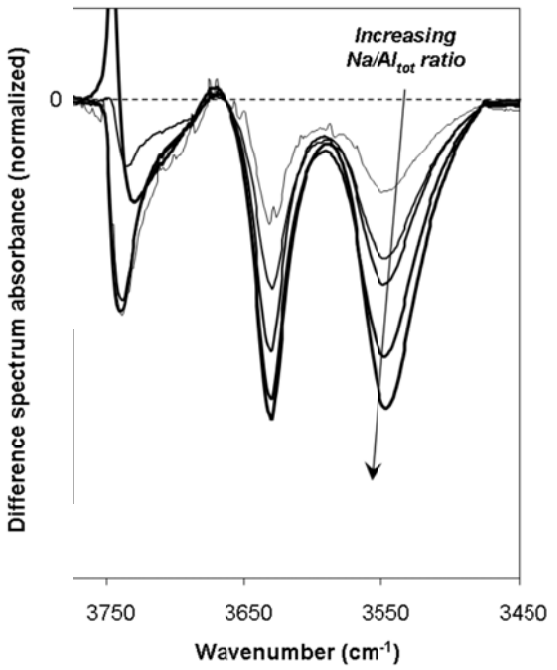


**Figure 8.12.** Difference IR spectra of CD-HUSY samples with increasing $Na/Al_{tot}$ ratio (lighter to darker: 0.15, 0.17, 0.25, 0.33, 0.46) with respect to CD-HUSY; absorbance normalized to framework vibrations (1750-2100 $cm^{-1}$).

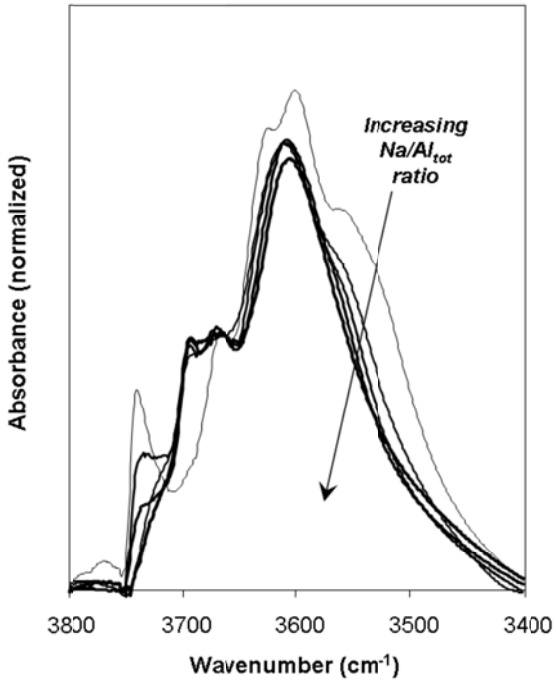


**Figure 8.13.** IR spectra of H-USY samples with increasing Na/Al$_{tot}$ ratio (lighter to darker: 0.00, 0.13, 0.16, 0.20, 0.25); absorbance normalized to framework vibrations (1750-2100 cm$^{-1}$).

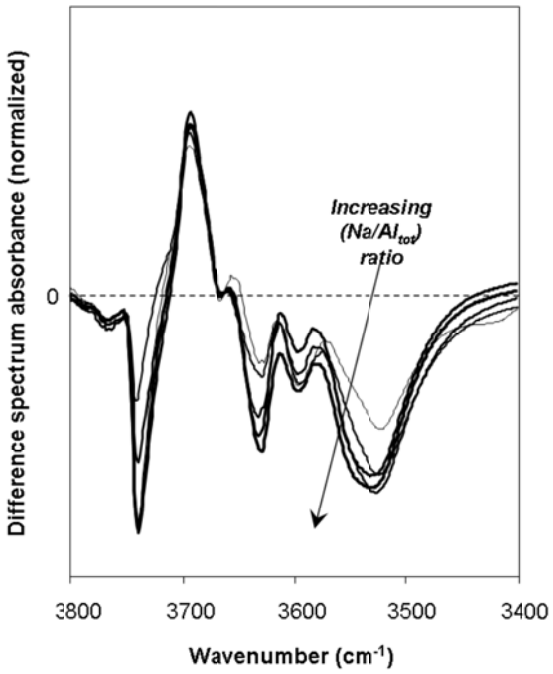


**Figure 8.14.** Difference IR spectra of H-USY samples with increasing Na/Al$_{tot}$ ratio (lighter to darker: 0.11, 0.13, 0.16, 0.20, 0.25) with respect to H-USY; absorbance normalized to framework vibrations (1750-2100 cm$^{-1}$).

### *8.6.4 Titration of $H^+$ Sites with Dimethyl Ether*

The number of $H^+$ sites on zeolite samples was determined by titration with dimethyl ether (DME) at 438 K, which reacts with $H^+$ sites to form surface $CH_3$ groups (0.5:1 stoichiometry) [35]. A mixture of DME and Ar (68% DME, 32% Ar, Praxair) was flowed (0.45 $cm^3\ s^{-1}$) through a sample loop (0.250 mL) and pulsed over zeolite samples in a He carrier stream (14.2 $cm^3\ s^{-1}\ g^{-1}$; 99.999%, Praxair) at 10 second intervals. Only Ar (m/z = 40) was detected in reactor effluent from initial pulses of DME over H-USY (Fig. 8.15), reflecting the fast and irreversible titration of $H^+$ with $CH_3$ on the timescale of the experiment. DME (m/z = 45) was only detected in the reactor effluent after all $H^+$ sites had been replaced with $CH_3$ groups. Thus, the number of $H^+$ sites was determined from the number of pulses for which DME did not appear in the effluent.

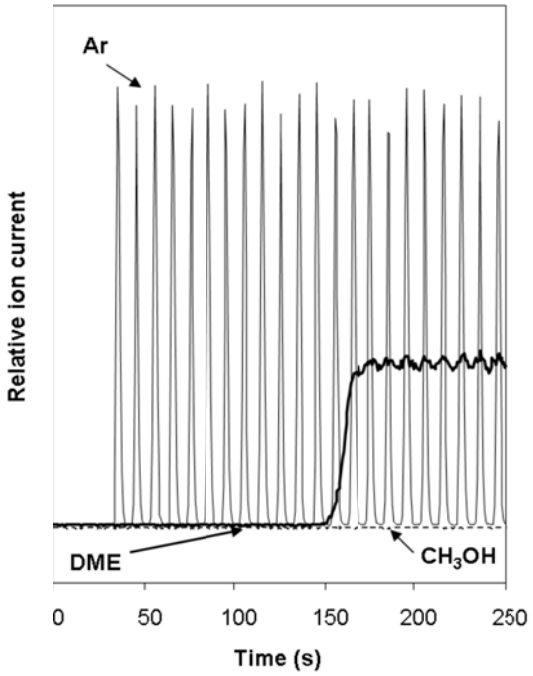


**Figure 8.15.** Mass spectra signals of Ar (m/z = 40; thin line), DME (m/z = 45; thick line) and $CH_3OH$ (m/z = 32; thin dotted line) during DME/Ar pulses on H-USY (438 K).

### *8.6.5 Mobility and Accessibility of $H^+$ Sites*

Here, we discuss in further detail the accessibility of $H^+$ sites in FAU zeolites to titrants that preferentially reside within supercages or sodalite cages. Infrared spectra of CD-HUSY show acidic OH groups vibrating in supercage (3630 $cm^{-1}$) and sodalite cage (3550 $cm^{-1}$) environments [10]. Spectra of CD-HUSY were recorded upon exposure to increasing amounts of pyridine at 298 K (Fig. 8.6) and 450 K (not shown); experimental details are given in section 2.2. Pyridine titrants are too large to enter sodalite cages, yet intensities of IR bands for both acidic OH groups decreased concurrently with increasing pyridine uptake and become undetectable at

pyridine/$Al_f$ uptakes of 0.8 (Fig. 8.6). These data are consistent with pyridine uptakes that would completely suppress $CH_3OH$ dehydration rates (0.8 pyridine molecules per $Al_f$; Fig. 8.5).

Monomolecular isobutane activation rate constants (per residual $H^+$; Fig. 8.8) were independent of $Na^+$ content on H-USY and CD-HUSY samples, indicating that $Na^+$ stoichiometrically titrates all protons, which are catalytically-equivalent within each sample. $Na^+$ titrants preferentially reside within sodalite cages [51], yet replace protons without preference, consistent with infrared spectra of Na-exchanged CD-HUSY (Fig. 8.3) and H-USY (Fig. 8.4) samples that show band areas for both supercage (3630 $cm^{-1}$) and sodalite cage (3550 $cm^{-1}$) OH groups that decrease concurrently with increasing $Na^+$ content.

Taken together, these data indicate that protons migrate across all four oxygen atoms connected to $Al_f$ atoms at identical T-sites on CD-HUSY ($Si/Al_f$ = 10.1; Table 8.5) at these conditions; in turn, protons can interact with reactant or titrant molecules that can only access FAU supercages. FAU zeolites with $Si/Al_f$ ratios below 5.8 would require the presence of $Al_f$ pairs [8], which may restrict proton mobility and cause some $H^+$ sites to reside permanently within sodalite cages. In such cases, pyridine preferentially titrates $H^+$ sites located within FAU supercages and cannot access all $H^+$ sites confined within sodalite cages, even at saturation uptakes [52]; thus, not all protons would be accessible to reactant molecules (e.g. isobutane) and participate in catalytic turnovers. The complex features present in the OH infrared spectrum of H-USY preclude a similar analysis upon titration with pyridine, but its low $Al_f$ content ($Si/Al_f$ = 6.1; Table 8.5) does not require the presence of paired $Al_f$ atoms. Therefore, it is reasonable to expect that all $Al_f$ atoms in H-USY are isolated from each other and that, in turn, all protons on H-USY are mobile and accessible to reactants or titrants that can reside only within supercages.

### *8.6.6 Monomolecular Isobutane Activation on Acidic Zeolites*

Isobutane activation by monomolecular routes form equimolar amounts of $CH_4$ and $C_3H_6$ from cracking steps, and $H_2$ and i-$C_4H_8$ from dehydrogenation steps. Measured first-order rate constants for isobutane cracking and dehydrogenation did not depend on space velocity and gave non-zero values upon extrapolation to zero residence time (Fig. 8.16), indicating that these products were formed in primary paths and did not enter secondary routes. Isobutane cracking led to the formation of $CH_4$ and $C_3H_6$ in equimolar ratios that did not depend on space velocity (Fig. 8.16), consistent with monomolecular cracking events. Monomolecular isobutane dehydrogenation led to the formation of i-$C_4H_8$, which was present in higher than equilibrium amounts relative to linear butene isomers at all space velocities tested; i-$C_4H_8$/1-$C_4H_8$ ratios decreased towards equilibrium ratios with increasing residence time, while ratios of 2-$C_4H_8$/1-$C_4H_8$ and cis-2-$C_4H_8$/trans-2-$C_4H_8$ isomers did not depend on space velocity (Fig. 8.17). These data indicate that skeletal isomerization between linear and branched $C_4H_8$ isomers is not equilibrated but double-bond isomerization among linear $C_4H_8$ isomers is equilibrated, consistent with $C_4H_8$ isomer distributions formed from monomolecular n-$C_4H_{10}$ dehydrogenation [44]. The absence of $C_{5+}$ species in product chromatograms confirmed the absence of bimolecular reactions over the range of space velocities and pressures studied.

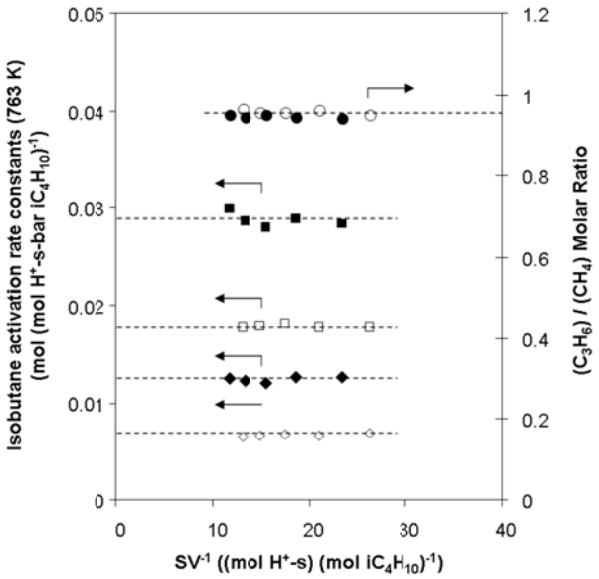


**Figure 8.16.** Measured rate constants (763 K) for monomolecular isobutane cracking (◆,◇) and dehydrogenation (■,□) and $(C_3H_6)/(CH_4)$ molar ratios (●,○) as a function of space velocity (SV) on (a) H-USY (closed symbols) and (b) CD-HUSY (open symbols).

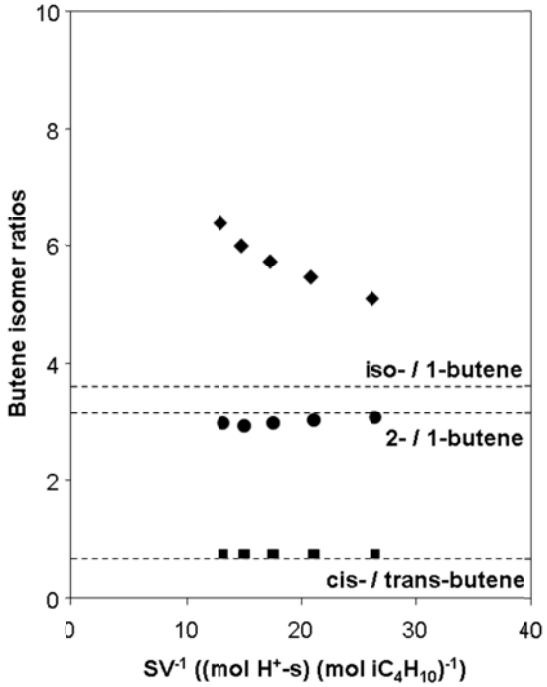


**Figure 8.17.** Distribution of butene isomers formed from monomolecular i-$C_4H_{10}$ dehydrogenation (763 K) on CD-HUSY as a function of space velocity (SV), shown as i-$C_4H_8$/1-$C_4H_8$ (◆), 2-$C_4H_8$/1-$C_4H_8$ (●) and cis-2-$C_4H_8$/trans-2-$C_4H_8$ (■) ratios. Horizontal dashed lines indicate equilibrium ratios (763 K).

*8.6.7 Methanol Dehydration to Dimethyl Ether on Brønsted Acids*

The effects of acid strength and van der Waals solvation on rate constants for $CH_3OH$ dehydration to DME on Brønsted acids have been examined in detail elsewhere [45]; here, we include an abridged version to supplement the discussion in this manuscript. Density functional theory calculations on tungsten Keggin polyoxometalate (POM) clusters indicate that $CH_3OH$ dehydration proceeds by the quasi-equilibrated adsorption of two $CH_3OH$ molecules at a proton to form protonated dimer intermediates (Steps 1-3, Scheme 8.3), which directly eliminate $H_2O$ and form DME in a single concerted kinetically-relevant step (Step 4, Scheme 8.3); DME then desorbs from the catalyst surface in a quasi-equilibrated step (Step 5, Scheme 8.3). Dehydration rates on Keggin POM clusters and zeolite H-BEA, normalized by the number of accessible protons determined from titrations with 2,6-di-*tert*-butylpyridine, were accurately described by Langmuir dependences on $CH_3OH$ pressure:

$$\frac{r}{\left[H^+\right]} = \frac{k_{mono} P_{CH_3OH}}{1 + \left(k_{mono}/k_{dimer}\right) P_{CH_3OH}} . \tag{8.22}$$

where $k_{mono}$ and $k_{dimer}$ are the measured first and zero-order rate constants, respectively.

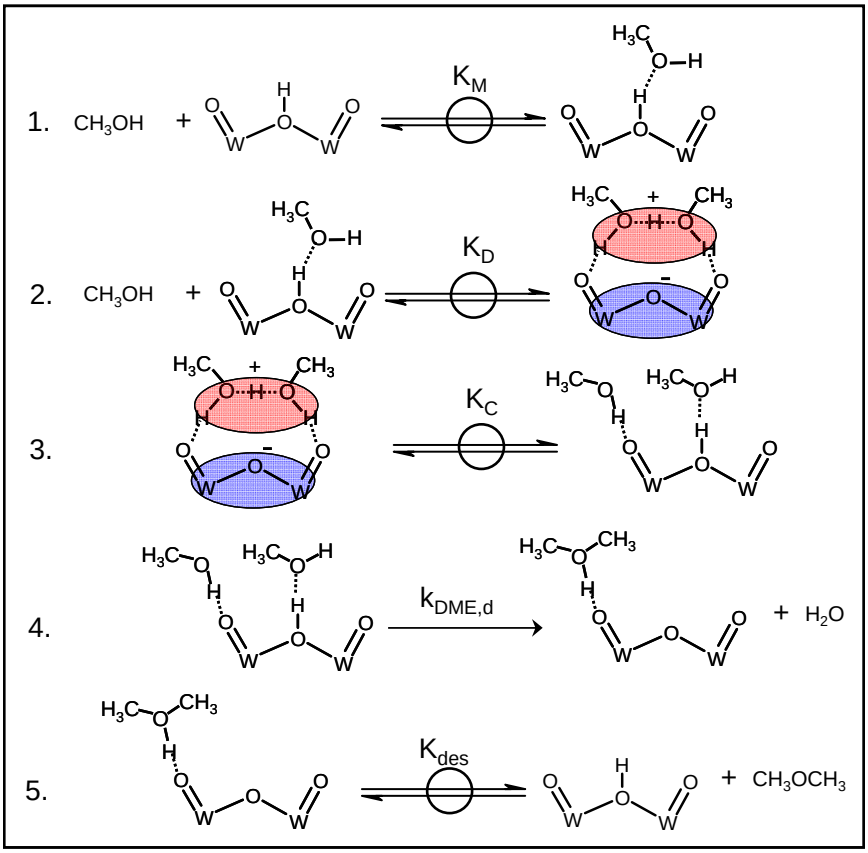


**Scheme 8.3.** Elementary steps for $CH_3OH$ dehydration on solid acids. Dashed lines represent H-bonding interactions (adapted from [45]).

The well-defined structure of Keggin POM clusters permits accurate calculations of their deprotonation energies (DPE), a rigorous and non-probe specific measure of Brønsted acid strength, from theoretical treatments. The DPE values for these clusters increase monotonically with decreasing central atom valence (P, Si, Al, Co) and increasing number of charge-compensating protons, without concomitant changes in structure. Rate constants for $CH_3OH$ dehydration measured on Keggin POM, together with those for H-BEA, whose DPE can also be estimated by theory [46], allowed for the development of relations between acid strength, composition, and function [45]. Values of $k_{dimer}$ reflect the free energies of DME formation transition states (Step 4, Scheme 8.3) relative to protonated dimers; they depend predominantly on DPE because the stabilization of transition states and dimers by van der Waals forces are similar. Values of $k_{mono}$ reflect the free energies of the same transition state with respect to one adsorbed $CH_3OH$ and one gas-phase $CH_3OH$ molecule; these values depend on DPE and solvation properties of the catalyst, which affect the stability of transition states and $CH_3OH$ monomers to different extents [45].

### *8.6.8 Assessment of Solvation Effects Among Acidic Zeolites From Methanol Dehydration Rate Constants*

Values of $k_{dimer}$ among H-USY, CD-HUSY and H-BEA zeolites are similar (within a factor of 1.3, Table 8.6), indicating that their acid sites are similar in strength. Yet, any differences among $k_{dimer}$ values, *if they were to depend solely on acid strength (DPE)*, would also be reflected in $k_{mono}$ values because they depend on both DPE and solvation effects. Relations developed elsewhere between methanol dehydration rate constants and DPE values indicate that $k_{dimer}$ values are *less sensitive* to DPE ($d[\ln(k_{dimer})]/d(DPE) = -0.028$) than $k_{mono}$ ($d[\ln(k_{mono})]/d(DPE) = -0.093$) [45], because changes in acid strength similarly influence the energies of charged DME formation transition states and charged $CH_3OH$ dimer intermediates, but not relatively uncharged $CH_3OH$ monomers.

**Table 8.6.** Measured $CH_3OH$ dehydration (433 K) zero-order ($k_{dimer}$) and first-order ($k_{mono}$) rate constants on H-USY, CD-HUSY and H-BEA. Values of $k_{mono,Zhyp}$ calculated using Eq. (8.25) and of $\chi$ using Eq. (8.26).

| Zeolite | $k_{dimer}$ ($/10^{-3}$ (mol DME) (mol $H^+$-s)$^{-1}$) | $k_{mono}$ ($/10^{-3}$ (mol DME) (mol $H^+$-kPa $CH_3OH$-s)$^{-1}$) | $k_{mono,Zhyp}$ ($/10^{-3}$ (mol DME) (mol $H^+$-kPa $CH_3OH$-s)$^{-1}$) | $\chi$ |
|---|---|---|---|---|
| H-BEA | 2.9 | 0.96 | 0.11 | 8.5 |
| H-USY | 4.1 | 0.94 | 0.36 | 2.6 |
| CD-HUSY | 3.8 | 0.28 | 0.28 | 1.0 |

Here, we examine the effects of solvation in H-USY (or in H-BEA), relative to CD-HUSY ($Z_{ref}$), by comparing its measured $k_{mono}$ value (Table 8.6) to the expected $k_{mono}$ value for a hypothetical CD-HUSY zeolite ($Z_{hyp}$) with the DPE required to give the measured $k_{dimer}$ value on H-USY. If the sensitivities of $k_{dimer}$ and $k_{mono}$ values on DPE are assumed to be the same as found on POM clusters, then the rate constants on $Z_{hyp}$ are given by:

$$\ln\left(\frac{k_{dimer,Z_{hyp}}}{k_{dimer,Z_{ref}}}\right)=\left(-0.028\right)\left(DPE_{Z_{hyp}}-DPE_{Z_{ref}}\right), \tag{8.23}$$

$$\ln\left(\frac{k_{mono,Z_{hyp}}}{k_{mono,Z_{ref}}}\right)=\left(-0.093\right)\left(DPE_{Z_{hyp}}-DPE_{Z_{ref}}\right). \tag{8.24}$$

Combining Eqs. (8.23) and (8.24) gives:

$$\ln\left(\frac{k_{mono,Z_{hyp}}}{k_{mono,Z_{ref}}}\right)=\left(\frac{-0.093}{-0.028}\right)\ln\left(\frac{k_{dimer,Z_{hyp}}}{k_{dimer,Z_{ref}}}\right). \tag{8.25}$$

Thus, the measured $k_{dimer}$ values on H-USY ($k_{dimer,Z_{hyp}}$) and on CD-HUSY ($k_{dimer,Z_{ref}}$), together with the measured $k_{mono}$ value on CD-HUSY ($k_{mono,Z_{ref}}$) and Eq. (8.25), can be used to calculate $k_{mono,Z_{hyp}}$ values (Table 8.6).

In turn, any *differences* in solvation between H-USY (or H-BEA) and CD-HUSY are reflected in the ratio of measured-to-expected $k_{mono}$ values, defined by the parameter $\chi$:

$$\chi=\frac{k_{mono}}{k_{mono,Z_{hyp}}}, \tag{8.26}$$

where values of $\chi$ greater than unity reflect stronger solvation effects relative to CD-HUSY, and vice versa. Values of $\chi$ are 2.6 on H-USY and 8.5 on H-BEA (Table 8.6), indicating that solvation effects are stronger, and pore sizes concomitantly smaller, on H-BEA (~0.7 nm diameter channels) than on H-USY than on CD-HUSY (~1.3 nm diameter supercages).

## 8.7 References


(1) Kerr, G. T. *J. Phys. Chem.* **1967**, *71*, 4155.
(2) Kerr, G. T. *J. Phys. Chem.* **1968**, *72*, 2594.
(3) Kerr, G. T. *J. Catal.* **1969**, *15*, 200.
(4) Kerr, G. T. *J. Phys. Chem.* **1969**, *73*, 2780.
(5) Sierka, M.; Eichler, U.; Datka, J.; Sauer, J. *J. Phys. Chem. B* **1998**, *102*, 6397.
(6) Sohn, J. R.; Decanio, S. J.; Fritz, P. O.; Lunsford, J. H. *J. Phys. Chem.* **1986**, *90*, 4847.
(7) Beyerlein, R. A.; McVicker, G. B.; Yacullo, L. N.; Ziemiak, J. J. *J. Phys. Chem.* **1988**, *92*, 1967.
(8) Barthomeuf, D. *Mater. Chem. Phys.* **1987**, *17*, 49.
(9) Shertukde, P. V.; Hall, W. K.; Dereppe, J. M.; Marcelin, G. *J. Catal.* **1993**, *139*, 468.
(10) Xu, B.; Bordiga, S.; Prins, R.; van Bokhoven, J. A. *Appl. Catal. A* **2007**, *333*, 245.
(11) McDaniel, C. V.; Maher, P. K. U. S., 1966.
(12) McDaniel, C. V.; Maher, P. K. U. S., 1969.
(13) Biaglow, A. I.; Parrillo, D. J.; Kokotailo, G. T.; Gorte, R. J. *J. Catal.* **1994**, *148*, 213.
(14) Lonyi, F.; Lunsford, J. H. *J. Catal.* **1992**, *136*, 566.
(15) Beyerlein, R. A.; McVicker, G. B.; Yacullo, L. N.; Ziemiak, J. J. *Preprints - ACS* **1986**, 190.
(16) Fritz, P. O.; Lunsford, J. H. *J. Catal.* **1989**, *118*, 85.
(17) Barthomeuf, D.; Beaumont, R. *J. Catal.* **1973**, *30*, 288.
(18) Kung, H. H.; Williams, B. A.; Babitz, S. M.; Miller, J. T.; Snurr, R. Q. *Catal. Today* **1999**, *52*, 91.
(19) Williams, B. A.; Miller, J. T.; Snurr, R. Q.; Kung, H. H. *Microporous Mesoporous Mater.* **2000**, *35-6*, 61.
(20) Williams, B. A.; Ji, W.; Miller, J. T.; Snurr, R. Q.; Kung, H. H. *Appl. Catal. A* **2000**, *203*, 179.
(21) Williams, B. A.; Babitz, S. M.; Miller, J. T.; Snurr, R. Q.; Kung, H. H. *Appl. Catal. A* **1999**, *177*, 161.
(22) Skeels, G. W.; Breck, D. W. U. S., 1987.
(23) Corma, A.; Fornes, V.; Rey, F. *Applied Catal.* **1990**, *59*, 267.
(24) Sohn, J. R.; Decanio, S. J.; Lunsford, J. H.; Odonnell, D. J. *Zeolites* **1986**, *6*, 225.
(25) Jorik, V. *Zeolites* **1993**, *13*, 187.
(26) Baertsch, C. D.; Komala, K. T.; Chua, Y. H.; Iglesia, E. *J. Catal.* **2002**, *205*, 44.
(27) Kraus, H.; Muller, M.; Prins, R.; Kentgens, A. P. M. *J. Phys. Chem. B* **1998**, *102*, 3862.
(28) Pellet, R. J.; Blackwell, C. S.; Rabo, J. A. *J. Catal.* **1988**, *114*, 71.
(29) Omegna, A.; van Bokhoven, J. A.; Prins, R. *J. Phys. Chem. B* **2003**, *107*, 8854.
(30) Omegna, A.; Prins, R.; van Bokhoven, J. A. *J. Phys. Chem. B* **2005**, *109*, 9280.
(31) Breck, D. W. *Zeolite Molecular Sieves*; John Wiley & Sons: New York, **1974**.
(32) Xu, B.; Rotunno, F.; Bordiga, S.; Prins, R.; van Bokhoven, J. A. *J. Catal.* **2006**, *241*, 66.
(33) Eder, F.; Stockenhuber, M.; Lercher, J. A. *J. Phys. Chem. B* **1997**, *101*, 5414.
(34) Borovkov, V. Y.; Alexeev, A. A.; Kazansky, V. B. *J. Catal.* **1983**, *80*, 462.
(35) Cheung, P.; Bhan, A.; Sunley, G. J.; Iglesia, E. *Angew. Chem. Int. Ed.* **2006**, *45*, 1617.
(36) van Bokhoven, J. A.; Roest, A. L.; Koningsberger, D. C.; Miller, J. T.; Nachtegaal, G. H.; Kentgens, A. P. M. *J. Phys. Chem. B* **2000**, *104*, 6743.
(37) Hunger, M.; Engelhardt, G.; Weitkamp, J. *Microporous Mater.* **1995**, *3*, 497.

(38) Gounder, R.; Iglesia, E. *Angew. Chem. Int. Ed.* **2010**, *49*, 808.
(39) Lombardo, E. A.; Hall, W. K. *J. Catal.* **1988**, *112*, 565.
(40) Stefanadis, C.; Gates, B. C.; Haag, W. O. *J. Mol. Catal.* **1991**, *67*, 363.
(41) Milas, I.; Nascimento, M. A. C. *Chem. Phys. Lett.* **2003**, *373*, 379.
(42) Kazansky, V. B.; Frash, M. V.; van Santen, R. A. *Appl. Catal. A* **1996**, *146*, 225.
(43) Zheng, X. B.; Blowers, P. *J. Phys. Chem. A* **2006**, *110*, 2455.
(44) Gounder, R.; Iglesia, E. *J. Am. Chem. Soc.* **2009**, *131*, 1958.
(45) Carr, R. T.; Neurock, M.; Iglesia, E. *J. Catal.* **2011**, *278*, 78.
(46) Brändle, M.; Sauer, J. *J. Am. Chem. Soc.* **1998**, *120*, 1556.
(47) Sauer, J.; Sierka, M. *J. Comput. Chem.* **2000**, *21*, 1470.
(48) Eder, F.; Lercher, J. A. *J. Phys. Chem.* **1996**, *100*, 16460.
(49) Cotterman, R. L.; Hickson, D. A.; Cartlidge, S.; Dybowski, C.; Tsiao, C.; Venero, A. F. *Zeolites* **1991**, *11*, 27.
(50) Fichtner-Schmittler, H.; Lohse, U.; Engelhardt, G.; Patzelova, V. *Cryst. Res. Technol.* **1984**, *19*, K1.
(51) Frising, T.; Leflaive, P. *Microporous Mesoporous Mat.* **2008**, *114*, 27.
(52) Khabtou, S.; Chevreau, T.; Lavalley, J. C. *Micropor. Mater.* **1994**, *3*, 133.